An Analysis of Contact Stiffness and Frictional Receding Contacts

Thesis subimitted for the degree of DPhil in Engineering Science

Kurien Stephen Parel

Christ Church

University of Oxford

Michaelmas 2017

Acknowledgements

Research presented in this doctoral thesis was supervised by Prof David Nowell and Prof David Hills. Prof Nowell provided guidance on the investigation into contact stiffness properties, the subject of Part II of this thesis, while Prof Hills advised on the study of receding contacts, described in Part III. Dr Robert Paynter contributed to discussions in relation to Part II as well as Chapter 6 of Part III, and brought me up to speed regarding the operation of testing equipment. Technicians, Neil Warland and Wolfgang Mix, made the components and assisted with the alignment of the experimental rig described in Chapter 2. Jeffrey Fullerton made the surfaces for some of the test pads with EDM.

Funding for this research work was provided by Technology Strategy Board grant (SILOET II), Rolls Royce research funding, and grants from Christ Church.

I would like to thank Dr Kiran Vijayan who provided me encouragement and advice from start to finish and my colleagues at the Solid Mechanics group and Christ Church. In particular, I would like to acknowledge Dr Ananya Renuka Balakrishna and Dr Elsiddig Elmukashfi, for their conversation and support throughout the years, as well as Jack Kelly, Alex Pappas, and Alex Phillips — my friends from Christ Church. I would also like to thank Dr Rodolfo Fleury, Dr Jianan Hu, and João Sahadi for being excellent colleagues. Dr Matthew Ryder provided much needed comic relief in the last few months, as did discussions with my numerous friendly colleagues in the Solid Mechanics group throughout the years: Dr Tuncay Yalçinkaya, Dr Kwanlae Kim, Dr Yueting Sun, Dr Mahdi Mahmoud, Rangarajan Ramesh, Suchandrima Das, Hendrick Andresen, Marzena Tkaczyk, Jimmy Chen and many others.

My aunt, Amenia Joseph, cheered me along the DPhil, while undertaking cancer treatment, succumbing only a few months before I submitted my thesis. My father, Dr Stephen Parel has supported my academic endeavours throughout. The start of this doctoral programme coincided with the formal diagnosis of my grandfather with dementia. His gradual mental decline was concurrent with my progress in this course. He passed away a month before the *viva voce*. My grandmother, burdened with the care for my grandfather, also passed away during this period of study. Since my grandparents encouraged and supported me the most, more so than anyone else, it has been my intention for sometime, even before they died, to dedicate this thesis to them.

For Prof Jacob Joy and Mrs Elsie Joy,

Thottathikunnath Mannully

Just like moons and like suns,

With the certainty of tides,

Just like hopes springing high,

Still I'll rise.

— Maya Angelou

Abstract

The relationship between interfacial displacement and load for rough contacts is determined by the contact stiffness. The tangential contact stiffness for ground Ti-6Al-4V surfaces is measured to linearly decrease with the application of tangential load, approaching zero at slip. At the beginning of the application of tangential load, for ground surfaces, the ratio of the tangential contact stiffness to the normal contact stiffness is seen to be approximately half the Mindlin ratio, consistent with many other published experimental studies. Measurements of normal contact stiffness for ground surfaces conform to a model that posits a linear relationship between normal contact stiffness and normal load. An equivalent surface roughness parameter is defined for two surfaces in contact; and the normal contact stiffness for ground surfaces is observed to be inversely proportional to this parameter. These results indicate a straightforward means to estimate both normal and tangential contact stiffness at different loads for ground surfaces of known surface roughness.

Single asperity models were constructed to simulate the effect of different frictional laws and plasticity on the tangential displacement of an asperity contact. Further, multi-asperity modelling showed the effect of different normal load distributions on the tangential behaviour of interfaces. In addition, normal contact stiffness was modelled for a grid of asperities in which asperity interaction was permitted, i.e. displacement at an asperity was affected by the loading at all asperity contacts.

The second part of the thesis analyses plane receding contacts, assuming linear elasticity, and perfectly smooth interfaces with a friction law. Receding contacts, though ubiquitous in mechanical and structural components, such as in bolted joints, are difficult to model with conventional methods such as finite elements. One promising method of analysis is the distributed dislocation technique. However, current methods require the distribution of dislocations to be bounded to zero or singular at the ends of the area of application, which is not appropriate to model many receding contacts. A receding contact problem for which the required form of the distributed dislocations is bounded-bounded was solved. Then, a fundamental 2D frictional receding contact problem involving a homogeneous linear elastic infinite layer pressed by a line load onto a half-plane of the same material was analysed. This was done by the insertion of preformed distributed dislocations (or eigenstrains), which take into account the correct form of the separation of the interface at points away from the area of loading, along with corrective bounded-bounded distributions. The general method of solution was further refined and adapted to solve three other receding contact problems. The solutions demonstrated the robustness and applicability of this new procedure.

Contents

Nomenclature

β_n	Fit parameter equal to the slope of the normal load and normal contact stiffness relationship.
β_t	Fit parameter equal to the slope of the tangential load and tangential contact stiffness relationship.
Δ_n	Reference tangential displacement
Δ_x	Tangential displacement
κ	Kolosov's constant
μ	Modulus of rigidity
ν	Poisson's ratio
σ_v	Maximum von Mises stress if the material were purely elastic
σ_y	Yield stress
σ_{rms}	Standard deviation of unloaded interface gap
$\sigma_{xyA}(x)$, $\sigma_{yyA}(x)$	Traction components due to preformed climb dislocation distribution
$\sigma_{xyb(x)}$, $\sigma_{yyb}(x)$	Bilateral traction components
a	Location of the slip-stick transition point
A_c	Real contact area
A_n	Nominal contact area
b	Location of the slip-separation transition point
b_x	Burgers vector for a discrete glide dislocation
$B_x(x)$	Glide dislocation density
b_y	Burgers vector for a discrete climb dislocation
$B_y(x)$	Climb dislocation density
c	Thickness of the infinitely long layer
C_c	Coupling constant, the ratio K_{t0}/K_n
E	Young's modulus
e	Location of an arbitrarily chosen remote point
f	Coefficient of friction
h_{rms}	Long wavelength root mean square roughness parameter derived from the roughness power spectrum
k_l	Slope of the layer interface at remote points
K_n	Normal contact stiffness
K_t	Tangential contact stiffness
K_{bn}	Normal bulk stiffness
K_{bn}	Tangential bulk stiffness
K_{t0}	Tangential contact stiffness at zero tangential load
K_{tn}	Total normal stiffness
K_{tt}	Total tangential stiffness
$N(x)$	Normal traction
P	Normal load
p	Pressure
P_0	Fit parameter equal to the normal load at zero normal contact stiffness, as per model
p_0	Maximum normal pressure in an Hertzian contact
P_n	Normal load applied to rough interfaces
p_n	Nominal normal interface pressure P_n/A_n
P_t	Total normal load as the sum of normal loading applied to all the asperities

Q Tangential load

Q_n Reference tangential load

Q_s Fit parameter equal to the tangential load at slip

Q_t Tangential load applied to rough interfaces

R Radius of curvature

R_a, R_q and R_z Profile roughness parameters

r_c Contact radius

$S(x)$ Shear traction

S_a, S_q and S_z Areal roughness parameters

S_q^e An equivalent roughness parameter to characterise two rough surfaces in contact

$u_1(x)$ and $v_1(x)$ Tangential and vertical displacement of the half-plane contact surface

$u_2(x)$ and $v_2(x)$ Tangential and vertical displacement of the layer contact surface

u_c Tangential contact displacement

$U_g(x)$ Gap between rough interfaces

U_m Mean interface gap

v_c Normal contact displacement

w Width of the pressure patch or the no-pressure zone

DDT Distributed Dislocations Technique

FEA Finite Element Analysis

Note on shorthand used:

1. In Chapter 3, $\check{v} \equiv v/r_c$, where v is any variable.
2. In Part III, $\hat{v} \equiv v/c$, where v is any variable.

Part I

Introduction

Introduction

Analysis of contact interface is of both theoretical and practical interest. Even now many fundamental properties of surfaces in contact, such as the nature of friction, remain unanswered [1]. Knowledge of the behaviour of solids in contact is required for many practical purposes, such as for predicting wear, formation of cracks, and vibration analysis, particularly in safety-critical applications, such as for jet turbine design in the aerospace industry. This thesis investigates key questions in two fundamental areas of contact mechanics where there is a current lack of knowledge– the properties of contact interface stiffness and the behaviour of receding contacts. Both problems have significance to the modelling of practical situations. Contact stiffness properties affect not only contact tractions, which are used in many contact models to predict failure, such as by fretting fatigue, but also are known to effect the natural frequency of a system, which is an important parameter in designing systems, such as engines, without excessive operational vibration [2]. Receding contacts, despite the lack of literature on them, are ubiquitous in mechanical and structural components, such as in bolted joints, and knowledge of their properties is relevant to predict the structural performance of various components.

Contact analysis is usually performed by either assuming the contact is perfectly smooth or by recognising that real interfaces, despite appearances, are rough and involve the contact of several asperities. Contact stiffness is a parameter that describes the interface displacement behaviour with loading when the interface is modelled as rough. Further, contacts between surfaces are are classified into three types– incomplete, complete and receding [3, p.40]. See Figure 1. In incomplete contacts the contact area is not defined by the geometry of the contact interface and increases with the application of normal load. The Hertzian contact between a sphere and a half-space would be an example. In complete contacts, the geometry of at least one of the contact interfaces determines the contact area, and the contact area remains the same regardless of normal loading. For instance the contact between a block and a half-space is a complete contact. Receding contacts are those contact interfaces for which the contact area reduces with the application of load, such as a layer pressed on half-space. In many cases the reduction in contact area is discontinuous with significant area of the interface coming out of contact with the application of an infinitesimal normal load, making

these contacts very difficult to model, such as with finite elements. Despite receding contacts being one of the three major types of contact and present in a variety of components (a bolted joint for example), the existing literature on them is sparse, particularly with regards to its fundamental frictional behaviour.

This thesis is divided into four parts. Part I is the current part– the introduction. The results of the investigation into contacts as rough interfaces such as regarding contact stiffness properties are presented in Part II. The analysis of receding contacts with theoretically smooth interefaces is presented in Part III. Part IV is the conclusion.

Part II of this thesis deals with investigation into the properties of rough contacts, particularly in relation to the contact stiffness properties of Ti-6Al-4V interfaces. Chapter 1 provides a detailed introduction and literature review for the measurement and modelling of rough contact interfaces. Chapter 2 details the experimental process used and the analysis of the results from the measurement of contact stiffness values for Ti-6AL-4V interfaces. Chapter 3 describes the asperity level analysis conducted to understand mechanisms underlying contact stiffness properties.

The research questions addressed in Part II are the following

1. Regarding contact stiffness properties of Ti-6Al-4V interfaces:
    - What is the observed form of the relationship between normal loading and normal contact stiffness?
    - What is the observed form of the relationship between tangential loading and tangential contact stiffness, at a given normal load?
    - How does experimental measurements of contact stiffness relate to theoretical models, such as regarding the effect of loading and surfaces roughness?
    - How can surface textures affect the contact stiffness for Ti-6Al-4V interfaces?
2. Regarding theoretical asperity to asperity contact properties
    - For linear elastic asperities in contact how does different friction laws affect the tangential displacement and tangential load relationship?
    - How is this relationship affected when plastic yielding is permitted?
    - For interfaces with multiple asperity contacts, how do different asperity normal loading distributions affect the tangential displacement and tangential load relationships for these interfaces?
    - When asperity interactions are permitted, i.e. the displacements on each asperity is affected by loading on other asperity locations, what is the normal load and normal contact stiffness relationship for a given contact area?

The key findings from Part II are as follows.

1. For ground Ti-6Al-4V interfaces, the tangential contact stiffness is seen to be linearly related to tangential load, and the normal contact stiffness is seen, consistent with published models, linearly related to normal load. Furthermore the experimental measurements imply that the ratio of the tangential contact stiffness and normal contact stiffness at the zero tangential loading is a constant independent of normal loading, consistent with theoretical models. The coefficients of friction deduced from the tangential contact stiffness and tangential load relationship for the interfaces were seen to be around 0.2, which is the expected values for these surfaces. Further the normal contact stiffness is seen to have an inverse relationship with surface roughness, consistent with published models. For surfaces with structured textures, the normal contact stiffness was not seen affected by surface texturing but the tangential contact stiffness appeared to be affected.

2. The results of the theoretical investigation into asperity contact properties indicated for a range of loading, with appropriate normalisation used, the Coulomb friction relationship between tangential load and tangential displacement of two asperities in contact can be used to approximate the relationship with different interface laws. Further, the relationship for stuck elastic asperities in contact can also approximate the relationship when plasticity is permitted with an appropriate change in normalisation. The effect of different load distributions on the asperity contacts for a multi-asperity interface can be approximated at certain loads by that of a single asperity interface with an appropriate multiplier. Finally a model of normal contact stiffness is derived which can be used to estimate the normal contact stiffness when the real to apparent contact area and the number of asperity contacts are known. This model permits 'asperity interaction'.

Part III of this thesis presents the results from the analysis of theoretically perfectly smooth interfaces between semi-infinite surfaces, to analyse the fundamental frictional behaviour of receding contacts. Research questions addressed in this part are the following

- How can the distributed dislocations technique be used to deduce the contact tractions and interface displacements in a receding contact situation?

- What are the tractions and the interface displacements for the most fundamental 2D receding contact problem of the semi-infinite layer on a half-plane loaded by a line load?

- How can distributed dislocations densities be inserted to solve receding contact problems that involve separation at remote points?

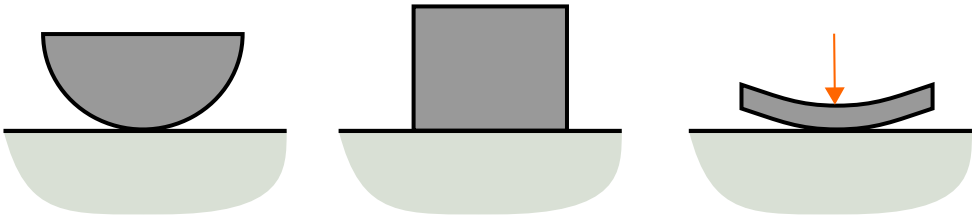

Figure 1: The three types of contacts.

Chapter 4 provides an introduction and literature review for receding contacts. The distributed dislocations technique is an analytical method to analyse contact and crack behaviour. It is applied in Chapter 5 to solve a receding contact problem using the standard methods that allow for the insertion of bounded-bounded distributions of dislocations along the contact interface. In Chapter 6 a new procedure is developed so that distributions of dislocations can be used to model a fundamental receding contact problem of an infinitely long linear elastic layer pressed by a line load onto a half-plane with a frictional interface, that involves the separation of surfaces at all remote points. This method is further refined and applied to solve three further receding contact problems with three different pressure distributions in Chapter 7, to show the applicability of this new procedure to different receding contact problems. Chapter 8 presents the results of some finite element modelling of receding contacts. The results are compared with the values obtained by the analysis with distribution of dislocations.

The key findings from Part III are

1. Solutions for the contact tractions and the interface displacements were found for all five problems by the insertion of distributions of dislocations.

2. A new procedure was developed in Chapter 6 to insert distributions of dislocations to account for the lift-off the layer at remote points, and was shown in Chapter 7 to be applicable in the study of other receding contact problems.

3. Finite element modelling for contacts of finite dimensions showed good agreement with the solutions from the distributed dislocation technique. This supported the analysis with distributions of dislocations and demonstrated that the solutions obtained are applicable to some contacts of finite dimensions.

Part IV is the conclusion. It provides a summary of the main findings of this thesis with their limitations and suggestions for future work.

Part II

Analysis of Rough Contacts

Chapter 1

Introduction to Rough Contacts and Literature Review

1.1 Introduction

When two bodies in contact are subject to loading, the relative displacements of points on either side of the contact is greater in actuality than that predicted by a theoretical model that assumes the contact interfaces are perfectly smooth. This is because real contact surfaces are rough and higher stress states at asperity tips lead to a greater displacement of points near the contact region under loading [4]. This additional relative normal displacement of two points orthogonally on either side of the contact interface due to the presence of the contact is defined for the purposes of this study as the normal contact displacement, u_c, and the additional tangential displacement when tangential loading is applied is defined as the tangential contact displacement, v_c. The slope of the normal load, $-P_n$, and normal contact displacement relationship provides the normal contact stiffness, K_n, at that loading. Similarly, the slope of the tangential load, Q_t, and tangential contact displacement, v_c, provides the tangential contact stiffness value, K_t [4].

For plane contacts the difference between the total compliance of two bodies in contact and the bulk compliance (the compliance if the two objects were fused as one in the case of plane contacts) gives the contact compliance. The reciprocal of contact compliance is the contact stiffness. Therefore for two bodies in contact (see Figure 1.1), K_{tn} is the total normal stiffness, K_{bn} is the normal bulk stiffness, K_{tt} is the total tangential stiffness, and K_{bt} is the tangential bulk stiffness, the normal contact stiffness, K_n, is given by

$$\frac{1}{K_n} = \frac{1}{K_{tn}} - \frac{1}{K_{bn}}, \tag{1.1}$$

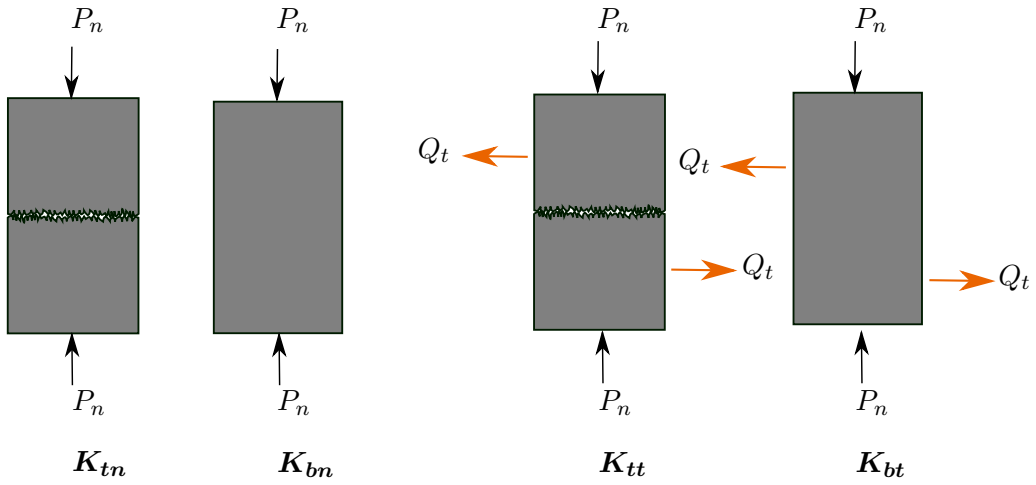

Figure 1.1: For two bodies under normal load (top), the relationship between normal contact stiffness and the total normal stiffness and the normal bulk stiffness is given by equation (1.1). Under both normal and tangential loading (bottom), the relationship between tangential contact stiffness and the total tangential stiffness and the tangential bulk stiffness is given by equation (1.2).

and the tangential contact stiffness, K_t, is given by

$$\frac{1}{K_t} = \frac{1}{K_{tt}} - \frac{1}{K_{bt}}. \tag{1.2}$$

Contact stiffness is an important parameter for many applications. Contact stiffness properties are believed to affect damping, wear, heat transfer, electric conductance and also tire noise in a tire-road contact [5]. Significantly for industry, contact stiffness values are required for calculations of natural frequencies of systems [2] such as in turbines, for vibration modelling. Also of practical importance, most contact models neglect contact compliances in the computation of the contact tractions, which feed into the modelling of failure mechanisms such as fretting fatigue and wear. Knowledge of contact stiffness can assist in calculating contact tractions more accurately and therefore improve the accuracy of these models. Furthermore, models of the properties of both static and sliding friction, such as rate and state models, recognise that both coefficients of friction are dependent on the loading and interaction history of the interfaces [6] [7] [8]. Knowledge of tangential contact stiffness relationship with tangential load can be used to find the relative interface displacements and loading up till the onset of sliding, and is likely to be relevant in the study of the fundamental the properties static and sliding friction [8] [9].

Though there are many models and published measurements of normal and tangential contact stiffness with normal load (see Section 1.3) there is a dearth of studies on the effect of tangential loading on tangential contact stiffness. Furthermore, due to the small displacements (sub micron) involved, particularly for metal interfaces, contact stiffness measurements have been prone to sig-

nificant errors due to external compliances affecting the displacement measurement system. More recently digital image correlation has shown promise in measuring displacements very near to the contact interface accurately without the measurements being affected by external compliances [10]. However no serious attempt has been made to construct a model of contact stiffness from the measurements made with digital image correlation or to relate the measurements with theoretical models. This present study aims to find an empirical relationship between normal and tangential loading (applied quasi-statically) and surface texture parameters of the interfaces with normal and tangential contact stiffness, for Ti-6Al-4V interfaces. Recently Medina et al. using asperity modelling developed a theoretical model that relates contact stiffness properties to surface texture and normal loading [4]. The results from the contact stiffness measurements is provided in Chapter 2. The measurement results are compared with the predictions of this and other published models.

To further the understanding of the underlying mechanisms that are likely to contribute to contact stiffness properties, two single asperity models and two multi-asperity models were constructed. These models and the results from them are discussed in Chapter 3.

The definition of contact stiffness used in Chapter 2 was chosen to ensure the contact stiffness values measured were isolated from the effects of bulk compliances. Some discussion is required regarding how the definition used in this study relates to the definitions used in other experimental measurements and published models. This is provided is Section 1.2. Section 1.3 provides an overview of published theoretical contact stiffness models, and Section 1.4 provides a summary of various experimental methods used to measure contact stiffness values.

1.2 Note on the Definition of Contact Stiffness

It should be noted that the definition of contact displacement used in this study differs from that used in other studies. Mulvihill et al. measured contact stiffness using the displacement of two points on either side of the contact interface and noted the relative distance of the chosen points affected the measurement of contact stiffness, particularly at high loads [10]. This effect is due to bulk deformation of material between the two points and the definition adopted in this current study reflects the need to ensure the contact displacement measured is unaffected by bulk deformation.

Furthermore, contact models by Persson and many others define normal contact stiffness as the differential of normal load with respect to the mean interfacial separation (or mean gap) between the surfaces in contact. The mean gap is the expectation of the gap, $< U_g(x) >$, where $U_g(x)$ is the gap between the surfaces at coordinate x (i.e. the distance between the mean surface height lines of both surfaces). In effect, contact displacement in these models is the relative displacements of the mean surface lines. While this definition may be useful for constructing contact models to

understand contact stiffness relations, laboratory measurement of the mean gap between surfaces for two rough surfaces is in many cases impractical. Where measurements have been conducted, one of the surfaces is nominally smooth and the other is assumed relatively rigid. Wang et al. for instance compared their theoretical model with the results from the measurement of normal contact stiffness for rubber pressed against asphalt. Knowing the surface profile of asphalt from surface profilometry and assuming the rubber contact surface is perfectly smooth, or sufficiently so, and the asphalt surface is relatively rigid (i.e. location of its mean surface height line is assumed not change during testing), by measuring the displacement of the rubber interface, the mean gap between the interfaces was found at given loads [5].

The definition of contact stiffness used in this study is more practical in the sense it can be measured more straightforwardly in a laboratory setting when there are two rough surfaces in contact, since it can be computed from the displacement field near the contact interface, without asperity level measurements. Nonetheless since the definition of contact displacement used in this study and in the Persson and similar models are related to the relative displacements of points very near and on either side of the contact interface, the values of contact displacement as per the two definitions are probably similar.

Other studies such as by Shi and Polycarpou [11] do not clearly distinguish between bulk and contact stiffness. For instance Shi and Polycarpou define the contact stiffness for a smooth Hertizian contact as the differential of the relative approach with normal loading. In many cases, particularly with low loads and certain geometries the effect of bulk deformation may be negligible, and therefore comparability of results is dependent on the loading and geometry. Asperity models of contact interface of the Greenwood and Williamson kind tend to define contact displacement as the relative approach of the asperities in contact, or the relative displacement of the mean asperity height [4][11]. The contact displacement values from these models should be comparable to the values from the current study, since these models assume the bulk of the material is rigid, and the relative approach is only due to the deformation due to the presence of asperity contacts. See Figure 1.2 for illustration of the different definition of normal contact displacement.

There are not many published studies on tangential contact stiffness measurement or modelling, but similar care needs to be taken to isolate the effect of the bulk matter deformation when comparing results.

1.3 Models of Contact Stiffness Properties

In general, interface models to study contact stiffness properties can be classified into to two types: asperity based models, such as models of the Greenwood and Williamson kind, and models that

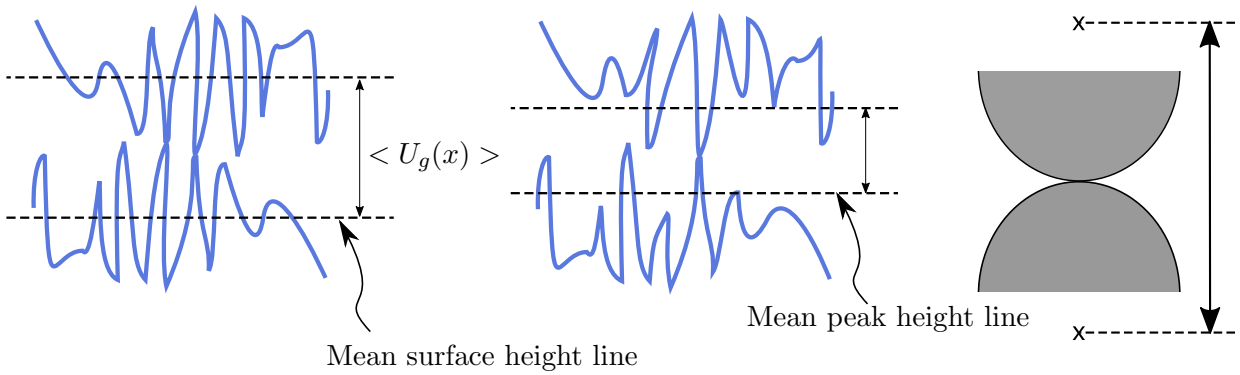

Figure 1.2: Different definitions of normal contact displacements. **Left**: contact displacement is defined as the change in the mean gap, $< U_g(x) >$, or the change in the distance between the mean surface lines. **Middle**: contact displacement is defined as the change in the distance between lines drawn at the locations of the average asperity heights of both surfaces. **Right**: contact displacement is defined as the relative approach of remote points away from the contact interface.

take into account the fractal nature of the surfaces, such contact interface models using Persson's contact theory.

Asperity based models of the Greenwood and Williamson kind make many of the assumptions made by Greenwood and Williamson in their original study that showed that for rough elastic contacts the actual contact area is proportional to normal load for relatively low loads [12]. The assumptions made in the original model are [12][13]:

1. The contact surface is isotropic.
2. Asperities have spherical geometries at the tip.
3. The asperity tips have the same radius of curvature.
4. The asperities are far apart that there is no interaction between them.
5. The bulk material does not deform and deformation only occurs at the asperities.
6. Deformation is elastic and Hertzian.
7. The asperity heights are random variables with a Gaussian distribution.

Refinements to this model were made by others by relaxing a few of the assumptions. Chang, Etsion and Bogy implemented a plasticity criteria with volume conservation [13]. Other studies have looked at anisotropic surfaces and for asperities with different radii of curvature, but these did not show significant difference in the results with the original model [13]. Bush, Gibbson and Thomas approximated the asperity tips as paraboloids and modelled the surface roughness

occurring on many scales, and found a similar linear relationship between load and real contact area [14] [15]. This model also assumed the asperities were independent of each other.

Since these models do not take into account the interaction of asperities (i.e. the effect of loading on one asperity on the displacements and loading on another), they are valid only for $A_c << A_n$, where A_c is the real contact area and A_n is the nominal or apparent contact area. As noted by Persson, in effect in the Greenwood and Williamson model, the contact surfaces consist of elastic features on a rigid base [16]. More recently Ciavarella, Greenwood, and Paggi have developed a model that takes into account the interaction of asperities at higher loads. They did this in an iterative process. They followed the Greenwood and Williamson formulation with the mean height of the asperities reduced by the mean displacement of the elastic surface loaded by the mean nominal pressure found from the previous iteration [17].

Greenwood and Williamson did not calculate the contact stiffness properties for their model in their original paper. Shi and Polycarpou note that the load and relative approach relationship given by a Guassian distribution of asperity heights in the Greenwood and Williamson model does not have a closed form solution [11]. Following Polycarpou and Etsion [18], Shi and Polycarpou used an exponential function that fits the tail end of the Gaussian distribution (which is appropriate for most practical cases, when only the higher asperities make contact) to find an approximate relationship between normal contact stiffness and load for a Greenwood and Williamson contact model [11]. The relationship they derived is given by

$$|K_n| = \left| \frac{\lambda_f}{R_q} P_n \right|, \tag{1.3}$$

where λ_f is a curve-fitting parameter equal to 3, and R_q is a root mean roughness of the rough surface.

More recently, Medina et al. also developed an asperity model of the Greenwood and Williamson kind to analyse normal and tangential contact stiffness properties for a rough surface in contact with low normal loading [4]. Assuming an exponential distribution of asperities heights, arguing only the highest asperities are in contact at low normal loads and that the top end of a Gaussian distribution of asperity heights can be approximated by an exponentially decaying function, they deduced the expression for the total normal contact stiffness at low normal loads when there is no slip is given by

$$K_n = \frac{P_n}{\sigma_{rms}}. \tag{1.4}$$

where σ_{rms} is the standard deviation of the distance between the surface profiles in the unloaded condition. The relationship between tangential contact stiffness (at zero tangential load) is derived to be proportional to the normal contact stiffness, i.e.

$$K_t = C_c K_n, \tag{1.5}$$

where C_c is a constant, given by the Mindlin ratio, i.e. [4].

$$\frac{2(1-\nu)}{2-\nu}. \tag{1.6}$$

The Mindlin ratio is the ratio of the total tangential stiffness to the total normal stiffness of an elastic sphere in contact with an elastic half-space. Campañá et al. also found the tangential contact stiffness for rough contacts is given by the above relationship using theoretical and computer simulations [19]. They however note that in a large number of experimental measurements, the ratio K_t/K_n was found to be around half the theoretical value given by the Mindlin ratio. They also provide a summary of the results from these experimental measurements [19]. The ratio, $K_t/K_n = C_c$, is referred to in this thesis as the coupling constant.

Asperity based models are criticised by Persson for not taking into account that real contacts interfaces are fractal and for neglecting effects of asperity interaction [16]. According to Persson, the Greenwood and Williamson model would give an incorrect relationship between pressure and the mean gap or interfacial separation between the surfaces:

$$p_n \sim U_m e^{-b_p U_m^2},$$

where p_n is the normal pressure $(-P_n/A_n)$, U_m is mean gap between the surfaces and b_p is a constant [16]. Persson developed an energy based model to analyse the contact between elastic fractal surfaces [20] [21]. Persson's model is meant to be exact at $A_c = A_n$ (the model was initially derived for rubber like materials), but an approximate form is claimed to be accurate for $A_c < A_n$[16]. Persson's contact theory also showed that contact area is proportional to normal load for a wide range of loading [14]. Applying his theory at low loads, Persson deduced that the normal contact stiffness is proportional to normal load. The load and mean gap relationship is given for low loads by

$$p_n \sim p_c e^{-U_m/U_0}, \tag{1.7}$$

where U_o is a parameter that depends on the fractal surface profile [16]. This relationship implies the normal contact stiffness is given by

$$\frac{K_n}{A_n} = \frac{p_n}{U_o}. \tag{1.8}$$

For surfaces with fractal dimension near 2 (i.e. many common surfaces), $U_o \approx \gamma_p h_{rms}$, where $\gamma_p \approx 0.4$ [5] and h_{rms} is the long-wavelength root mean square roughness parameter derived from the roughness power spectrum. Pei et al. used finite elements to model contact area with respect to load for fractal surfaces which had elastic properties and then and Hyun et al. made a similar model with elasto-plastic properties [22] [23]. The elastic model was consistent with Persson's theory. In addition, Akarapu et al. modelled a self-affine rigid rough surface in contact with a flat elastic substrate with molecular dynamics and found their results were consistent with the Persson normal contact stiffness model with $\gamma_p \approx 0.48$ [24]. Furthermore experimental measurements by Wang et al. showed agreement with the Persson model [5].

Pohrt and Popov have studied normal contact stiffness for self-affine surfaces using boundary element method, and the results were compared with those from a new method for analysing contacts, dubbed the 'Method of Reduction of Dimensionality' [25]. The results showed a power law relationship between normal load and normal contact stiffness, for very low loads. While the method of reduction of dimensionality is disputed in the literature, particularly by Persson [26], a sublinear power-law relationship between normal contact stiffness and load was observed in the models by Pastewka et al. [27]. Pasteweka et al. noted that this was a 'finite size effect', and that for a wider range of pressures the normal contact stiffness is proportional to pressure. They also calculated the exponents in the power-law relationship between stiffness and load by adapting Persson's contact mechanics theory for a finite size contact interface [27]. It should be noted that both asperity models and models with fractal surfaces are only usually valid for sufficiently high loads when the contact properties are determined by a statistically large number of contact points.

While there are many studies investigating the relationship between normal and tangential contact stiffness and normal load, there are far fewer in the literature regarding the effect of tangential load on tangential contact stiffness. The most relevant study is that by Paggi et al [28]. They analysed tangential contact stiffness behaviour using the boundary element method. Contacts were modelled using the Greenwood and Williamson approach and also as self-affine fractal surfaces. This model showed that with application of tangential loading, slip occurs at the sides of the contact area and progress inwards with increase in tangential loading. The model with the Greenwood and Williamson approach derived a linear relationship between tangential load and

tangential contact stiffness and the model with the fractal surfaces derived a power-relationship between tangential load and tangential contact stiffness, with the relationship depending on the Hurst exponent of the fractal geometry [28].

1.4 Contact Stiffness Measurement Methods

There are two main methods to measure contact stiffness, described in the literature. The first is by sending ultra-sound pulses and analysing the proportion of the waves reflected at the interface [29]. The second method is to measure the contact displacement and load relationship. The slope of the load and contact displacement curve provides the contact stiffness values at different loads [9] [30] [31] [10]. Measurement of the load is usually accomplished by a load cell. The contact displacement can be measured by different means, such as with a Laser Nanosenser [31] or digital image correlation [30]. The digital image correlation method for determining the contact displacement has the advantage that the displacements of the points near the contact surface can be determined accurately, while other measurement techniques that measure the displacements of points further away from the contact may often be affected by other system compliances.

Eriten et al. and Shi and Polycarpou have also used the contact resonance method to measure contact stiffness. This involves measuring the resonance frequency of a system with the contacting surfaces and without the contact surfaces (a monolithic component is used instead of the two components in contact). The results are compared to deduce the contact stiffness [31] [11].

Published results of the measured values of contact stiffness from the different methods are often for components of different contact geometries, materials and under different loading conditions. Hence, the different methods cannot be easily compared. Mulvihill et al. used both an ultra-sound method and digital image correlation to measure the contact stiffness of the same contact interface and loading [32] [10]. Tests were conducted to determine the normal contact stiffness at different normal loads and the tangential contact stiffness at different tangential loads. The ultrasound method assumed a spring model that was proposed by Schoenberg [33]. Mulvihill et al. found that the values of contact stiffness, both normal and tangential, determined from the ultrasound technique were 2-3 times higher than the values measured by digital image correlation. It was argued that the ultrasound method measured the local unloading stiffness while digital image correlation method measured the appropriate contact stiffness for the given loading state. Measurements were made only for the loading portion of the load displacement curve [10].

Digital image correlation is used in this study, since it is likely to be more accurate than other displacement measurement techniques, which are often affected by external compliances. In many cases these external compliances could be considered negligible. However since contact

displacements are relatively small in magnitude, these external compliances could add significant error. Furthermore, unlike the ultrasound method and other methods, digital image correlation measurements provide the evolution of the contact stiffness with load. The main disadvantage of the digital image correlation measurement process is that displacements are measured at the outer surfaces of the components, rather than at the centre of the contact area. Therefore the measured contact stiffness values are for the interface near the edge, and measurement may be prone to error due to features such as rounded corners.

Chapter 2

Experimental Measurement of Contact Stiffness

2.1 Introduction

Measurements of both normal and tangential contact stiffness of Ti-6Al-4V specimens and pads in contact have been made using digital image correlation for different normal and tangential loads. Ti-6Al-4V is an important alloy used in the aerospace industry, particularly in jet turbine components. The surfaces of both the pads and specimens were characterised using optical profilometry beforehand, using focus variation method. For each test, the pad and the specimen are subjected to normal loading that is applied in increments. Once the maximum normal load value is reached, tangential load is applied cyclically in increments. After a few cycles of tangential loading, normal loading is incrementally reduced in the unloading step. Images are taken at each load increment, and digital image correlation is used to find the relationship between loading and contact stiffness for all the loading and unloading steps. The loads are applied quasi-statically.

Phenomenological models are found for the normal load relationship with normal contact stiffness and the tangential load with tangential contact stiffness. In order to quantitatively compare the surface roughness of two rough surfaces in contact, an equivalent roughness parameter is defined for both interfaces in contact used in all the tests. Detailed surface texture characteristics are also provided for the test interfaces in this study to assist any further investigation between surface texture and contact stiffness, since the interaction between two rough surfaces is complex (see Greenwood and Tripp [34] and Nayak [35]). The models used to fit the experimental data are compared with published physical models, and the relationship between surface texture and contact stiffness parameters are explored.

Results from nine tests are presented in this chapter. Six of these tests used ground specimens

and pads. Three of these involved a ground 'rough' specimen (S_q of 1.422 μm) in contact with ground pads at maximum normal loads of 4 kN, 8 kN and 12 kN, and three further tests with the same normal loading were conducted with a ground 'smooth' specimen (S_q of 0.687μm) with ground pads. All the pads were ground to the same specification, though there was some variation in the surface roughness (S_q varied from 0.623 to 1.460 μm).

Further 3 tests were conducted on specially manufactured surfaces with laser diffraction. These surfaces have grooved structures, of wavelengths of 10 μm, 5 μm and 2 μm respectively. The three structured surfaces were tested with pads that were machined with electron discharge machining (EDM) with maximum normal load of 8 kN (which corresponds to a nominal normal contact pressure of 400 MPa). The pads machined with EDM had similar roughness of S_q from 0.868 to 1.146 μm.

The objectives and the design of the experiments are described in section 2.2. The experimental setup and procedure used in this study is described in Section 2.3. The phenomenological models used to fit the experimental data are provided in Section 2.4. Section 2.5 provides information on the error analysis used. The results from the tests with the ground specimens are provided in Section 2.6 and they are discussed in Section 2.7. Similarly Section 2.8 provides the measurement results for the structured specimens, and these are discussed in Section 2.9. Section 2.10 is the conclusion of this chapter.

2.2 Experiment Objectives and Design

The purpose of these experiments is to deduce the form of the normal contact stiffness and normal load relationship as well as the form of the tangential contact stiffness and the tangential load relationship for Ti-6Al-4V interfaces, under quasi-static loading. The effect of surface roughness and structured features on the contact interface on contact stiffness properties is also explored.

The rig is designed so that the contact interfaces of nominal area of 20 mm^2 are loaded in the normal direction in increments to up to 12 kN, and tangential loading can be applied to the interfaces up to 1/8th of the maximum normal load applied. Tests were conducted with maximum normal loads of 4 kN, 8 kN and 12 kN. The normal loading was chosen so the maximum nominal normal contact pressure applied was between 200 to 600 MPa, within the elastic range (for the bulk of the material), and so results for the tangential contact stiffness properties can be obtained over a wide range of applied normal loading. Relatively high loads were used to produce relatively large displacements. Furthermore, the contact pressure is within the range of loading used in fretting fatigue tests and the stresses found in jet turbine components during operation [36] [37].

At the highest normal loading, for each test, tangential loading is applied quasi-statically in

increments. The maximum tangential load is limited to 1/8th of the normal load to avoid sliding. Five loading and unloading cycles were used in each test to measure the tangential contact stiffness properties. Further cycles were not preformed due to the logistical difficulties of manually running several quasi-static loading steps, and excessive number of cycles were avoided so as not to change the surface profile significantly during the running of the tests, such as due to wear, which could alter the physics of the interface behaviour. Wear is unlikely to occur after only a few cycles, which in addition do not involve gross sliding. Though the load and contact displacement behaviour of the contact interface is expected to stabilise since frictional shakedown of rough interfaces are known occur within a few cycles [38], the purpose of these experiments was to explore the tangential contact stiffness relationship with loading and the scope is limited to the investigation of the initial tangential contact stiffness during the first few loading cycles. Prior experimental studies such as Berthoud and Baumberger [9] and Mulvihill et al. [10] investigated the tangential contact stiffness only for the first loading cycle or step. This current study extends the exploration of tangential contact stiffness properties to the first few cycles of quasi-static loading. Future studies could look at how these properties evolve with several cycles, once significant changes in the interface profile, such as due to wear, occurs.

Contact interfaces of 4 mm by 5 mm were used. The test set-up was designed so that the displacements near the contact interface could be measured by digital image correlation for each load increment. This is so that the displacements very near the contact interface can be measured directly without the measurements being affected by external compliances. The length of the contact that can be seen from the direction of a camera is 4 mm. This is long enough so images can be taken of the central 1 mm of the interface, and the region photographed is sufficiently away from the edges. This way edge effects are avoided in the displacement measurements of the points near the contact.

The interfaces studied involved a pad in contact with a plane surface of a specimen. Flat and rounded pads were used to avoid high stress concentrations at the edges. Two ground specimens were used in this study, one rougher than the other. The 'rough specimen' has a surface roughness of S_q of 1.422 μm and the 'smooth specimen' has a surface roughness of S_q of 0.687μm. These interfaces were chosen since they were easy to manufacture with a grinding wheel and so there was a significant difference in the roughness of the interfaces studied. The pad surfaces in the tests with the ground specimens were ground to the same specification (i.e. grinding wheel settings) as the 'smooth specimen', though there was a significant variation in the roughness of the pad interfaces (S_q varied from 0.623 to 1.460 μm). This allowed measurement of contact stiffness properties to be conducted for a variety of interface roughness values found in common metallic interfaces.

Three 'structured' patterned surfaces were also tested at maximum normal load of 8 kN. The

loading was chosen so that the results obtained would be at the mid-range of loading applied in the tests with the ground interfaces. Patterns were produced by laser diffraction on the specimen surface by Carsten Gachot at Saarland University and involved grooves of 2 μm, 5 μm and 10 μm wavelengths, respectively. The aim of these tests is to study the effect of systematic patterning on contact stiffness properties. These particular groove geometries were selected since experimental measurement at Saarland University for similar interfaces showed significant variation in the coefficient of friction[1]. The testing reported here explored whether such patterning had a significant effect on the contact stiffness properties. Interfaces between these surfaces and pads machined by electron discharge machining (EDM) were studied. EDM was used to machine the pad surfaces since the process gave a more consistent finish than grinding. The roughness of pads in these tests had S_q from 0.868 to 1.146 μm.

Details of the experiment set-up and testing procedure is provided in the next section.

2.3 Contact Stiffness Measurement Procedure

2.3.1 Experimental Setup and Process

A new rig which is similar in design as that used by Mulvihill et al. [10] and Kartal et al. [30] was designed for these tests. See Figure 2.1. In this setup two flat and rounded pads are in contact with a specimen and are loaded as shown in Figure 2.2. See Appendix A for an engineering drawing of the pads and the specimens used (both drawn by Robert Paynter). The pad contact surface is of width 5 mm and length 4 mm, giving a nominal contact area of 20 mm^2. The specimen has a width 5 mm.

For the tests with ground specimens, tests were conducted with two specimens, one grounded to have a rougher profile than the other. The two specimens are referred to here as the 'rough specimen' (S_q of 1.422 μm) and the 'smooth specimen' (S_q of 0.687μm). Different tests were conducted with the same specimen at different locations. A fresh pair of pads is used in each test. The pads used in these tests were also ground (using similar settings as for the smooth specimen). The surface finishing of the both the the specimen and the pads had the machining lines width-wise, i.e. perpendicular to the direction of tangential loading.

There was no need to specially pattern the side surfaces of the pads or the specimen to assist the digital image correlation process, since machining marks are sufficient. The side edges of the pads were finished so that the machining marks were at an angle (curved) to the contact surface as shown in Figure 2.3. Machining features that are parallel to the contact surface or perpendicular to the contact surface would have made finding the tangential displacement vectors or normal

[1]Private communication with Carsten Gachot.

displacement vectors difficult with digital image correlation.

Tests with the structured surfaces used specially made specimens. The specimens were polished before laser diffraction were used to produce grooves of different wavelengths on the contact interface. These specimens were made and provided by Carsten Gachot at Saarland University, Germany. The grooves were patterned lengthwise and are in the direction of tangential loading. Patterning was done in sections that look like tiles. Electron discharge machining (EDM) was used in-house to machine the contact interface for the pads used for tests with the structured surfaces. EDM proved to provide a more consistent surface profile than grinding. Several iterations of grinding were required to make pads with appropriate flat and rounded profiles for testing with the ground specimens. The contact surface of the pads shaped by EDM lack any clear directional machining marks.

In the new rig, the pads are placed inside the pad holders which are housed in a cast iron block suspended from a frame. The specimen is connected to a single-actuator which can apply the shear loading ($2Q_t$). Normal load (P_n) is applied to the base of the pad holders by means of the pressure pumps, operated by hand. The LVDT seen in Figure 2.1 was used only in initial testing (not published here) to assist in the operation, since displacements are measured more accurately by digital image correlation. A light source is used to provide illumination. The lens and camera (behind the rig shown in right image of Figure 2.1) are positioned so that images are take at the centre of the flat and rounded contact interface between one of the pads and the specimen. The images are of resolution 1280 by 1024 pixels. The pixel length is calibrated before each test and is roughly 1μm. See Figure 2.4, for an example image.

Before each test the interface surfaces are cleaned with acetone and dried. The pad and the specimen are moved into place by the single actuator under displacement control. The specimen is allowed to rotate a little and a low amount of normal loading is applied by the pumps to press the pads gently onto the specimen to align the surfaces. This normal loading is then removed, and the screws in the specimen holder are tightened to fix the specimen into place.

Screws were put into the outer rim on either end of the cast-iron block holder to move the cast iron block, that carries the pad holders, to finely adjust the alignment of pad and specimen. By turning these screws, the cast-iron block can be moved away and towards the camera. The cast-iron block position is adjusted with these screws carefully until both the pad side surface and the specimen side surface are seen in focus together through the camera. Once this is achieved, the screws are tightened so that the cast-iron block cannot slide and move the pads out of focus. The tangential load measurement is set to zero once the specimen is moved up to the right location. The normal load measurement is set to zero so that the reading is zero when the pads and specimen are seen to first come into contact.

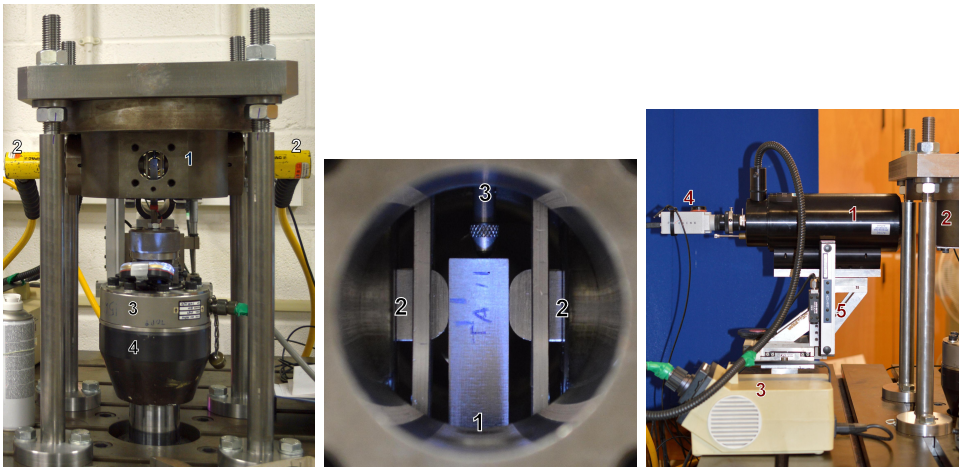

Figure 2.1: **Left**: The new test rig for measuring contact stiffness. 1: The cast iron block that holds the pad holders which hold the pads. 2: the pressure pumps that apply normal load onto the pads. 3: the load cell. 4: the single actuator that supplies the tangential loading. **Middle**: Close-up of the new test rig for measuring contact stiffness. 1: the specimen. 2: the pads. 3: the LVDT displacement sensor. **Right**: 1: The Questar lens, 2: the cast-iron block, 3: the light source and 4: the camera. Picture credit: Robert Paynter.

To conduct a test to measure normal contact stiffness, normal load is applied incrementally to the pad and specimen interfaces, using the hand-pumps. For each increment of load an image of one pad and specimen interface is taken. Similarly for measuring tangential contact stiffness, after the required normal load is applied, the shear load is applied by the single actuator incrementally, with images taken at each increment. The normal load pressure is monitored constantly and every now and then the pump is used to ensure the pressure is within the required value (usually with less than 0.1% variation from the required value). Generally, the normal load pressure was adjusted at the end of a loading or unloading step. Loading steps for which the tangential or normal load is increased are called the loading steps and those for which the load is decreased are called the unloading steps. Druck DPI 104 pressure guage with maximum rated pressure of 700 bar was used to measure the pneumatic pressure of the hand pump. The stated accuracy for the normal pressure gauge is 0.05% of the full scale (i.e. ± 0.035 MPa) [39].The total normal load applied is calculated by assuming the measured oil pressure is applied to the pads via an effective piston area of 6.5 cm^2 [40]. The load cell to measure the tangential load applied has been calibrated to be accurate within 1% of the reading.

Displacement control is used for the single actuator (that applies tangential load) during set-up and while applying normal loading till around 1 kN, afterwards the single actuator is put under load control. During the normal unloading step at the end of the tests, care is taken that the single actuator is changed to displacement control when the normal load is reduced below 1 kN.

The set of images obtained is analysed using digital image correlation as described in the next section to find the contact displacement values for each increment of load applied.

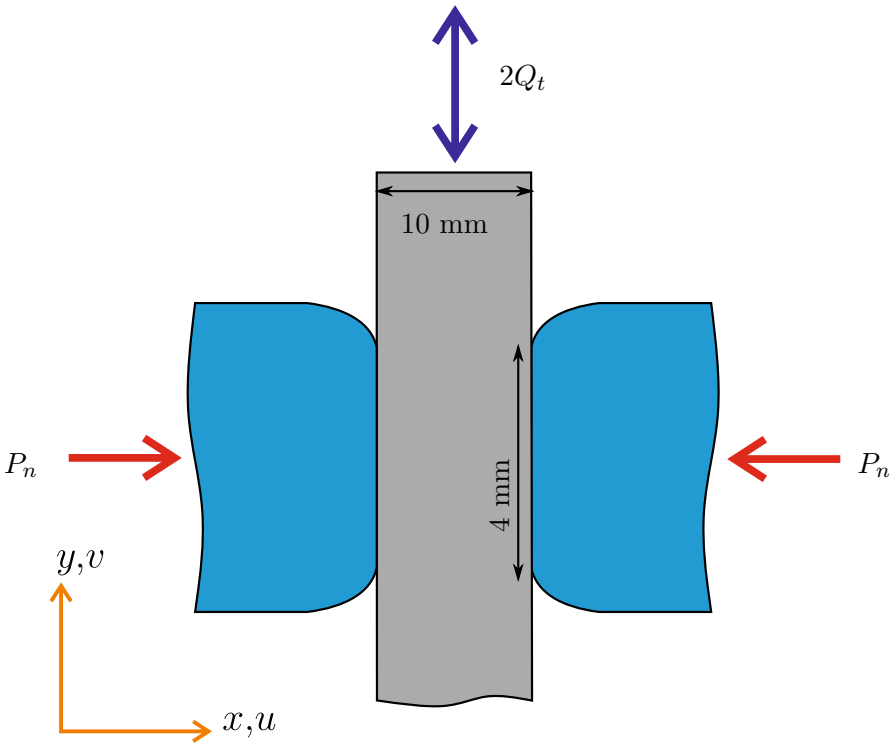

Figure 2.2: Specimen in contact with two pads and subject to normal load ($-P_n$) and shear load ($2Q_t$).

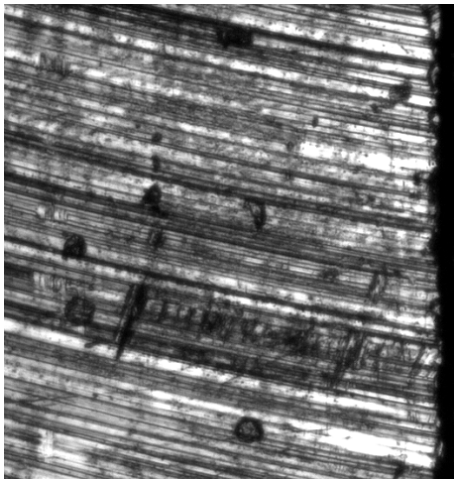

Figure 2.3: The side surface of the pad is machined so that the machining marks are at an angle to the contact surface to assist with the DIC process.

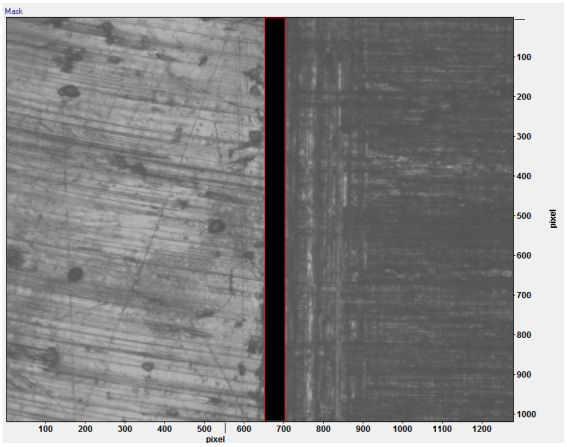

Figure 2.4: Example image taken of the area near the contact interface. A mask defined at the centre over the contact area. Pad is on the left and the specimen is on the right.

2.3.2 Digital Image Correlation Analysis to Find Displacement Field

Digital image correlation (with a fast Fourier transform algorithm) with Davis 8.3 Strainmaster software is used to find the displacement fields associated with each image. A mask is defined at the region of the contact interface as shown in Figure 2.4, and it is allowed to displace with the displacement vectors. Displacements are not found for points inside the masked region. Displacements for points on the pad and specimen are computed with the cross-correlation method with respect to a reference image frame (usually the first image taken in a cycle). Multiple-passes are used with the final window size usually of 64 by 64 pixels with 50% overlap for most tests (128 by 128 pixel final window size was used for a few tests). According to the software uncertainty wizard, window sizes of 64 x 64 correspond to an accuracy ('minimum detectable deformation/shift uncertainty') of 0.005 pixels and window sizes of 128 x 128 to 0.0025 pixels. The software finds the displacement at discrete points at locations defined by the window size. Top image of Figure 2.5 shows an example displacement field computed for points on the pad (left) and specimen (right). The blank area in the centre is where the mask is located. Arrows are plotted at the locations of points on both the pad and specimen. These arrows represent the displacement vectors at these locations.

Using Matlab, the displacement values are averaged for points with the same 'x' coordinate. Lines are fitted onto the displacement-position data for both the pad and the specimen for each frame. The step change in the displacement at centre of the masked region is calculated and provides the contact displacement value for that frame. See bottom of Figure 2.5. By fitting straight lines and measuring the distance between them at the centre, the contact displacement value measured is not affected but the bulk defomration of the material. u_c and v_c are the normal and tangential contact displacements. u_c is defined in this study as the difference between the normal displacement of the specimen and the pad near the contact (it has a negative value a during loading and a positive value during unloading). Similarly v_c is the difference between the tangential displacement of the specimen and the pad near the contact (it has a positive value during loading and a negative value during unloading).

The contact displacement values are plotted against load. It was found that exponential functions fit the normal load and normal contact displacement relationship and the tangential load and tangential contact displacement relationship. The least squares method is used to fit curves to the raw data for each loading and unloading step. The slope of the fitted curve provide the contact stiffness measurement at different loading values as shown in Figure 2.6 . The functions used to fit the data and the model of contact stiffness these fits imply is dicussed in Section 2.4.

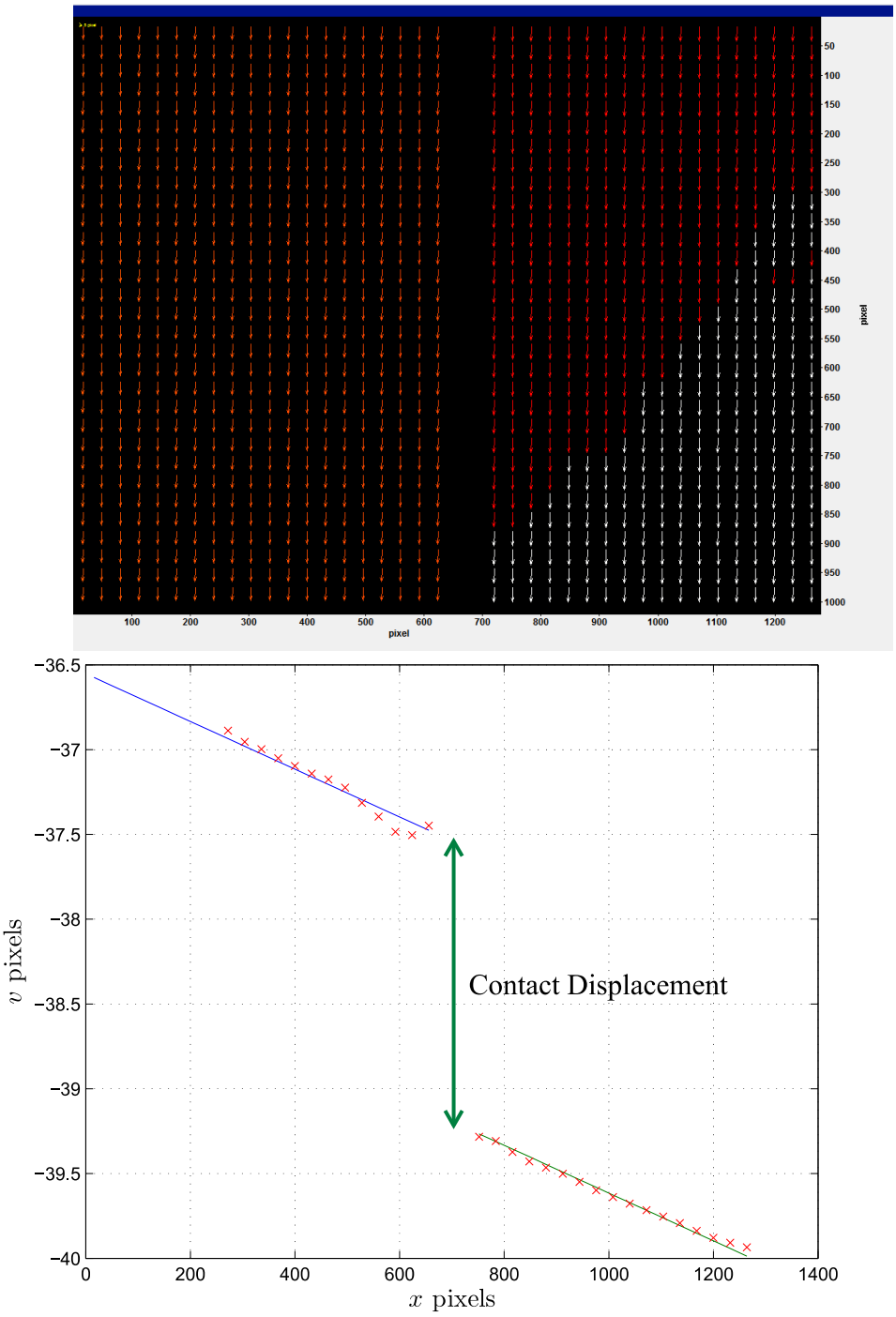

Figure 2.5: **Top**: Displacement field produced found by digital image correlation for points on the pad (left) and the specimen (right) during tangential loading. The arrows represent displacement vectors for points on the pad and specimen. The central area is masked. **Bottom**: Contact displacement is found as the gap between the lines that fit the mean displacement data.

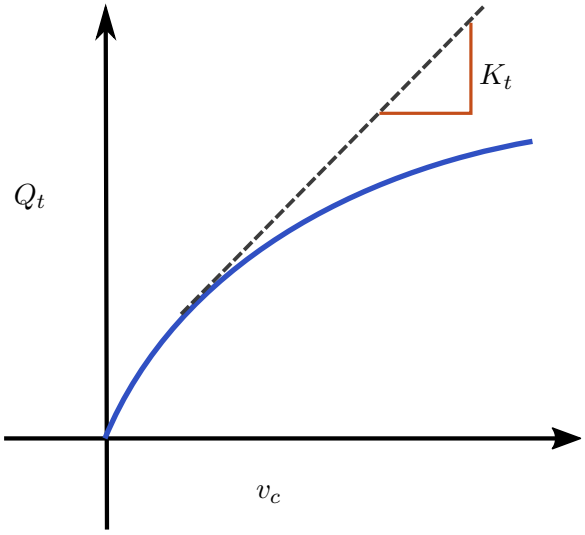

Figure 2.6: The slope of the fitted curve of the load (Q_t) and contact displacement (v_c) data provides the contact stiffness (K_t).

2.3.3 Limitation of the Experimental Set-up And Configuration

The experimental set-up is limited due to the need to measure very small displacements while applying relatively large loads. The accuracy of the measured displacement values are limited by the resolution of the camera and lens and the quality of the images obtained (such as due to the focus), though the stated resolution of the digital image correlation algorithm is in the order of 0.005 pixels (corresponding to around 5 nm), and the limitations of manual alignment of the components. The experimental data is also limited by the accuracy of the the tangential load sensor, which has been calibrated to less than 1% accuracy, and the normal pressure gauge which has an accuracy of less than 5% for loads above 2 kN. Further the experimental set-up assumes the tangential loading is evenly applied to both pad surfaces, and the normal pressure over the centre of the pad and specimen interface is linearly related to the normal load applied to the pad. Furthermore, since the loading is applied quasi-statically and manually, the current set-up is not suited for obtaining data over a large number of loading cycles.

2.3.4 Surface Texture Measurement

Many models of contact interfaces suggest that surface texture affect the contact stiffness [4] [5] [9]. There is however a lack of knowledge and theory regarding the relationship between the surface texture properties of both surfaces in contact and the contact stiffness when two rough surfaces are in contact. Therefore, special care was taken to make detailed surface texture measurements of both test surfaces before testing.

An optical profilometer, the Alicona, was used to make both 3D and 2D measurements of the test surfaces, using the focus variation method. The focus variation method involves taking images of a surface with a light microscope at different focal lengths and on the basis of the sharpness of

each point in the images taken, it reconstructs the 3D profile of the surface [41].

The profile roughness parameters computed and provided for the test interfaces in the Appendix A are the following [41]

1. R_a, the arithmetic mean height of the profile.
2. R_q, the root mean square height of the profile.
3. R_z, the highest peak to valley distance in the profile.

The areal parameters measured and also provided in Appendix A are the following

1. S_a, the arithmetic mean height of the sample surface.
2. S_q, the root mean square height of the sample surface.
3. S_p, the highest peak height of an asperity in the sample surface.
4. Fractal dimension, a parameter that characterises the fractal nature of the surface.
5. S_{tr}, the texture aspect ratio parameter found by autocorrelation of the sample surface. It is a measure of the directional nature of the surface texture, and takes values between 0 and 1. Values near 1 suggest the surface texture is not directional (isotropic) and values near 0 suggest the surface texture is directional (anisotropic).

Measurement was done with reference to the Alicona manual [41], and with reference to the guidelines published in ISO standards, particularly ISO 4287, ISO 4288 and ISO 25178 standards [42] [43] [44]. ISO 4287 provides the definitions of profile parameters (such as the roughness parameter, R_a, for 2D texture characterisation); ISO 4288 provides some guidelines on how these profile parameters should be measured; and the ISO 25178 defines areal texture parameters (parameters to characterise the 3D surface profile).

On the basis of the guidance in the Alicona manual [41, p. 76] it was interpolated a vertical resolution of 50 nm with 20X magnifcation objective is suitable to characterise surfaces with roughness parameters $R_a \geq 0.25$ and $R_z \geq 2\mu$m. All the surfaces measured satisfy this criteria. No guidance is provided in the manual or the relevant ISO standards regarding suitable lateral resolution for measurement. The recommended r_{tip}, the maximum radius of the stylus profilometer tip, as per ISO 3274, for roughness measurements with cut-off wavelenght, λ_c, of 80 μm to 800 μm is 2 μm [45, p. 35]. A lateral resolution fo 2.01 μm was used in all the measurements, which allows roughness profile to measured on a profile line of less than 700 nm width (minimum profile width line is the pixel length of the Alicona 3D surface profile).

ISO 4288 standard provides guidelines on the cut-off wavelength, λ_c, and evaluation lengths (the length of the profile line) required for profile roughness measurements. See also page 72 of the manual [41]. Surface profile features that have wavelengths greater than the cut-off wavelength are filtered out in the computation of roughness profile parameters. For surfaces with measured R_a values between 0.1 and 2 μm, the recommended λ_c value is 800 μm, and the required evaluation length is 4 mm. All measured surfaces had roughness value within this band and hence λ_c of 800 μm was used. The Alicona discards 10% of the profile line length on either side, meaning a profile line of 5 mm is required to comply with IS0 4288 guidelines. As per ISO 4287, the evaluation length is divided into several sampling lengths, equal in length to the cut-off wavelength, and roughness parameters, including R_a, R_q, and R_z, should be found by averaging the values obtained from each sampling length [42].

The roughness parameters calculated are the average of the values 5 measurements with profile lines of 1 pixel width (usually around 670 nm). The profile roughness measurements were done lengthwise for the tests with ground specimens (in direction of tangential loading), with the profile line perpendicular to the machining marks from grinding. Measurements of specimen roughness parameters used 5 mm profile lines (and comply with the ISO 4288 standard). The length of the pad interface was 4 mm, so 4mm profile lines were used. Since the values are obtained by the average of 5 measurements, the results are believed to be robust.

The roughness parameters for the pads shaped by EDM were measured similarly lengthwise (with profile lengths of 4 mm). For the structured surfaces however both lengthwise (parallel to the manufactured grooves) and widthwise (perpendicular to the grooves), roughness measurements were made (with profile lengths of 5 mm).

Guidance could not be found regarding the size of sample areas or cut-off wavelengths for measuring areal surface parameters, other than to use a suitable cut-off wavelength that removes profile features [41, p. 74]. The same cut-off wavelength used in the profile measurements of 800 μm was found suitable and used for the calculation of areal parameters. A sample area of 2 mm^2 was used for all the surfaces.

The scans used to measure the roughness and areal parameters of the patterned surfaces had a lateral resolution of 2.01 μm, could not sufficiently evaluate the groove patterns, particularly for the specimen with 2 μm groove wavelength. In order to fully characterise the structured surfaces, the surfaces were scanned also with 100X objective lens with a lateral resolution of 500 nm (near the maximum lateral resolution capability of the Alicona profilometer) and vertical resolution of 50 nm. Roughness profiles of length 1 mm perpendicular to the grooves with cut-off wavelengths slightly above the wavelengths of the groove features were used to characterise the patterns. The roughness parameters found this way are a measure of the surface patterning, filtering out longer

wavelength surface features.

2.3.5 Equivalent Surface Roughness Parameter For Two Surfaces

As noted earlier, there is a need to characterise the surface properties of two rough surfaces in contact. The most commonly used parameter to characterise surface roughness in contact models is the root mean square height of the contact surface. This corresponds to the areal parameter S_q. In this section an equivalent S_q^e parameter is defined that characterises two surfaces as one such that the probability distribution function of the gap between an equivalent surface and a flat surface is the same as that for the gap between the two rough surfaces. The definition of an equivalent surface used here is similar to one defined by Nayak to characterise the roughness of two surfaces in contact in a theoretical model [35], though here the areal surface roughness parameters obtained for real surfaces are used to characterise real surfaces.

Greenwood and Tripp note that two rough surfaces in contact, provided certain conditions are met, can be modelled exactly in a Greenwood and Williamson type contact model by an equivalent rough surface and a smooth surface, where the the curvature of the asperities of the equivalent surface is equal to the sum the curvatures of the asperities of the two rough surfaces and the asperity height distribution of the equivalent surface is equal to the distribution of the sum of the asperity heights of the two rough surfaces. The required conditions include: both rough surfaces must have the same number of asperities; each asperity must be exactly in line with each other; and all asperities on each surface have the same curvature. Greenwood and Tripp went on to show that misalignment of the asperities of the two rough surfaces did not significantly affect many of the results from certain elastic and plastic models [34].

The equivalent surface described in this section has a surface height distribution equal to the distribution of the sum of the surface heights of the two surfaces and is therefore broadly analogous in definition to the equivalent surface described by Greenwood and Tripp.

If the distance between the mean lines of both surfaces is U_m, the gap at coordinate x is given by

$$U_g(x) = U_m - (h_1(x) + h_2(x))$$

where $h_1(x)$ and $h_2(x)$ are the heights from the mean lines of the two surfaces at x. Values for $h_1(x)$ and $h_2(x)$ are taken as positive in the direction towards the interface. See Figure 2.7.

As was done by Nayak, assuming both $h_1(x)$ and $h_2(x)$ are normally distributed random variables with variance of both distributions equal to S_{q1}^2 and S_{q2}^2, where S_{q1} and S_{q2} are the root mean square heights of the surfaces (i.e. assuming the two surfaces have normally distributed heights), the mean value for the gap $U_g(x)$ is U_m and the variance of the gap is $S_{q1}^2 + S_{q2}^2$. This is because

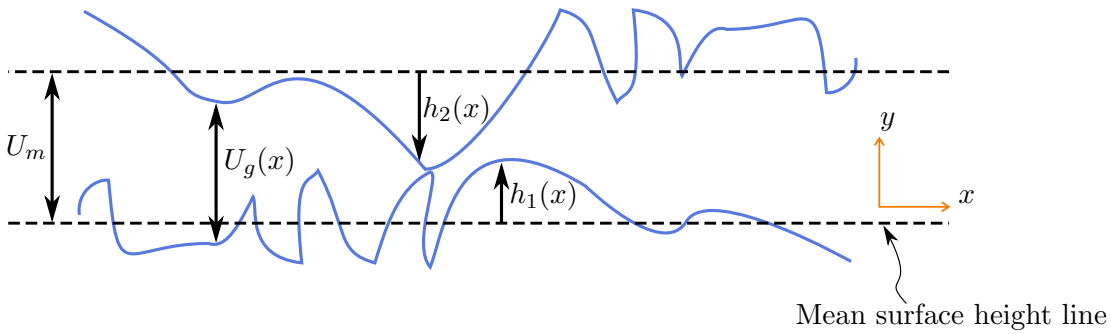

Figure 2.7: Computation of an equivalent surface roughness parameter for two rough surfaces in contact.

the probability distribution of the sum of two normally distributed independent random variables is a normal distribution with the mean value equal to the sum of the means and a variance equal to the sum of the variances.

A flat surface in contact with a rough surface with root mean square height of $\sqrt{S_{q1}^2 + S_{q2}^2}$ will result in a gap with the same probability distribution function. Therefore the equivalent surface for two rough surfaces in contact can be characterised by the roughness parameter S_q^e given by

$$S_q^e = \sqrt{S_{q1}^2 + S_{q2}^2}. \tag{2.1}$$

Nayak derived a similar parameter for his theoretical model [35].

2.4 The Phenomenological Models

The results from the tests conducted showed that both the normal load versus normal contact displacement data and the tangential load versus tangential contact displacement data can be fitted very well with an exponential function of the forms

$$-P_n = \alpha_n e^{\beta_n(-u_c)} + P_0 \tag{2.2}$$

$$Q_t = \alpha_t e^{\beta_t v_c} + Q_s, \tag{2.3}$$

where α_n, β_n and P_0 are fitting parameters for the normal load versus normal contact dis-

placement data, and α_t, β_t and Q_s, are fitting parameters for the tangential load versus tangential contact displacement data. A separate set of parameters are found for each loading and unloading steps. See Figures 2.8 and 2.14 for examples of experimental data fitted with the above models.

The choice of this model is significant. Firstly, as discussed previously, various contact models suggest an exponential relationship as given in equation(2.2) between the normal load and normal contact displacement, albeit it should be noted as discussed previously contact displacement may be defined differently from that used in this study in some of these theoretical models. Secondly, this model leads to a simple linear relationship between contact stiffness and loading, and therefore can be applied straightforwardly in practical situations. However, most importantly both of these models were seen to fit the experimental data from various tests.

Contact stiffness is the differential of the load displacement curve and the above models lead to the following relationship between normal and tangential contact stiffness with normal and tangential loading

$$K_n = \beta_n(-P_n - P_0), \tag{2.4}$$

$$K_t = \beta_t(Q_t - Q_s). \tag{2.5}$$

Since it is reasonable to expect normal contact stiffness to tend to zero at zero normal load, the magnitude of P_0 parameter could reflect in part to an offset between the actually applied normal load and the measured normal load. Further it could imply the initial load was taken up by misalignment between the surfaces. It should be noted that models that posit a linear relationship between load and stiffness is only valid for sufficiently high normal loading, since at lower loads only a few asperities are in contact and the results obtained from the modelling of a statistically large number of asperity contacts are not applicable at this regime.

By contrast, the results from a good number of experimental testing show the model for the relationship between tangential loading and tangential contact stiffness fits the data very well for all values of tangential loading. Q_s is the value of tangential loading at which K_t becomes zero, i.e. at slip. Q_s is therefore the tangential load at slip and so for loading steps

$$Q_s = f(-P_n).$$

(For unloading steps $Q_s = -f(-P_n)$.) Equation (2.5) for loading steps can be written as

$$K_t = \frac{-K_{t0}}{f(-P_n)} Q_t + K_{t0} \tag{2.6}$$

where K_{t0} is the tangential contact stiffness at zero tangential load. Models in the literature suggest K_{t0} is related to K_n, the normal contact stiffness, by a constant of proportionality. If C_c is the constant of proportionality then

$$K_t = \frac{-C_c K_n}{f(-P_n)} Q_t + C_c K_n \tag{2.7}$$

A similar relation can be derived for unloading steps. The key implication of this model is hence if the coefficient of friction, the C_c value and the normal contact stiffness at zero load are known, the tangential contact stiffness can be found for any given tangential load by the above relation.

Furthermore,

$$\begin{aligned} \beta_t &= \frac{-C_c K_n}{f(-P_n)} \\ &= \frac{C_c \beta_n (-P_n - P_0)}{f(-P_n)} \\ &\approx \frac{C_c \beta_n}{f}, \end{aligned}$$

assuming $\frac{P_0}{P_n}$ is sufficiently small and is due to experimental error. This implies β_t is a load independent quantity and proportional to β_n.

2.5 Error Analysis

2.5.1 Introduction

To provide an indication of measurement errors, results are presented with margin of errors. The margin of error values are based on the error bounds of the fitting parameters, used in equations (2.2) and (2.3), for 95% confidence, and the estimated error of the load cell readings. This error analysis assumes the exponential model used to fit the data is valid and the scatter from the fitted curve is due to experimental error. The margin of error values are provided to give an approximate indication of the quality of the results obtained, and an indication of how well the model fits the observed values.

For quantities that are a function of variables (such as the fit parameters), the error is assumed

to propagate using error propagation rules described below, which assume the error values for the component variables are uncorrelated and are normally distributed.[2] The rules to calculate error propagation [46]:

1. For addition and subtraction[3]

$$V = a \pm b,$$

$$\delta V = \sqrt{(\delta a)^2 + (\delta b)^2}$$

2. For multiplication and division

$$V = \frac{a \times b}{c},$$

$$\frac{\delta V}{|V|} = \sqrt{\left(\frac{\delta a}{a}\right)^2 + \left(\frac{\delta b}{b}\right)^2 + \left(\frac{\delta c}{c}\right)^2}$$

2.5.2 Physical Sources of Error

The sources of experimental error include measurement error of the load cells, the error of the displacement values from digital image correlation, misalignment of the surfaces, and other vibration and motions that could have affected the displacement readings. The predominant sources for error is expected to be on the measurement of the displacement from digital image correlation, since the errors on the calibration on the load measurement is relatively low–1 to 5%.

The tangential load cell and controller has been calibrated to less than 1% error, and the uncertainty on the tangential loading is taken as 1%. The stated error of the normal pressure gauge measurement is 0.035 MPa [39] (which measures the oil pressure applied via a effective area of 6.5 cm^2 of the piston (as per the specification sheet for the pump [40]) pushing onto the pads), and the digital image correlation process has a stated accuracy of 0.005 pixels (which is roughly 0.005 microns). The uncertainty of the piston area is taken as 1%. This can be estimated on the basis of standard manufacturing tolerances or following Taylor [46] the error can be assumed as $\pm$ 0.05 cm^2 on the basis of the number of significant figures used in specification sheet to state the effective area. Before loading was applied the normal load was zeroed at the pressure when the pad made first contact with specimen, to remove an initial offset due to loading taken up by frictional resistance of the piston. This was done manually with confidence of $\pm$0.1 MPa.

The error in normal load measurement is estimated to be given by (Taking P_n = Area of Piston$\times$

[2]The covariance of the parameters is neglected.
[3]Alternatively $\delta V = \delta a + \delta b$ is a simpler and more conservative estimate for the error [46].

Pressure) [4]

$$\frac{\delta P_n}{P_n} = \sqrt{0.01^2 + \left(\frac{0.135\ \text{MPa}}{p_n}\right)^2}$$

where p_n is the pressure reading from the pressure gauge in MPa. This expression is used to calculate the error on P_n during the normal loading steps. During application of tangential loading the pressure reading varies slightly (though was kept well within 1% of the target value), the error on the normal loading value during the tangential loading step is taken as

$$\frac{\delta P_n}{P_n} = \sqrt{0.01^2 + \left(\frac{0.135\ \text{MPa}}{p_n} + 0.01\right)^2},$$

adding another 1% uncertainty to the pressure reading. The error of the normal loading is within 5% (for loads above 2 kN). Assuming the load and contact displacement relationship is in reality on a smooth curve, the observed scatter from a smooth relationship is therefore due to measurement errors from both the load sensors and measurement of contact displacements. When the scatter from the fitted curves is large, it is likely due to significant errors in the displacement measurement, since the errors from the load sensors can not account for a large scatter.

2.5.3 Error Analysis On the Basis of Fitting Uncertainty

Contact stiffness measured is calculated on the basis of the fit parameters of the curve used to fit the experimental data. In order to estimate the margin of error for the parameters determined, the uncertainty of the fit parameters found from least squares fitting process is used. For calculation of margin of error on the normal contact stiffness values, since $K_n = \beta_n(-P_n - P_0)$,by multiplication rule

$$\frac{\delta K_n}{|K_n|} = \sqrt{\left(\frac{\delta \beta_n}{\beta_n}\right)^2 + \left(\frac{\delta(-P_n - P_0)}{-P_n - P_0}\right)^2} \tag{2.8}$$

where P_n is the normal load and the error[5] $\delta(-P_n - P_0) = \sqrt{(\delta P_n)^2 + (\delta P_0)^2}$.

The error for tangential contact stiffness value at $Q_t = 0$, K_{t0}, is calculated by

$$\frac{\delta K_{t0}}{|K_{t0}|} = \sqrt{\left(\frac{\delta \beta_t}{\beta_t}\right)^2 + \left(\frac{\delta Q_s}{Q_s}\right)^2} \tag{2.9}$$

(Taking $K_{t0} = \beta_t Q_s$). The coefficient of friction derived from the tangential tests is defined by

[4]This assumes the total uncertainty in the pressure reading is 0.135 MPa on the basis of the gauge uncertainty and the estimated uncertainty of the zero value- found by the simpler estimate of total error by summation of the individual error components.

[5]Assuming the estimated error on the normal loading is with 95% confidence and is normally distributed.

$f = \left|\frac{Q_s}{P_n}\right|$, where P_n is the normal load, and the margin of error is hence given by

$$\frac{\delta f}{f} = \sqrt{\left(\frac{\delta Q_s}{Q_s}\right)^2 + \left(\frac{\delta P_n}{P_n}\right)^2} \tag{2.10}$$

An additional 1% uncertainty is added to the uncertainty of the Q_s parameter (the estimated tangential load at slip from the fitted curves) on top of the uncertainty deduced from the fitting process to take into account additional error in the measurement of tangential load[6].

Addition rule is used to find the margin of error values for mean values. Mean values of K_{t0}, β_t, and f are found for loading and unloading steps combined using values of each of these quantities only for steps in which the margin of error values for K_{t0} were less than 50%. The mean values for all steps combined for each test are computed using the same criteria. The coupling constant C_c is given by $\frac{K_{t0}}{K_n}$. The margin of error for this value is found by the division rule for error propagation.

2.5.4 Mean Row Stiffness Error Analysis with Student's t-Distribution

In the calculation of contact displacement the mean displacement field was used. Digital image correlation was used to compute displacement values for a grid of points with x and y coordinates on both the pad and specimen. The displacements for all points with the same x-coordinate were averaged, and the change in displacement near the contact region was estimated, as explained in Section 2.3.2.

To estimate error in an another way, contact displacement is found in a similar way for each row of points (i.e. points with the same y coordinate) in the displacement field. Load-contact displacement curves are plotted for each row and contact stiffness values are found for each load-step. This process is used to estimate the variability of the stiffness values measured from each row of pixels.

$$\bar{K_0} = \frac{\Sigma K_0^i}{n}$$

where $\bar{K_0}$ is the mean row stiffness value computed as the average of the stiffness values found for each row at zero tangential load – the K_0^i values – , and n is the number of rows, or y coordinate values in the displacement field. Assuming the error in the stiffness values found from each row is random and distributed normally, the confidence interval limits, of 95%, are found using a Student's t-distribution of order $n - 1$. Student's t-distribution is used since it can estimate the error probability distribution when the sample size is low and the distribution is expected to be normal [47].

[6]This is assuming an extreme case that 1% error of the tangential load cell is systematic and due to non-linearity of the load cell, i.e. it does not contribute to the calculated uncertainty of the fit parameter. The effect of this additional uncertainty is however very small, consistent with the expectation that there is greater uncertainty in displacement measurement.

If $T_{inv}(97.5\%, n-1)$ is the random variable for which the cumulative probability according to a Student's t-distribution of order $n-1$ is 97.5%, then the confidence intervals for $\bar{K_0}$ (defined from K_0^{min} to K_0^{max}) are given by [47]

$$K_0^{max} = \bar{K_0} + \frac{S}{\sqrt{n}} T_{inv}(97.5\%, n-1),$$

$$K_0^{min} = \bar{K_0} - \frac{S}{\sqrt{n}} T_{inv}(97.5\%, n-1),$$

where S is the sample variance given by

$$S = \frac{1}{n-1} \sum_{i}^{n} (K_0^i - \bar{K_0})^2.$$

2.6 Results for Ground Interfaces

Tests with the 'rough specimen' (S_q of 1.422 μm) are given code names RU1, RU2, RU3. The maximum normal loads used in the three tests are 4 kN, 8 kN, and 12 kN respectively. Similarly tests with the 'smooth specimen' (S_q of 0.687μm) are given code names SU1, SU2, SU3, and the maximum normal loads applied are also 4 kN, 8 kN, and 12 kN respectively.

Table A.1 in Appendix A provide the roughness and areal surface texture properties of the two specimens and the pair of pads used in the 6 tests with ground surfaces. The two pads used in each test are referred to as Pad A and Pad B. Pad A is in contact with the side A of the specimen and Pad B is in contact with side B of the specimen. The images were taken for the interface between Pad B and side B of the specimens, and therefore the surface parameters for these surfaces are the most significant in analysing the results.

Figures 2.8 to 2.13 provide the results for the normal loading and unloading steps in each test. In each figure, the figures at the top are for the loading steps and the figures at the bottom are for the unloading steps. The figures on the left provide the contact displacement and normal load relationship measured and are fitted with curves using the exponential function described in Section 2.4. The figures on the right show the normal contact stiffness and normal load relationship deduced from the fitted curves. Upper and lower error lines are plotted as well in the stiffness plots, on the basis of the errors computed with equation (2.8).

Figures 2.14 to 2.17 provide the results from the tangential loading steps for test RU1 with normal load, $-P_n = 4$ kN. It should be noted the sign of the tangential load, Q_t, is consistent with the calibration of the single actuator of the rig. Q_t is positive when the specimen is pulled down and Q_t is negative when the specimen is pushed up. The load cell measures $2Q_t$, and it is assumed that the load is distributed onto both pads equally.

Figure 2.14 provides the tangential contact displacement and tangential load data with the fitted curves using the exponential function described in Section 2.4. Figure 2.15 shows the tangential contact stiffness and tangential load relationship derived from these fits. The figure on the top is for the first two loading and unloading steps. The figure on the bottom is for all steps. The figure on bottom shows that the relationship derived for most steps are similar. Figure 2.16 shows the coefficient of friction (top) and the slope of the tangential contact stiffness and tangential load relationship, β_t, (bottom). The values for the loading steps are in the figures on the left and the values for the unloading steps are on the right. The coefficient of friction is derived from the x intercept of the tangential load and tangential contact stiffness relationship – the load at which stiffness approaches zero is the load at slip. This divided by normal load $-P_n$ provides the coefficient of friction, f, value for that load step. The error bars are computed as described in Section 2.5.1.

The top of Figure 2.17 provides the tangential contact stiffness values at zero tangential loads, K_{t0}. The values for the loading step are plotted on the left and those for the unloading step are plotted on the right. Error bars are provided to display the margin of error values computed as described in Section 2.5.1. Bottom of Figure 2.17 provide tangential contact stiffness values at zero tangential loads, K_{t0}, found as the 'the mean row stiffness' plotted with the error bars found using Student's t-distribution as described in Section 2.5.4. The maximum and minimum K_{t0} values of the values computed for all the rows are plotted as well, along with the K_{t0} found from the mean displacement field. Tables A.2 and A.3 in Appendix A provide the values found from the loading and unloading steps from the mean displacement field. Tables A.4 and A.5 provide the values plotted for the mean row stiffness plots.

Similar plots as described above for all the other tests with ground specimens (from tests RU2 to SU3) are given in Figures 2.18 to 2.39. Also, data values used in these plots are provided in Tables A.6 to A.25 in Appendix A.

2.6.1 Normal Stiffness Test Results

Test RU1 4kN Normal Load

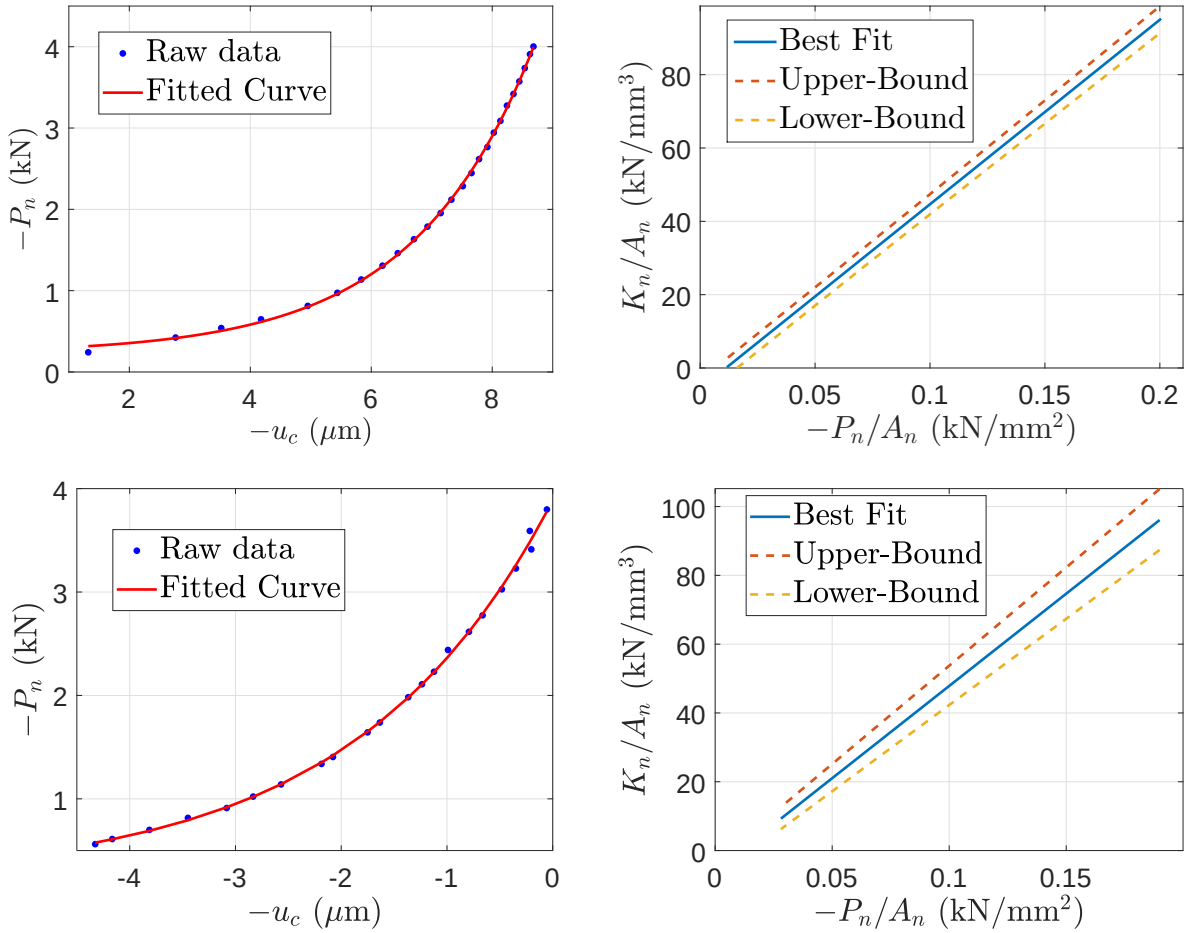

Figure 2.8: Results from RU1 test with maximum normal load of $-P_n = 4$ kN. **Top**: Results from the loading step. **Bottom**: Results from the unloading step. **Left**: Normal contact displacement and normal load relationship. **Right**: Normal contact stiffness and normal load relationship

Test RU2 8kN Normal Load

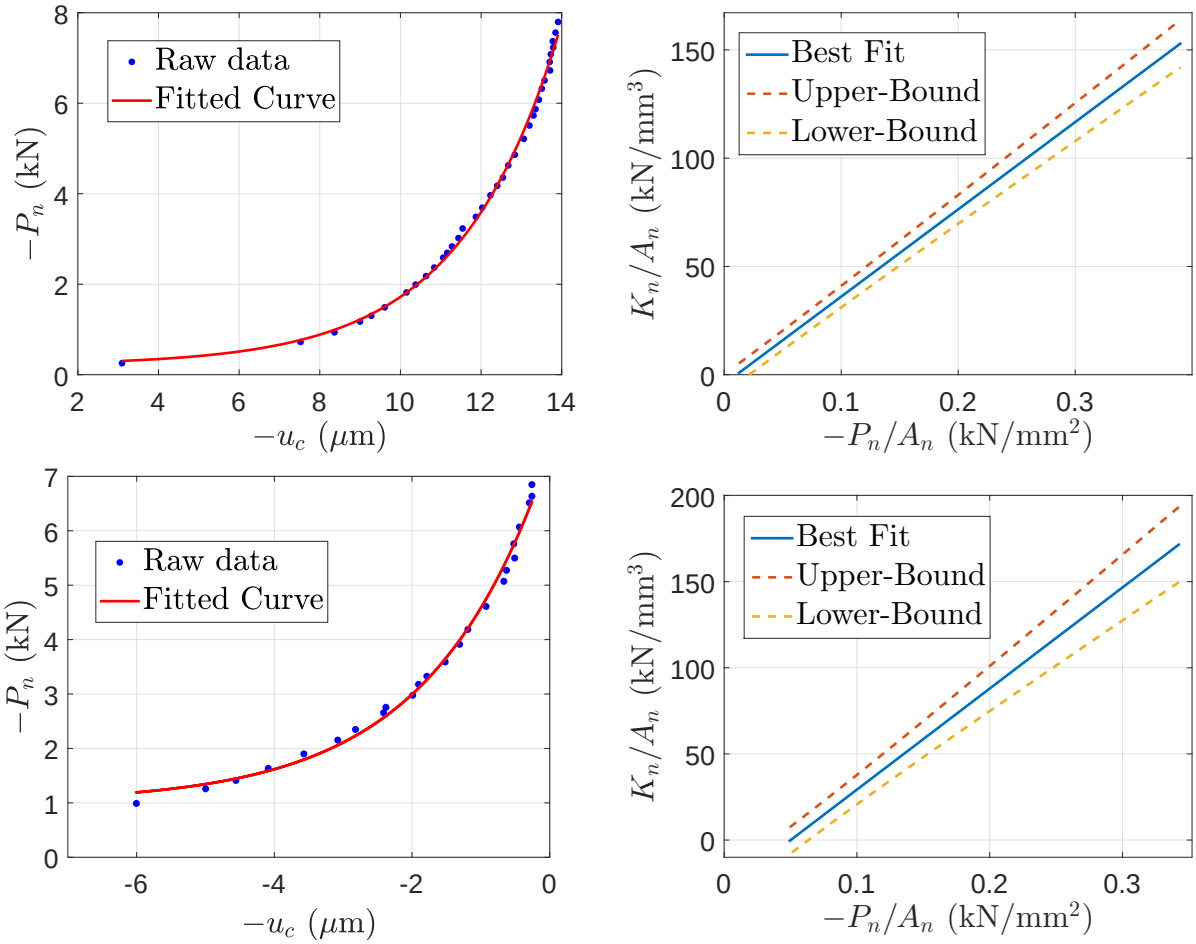

Figure 2.9: Results from RU2 test with maximum normal load of $-P_n = 8$ kN. **Top**: Results from the loading step. **Bottom**: Results from the unloading step. **Left**: Normal contact displacement and normal load relationship. **Right**: Normal contact stiffness and normal load relationship

Test RU3 12kN Normal Load

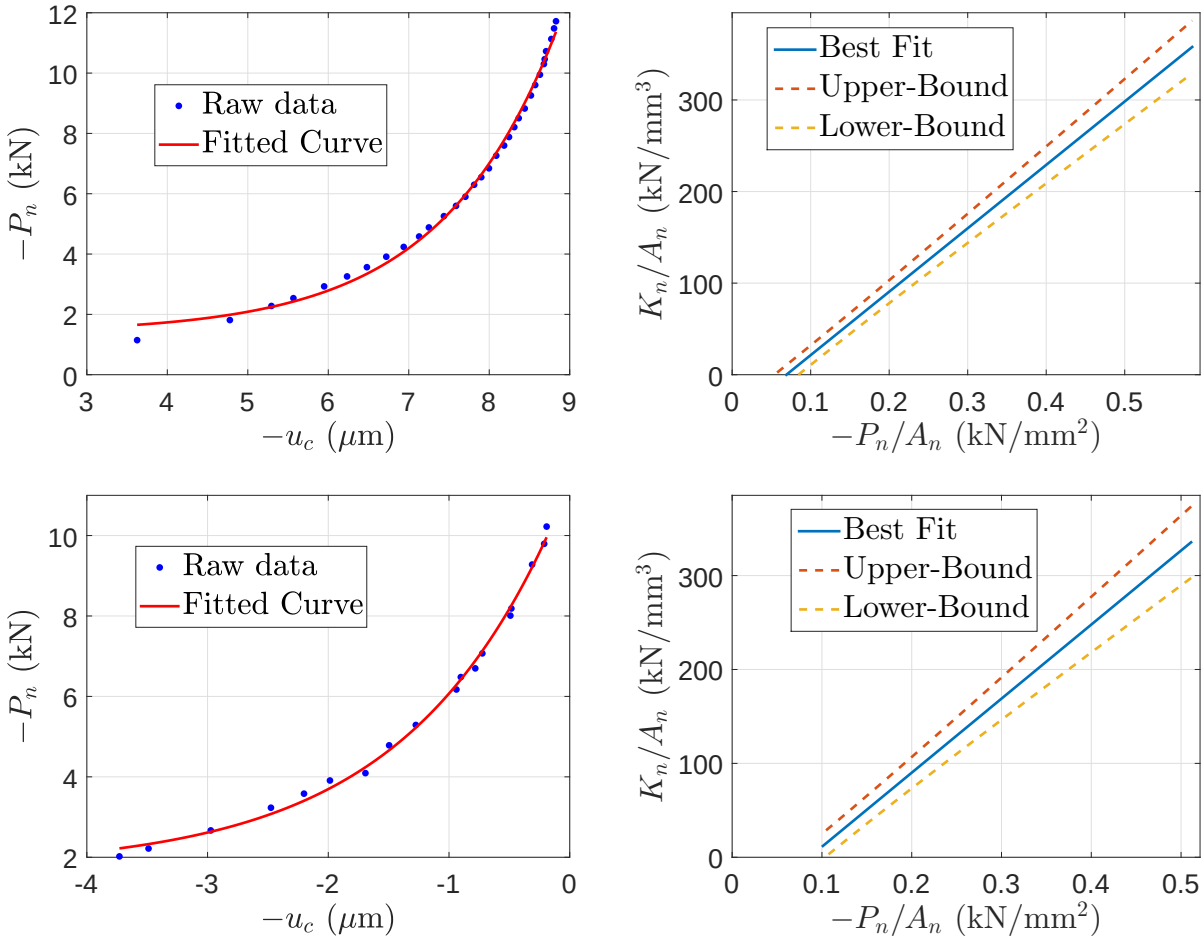

Figure 2.10: Results from RU3 test with maximum normal load of $-P_n = 12$ kN. **Top**: Results from the loading step. **Bottom**: Results from the unloading step. **Left**: Normal contact displacement and normal load relationship. **Right**: Normal contact stiffness and normal load relationship

Test SU1 4kN Normal Load

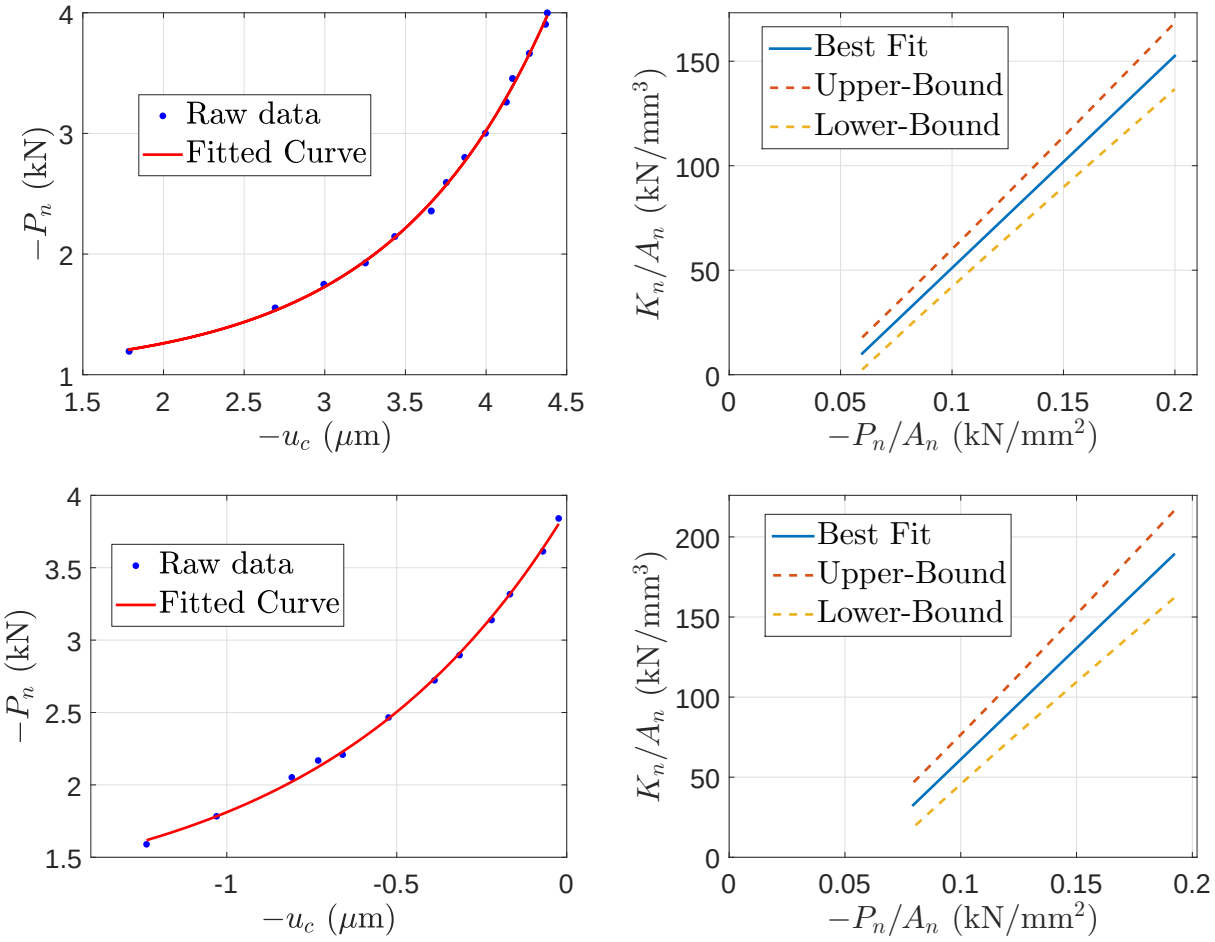

Figure 2.11: Results from SU1 test with maximum normal load of $-P_n = 4$ kN. **Top**: Results from the loading step. **Bottom**: Results from the unloading step. **Left**: Normal contact displacement and normal load relationship. **Right**: Normal contact stiffness and normal load relationship

Test SU2 8kN Normal Load

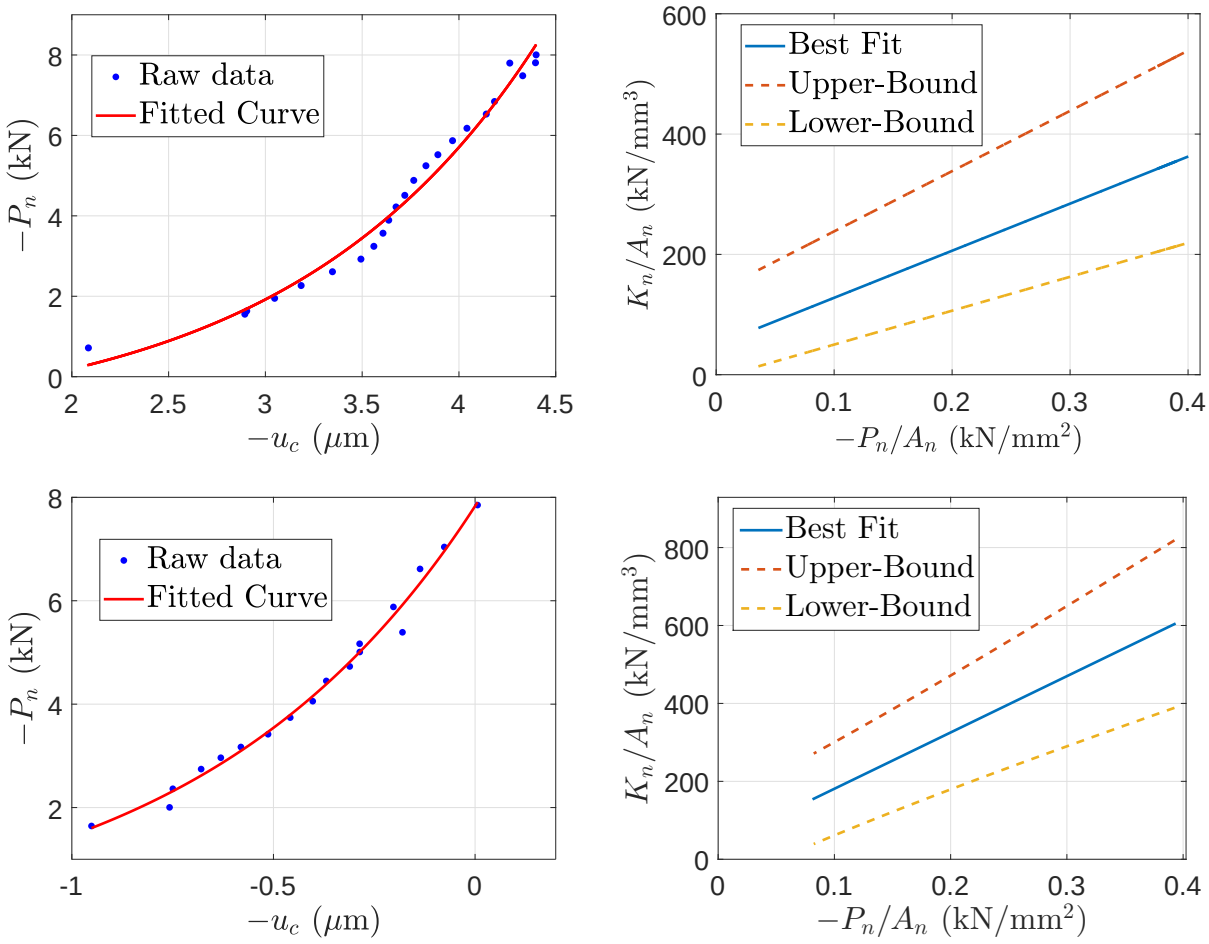

Figure 2.12: Results from SU2 test with maximum normal load of $-P_n = 8$ kN. **Top**: Results from the loading step. **Bottom**: Results from the unloading step. **Left**: Normal contact displacement and normal load relationship. **Right**: Normal contact stiffness and normal load relationship

Test SU3 12kN Normal Load

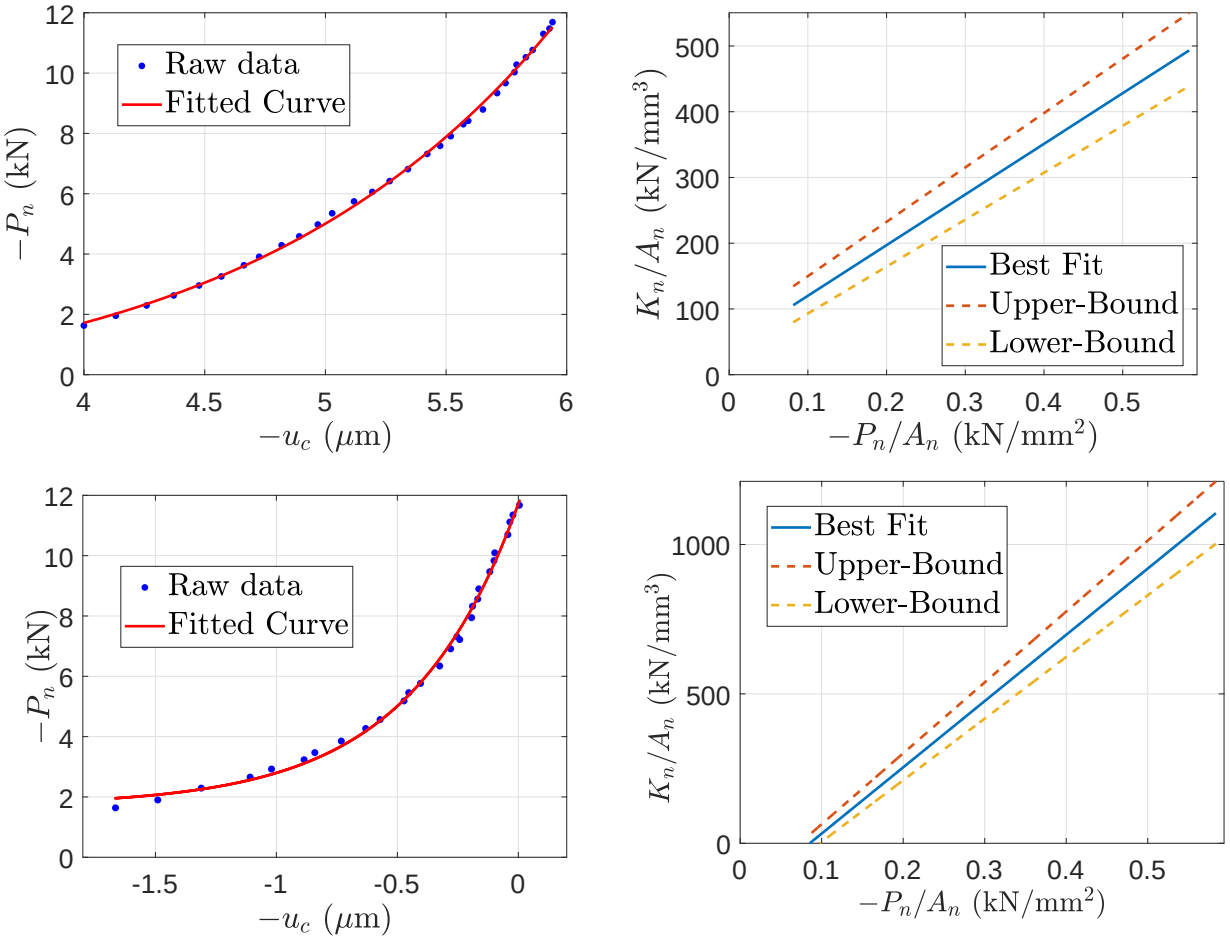

Figure 2.13: Results from SU3 test with maximum normal load of $-P_n = 12$ kN. **Top**: Results from the loading step. **Bottom**: Results from the unloading step. **Left**: Normal contact displacement and normal load relationship. **Right**: Normal contact stiffness and normal load relationship

2.6.2 Tangential Stiffness Test Results

Test RU1, with 4kN Normal Load

The model is seen to fit both the loading and the unloading steps well, however the $|\beta_t|$ parameter for the loading steps is twice that for the unloading steps (they should be the same). The coefficients of friction determined from the loading steps are also double that from the unloading steps. The error bars for the coefficient of friction values determined by the unloading steps are smaller and the values are near 0.2 which is the value determined in other tests, suggesting the unloading step values are probably more reliable. The K_{t0} values determined in both loading and unloading steps are similar.

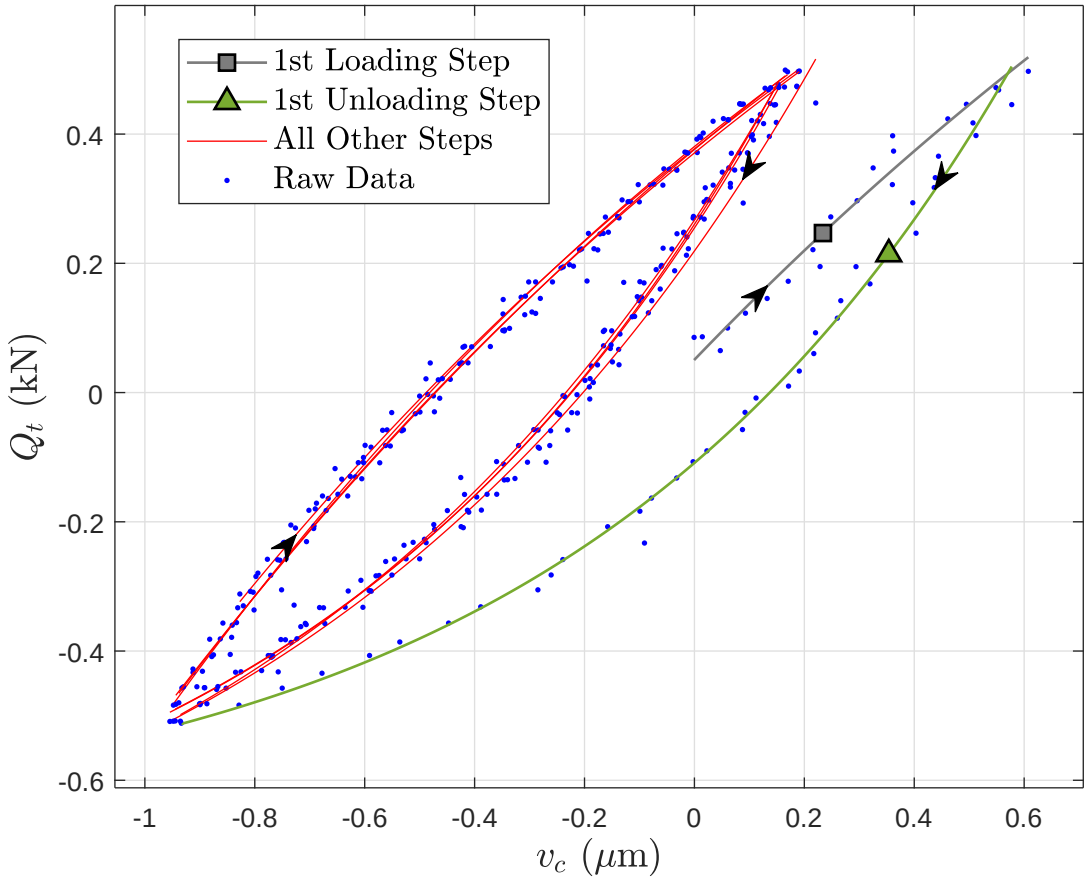

Figure 2.14: Plot of the tangential load and tangential contact displacement relationship, with fitted curves using exponential functions. The result is from the RU1 test for the tangential loading steps with normal load of $-P_n = 4$ kN.

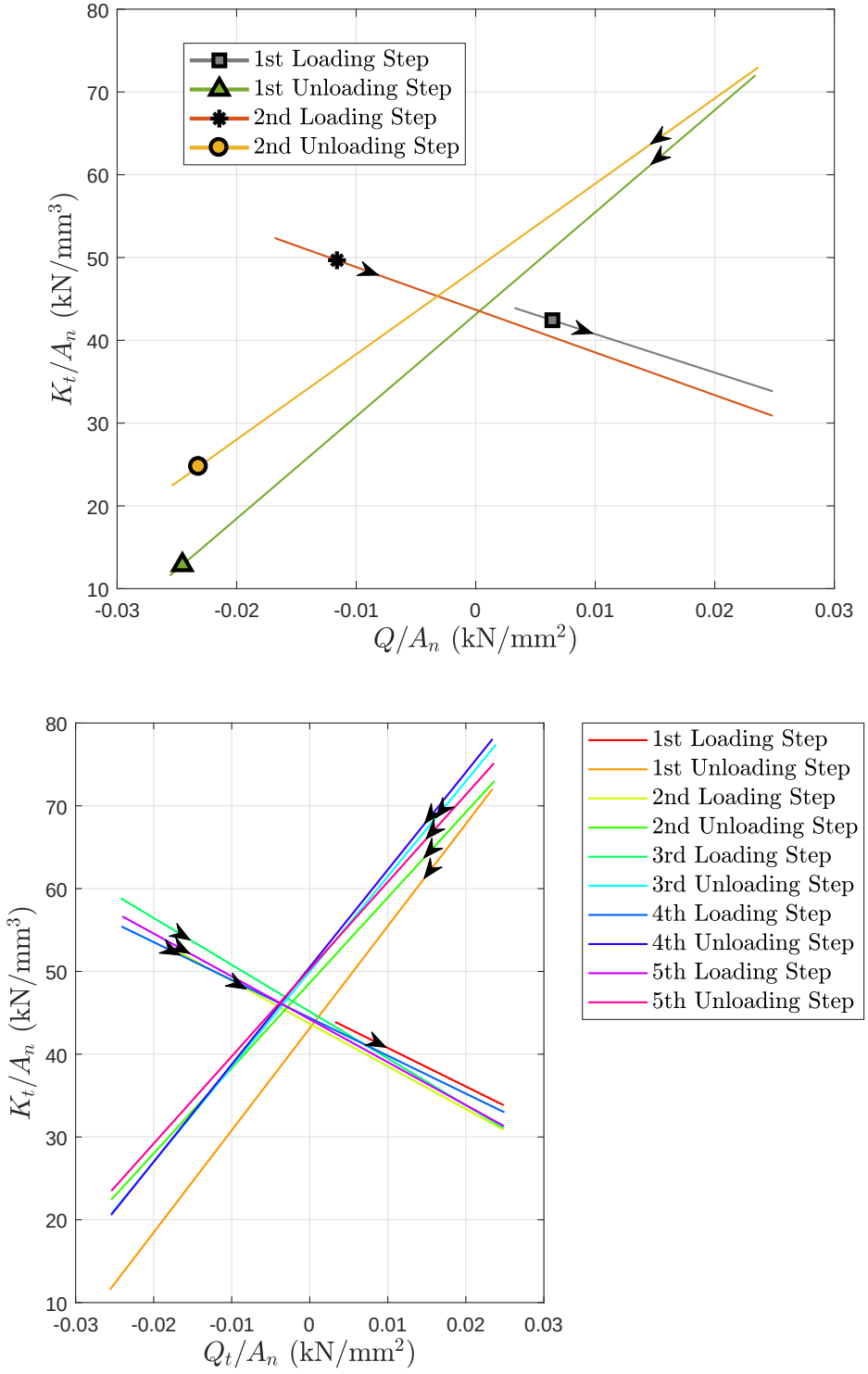

Figure 2.15: Plots of the tangential load and tangential contact stiffness relationship obtained. **Top**: Plots for the first two loading and unloading steps. **Bottom**: Plots for all loading steps. The results are from the RU1 test for the tangential loading steps with normal load of $-P_n = 4$ kN.

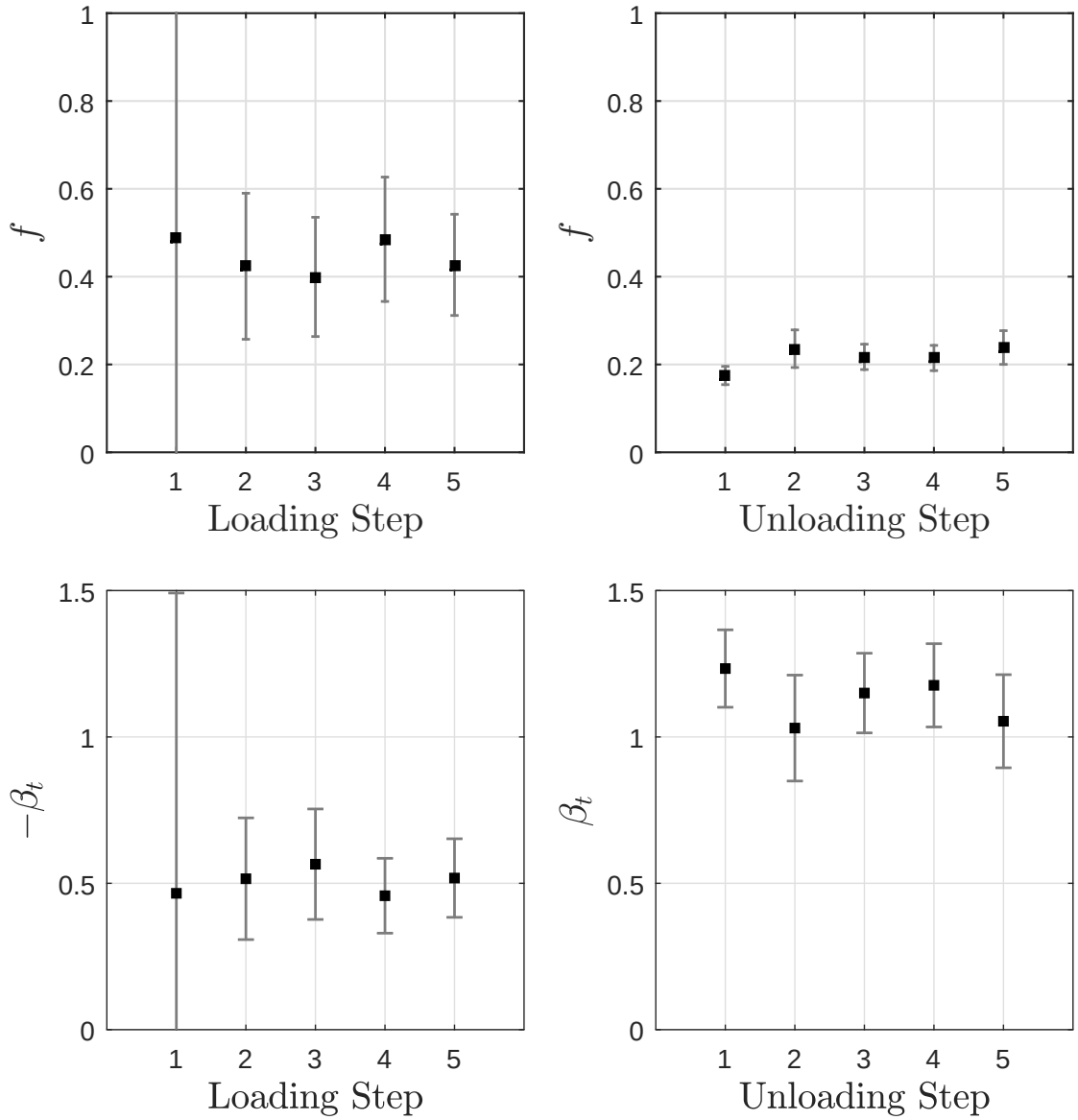

Figure 2.16: **Top**: Coefficient of friction deduced from the derived tangential contact stiffness and tangential load relationship with error bars due to fitting uncertainties for 95% confidence. **Bottom**: The slope of the tangential contact stiffness and tangential load relationship derived for each step with error bars due to fitting uncertainties for 95% confidence. **Left**: Results for the loading steps. **Right**: Results for the unloading steps. The results are from the RU1 test for the tangential loading steps with normal load of $-P_n = 4$ kN.

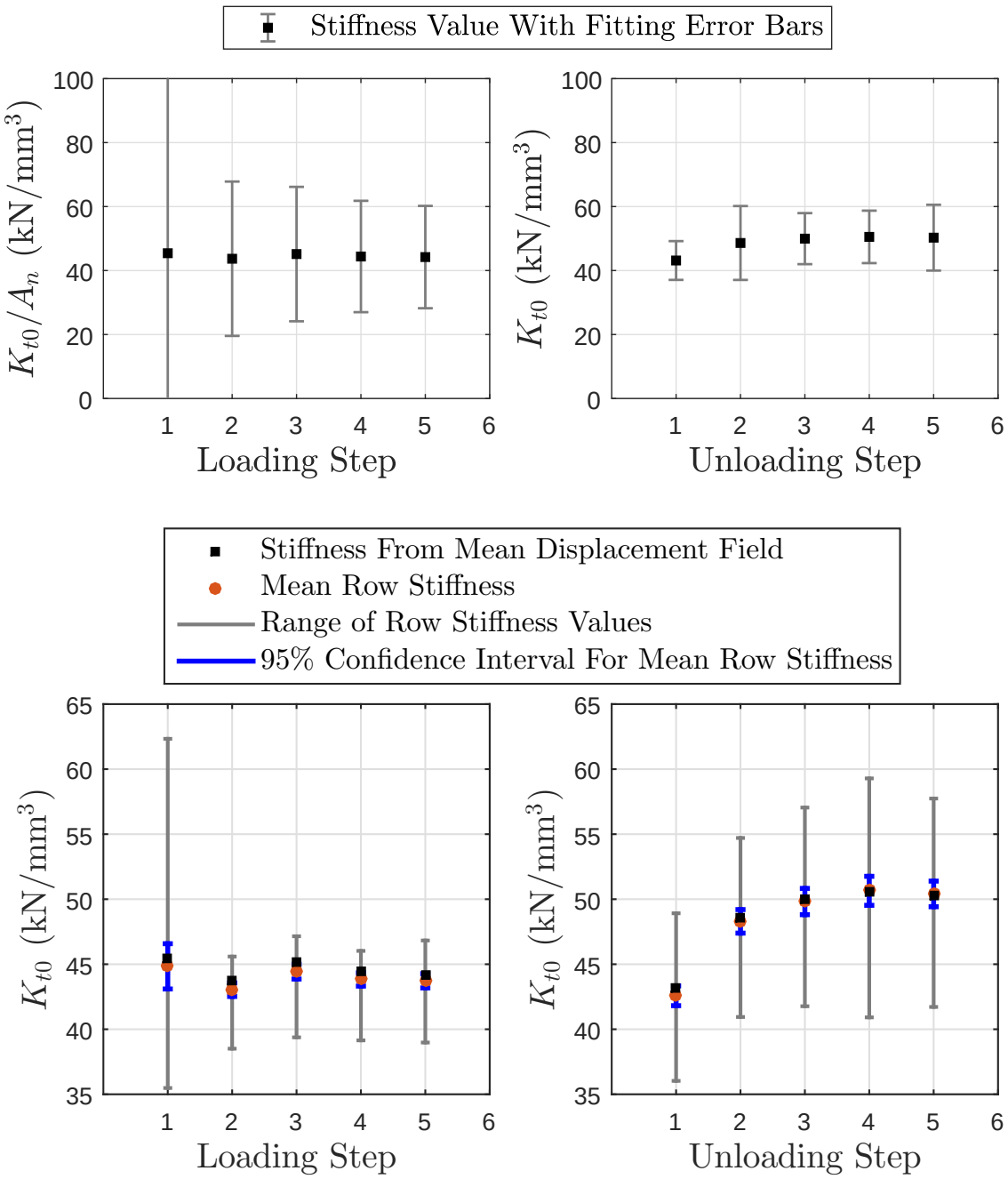

Figure 2.17: **Top**: The tangential contact stiffness at zero tangential load deduced from the derived tangential contact stiffness and tangential load relationship with error bars due to fitting uncertainties for 95% confidence. **Bottom**: The mean row tangential contact stiffness at zero tangential load with error bars from the Student's t-distribution for 95% confidence along with the maximum and minimum values for all the rows. The K_{t0} obtained from the mean displacement field (the values in the top figures) is plotted as well. **Left**: Results for the loading steps. **Right**: Results for the unloading steps. The results are from the RU1 test for the tangential loading steps with normal load of $-P_n = 4$ kN.

Test RU2 8kN Normal Load

The $|\beta_t|$ parameter is seen to be similar for both loading and unloading steps, and the coefficient of friction is seen to be around 0.2 for all steps. The margin of errors of the parameters computed are relatively small, suggesting the model fits the experimental data well.

It is noted that there appears to be a gap in the tangential load and tangential contact displacement data at the highest value of tangential load. See top corner of the load displacement plot in Figure 2.18. This seems due to a slight additional loading applied after obtaining the final image from the loading step and before the loading was reversed. This trend looks systematic, in this test, though less so in other tests. Minor adjustments were sometimes made to the normal loading at the end of some tangential loading steps. It is likely at the completion of the loading steps, a slight additional tangential load was applied by the controller, while the test cycle was paused to make the adjustments, before the tangential load was reduced. This slight additional loading would have lead to an increase in the contact displacement, not captured by digital image correlation process, before the loading was reversed.

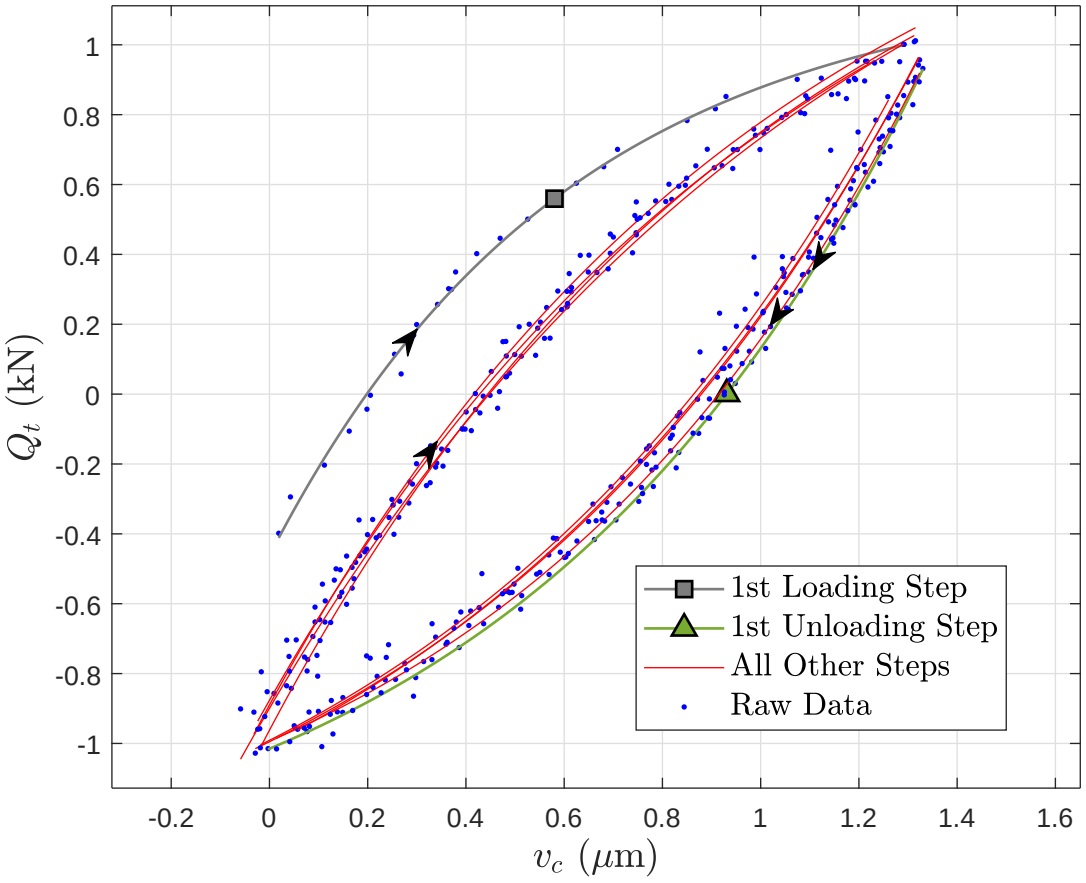

Figure 2.18: Plot of the tangential load and tangential contact displacement relationship, with fitted curves using exponential functions. The result is from the RU2 test for the tangential loading steps with normal load of $-P_n = 8$ kN.

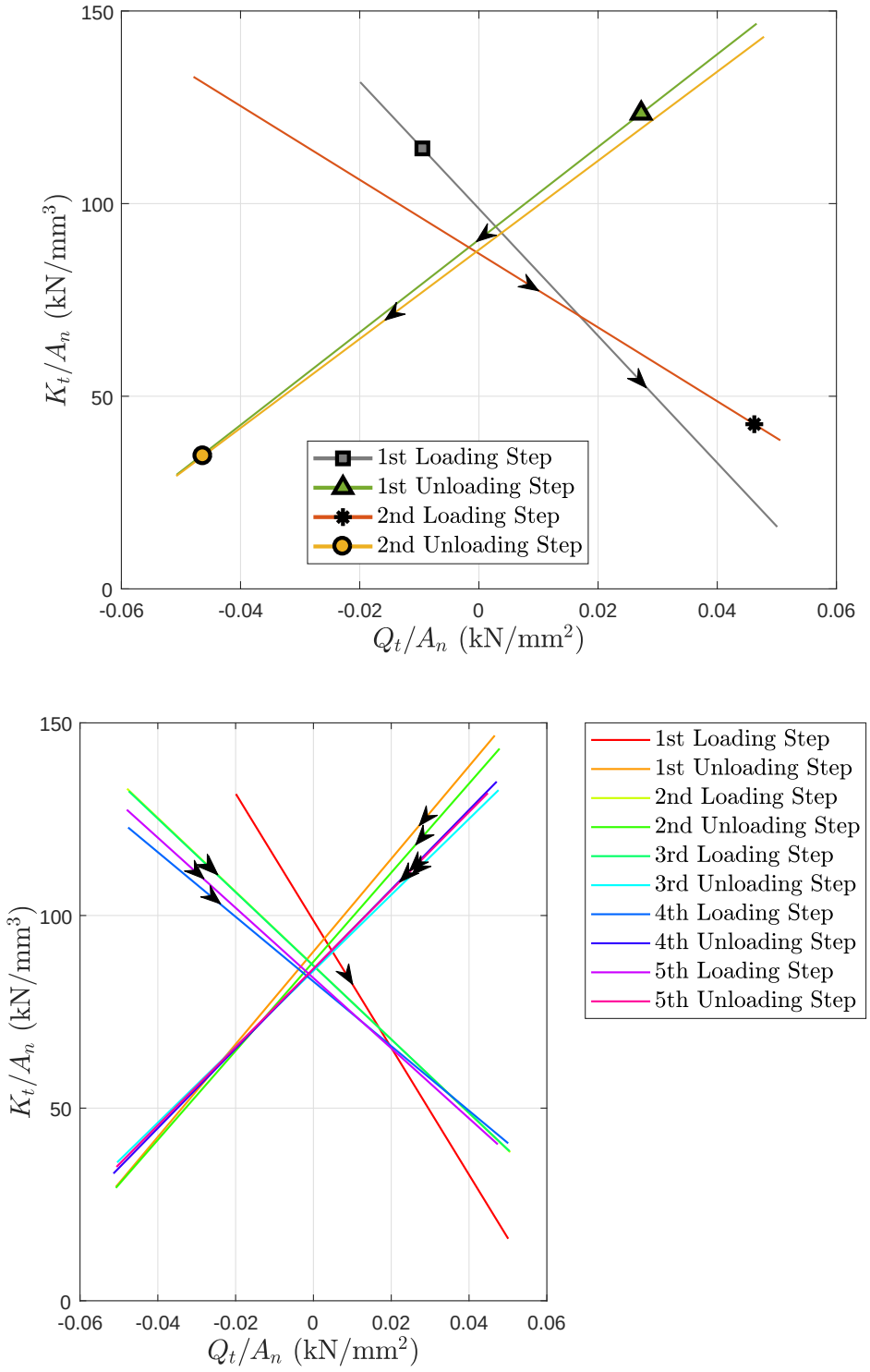

Figure 2.19: Plots of the tangential load and tangential contact stiffness relationship obtained. **Top**: Plots for the first two loading and unloading steps. **Bottom**: Plots for all loading steps. The results are from the RU2 test for the tangential loading steps with normal load of $-P_n = 8$ kN.

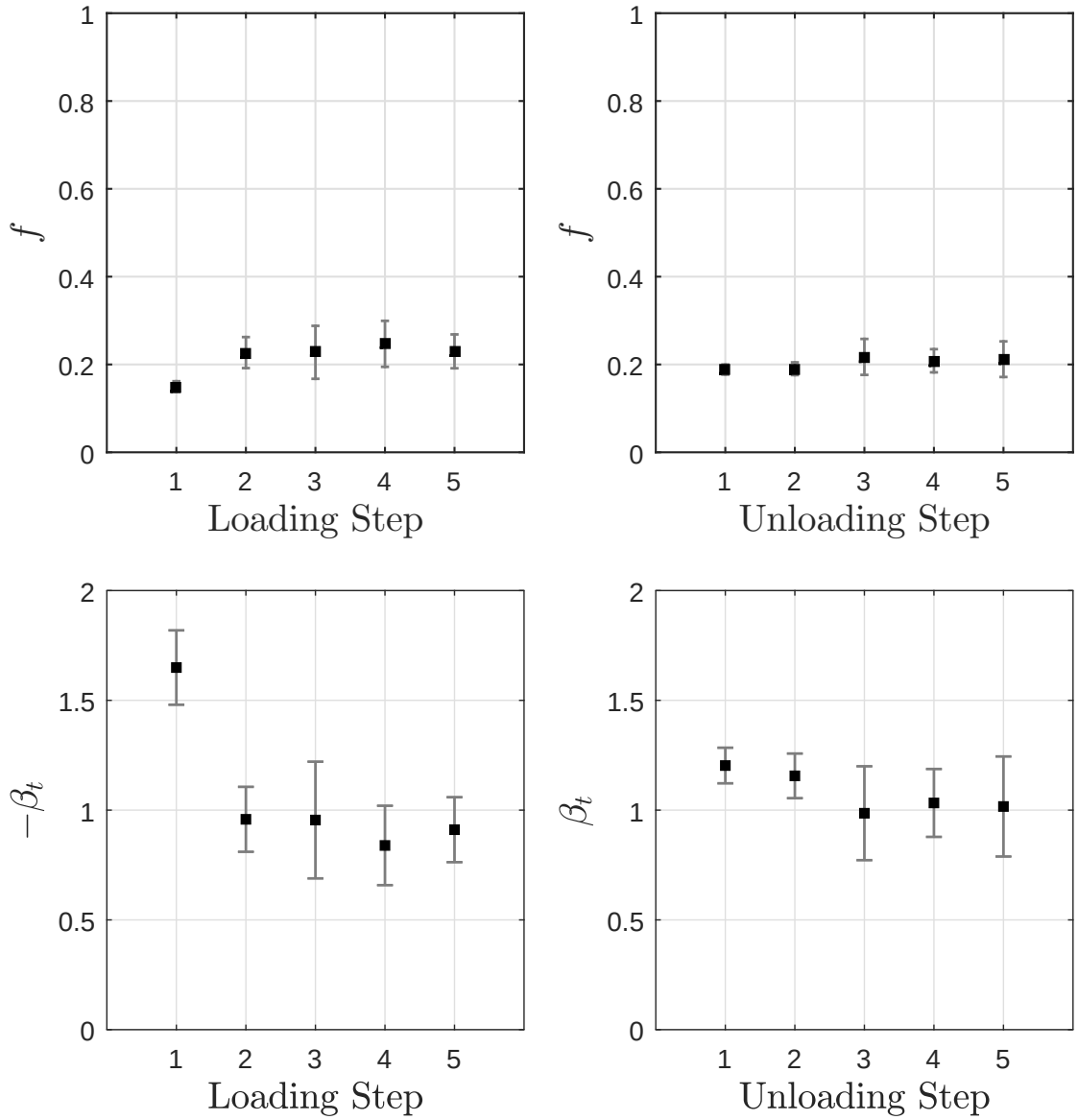

Figure 2.20: **Top**: Coefficient of friction deduced from the derived tangential contact stiffness and tangential load relationship with error bars due to fitting uncertainties for 95% confidence. **Bottom**: The slope of the tangential contact stiffness and tangential load relationship derived for each step with error bars due to fitting uncertainties for 95% confidence. **Left**: Results for the loading steps. **Right**: Results for the unloading steps. The results are from the RU2 test for the tangential loading steps with normal load of $-P_n = 8$ kN.

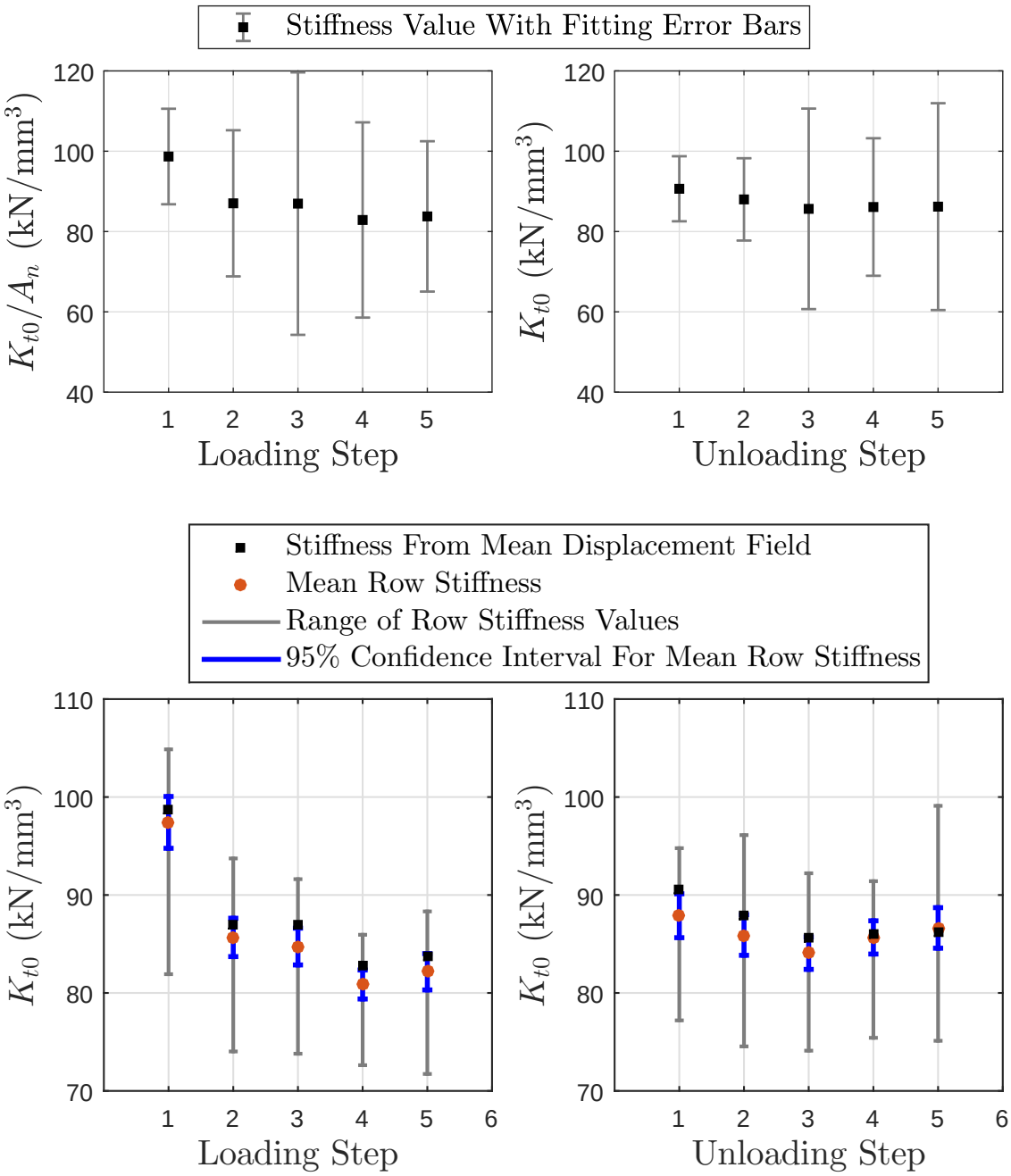

Figure 2.21: **Top**: The tangential contact stiffness at zero tangential load deduced from the derived tangential contact stiffness and tangential load relationship with error bars due to fitting uncertainties for 95% confidence. **Bottom**: The mean row tangential contact stiffness at zero tangential load with error bars from the Student's t-distribution for 95% confidence along with the maximum and minimum values for all the rows. The K_{t0} obtained from the mean displacement field (the values in the top figures) is plotted as well. **Left**: Results for the loading steps. **Right**: Results for the unloading steps. The results are from the RU2 test for the tangential loading steps with normal load of $-P_n = 8$ kN.

Test RU3 12kN Normal Load

Similar results for the $|\beta_t|$ parameter were obtained for all the loading and unloading steps except for the unloading steps 3, 4, and 5, for which the margin of error values for the measured parameters were very high, indicating the results from these steps are unreliable. From all other loading and unloading steps, which had lower margin of error values, the coefficient of friction value of the interface was measured to be near 0.2.

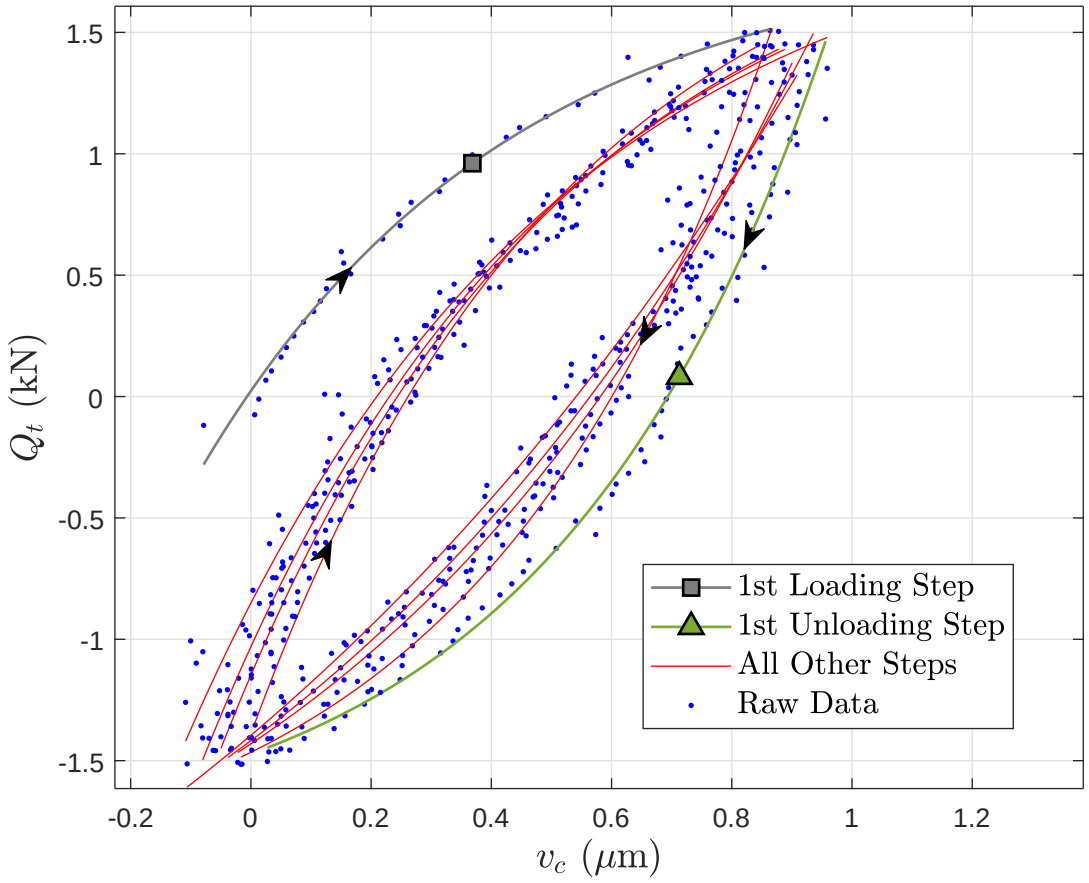

Figure 2.22: Plot of the tangential load and tangential contact displacement relationship, with fitted curves using exponential functions. The result is from the RU3 test for the tangential loading steps with normal load of $-P_n = 12$ kN.

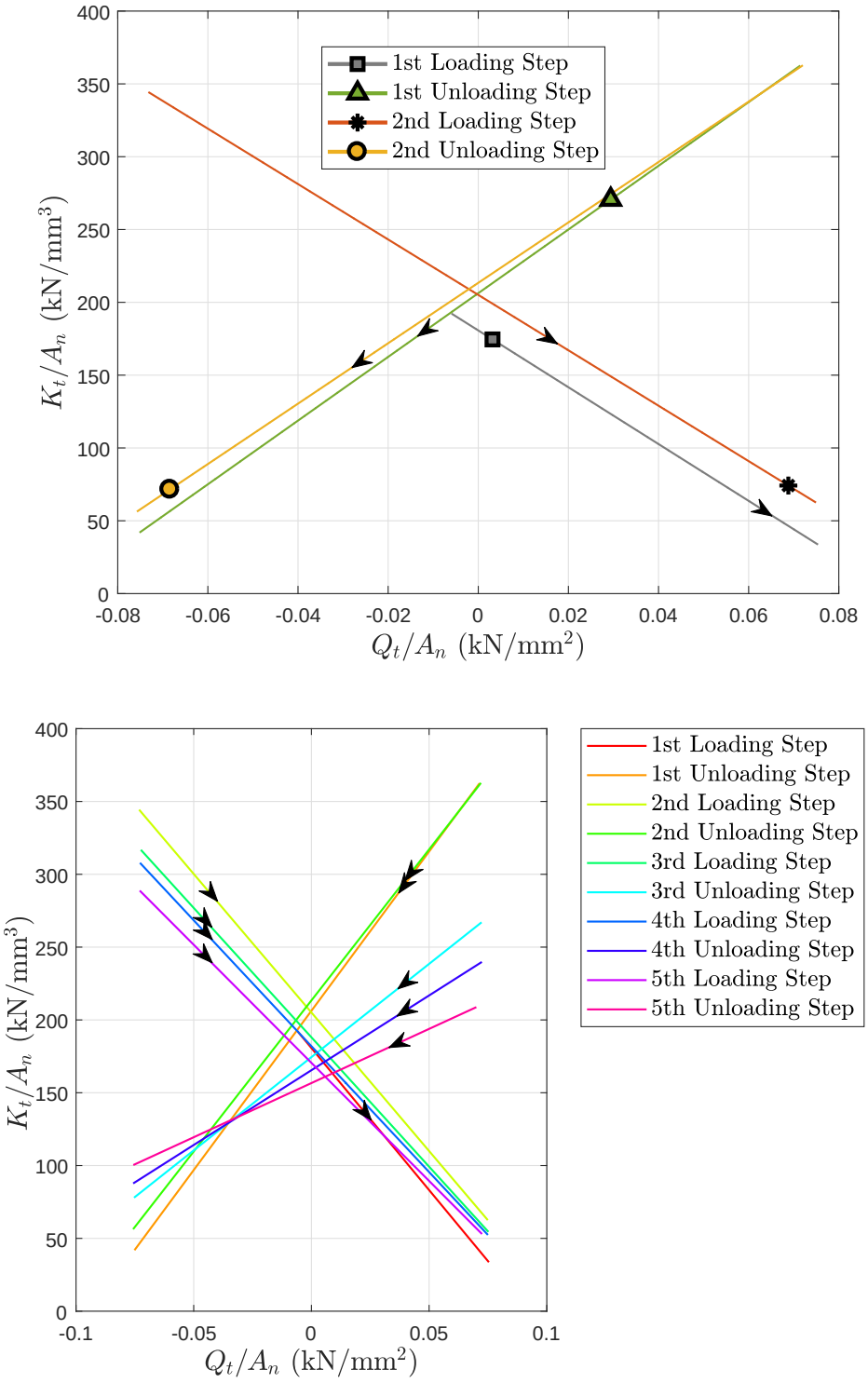

Figure 2.23: Plots of the tangential load and tangential contact stiffness relationship obtained. **Top**: Plots for the first two loading and unloading steps. **Bottom**: Plots for all loading steps. The results are from the RU3 test for the tangential loading steps with normal load of $-P_n = 12$ kN.

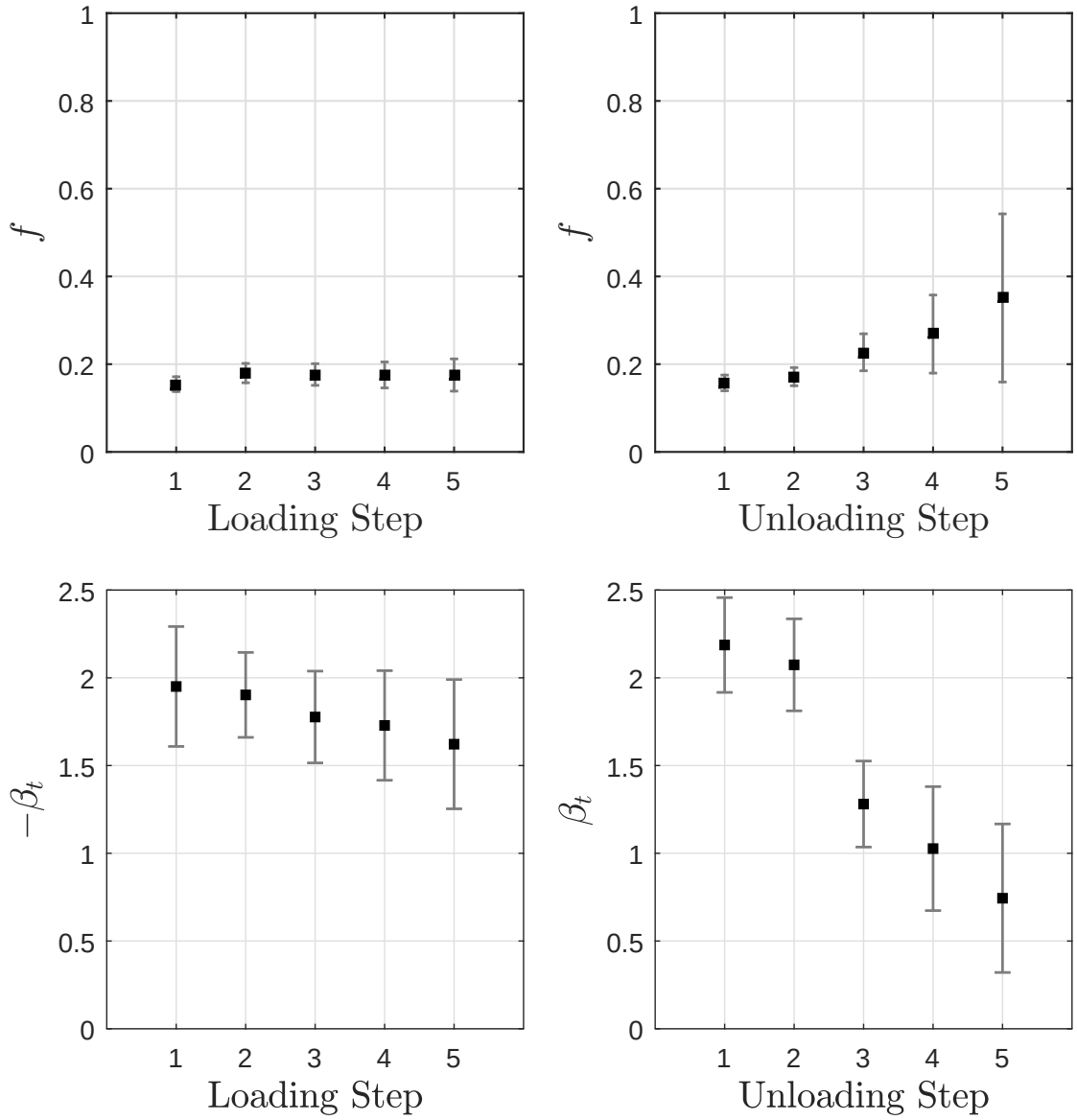

Figure 2.24: **Top**: Coefficient of friction deduced from the derived tangential contact stiffness and tangential load relationship with error bars due to fitting uncertainties for 95% confidence. **Bottom**: The slope of the tangential contact stiffness and tangential load relationship derived for each step with error bars due to fitting uncertainties for 95% confidence. **Left**: Results for the loading steps. **Right**: Results for the unloading steps. The results are from the RU3 test for the tangential loading steps with normal load of $-P_n = 12$ kN.

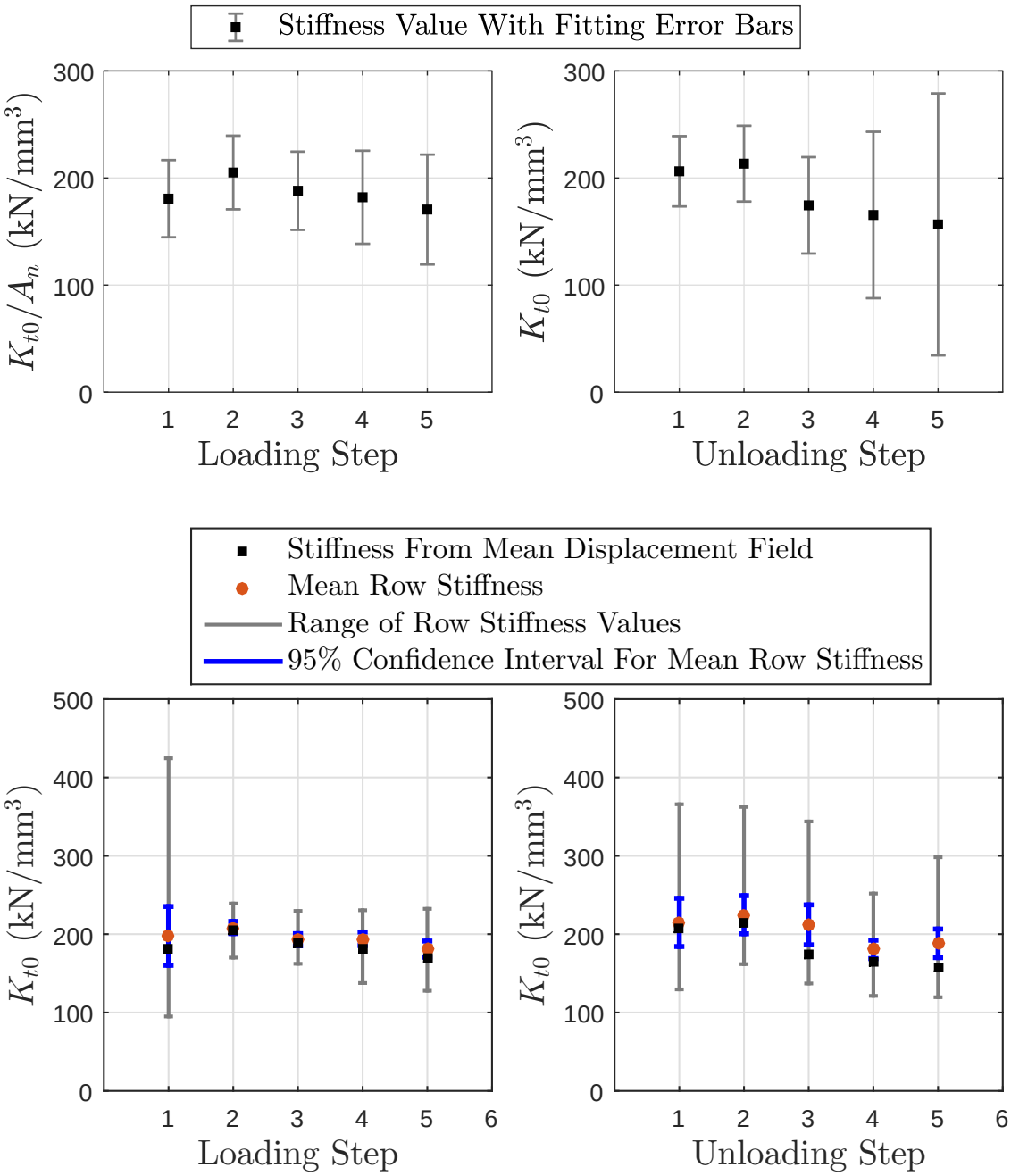

Figure 2.25: **Top**: The tangential contact stiffness at zero tangential load deduced from the derived tangential contact stiffness and tangential load relationship with error bars due to fitting uncertainties for 95% confidence. **Bottom**: The mean row tangential contact stiffness at zero tangential load with error bars from the Student's t-distribution for 95% confidence along with the maximum and minimum values for all the rows. The K_{t0} obtained from the mean displacement field (the values in the top figures) is plotted as well. **Left**: Results for the loading steps. **Right**: Results for the unloading steps. The results are from the RU3 test for the tangential loading steps with normal load of $-P_n = 12$ kN.

Test SU1 4kN Normal Load

Data was obtained only for two loading steps and for three unloading steps. Since the specimen surface were smooth, the contact displacement values are lower than that for the tests with the 'rough specimen' (S_q of 1.422 μm), and hence prone to greater error in measurement. The margin of error for the results obtained from the unloading steps were significantly lower than those from the loading steps. The coefficient of friction from the unloading steps were measured near 0.2.

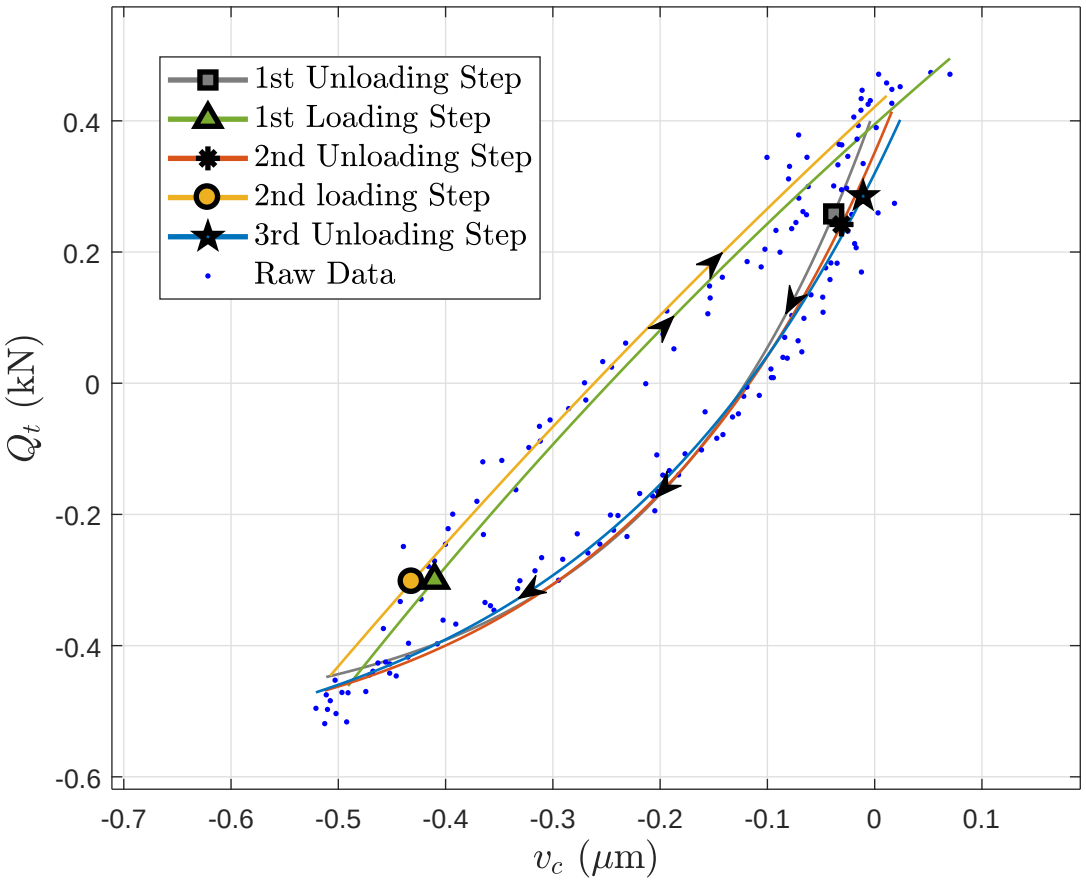

Figure 2.26: Plot of the tangential load and tangential contact displacement relationship, with fitted curves using exponential functions. The result is from the SU1 test for the tangential loading steps with normal load of $-P_n = 4$ kN.

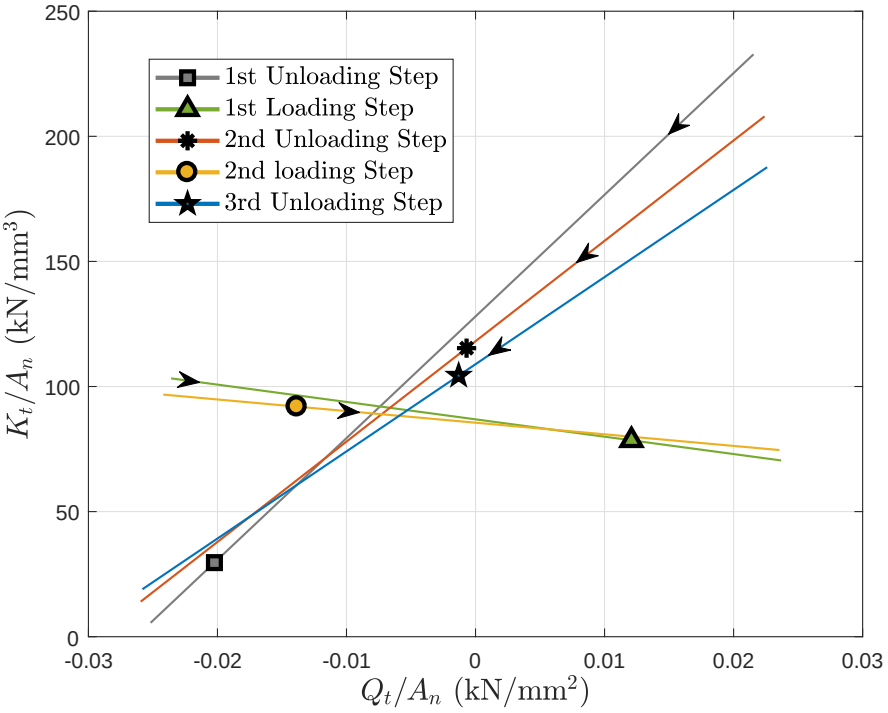

Figure 2.27: Plots of the tangential load and tangential contact stiffness relationship obtained. The results are from the SU1 test for the tangential loading steps with normal load of $-P_n = 4$ kN.

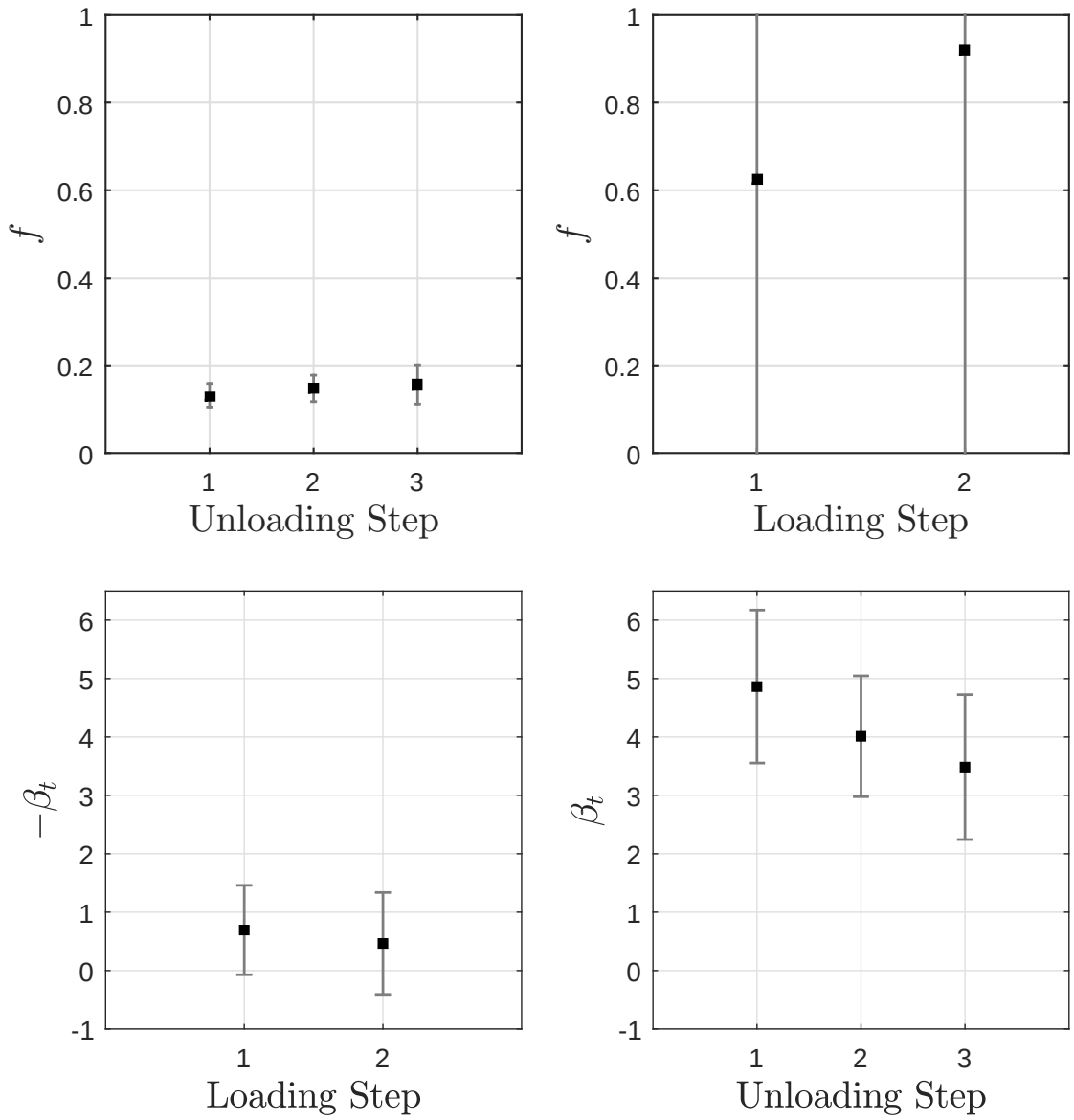

Figure 2.28: **Top**: Coefficient of friction deduced from the derived tangential contact stiffness and tangential load relationship with error bars due to fitting uncertainties for 95% confidence. **Bottom**: The slope of the tangential contact stiffness and tangential load relationship derived for each step with error bars due to fitting uncertainties for 95% confidence. **Left**: Results for the loading steps. **Right**: Results for the unloading steps. The results are from the SU1 test for the tangential loading steps with normal load of $-P_n = 4$ kN.

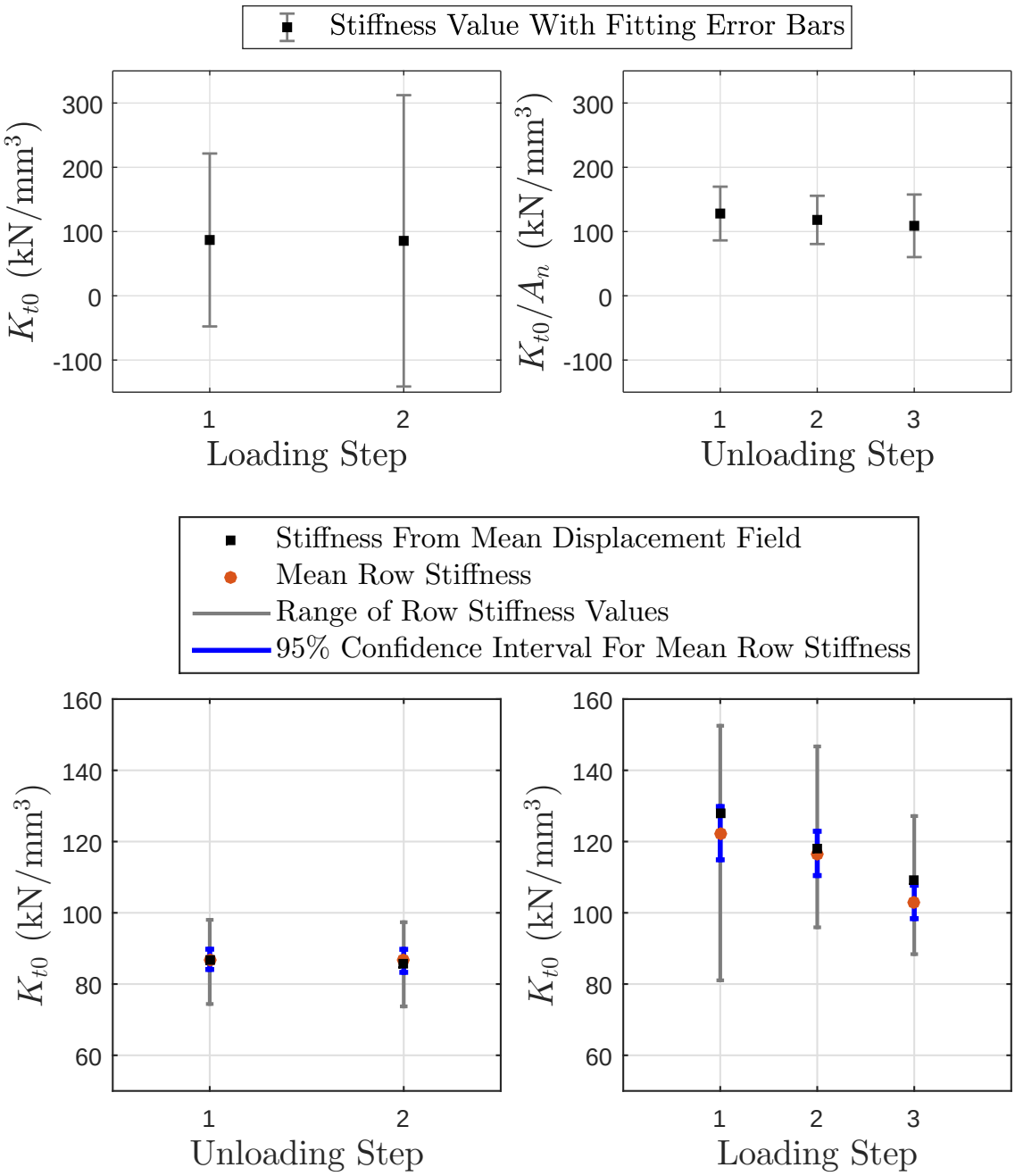

Figure 2.29: **Top**: The tangential contact stiffness at zero tangential load deduced from the derived tangential contact stiffness and tangential load relationship with error bars due to fitting uncertainties for 95% confidence. **Bottom**: The mean row tangential contact stiffness at zero tangential load with error bars from the Student's t-distribution for 95% confidence along with the maximum and minimum values for all the rows. The K_{t0} obtained from the mean displacement field (the values in the top figures) is plotted as well. **Left**: Results for the loading steps. **Right**: Results for the unloading steps. The results are from the SU1 test for the tangential loading steps with normal load of $-P_n = 4$ kN.

Test SU2 8kN Normal Load

Again, results with low margin of error were not obtained for all loading and unloading steps. Loading steps 2 to 5 provided values with relatively lower margin of error values and the coefficient of friction from these tests were in the reasonable range of around 0.2. The results from the unloading steps however were prone to significant errors, though the K_{t0} values determined from most steps were still of a similar magnitude.

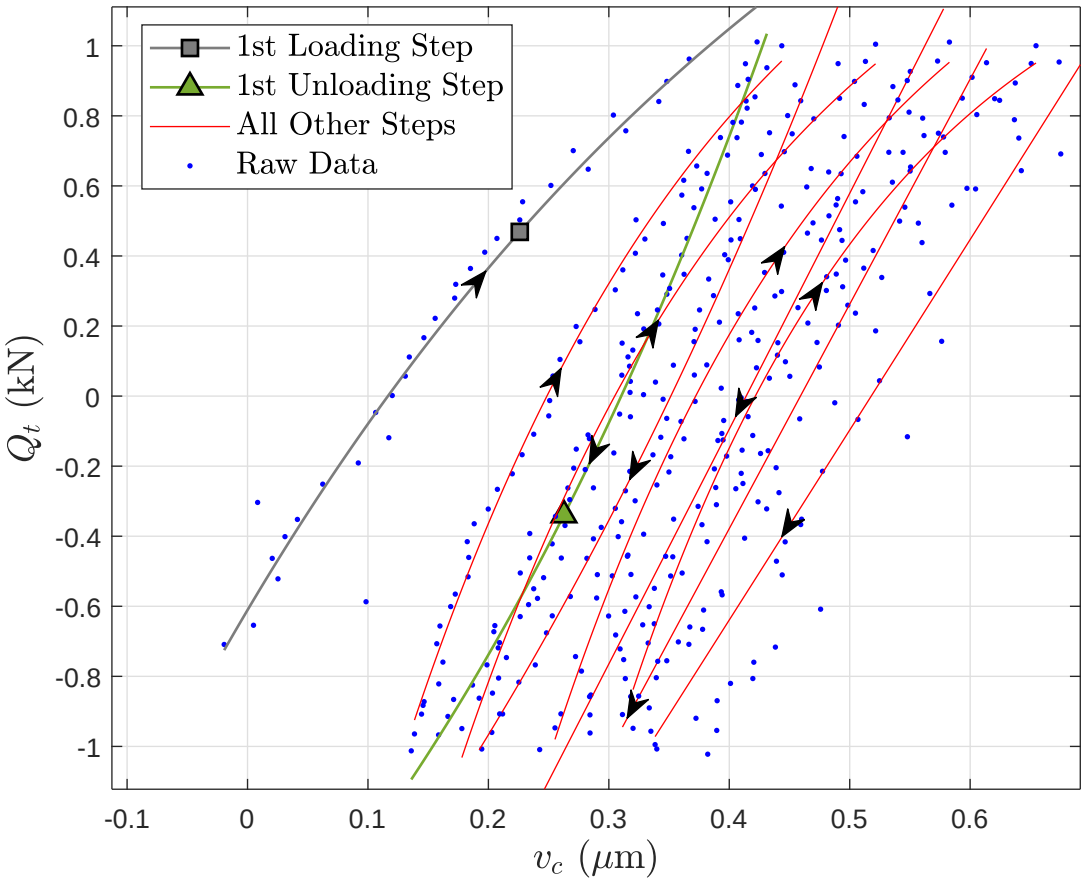

Figure 2.30: Plot of the tangential load and tangential contact displacement relationship, with fitted curves using exponential functions. The result is from the SU2 test for the tangential loading steps with normal load of $-P_n = 8$ kN.

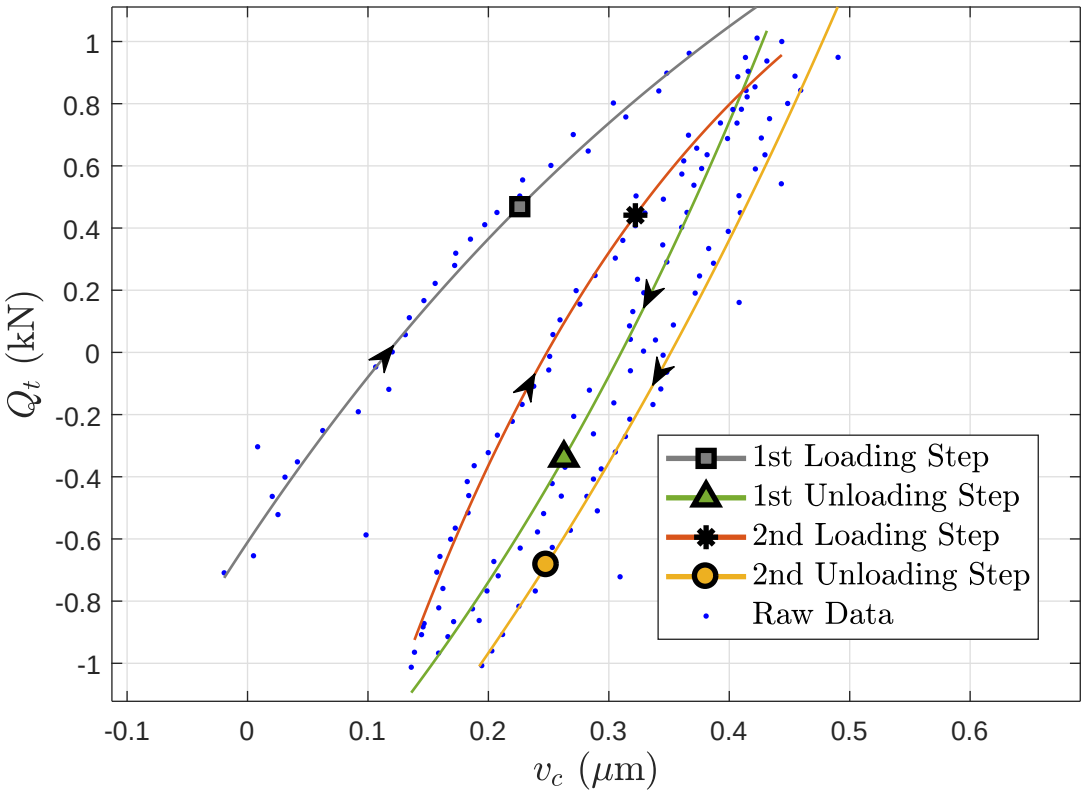

Figure 2.31: Plot of the tangential load and tangential contact displacement relationship, with fitted curves using exponential functions for two loading and unloading steps. The result is from the SU2 test for the tangential loading steps with normal load of $-P_n = 8$ kN.

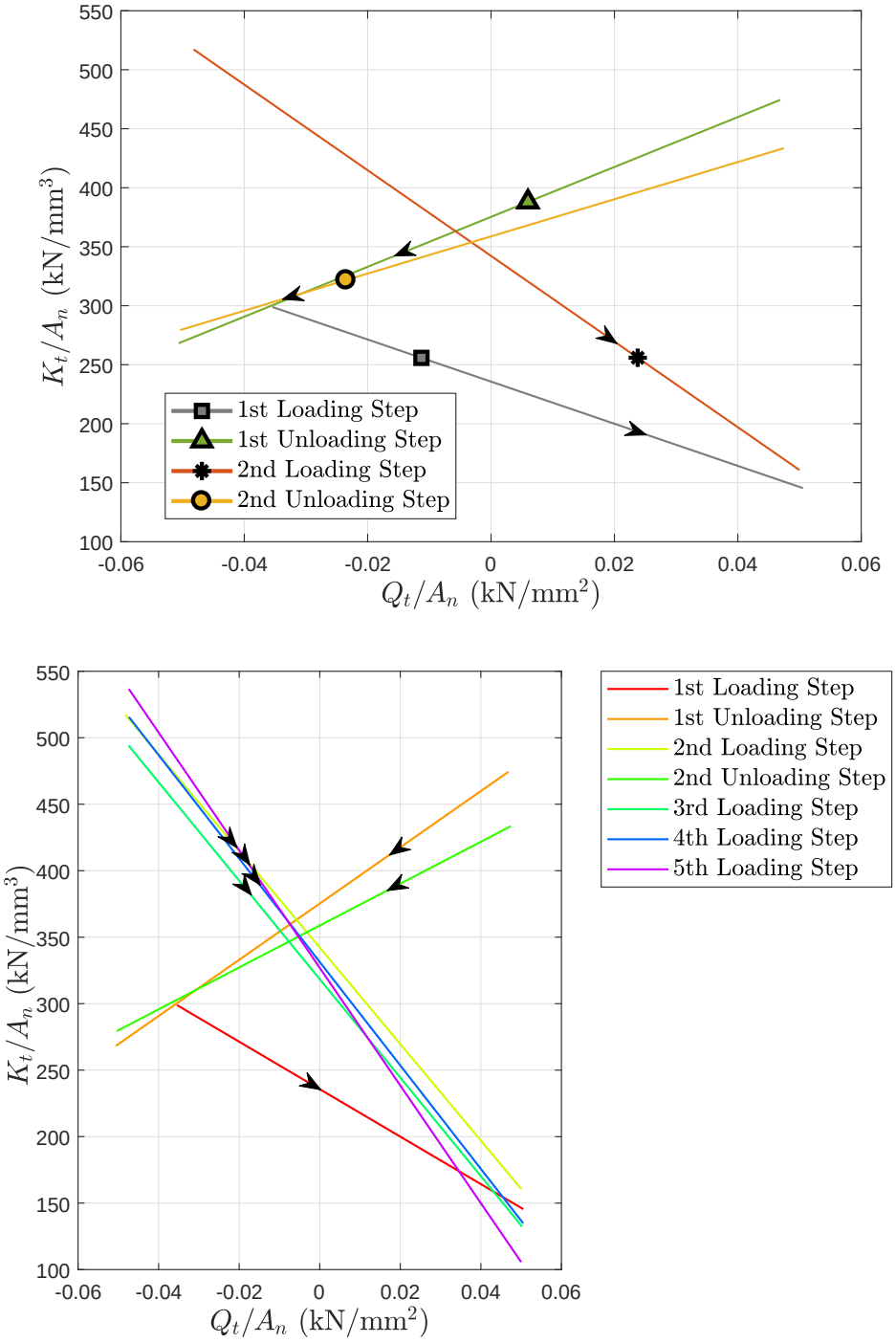

Figure 2.32: Plots of the tangential load and tangential contact stiffness relationship obtained. **Top**: Plots for the first two loading and unloading steps. **Bottom**: Plots for all loading steps. The results are from the SU2 test for the tangential loading steps with normal load of $-P_n = 8$ kN.

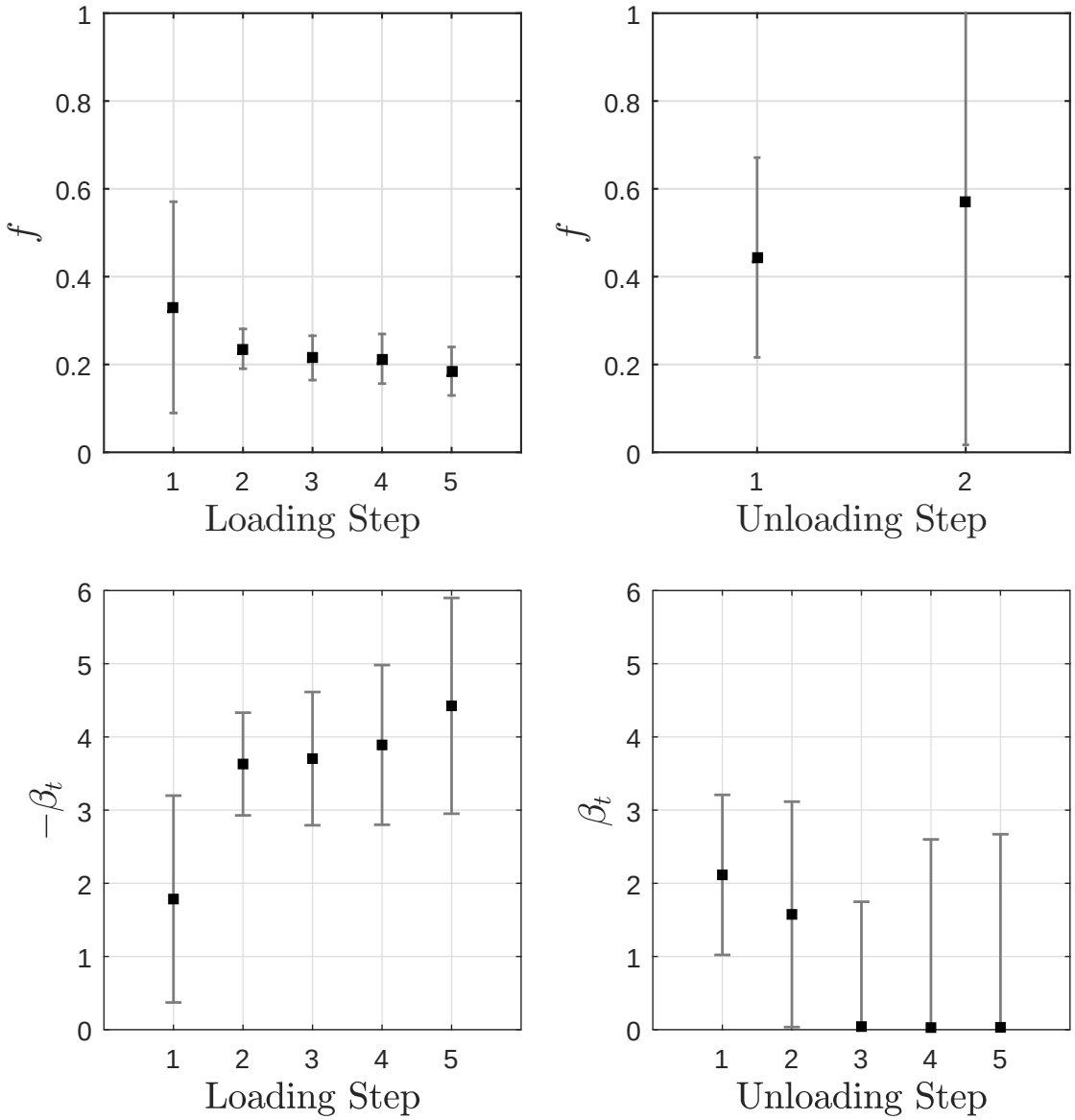

Figure 2.33: **Top**: Coefficient of friction deduced from the derived tangential contact stiffness and tangential load relationship with error bars due to fitting uncertainties for 95% confidence. **Bottom**: The slope of the tangential contact stiffness and tangential load relationship derived for each step with error bars due to fitting uncertainties for 95% confidence. **Left**: Results for the loading steps. **Right**: Results for the unloading steps. The results are from the SU2 test for the tangential loading steps with normal load of $-P_n = 8$ kN.

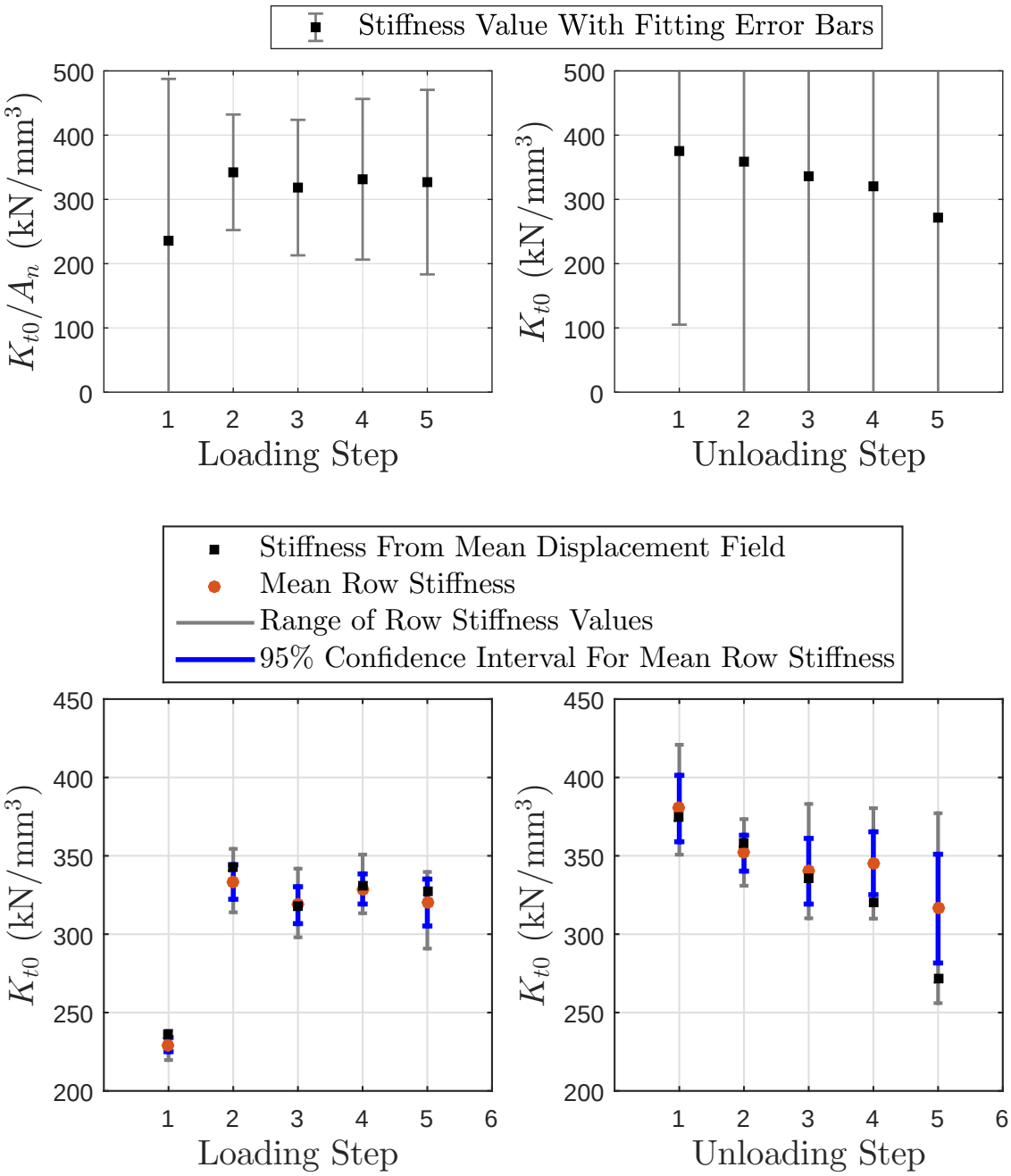

Figure 2.34: **Top**: The tangential contact stiffness at zero tangential load deduced from the derived tangential contact stiffness and tangential load relationship with error bars due to fitting uncertainties for 95% confidence. **Bottom**: The mean row tangential contact stiffness at zero tangential load with error bars from the Student's t-distribution for 95% confidence along with the maximum and minimum values for all the rows. The K_{t0} obtained from the mean displacement field (the values in the top figures) is plotted as well. **Left**: Results for the loading steps. **Right**: Results for the unloading steps. The results are from the SU2 test for the tangential loading steps with normal load of $-P_n = 8$ kN.

Test SU3 12kN Normal Load

As in the other tests with the 'smooth specimen' (S_q of 0.687μm), experimental error was significantly large for some steps. However, reasonable results with relatively low margin of error values were obtained for all the loading steps and unloading steps 1 and 2. The coefficient of friction determined from these steps were near 0.2.

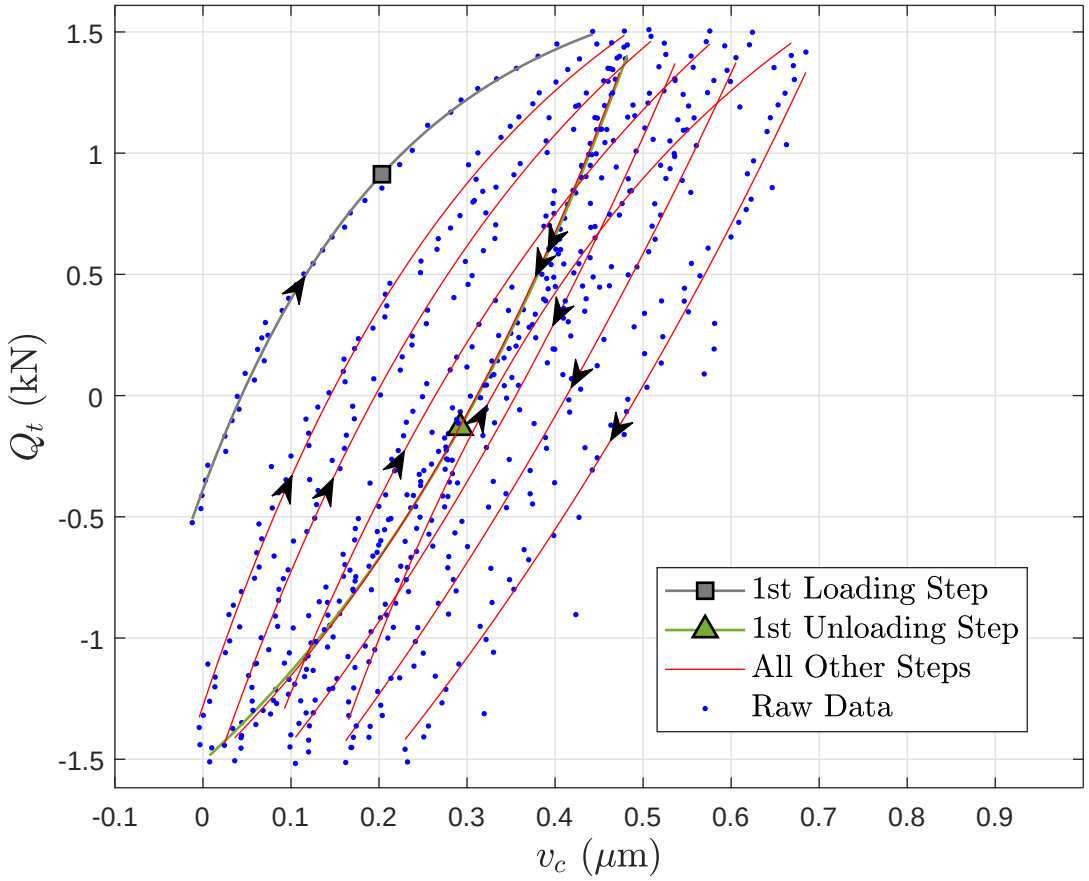

Figure 2.35: Plot of the tangential load and tangential contact displacement relationship, with fitted curves using exponential functions. The result is from the SU3 test for the tangential loading steps with normal load of $-P_n = 12$ kN.

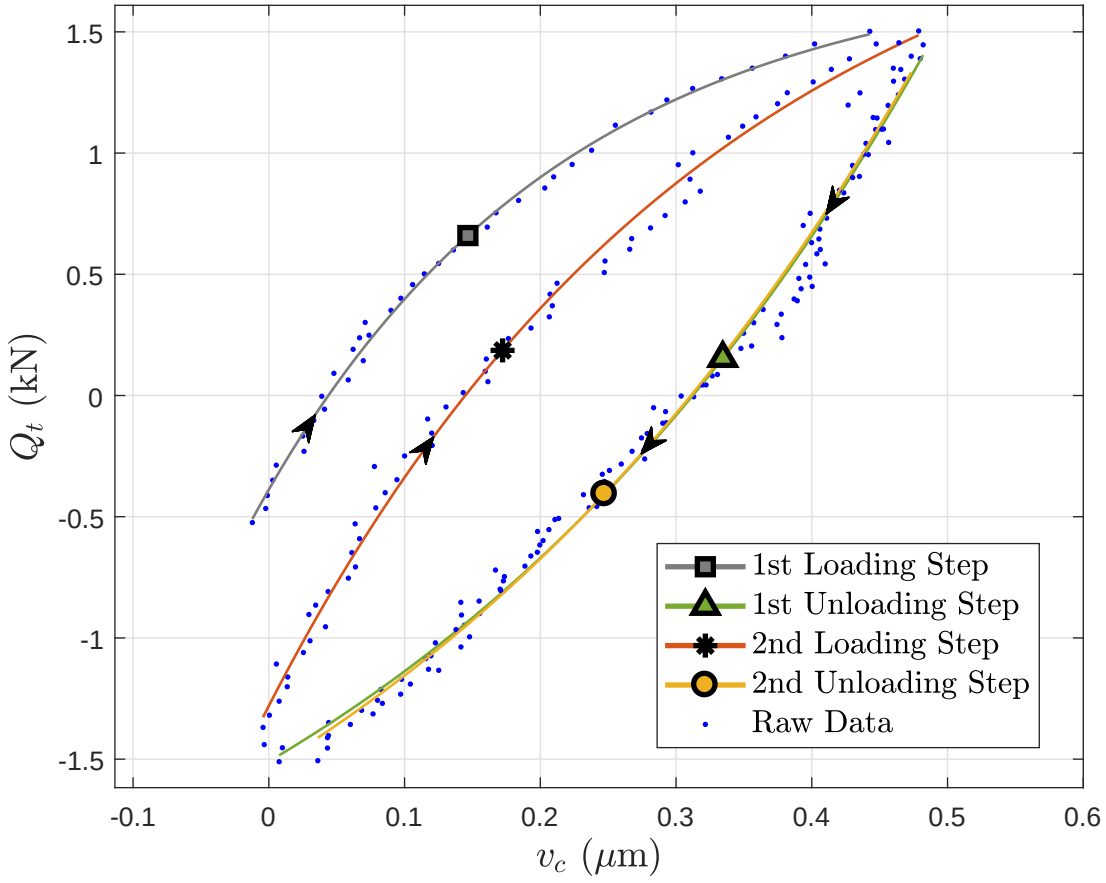

Figure 2.36: Plot of the tangential load and tangential contact displacement relationship, with fitted curves using exponential functions for the first two loading and unloading steps. The result is from the SU3 test for the tangential loading steps with normal load of $-P_n = 12$ kN.

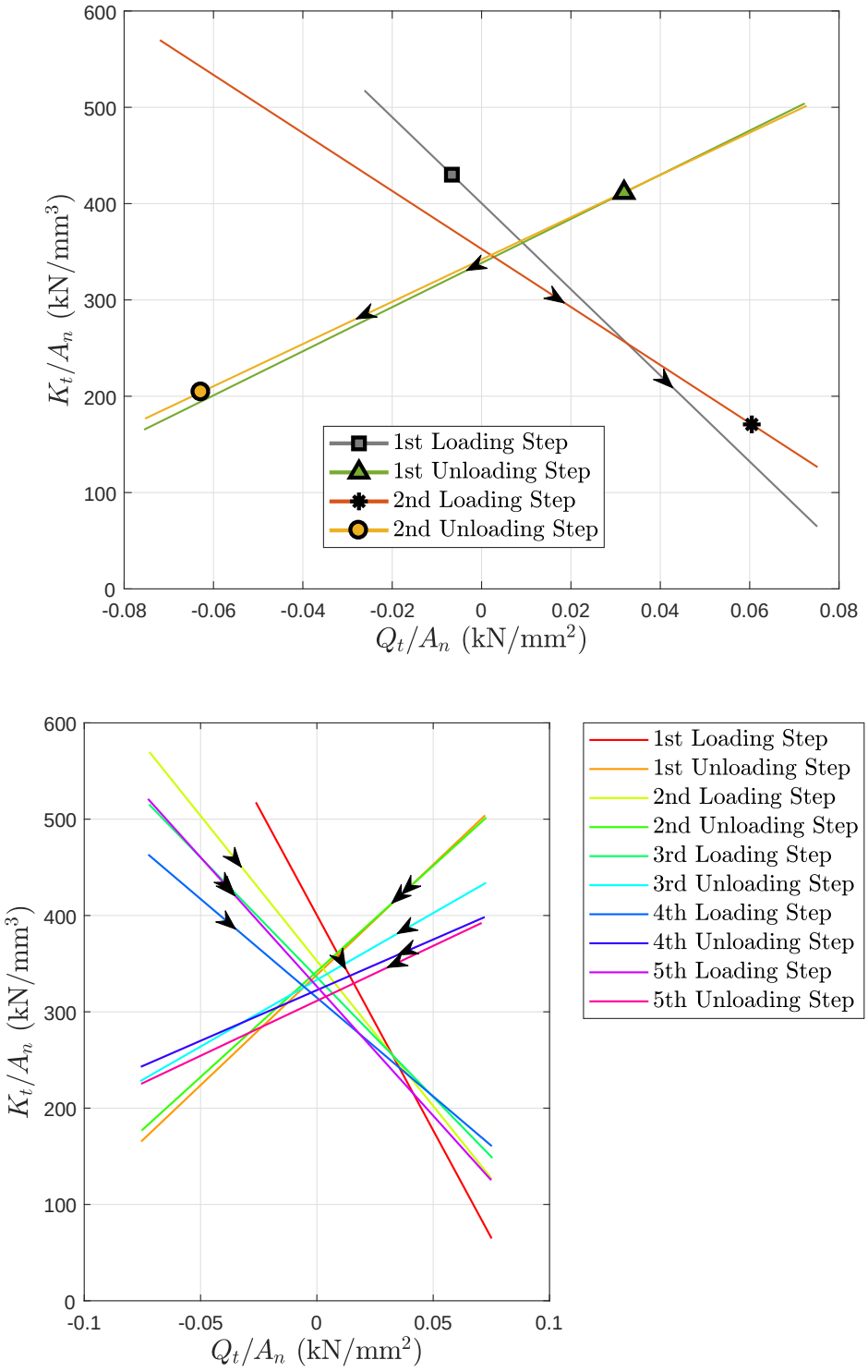

Figure 2.37: Plots of the tangential load and tangential contact stiffness relationship obtained. **Top**: Plots for the first two loading and unloading steps. **Bottom**: Plots for all loading steps. The results are from the SU3 test for the tangential loading steps with normal load of $-P_n = 12$ kN.

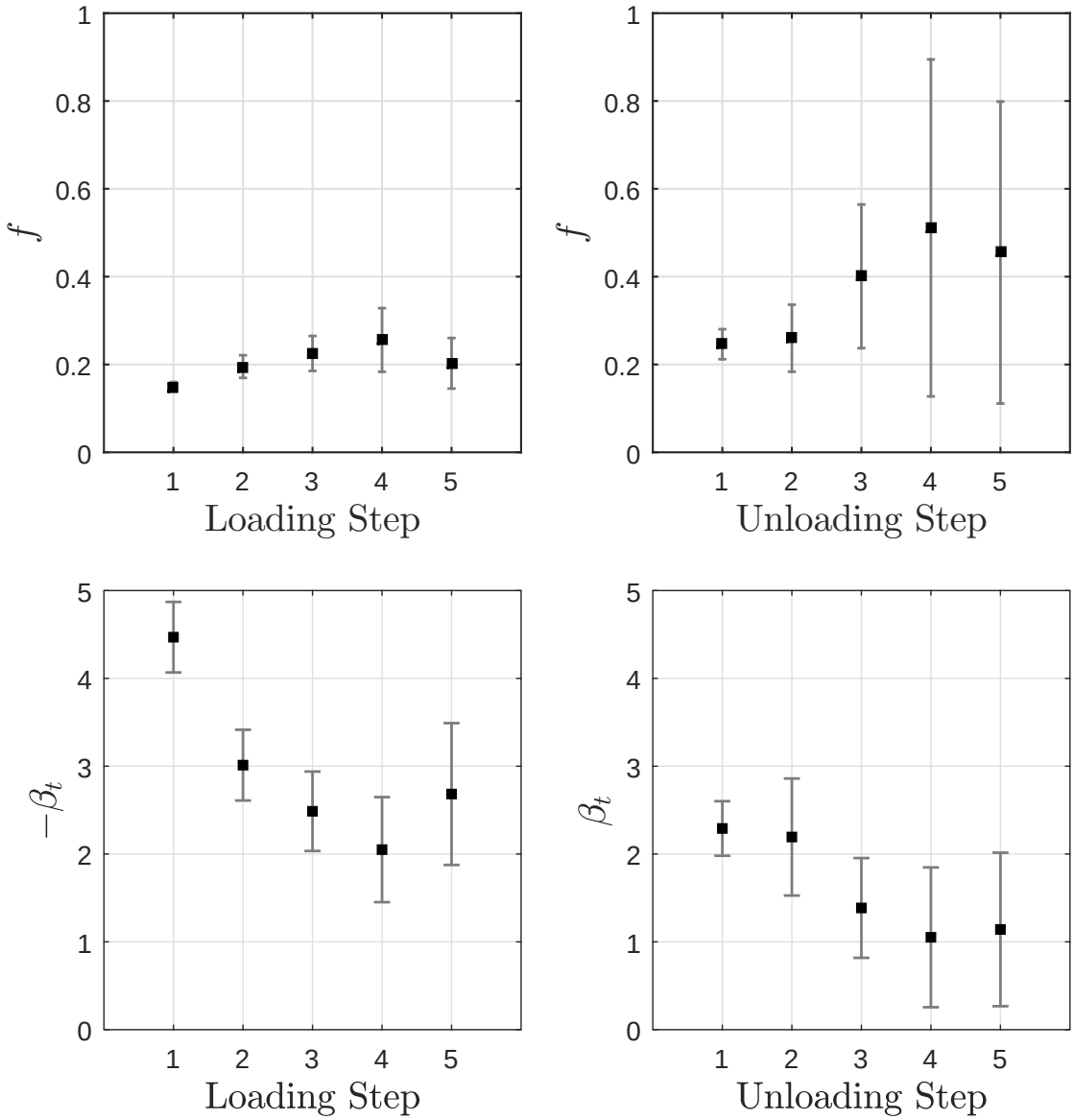

Figure 2.38: **Top**: Coefficient of friction deduced from the derived tangential contact stiffness and tangential load relationship with error bars due to fitting uncertainties for 95% confidence. **Bottom**: The slope of the tangential contact stiffness and tangential load relationship derived for each step with error bars due to fitting uncertainties for 95% confidence. **Left**: Results for the loading steps. **Right**: Results for the unloading steps. The results are from the SU3 test for the tangential loading steps with normal load of $-P_n = 12$ kN.

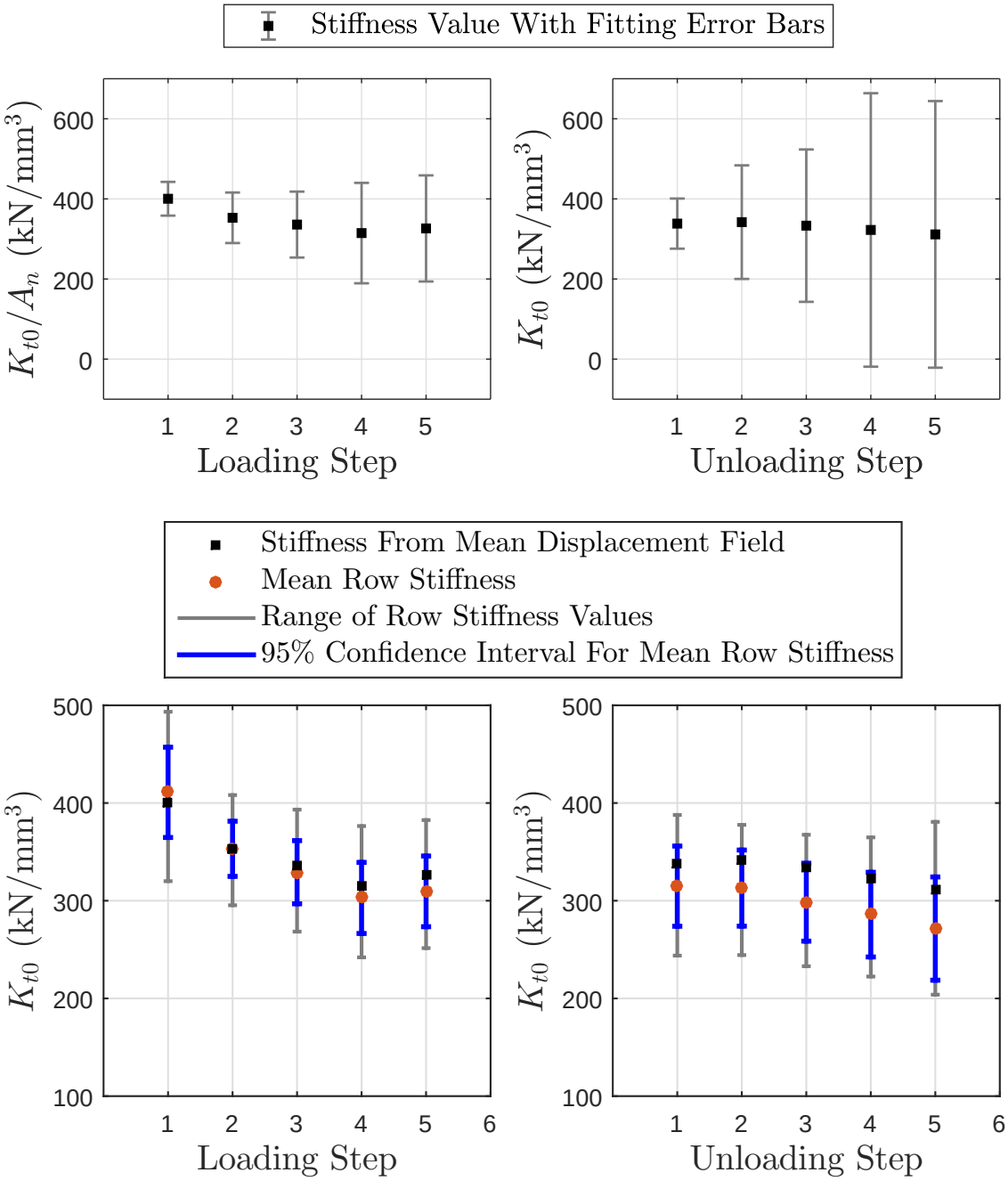

Figure 2.39: **Top**: The tangential contact stiffness at zero tangential load deduced from the derived tangential contact stiffness and tangential load relationship with error bars due to fitting uncertainties for 95% confidence. **Bottom**: The mean row tangential contact stiffness at zero tangential load with error bars from the Student's t-distribution for 95% confidence along with the maximum and minimum values for all the rows. The K_{t0} obtained from the mean displacement field (the values in the top figures) is plotted as well. **Left**: Results for the loading steps. **Right**: Results for the unloading steps. The results are from the SU3 test for the tangential loading steps with normal load of $-P_n = 12$ kN.

2.6.3 Note on the quality of the data obtained

The quality of the data obtained can be evaluated on the basis of the scatter of the data and the margin of error values calculated for the various fit parameters, and the stiffness relations derived from them. Further the margin of error of the mean row tangential contact stiffness can be used to provide an indication whether the tangential contact stiffness deduced from each row of pixels of the images taken varies significantly from row to row.

The error bars for the normal contact stiffness parameters for the 6 tests measured were generally low indicating the scatter from the mean curve was not significant. The margin of error for the fit parameters for most of the tangential loading and unloading steps for the tests with the 'rough specimen' (S_q of 1.422 μm) was not very high, though the errors calculated for some loading steps particularly from the tests with the 'smooth specimen' (S_q of 0.687μm) were very large (the margin of error for the K_{t0} parameter was greater than 50% for these steps). Many tangential loading steps in the tests with the 'smooth specimen' (S_q of 0.687μm) did however provide results with reasonable margins of error (with the margin of error for the K_{t0} parameter less than 50%).

The contact stiffness values are determined on the basis of the fitting parameters for the curves used to fit the contact displacement and load data. These parameters determine the shape of these curves. Relatively small scatter in the contact displacement with load data can lead to very large uncertainties in the shape of the curves and subsequently for the values of the fit parameters. These large uncertainties were seen particularly in the tangential loading steps with the 'smooth specimen' (S_q of 0.687μm). Given the tangential contact displacements observed in these tests were very small,– the change in these values over a whole tangential loading step were as low as 0.3 to 0.5 μm–, it was expected the error values for the fitting parameters for some of the loading steps would be high. The quality of the data obtained for the tests with the 'rough specimen' (S_q of 1.422 μm) was generally better. To calculate the mean values for each test only those loading steps with reasonably low uncertainties were used (when the margin of error for the K_{t0} parameter was less than 50%).

Nonetheless, for all the tests, the parameter K_{t0} calculated as the mean value of the values computed from each row of displacement data, had low margin of error as found using the Student's t-distribution as described in Section 2.5.4. See the bottom plots of Figures 2.17, 2.21, 2.25 ,2.29, 2.34 and 2.39. This indicates the change in the tangential contact displacement with tangential loading was consistent for each row of pixels.

2.7 Discussion of Test Results For Ground Interfaces

The measurements made from the normal loading and unloading steps for the 6 tests show the exponential relationship between normal load and normal contact stiffness fit the data well. (See Figures 2.8 to 2.13. Table 2.1 provides a summary). The adjusted R-square goodness of fit value for most loading and unloading steps from the 6 tests is greater than 0.99 (shown in Table 2.1).

The margin of error on the fitting parameters and the upper and lower bound lines used in the stiffness plots suggest the results from the 'rough specimen' (S_q of 1.422 μm) tests are of better quality than those from 'smooth specimen' (S_q of 0.687μm) tests. This is to be expected, since as seen in the plots of normal contact displacement versus normal load, there is significantly larger change in the contact displacement values in the tests with the 'rough specimen' (S_q of 1.422 μm). The change in the contact displacement values in the smooth tests are only around 2-3 μm for the whole range of loading applied, while in the tests with 'rough specimen' (S_q of 1.422 μm) the contact displacement values change by 5-12 μm for the same loading. It is expected that the error in the measurement of smaller displacements will be more significant. Errors will be affected by the image resolution and focus, experimental noise, and uncertainties from digital image correlation.

In Section 2.4, the magnitude of the fit parameter P_0 was discussed as being likely due to in part the initial loading being taken up in correcting misalignment of the surfaces. It's value could in part be due to an offset in the actual normal load and the measured load (due to improper zeroing of the normal load measurement). Further, a close inspection of some of the fitted curves suggest the actual slope of contact displacement and load relationship implied by the raw data ought to be steeper than the slope of the fitted lines for lower loads, suggesting the stiffness values obtained from the fitted curves are less accurate at lower loads for some of the tests. The magnitude of the P_0 value is more significant in the results with the 'smooth specimen' (S_q of 0.687μm), where the range of the change in contact displacement values is smaller.

The normal contact stiffness at the maximum normal load used in each test, which is the normal load applied during the tangential loading steps, is given in Figure 2.40, which also provides the slope of the normal contact stiffness and normal load relationship, β_n, found for the loading and unloading steps. Error bars representing the margin of error due to fitting uncertainties are plotted (as explained in Section 2.5.1).

It is seen that the normal contact stiffness increases with normal load. The model which was used to fit the contact displacement and load relationship would suggest a linear relationship. Further, as expected the normal contact stiffness is larger for the tests with the 'smooth specimen' (S_q of 0.687μm) than with the 'rough specimen' (S_q of 1.422 μm) for all three tests. The β_n value as per the model is load independent and the results show no significant trend. K_n values

(and the β_n values) computed from the unloading steps is generally larger than that for loading steps, though for the 'rough specimen' (S_q of 1.422 μm) the values are close to each other (and the confidence intervals often overlap). For the 'smooth specimen' (S_q of 0.687μm) particularly for the higher loads, significant increase is noted. Since the stiffness is the slope of the of the contact displacement curve, small changes in the contact displacement values can lead to significantly larger changes in the slope, suggesting the results become less accurate as the stiffness measured is higher. The unloading step is measured after a series of tangential loading steps and therefore it is reasonable to expect the normal contact stiffness to change as the interface texture is modified. The repeated cyclic tangential load under high normal loading could in effect blunt some asperities and make the interface smoother and thus increase the contact stiffness value.

Though the pads used in all the tests were ground to a similar specification, as seen in Table A.1 in Appendix A, there are some noticeable differences in the profile and areal roughness parameters for the pads used. It is noted that the profile roughness parameters are very similar to areal roughness parameters computed, giving confidence in the calculations from both methods. The relationship between the equivalent area roughness parameter derived and its product with the loading β_n value is given in Table 2.3. As per the model by Medina et al., see equation (1.4)

$$\beta_n = \frac{1}{\sigma_{rms}}, \tag{2.11}$$

where σ_{rms} is the standard deviation of the gap between the surfaces [4]. The equivalent surface roughness paramenter, S_q^e, is the estimated standard deviation of the interface gap as shown in Section 2.3.5. The value of the product $\beta_n S_q^e$ for the three tests are seen to be close to 1 in Table 2.3, suggesting the results from the normal contact stiffness measurements support the Medina model.

The results for the normal tests therefore support the proposition that the normal contact stiffness is proportional to normal loading and inversely proportional to the equivalent root mean square roughness of the interface. The linear relationship is consistent with numerous models of normal contact stiffness, both asperity models of the Greenwood and Williamson kind and fractal models using Persson contact theory.

Figures 2.14 to 2.39 and Tables A.2 to A.25 provide the results from the tangential loading steps. The exponential curves used to fit the raw data, particularly for the tests with the 'rough specimen' (S_q of 1.422 μm), have generally high goodness of fit values (the adjusted R-square goodness of fit values being mostly above 0.99). Furthermore, as with the normal tests, the error bars due to fit uncertainty are generally lower for the results from the test with the 'rough specimen' (S_q of 1.422 μm) than the tests with the 'smooth specimen' (S_q of 0.687μm). The goodness of fit for

the loading steps with the 'smooth specimen' (S_q of 0.687μm) were generally worse (though the adjusted R-square goodness of fit for most steps was above 0.96) and the margin of error on some loading steps were very significant. This is to be expected given the change in tangential contact displacement in the tests with 'rough specimen' (S_q of 1.422 μm) were in the order of 1 to 1.5 μm over a loading step, for the tests with the 'smooth specimen' (S_q of 0.687μm) it could be as low as 0.3 to 0.5 μm. The results with the 'smooth specimen' (S_q of 0.687μm) are therefore much more sensitive to experimental noise. Nonetheless decent results with reasonable margins of error were obtained from majority of the loading and unloading steps for the tests with the 'smooth specimen' (S_q of 0.687μm), though the strongest support for the model comes from the results with the 'rough specimen' (S_q of 1.422 μm). The K_{t0} values were consistent for nearly all steps in each test, even from loading and unloading steps with large fitting uncertainties (and margin of errors).

To avoid results that were clearly wrong from affecting the calculation of the mean values for each test, only those loading and unloading steps for which the tangential contact stiffness at zero tangential load, K_{t0}, that had a margin of error (computed as described in §2.5.1) less than 50% were used to calculate the mean values of K_{t0}, β_t and f. Table 2.2 provide the mean values for the loading steps, the unloading steps, and all steps combined. The table also lists which steps were used in the calculation of the mean values. The mean parameters are plotted in Figure 2.41. As with the parameter β_n no clear dependency with load is seen for parameter β_t.

Most significantly the mean coefficient of friction values for the contact interfaces obtained from all 6 tests were found to be around 0.15 to 0.3, which are within the expected range for these surfaces. Furthermore, nearly every loading and unloading step implied a coefficient of friction value in this region, when the margin of error was reasonable, as seen in Figures 2.16, 2.20, 2.24, 2.28, 2.33 and 2.38. The experimental measurements therefore strongly support a model of tangential contact stiffness that linearly decreases with tangential load as slip approaches. This is consistent with Greenwood and Williamson based modelling by Paggi et al. with boundary element method [28].

Figure 2.42 shows the ratio, C_c, between the mean K_{t0} value and the mean K_n at the normal load used in the tangential loading steps. While, the K_n values found for the 'rough specimen' (S_q of 1.422 μm) were reasonably similar for both loading and unloading steps, the values for the loading and unloading steps for the 'smooth specimen' (S_q of 0.687μm) were significantly different. Therefore in Table 2.4, the C_c constant derived on the basis of the mean, loading, and unloading K_n values are provided for all 6 tests.

Of much significance the C_c value for tests with the 'rough specimen' (S_q of 1.422 μm) are almost identical. This affirms the theory that this value is load independent. Furthermore the

theoretical value for elastic contacts (assuming the surfaces are isotropic) given by Mindlin ratio is

$$\frac{2(1-\nu)}{2-\nu}.$$

Numerous measurements of this constant have shown that the measured ratio is generally half of that given by the Mindlin ratio, probably due to plasticity and anisotropic surface texture [19]. Taking the Poisson's ratio for Ti-4Al-6V as 0.31 [48], the Mindlin ratio is 0.817, and half its value is 0.408. The results from the tests with the 'rough specimen' (S_q of 1.422 μm) are seen to be roughly half that predicted by the Mindlin ratio and is hence consistent with other published measurements. The values from the tests with the 'smooth specimen' (S_q of 0.687μm) are also not far away from this value and the margin of error on the values computed are relatively larger. Nonetheless, it is not possible to rule out that the C_c value is not related to surface texture, given the Mindlin ratio is strictly only valid for elastic isotropic surfaces. Since the value of C_c obtained from this measurement process and model used is consistent with many other published results, the validity of this measurement process and model is supported further.

While an increase in normal contact stiffness value was observed at the end of each test, no significant change in the tangential contact stiffness values was observed after the first loading step. For all the tests, the tangential contact stiffness values of the first loading step is slightly different from that of subsequent steps, however no significant change is observed afterwards, other than for some loading steps which were prone to significant uncertainties in measurement as quantified by the margin of error values on the parameters computed from these steps. This is consistent with theoretical analysis of frictional shakedown of surfaces which predict the interface behaviour stabilises after only a few cycles [38]. It is possible that after several cycles, say 100s, the contact stiffness properties may change due effects such as wear. Table 2.5 shows the surface roughness values of the pad interface before and after each test. Similar data was not available for the specimen surface. The surface roughness for all the pads reduced after the tests. The reduction for pads in the tests with the 'rough specimen' (S_q of 1.422 μm) was from 4-9 % and for the pads in the tests with the 'smooth specimen' (S_q of 0.687μm) the reduction was from 14-21 %.This is consistent with the increase in normal contact stiffness observed at the end of each test, particularly for the tests with the 'smooth specimen' (S_q of 0.687μm). However since no systematic trend was observed in the change of the tangential contact stiffness properties after the first tangential loading step, the changes in the surfaces profile may have mostly occurred during the first normal loading step and the first tangential loading step.

While the results of the experimental measurements support the model described in Section 2.4, possible sources of error should not be overlooked. To investigate the quality of the measurements,

tangential contact stiffness at zero tangential load was measured for each row in the displacement field as described in Section 2.5.4, and plotted in Figures 2.17, 2.21, 2.25 ,2.29, 2.34 and 2.39. The range of stiffness values found for each row was relatively small, and the 95% confidence interval on the basis of the Student's t-distribution was generally very small. Furthermore, the values computed for loading steps that had large margin of errors were similar to the values found from loading steps with better fits. This suggests that there is not a significant scatter within the displacement field, and that the fitted curves even for loading steps with significant margin of error may be suitable to provide reasonable estimates of the the K_{t0} parameter.

Results for some of the loading steps, particularly for the tests with the 'smooth specimen' (S_q of 0.687μm), showed significant margin of error, often for loading or unloading steps in one direction. This suggests minor misalignment between the pad and the specimen or image quality issues such as uneven focus had more significant impact on the measured values for the test with 'smooth specimen' (S_q of 0.687μm) where the displacements measured were much smaller.

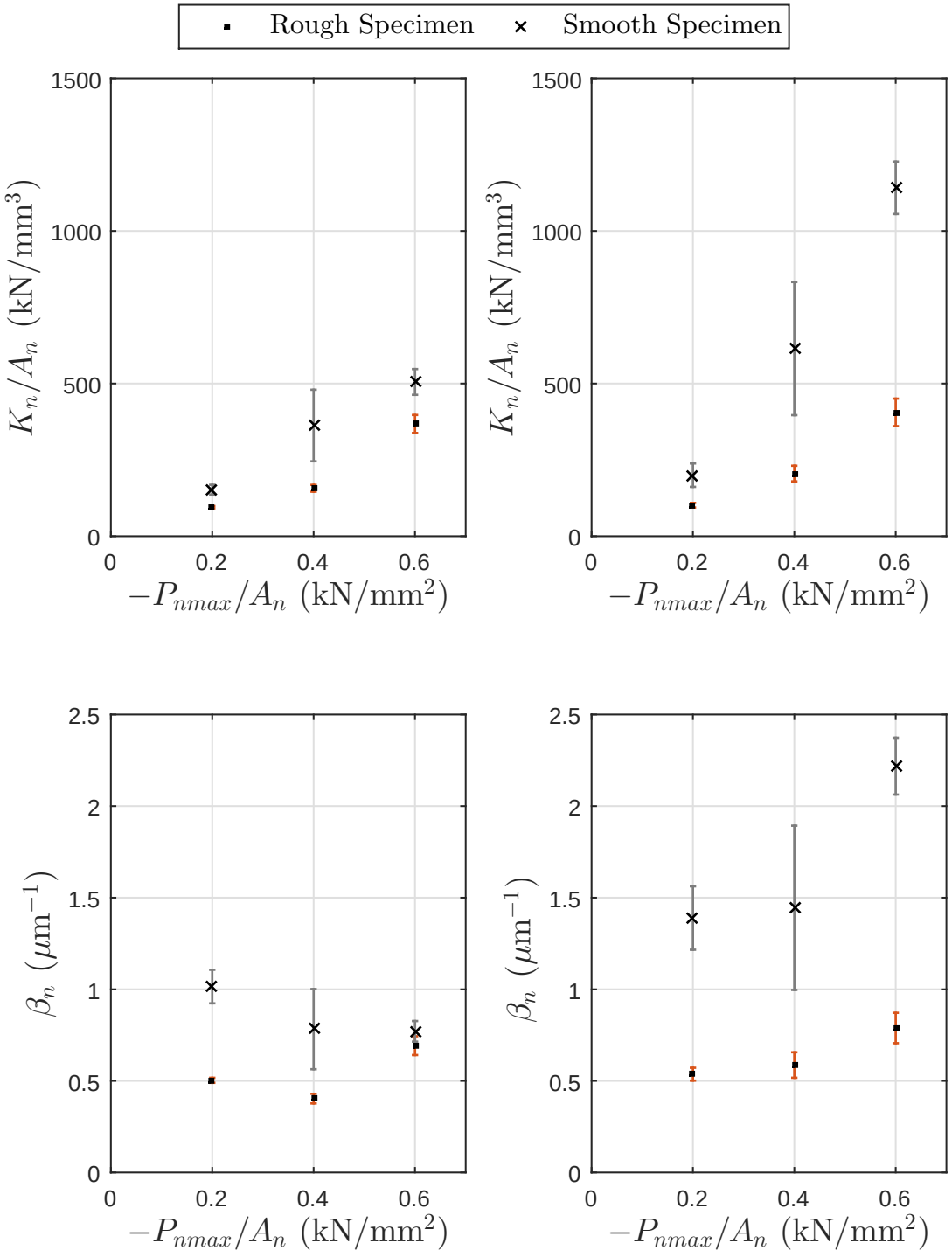

Figure 2.40: Results of the normal contact stiffness measurement. **Top**: The normal contact stiffness by nominal area at the highest normal load applied in the test, $-P_{nmax}$. **Bottom**: the slope of the normal load and normal contact stiffness relationship plotted against $-P_{nmax}/A_n$ for the test. **Left**: results from the loading step. **Right**: results from the unloading step.

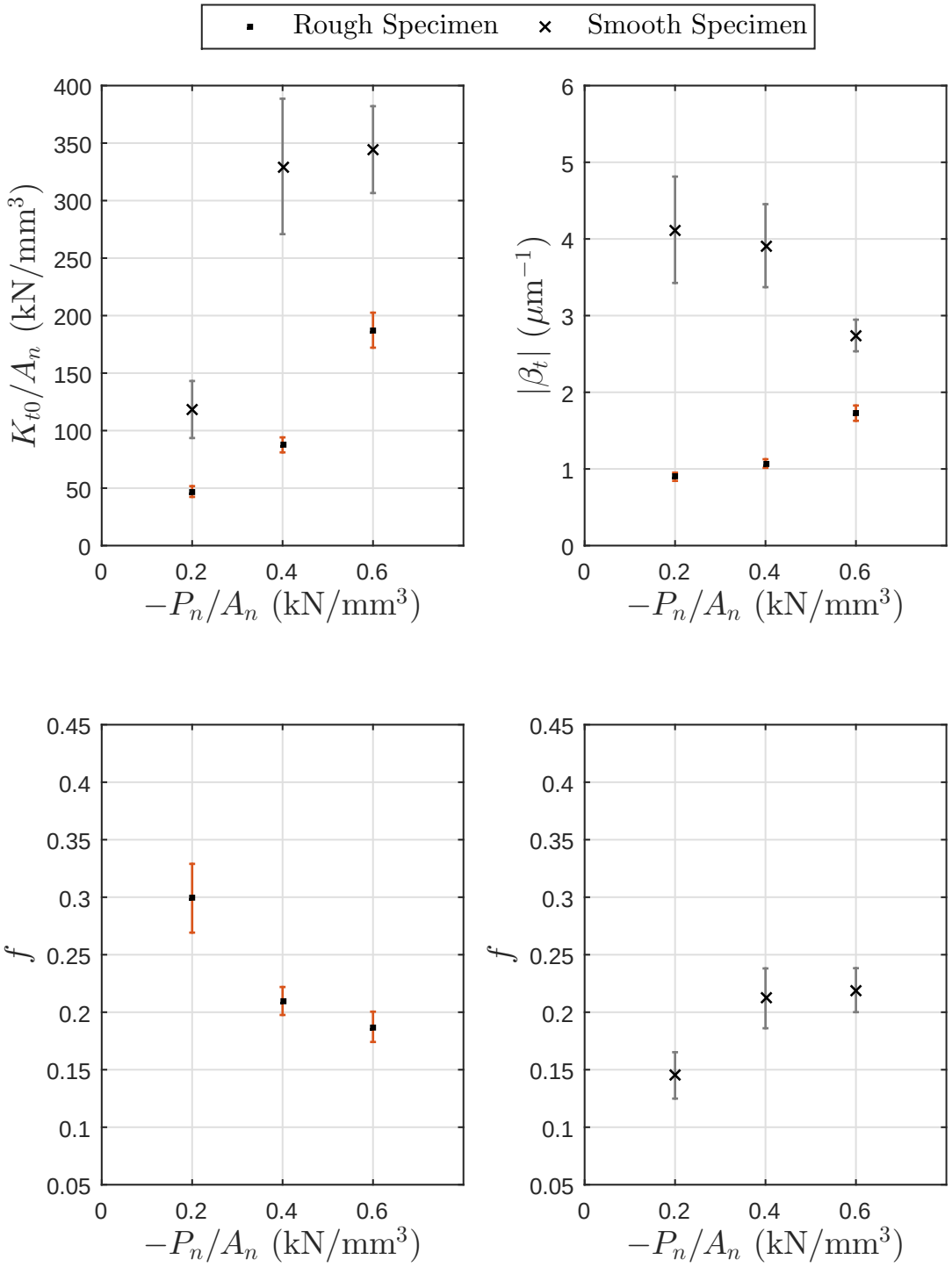

Figure 2.41: Results from the tangential contact stiffness measurements. **Top Left**: The mean tangential contact stiffness at zero tangential load by nominal area plotted against the normal loading used in the test, $-P_n/A_n$. **Top Right**: the mean absolute slope of the tangential load and tangential contact stiffness relationship plotted against the normal loading used in the test, $-P_n/A_n$. **Bottom Left**: mean coefficient of friction derived from each test with the 'rough specimen' (S_q of 1.422 μm) plotted against the normal loading used in each test. **Bottom Right**: mean coefficient of friction found from each test with the 'smooth specimen' (S_q of 0.687μm) plotted against the normal loading. Mean values were calculated only for those loading steps for which the fit error margin for the K_{t0} value was less than 50%.

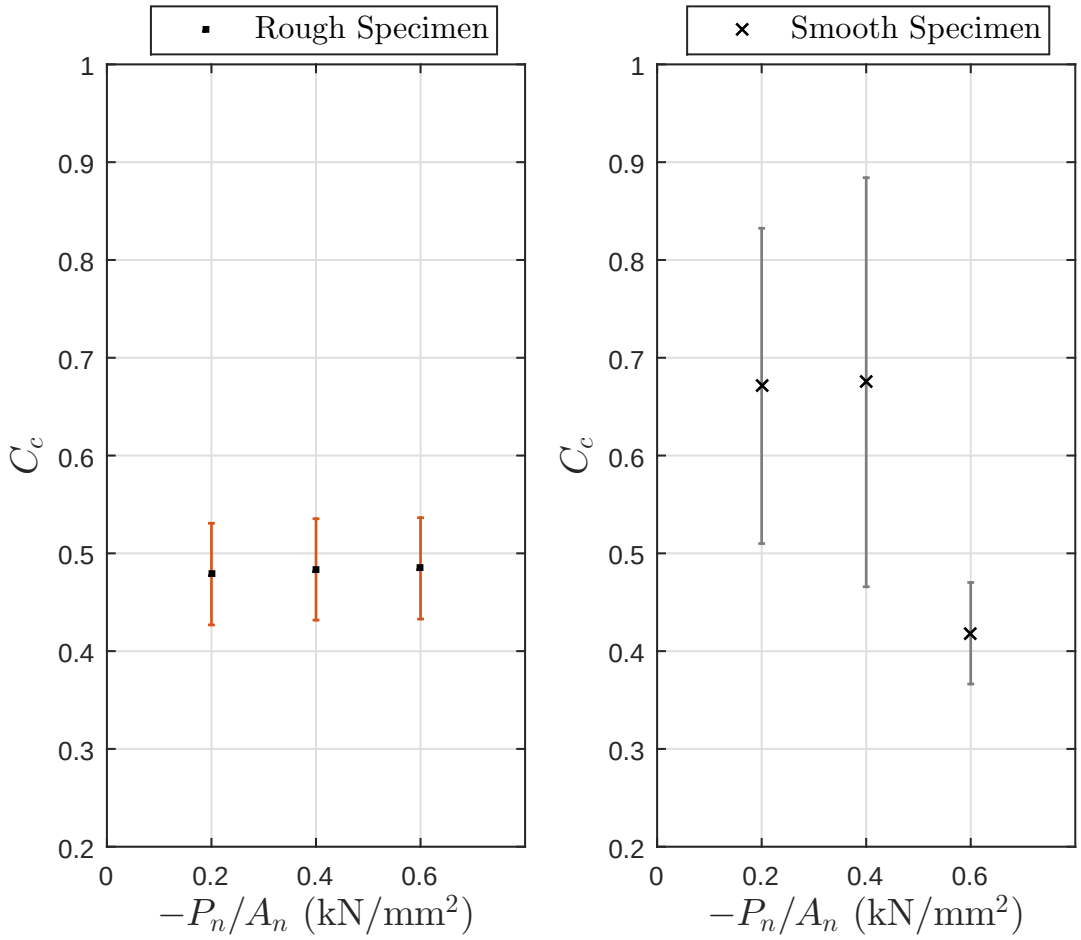

Figure 2.42: The ratio, $C_c = K_{t0}/K_n$, plotted against the normal load. **Left**: Values for the 'rough specimen' (S_q of 1.422 μm). **Right**: Values for the 'smooth specimen' (S_q of 0.687μm).

Test No.	GOF	$-P_{nmax}/A_n$ (kN/mm^3)	K_n/A_n (kN/mm^3)	K_n/A_n (kN/mm^3), margin of error	β_n (μm^{-1})	β_n (μm^{-1}), margin of error	α_n (kN)	α_n (kN), margin of error	P_0 (kN)	P_0 (kN), margin of error
Loading										
RU1	1.000	0.2	94.985	3.678	0.503	0.014	0.048	0.006	0.225	0.039
RU2	0.997	0.4	156.995	11.215	0.403	0.026	0.027	0.010	0.212	0.198
RU3	0.996	0.6	367.570	29.438	0.692	0.051	0.022	0.010	1.382	0.291
SU1	0.998	0.2	152.600	15.863	1.015	0.091	0.035	0.015	0.994	0.122
SU2	0.979	0.4	362.600	117.140	0.783	0.219	0.305	0.334	-1.267	1.491
SU3	0.999	0.6	505.235	42.208	0.770	0.056	0.130	0.048	-1.115	0.510
Unloading										
RU1	0.999	0.2	101.490	7.568	0.537	0.035	3.670	0.084	0.216	0.097
RU2	0.993	0.4	205.275	25.645	0.587	0.070	6.438	0.235	1.002	0.251
RU3	0.996	0.6	405.510	45.025	0.789	0.083	9.584	0.304	1.716	0.336
SU1	0.999	0.2	200.040	38.297	1.389	0.173	1.120	0.171	2.772	0.150
SU2	0.988	0.4	614.395	217.965	1.445	0.448	8.335	1.308	-0.505	1.459
SU3	0.997	0.6	1141.265	85.907	2.218	0.155	10.016	0.244	1.707	0.247
Mean										
RU1		0.2	98.238	4.207	0.520	0.038				
RU2		0.4	181.135	13.995	0.495	0.074				
RU3		0.6	386.540	26.897	0.741	0.097				
SU1		0.2	176.320	20.726	1.202	0.196				
SU2		0.4	488.498	123.724	1.114	0.499				
SU3		0.6	823.250	47.858	1.494	0.165				

Table 2.1: Data obtained from the normal loading and unloading steps for each test as well as the mean values are provided here. K_n/A_n value is the normal contact stiffness by nominal area at the highest normal load used in that test, P_{nmax}. The margin of error due to fitting uncertainties for a confidence interval of 95% and the adjusted R-squared goodness of fit (GOF) values for the fits used are provided.

Test No.	$-P_n/A_n$ (kN//mm^2)	K_{t0}/A_n (kN/mm^3)	K_{t0}/A_n (kN/mm^3), margin of error	β_t (μm^{-1})	β_t (μm^{-1}), margin of error	f	f, margin of error	Steps Used
Loading								
RU1	0.2	44.584	10.541	-0.514	0.088	0.437	0.076	3,4,5
RU2	0.4	87.862	9.963	-1.062	0.084	0.216	0.019	1,2,3,4,5
RU3	0.6	185.280	18.261	-1.796	0.138	0.172	0.012	1,2,3,4,5
SU1	0.2	–	–	–	–	–	–	–
SU2	0.4	329.716	58.875	-3.912	0.541	0.212	0.026	2,3,4,5
SU3	0.6	346.028	42.789	-2.940	0.248	0.206	0.021	1,2,3,4,5
Unloading								
RU1	0.2	48.505	4.035	1.129	0.068	0.216	0.015	1,2,3,4,5
RU2	0.4	87.322	8.368	1.079	0.074	0.203	0.015	1,2,3,4,5
RU3	0.6	189.895	25.494	1.642	0.143	0.206	0.026	1,2,3,4
SU1	0.2	118.349	24.785	4.120	0.693	0.145	0.020	1,2,3
SU2	0.4	–	–	–	–	–	–	–
SU3	0.6	340.153	77.500	2.242	0.368	0.253	0.042	1,2
Combined				($\lvert\beta_t\rvert$)				
RU1	0.2	47.034	4.689	0.898	0.054	0.299	0.030	
RU2	0.4	87.592	6.505	1.071	0.056	0.210	0.012	
RU3	0.6	187.331	15.209	1.728	0.100	0.187	0.013	
SU1	0.2	118.349	24.785	4.120	0.693	0.145	0.020	
SU2	0.4	329.716	58.875	3.912	0.541	0.212	0.026	
SU3	0.6	344.350	37.742	2.741	0.206	0.219	0.019	

Table 2.2: The mean values for stiffness at zero tangential load by nominal area, K_{t0}/A_n, the slope of the tangential contact stiffness and tangential load relationship, β_t, and the deduced coefficient of friction values are provided here for each test for the loading and unloading steps separately and combined. Only those steps for which the margin of error due to fitting for the K_{t0} value was less than 50% were used to calculate the mean values. The steps used are listed. The margin of error values due to fitting uncertainties for the mean values are provided.

Test No.	Equivalent S_q^e (μm)	$\beta_n S_q^e$
RU1	2.038	1.03
RU2	1.642	0.66
RU3	1.638	1.13
SU1	0.928	0.94
SU2	1.025	0.80
SU3	1.070	0.82

Table 2.3: The equivalent roughness parameter, S_q^e, for the interfaces in the tests with the ground specimens and the $\beta_n S_q^e$ value. The β_n values from the loading steps are used

	With average normal contact stiffness		With loading normal contact stiffness		With unloading normal contact stiffness	
Test No.	C_c	Margin of error	C_c	Margin of error	C_c	Margin of error
RU1	0.479	0.052	0.495	0.053	0.463	0.058
RU2	0.484	0.052	0.558	0.057	0.427	0.062
RU3	0.485	0.052	0.510	0.058	0.462	0.064
SU1	0.671	0.161	0.776	0.181	0.592	0.168
SU2	0.675	0.209	0.909	0.336	0.537	0.213
SU3	0.418	0.052	0.682	0.094	0.302	0.040

Table 2.4: The ratio, C_c, between the mean tangential contact stiffness at zero tangential load from all the tangential loading steps (loading and unloading) and the normal contact stiffness at the same normal load. The ratio is found using the mean normal contact stiffness, the loading normal contact stiffness, and the unloading normal contact stiffness for each test.

Test No.	S_q(nm) before test	S_q(nm) after test	Percent reduction
RU1	1460	1334	9%
RU2	822	785	4%
RU3	814	742	9%
SU1	623	489	21%
SU2	760	631	17%
SU3	821	704	14%

Table 2.5: Roughness of the pad surface before and after each test.

2.8 Results For Structured Surfaces

The three tests with structured surfaces are designated S1, S2, and S3. They involve specimens with texture wavelengths of 10 μm, 5 μm, and 2 μm, respectively.

The roughness and areal parameters of the structured surfaces and the pads used in testing are given in Tables A.26 and A.27 in Appendix A. As with tests with the ground surfaces, images were taken for the interface between the specimen and Pad B for each test. The surface roughness and areal parameters were found from scans of the surfaces with 20X objective lens with lateral resolution of 2.01 μm and vertical resolution of 50 nm. To characterise the structured surfaces further, scans with objective lens of 100X with lateral resolution 500 nm and vertical resolution

of 50 nm were made with cut-off wavelengths, λ_c, slightly above the structure wavelengths and are provided in Table 2.6. The R_a value from these scans is the arithmetic mean height of the structured surface, filtering out the larger wavelength features, and similarly the R_q is the root mean square height. Figure 2.43 provides images of the structured surface profile obtained. The grooves for the 10 μm and 5 μm wavelength surfaces are clearly seen. Mild striations are visible for the 2 μm surface. Figure 2.44 shows the 2D profiles of the structured surfaces with profile lines perpendicular to grooves, from the scans with the 100X objective lens and lower cut-off wavelengths. The top left image in Figure 2.43 is the top view of the 10 μm wavelength surface. The structured pattern were applied onto the surfaces of all three specimens in square tile like sections, each of which correspond to a single shot of the laser beam. In this image the boundary lines between a tile like section can be seen near the left edge and near the right edge. Figures 2.45 to 2.47 provide the contact stiffness results for normal loading and unloading steps in the same format as provided for the ground specimens in Section 2.6. The results from the tangential loading cycles are provided similarly in Figures 2.48 to 2.59, and Tables A.28 to A.39 in Appendix A.

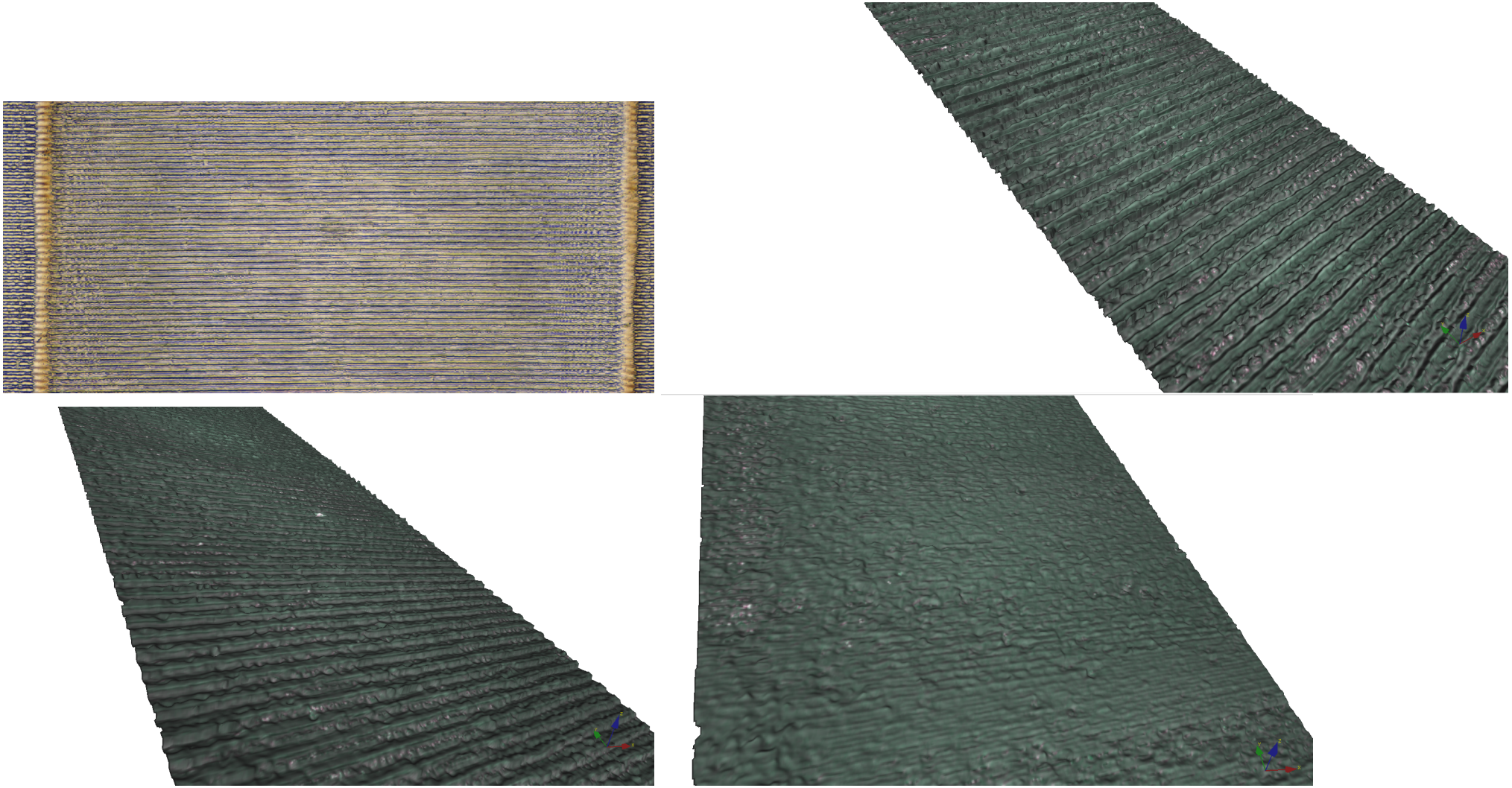

Figure 2.43: 3D profiles of the structured surfaces. **Top Left**: Top view of the 10 μm wavelength surface obtained with 20X objective lens. Top Right: 3D view of the 10 μm wavelength surface profile obtained with the 100X objective lens. **Bottom Left**: 3D view of the 5 μm wavelength surface profile obtained with the 100X objective lens. **Bottom Right**: 3D view of the 2 μm wavelength surface profile obtained with the 100X objective lens.

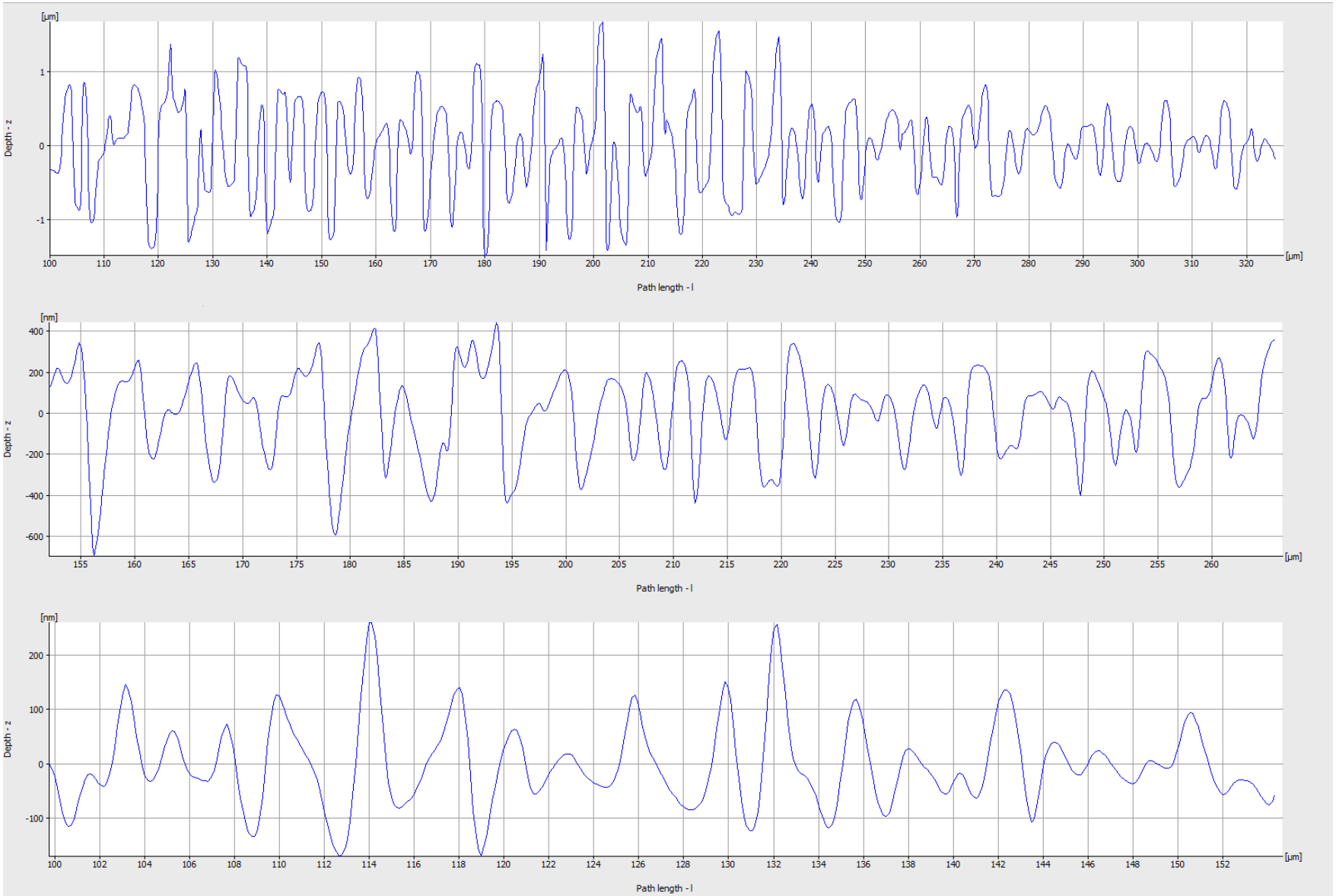

Figure 2.44: The profile scans of the textured surfaces. The profile line is drawn perpendicular to the grooves. **Top**: 10 μm wavelength surface with $\lambda_c = 20\mu$m. **Middle**: 5 μm wavelength surface with $\lambda_c = 10\mu$m . **Bottom**: 2 μm wavelength surface with $\lambda_c = 5\mu$m. 100X objective with 50 nm vertical resolution and 500 nm lateral resolution settings was used.

Test no.	Structure Wavelength	R_a (nm)	R_q (nm)	R_z (μm)	Profile length (mm)	Profile width (nm)	λ_c (μm)
S3	2 μm	56	73	0.503	1	167	5
S2	5 μm	193	243	1.495	1	167	10
S1	10 μm	456	583	3.203	1	167	20

Table 2.6: Parameters that characterise the surface structures are calculated from the average of 5 profile measurements, with profile lines normal to the grooves of the textures. Cut-off wavelengths slightly above the texture wavelengths are used to filter out larger wavelength surface features. Vertical resolution of 50 nm and lateral resolution of 0.5 μm, with the 100X magnification objective, were used.

2.8.1 Normal Stiffness Test Results

Test S1, with 10μm wavelength textured surface

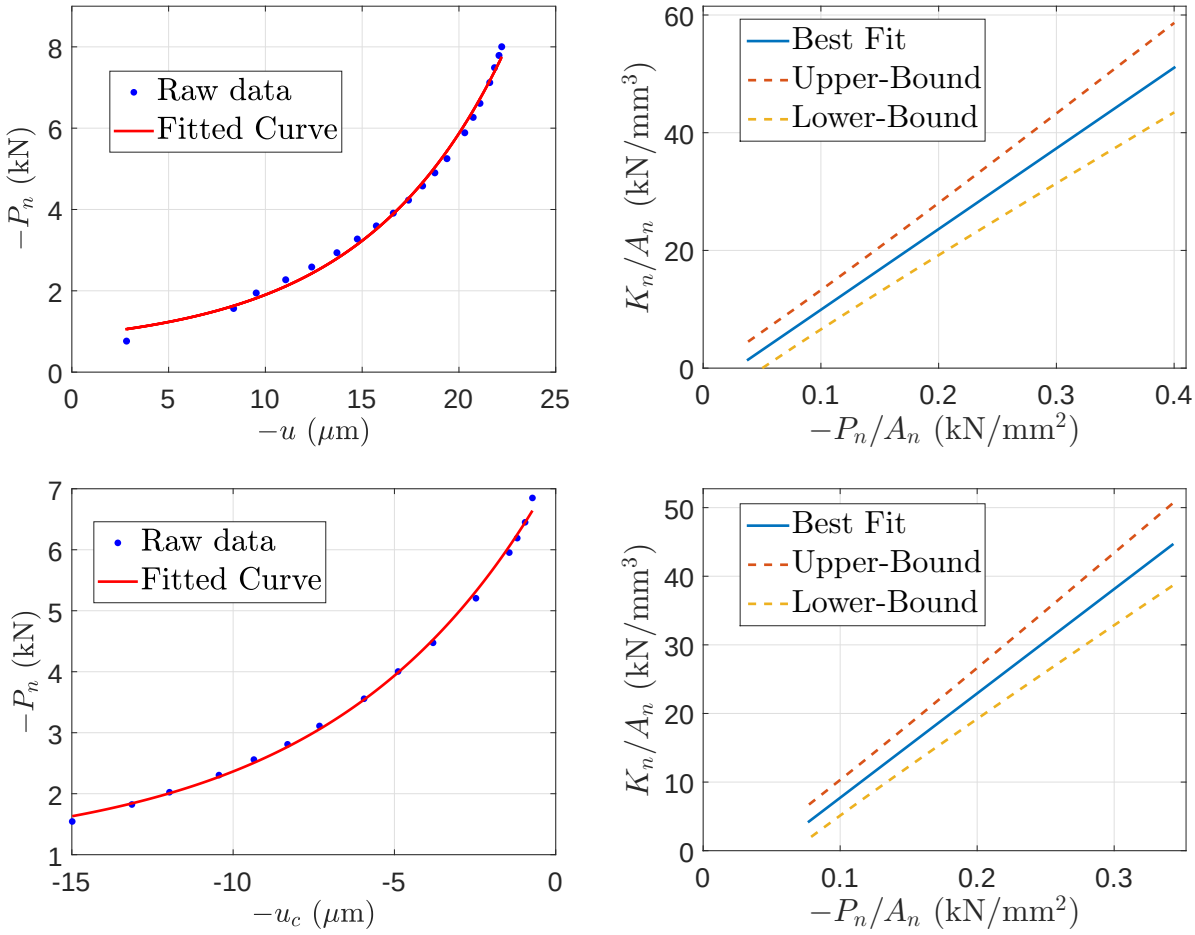

Figure 2.45: Results from S1 test with maximum normal load of $-P_n = 8$ kN. **Top**: Results from the loading step. **Bottom**: Results from the unloading step. **Left**: Normal contact displacement and normal load relationship. **Right**: Normal contact stiffness and normal load relationship.

Test S2, with 5μm wavelength surface

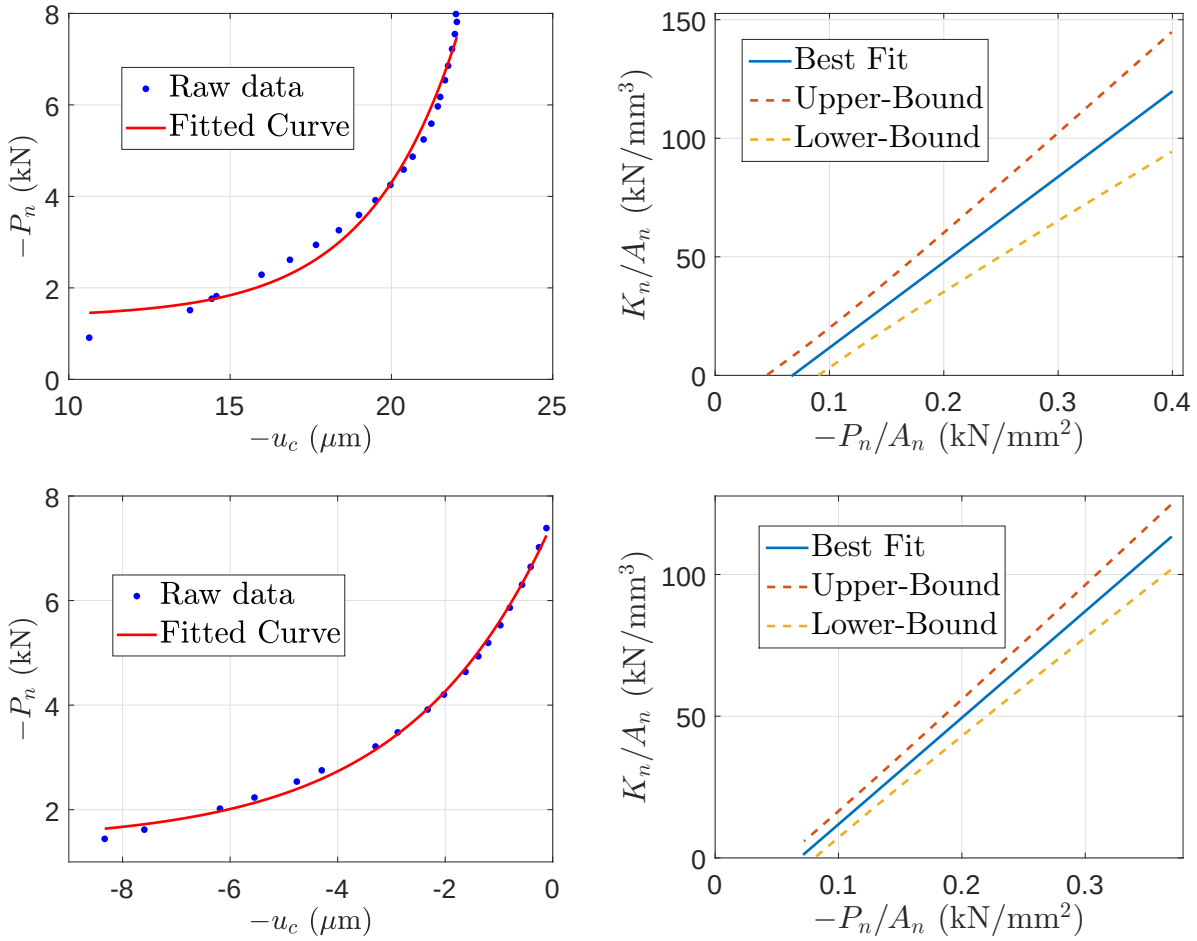

Figure 2.46: Results from S2 test with maximum normal load of $-P_n = 8$ kN. **Top**: Results from the loading step. **Bottom**: Results from the unloading step. **Left**: Normal contact displacement and normal load relationship. **Right**: Normal contact stiffness and normal load relationship.

Test S3, with 2μm wavelength surface

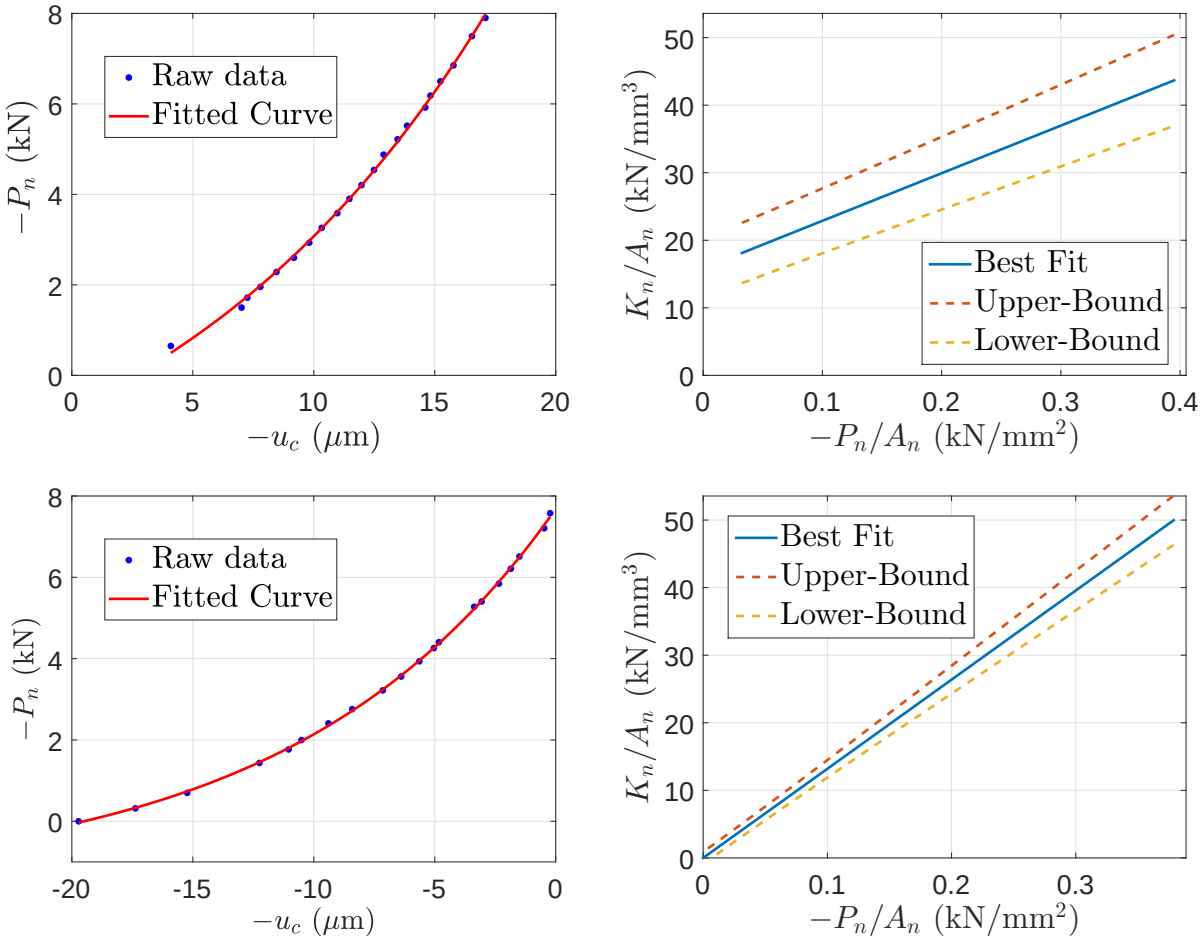

Figure 2.47: Results from S3 test with maximum normal load of $-P_n = 8$ kN. **Top**: Results from the loading step. **Bottom**: Results from the unloading step. **Left**: Normal contact displacement and normal load relationship. **Right**: Normal contact stiffness and normal load relationship.

2.8.2 Tangential Stiffness Test Results

Test S1 10μm wavelength surface

Though the exponential model was used to fit the experimental tangential load and tangential contact displacement data, the raw data near zero tangential load, particularly for the loading steps, seems to lie on an 'S' shape curve, which is not physically realistic. The unloading steps fitted better with the exponential model and the coefficient of friction from these steps is seen to be around 0.2, though the fitted curves for both loading and unloading steps gave similar values for K_{t0}.

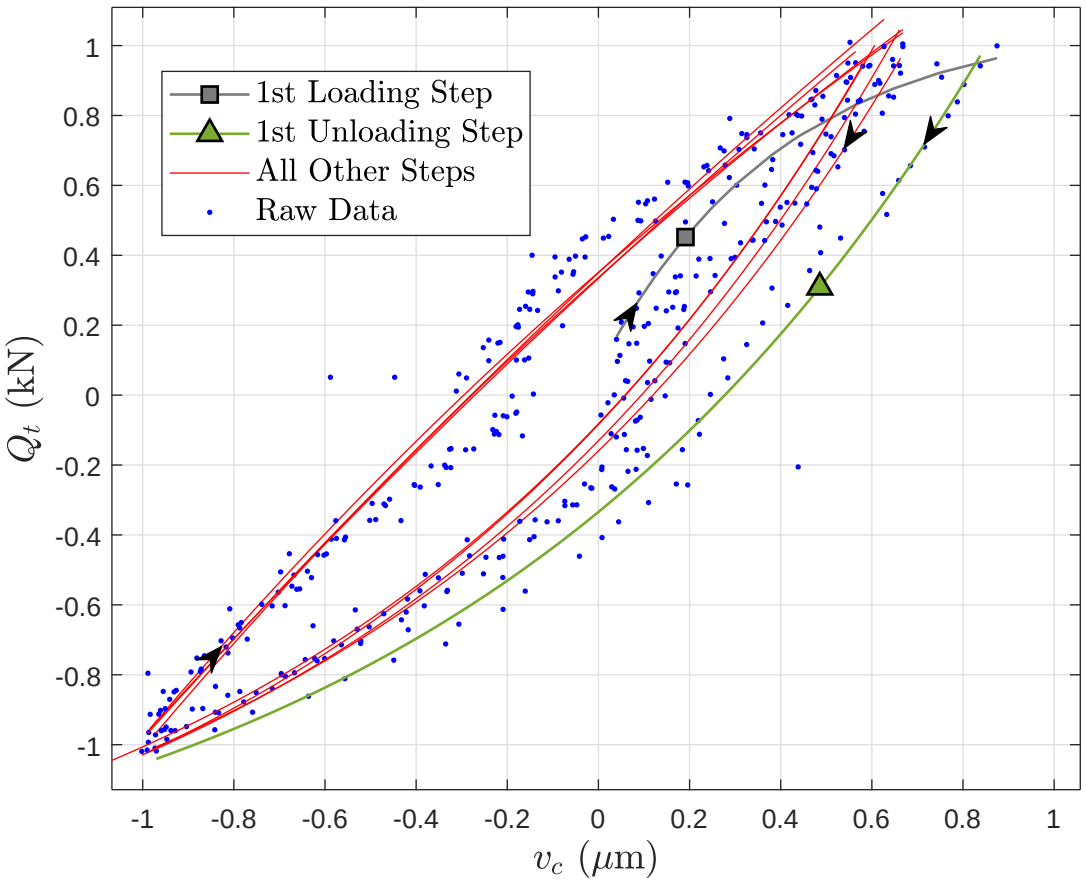

Figure 2.48: Plot of the tangential load and tangential contact displacement relationship, with fitted curves using exponential functions. The result is from the S1 test for the tangential loading steps with normal load of $-P_n = 8$ kN.

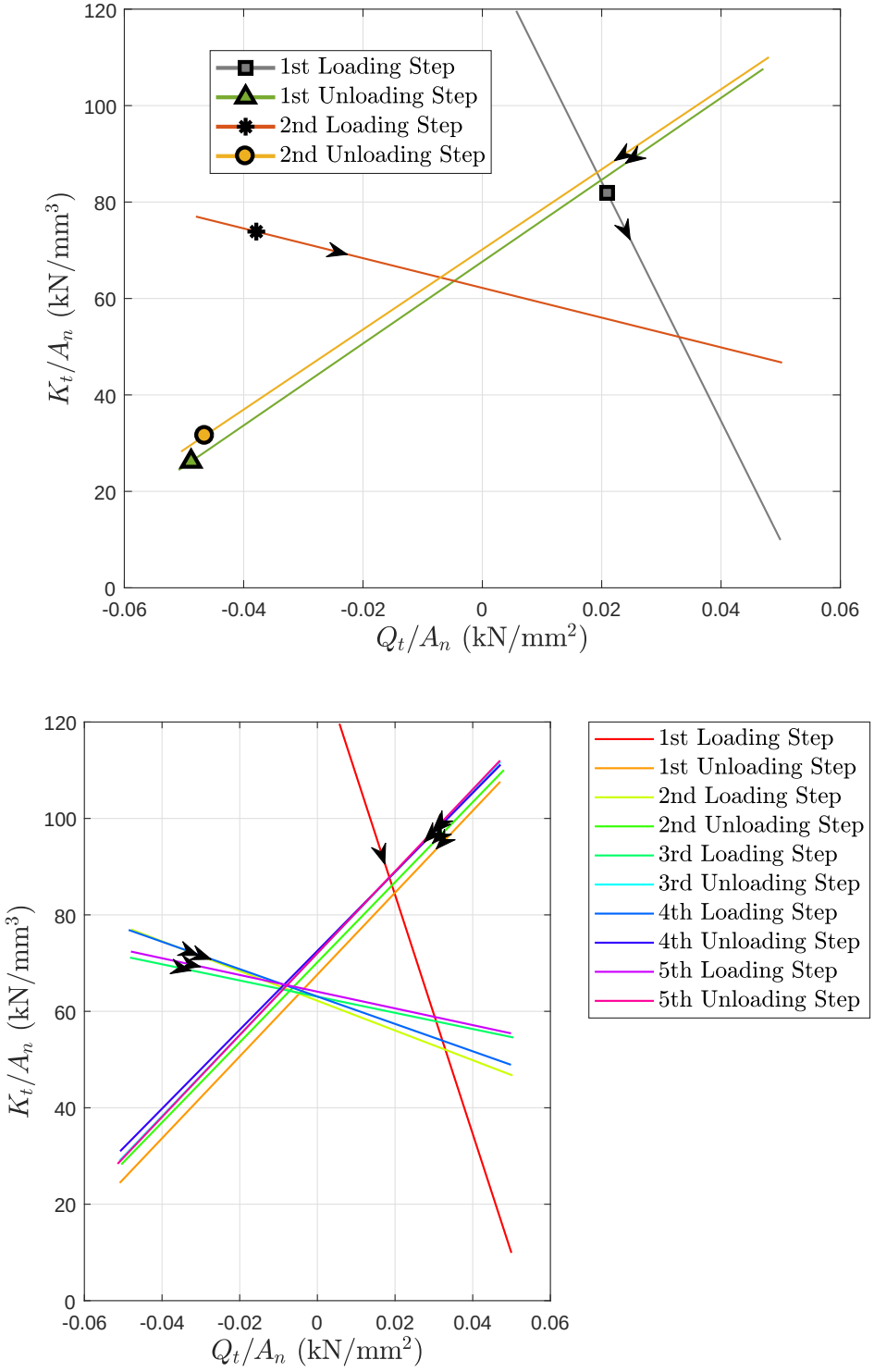

Figure 2.49: Plots of the tangential load and tangential contact stiffness relationship obtained. **Top**: Plots for the first two loading and unloading steps. **Bottom**: Plots with further loading steps. The results are from the S1 test for the tangential loading steps with normal load of $-P_n = 8$ kN.

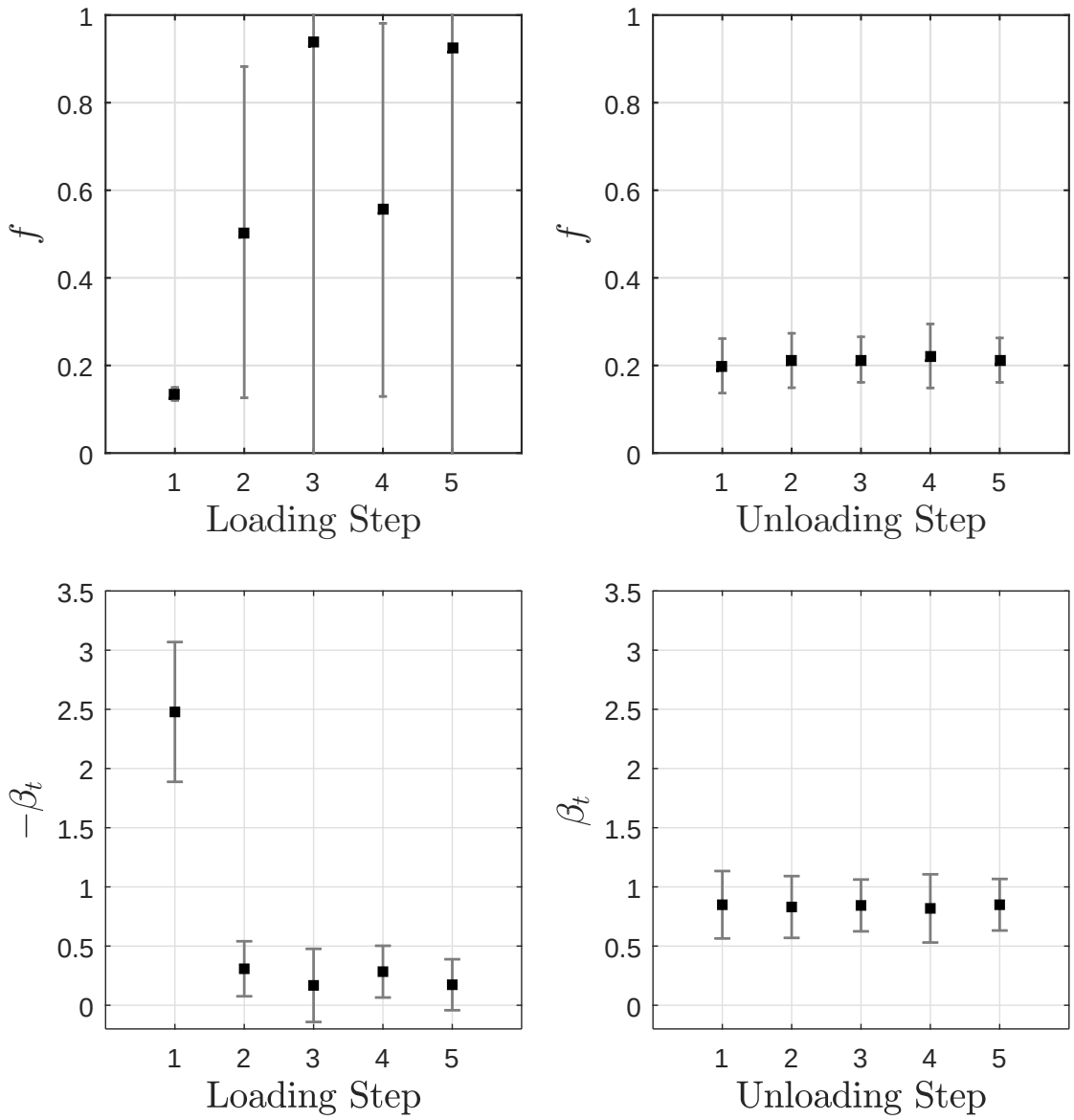

Figure 2.50: **Top**: Coefficient of friction deduced from the derived tangential contact stiffness and tangential load relationship with error bars due to fitting uncertainties for 95% confidence. **Bottom**: The slope of the tangential contact stiffness and tangential load relationship derived for each step with error bars due to fitting uncertainties for 95% confidence. **Left**: Results for the loading steps. **Right**: Results for the unloading steps. The results are from the S1 test for the tangential loading steps with normal load of $-P_n = 8$ kN.

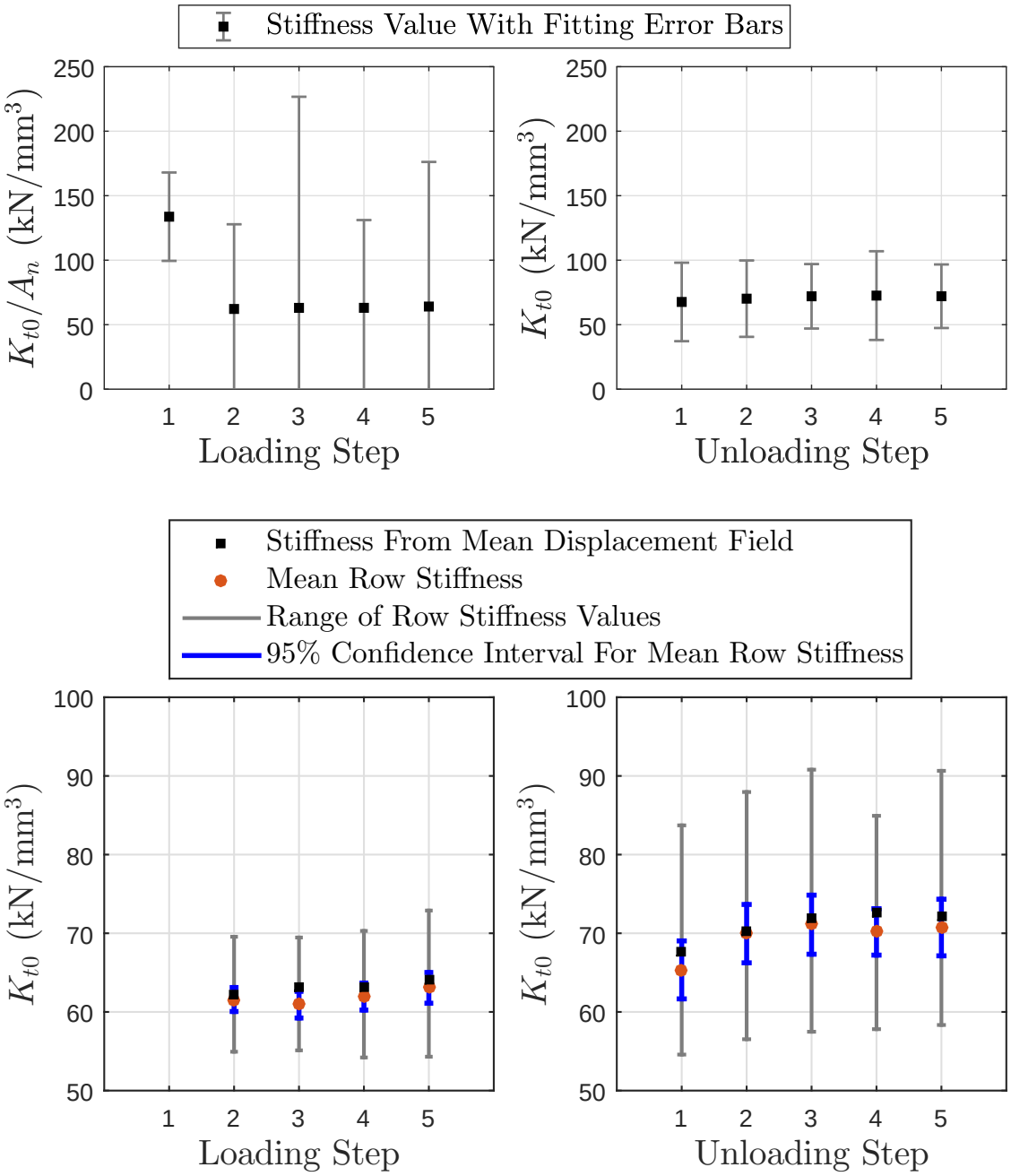

Figure 2.51: **Top**: The tangential contact stiffness at zero tangential load deduced from the derived tangential contact stiffness and tangential load relationship with error bars due to fitting uncertainties for 95% confidence. **Bottom**: The mean row tangential contact stiffness at zero tangential load with error bars from the Student's t-distribution for 95% confidence along with the maximum and minimum values for all the rows. The K_{t0} obtained from the mean displacement field (the values in the top figures) is plotted as well. **Left**: Results for the loading steps. **Right**: Results for the unloading steps. The results are from the S1 test for the tangential loading steps with normal load of $-P_n = 8$ kN.

Test S2 5μm wavelength surface

The data from the unloading steps fitted better with the exponential model, and coefficients of friction are found from those steps to be around 0.2 to 0.3. Similar values of K_{t0} were found from all steps, except the value from the first loading step which is larger in magnitude than the values from the subsequent steps.

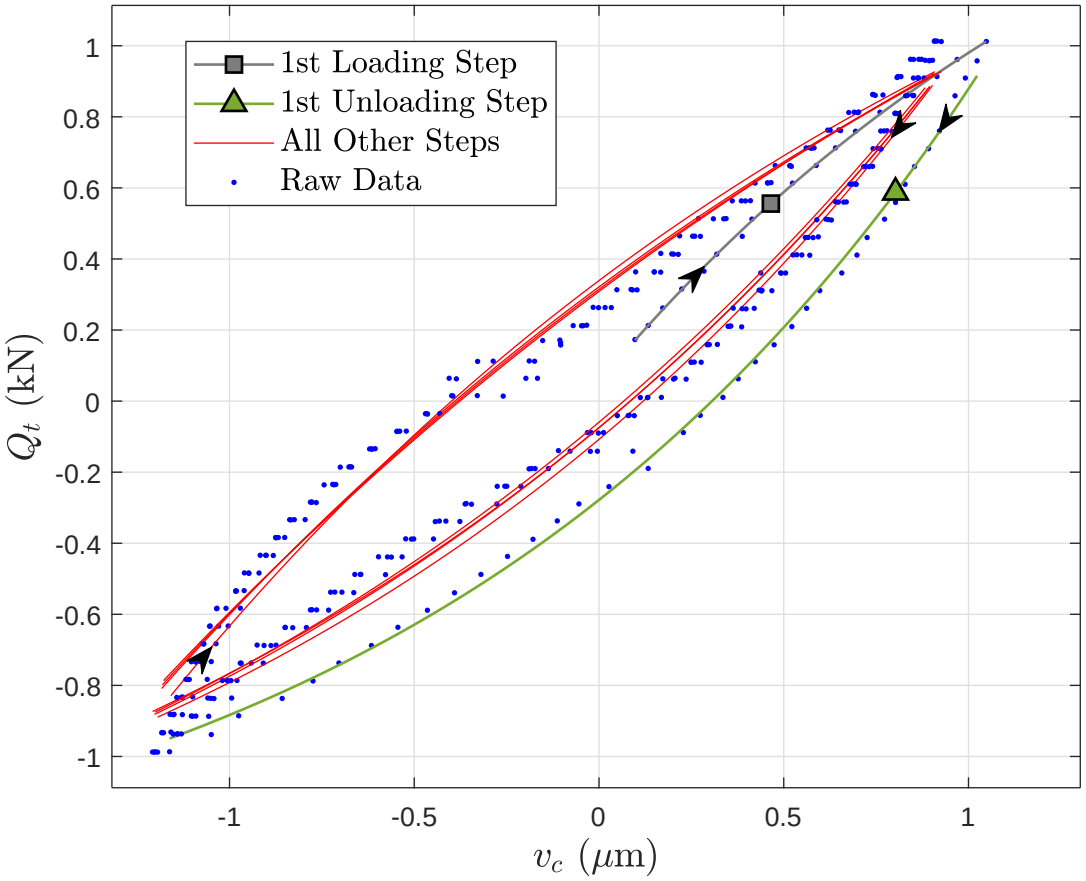

Figure 2.52: Plot of the tangential load and tangential contact displacement relationship, with fitted curves using exponential functions. The result is from the S2 test for the tangential loading steps with normal load of $-P_n = 8$ kN.

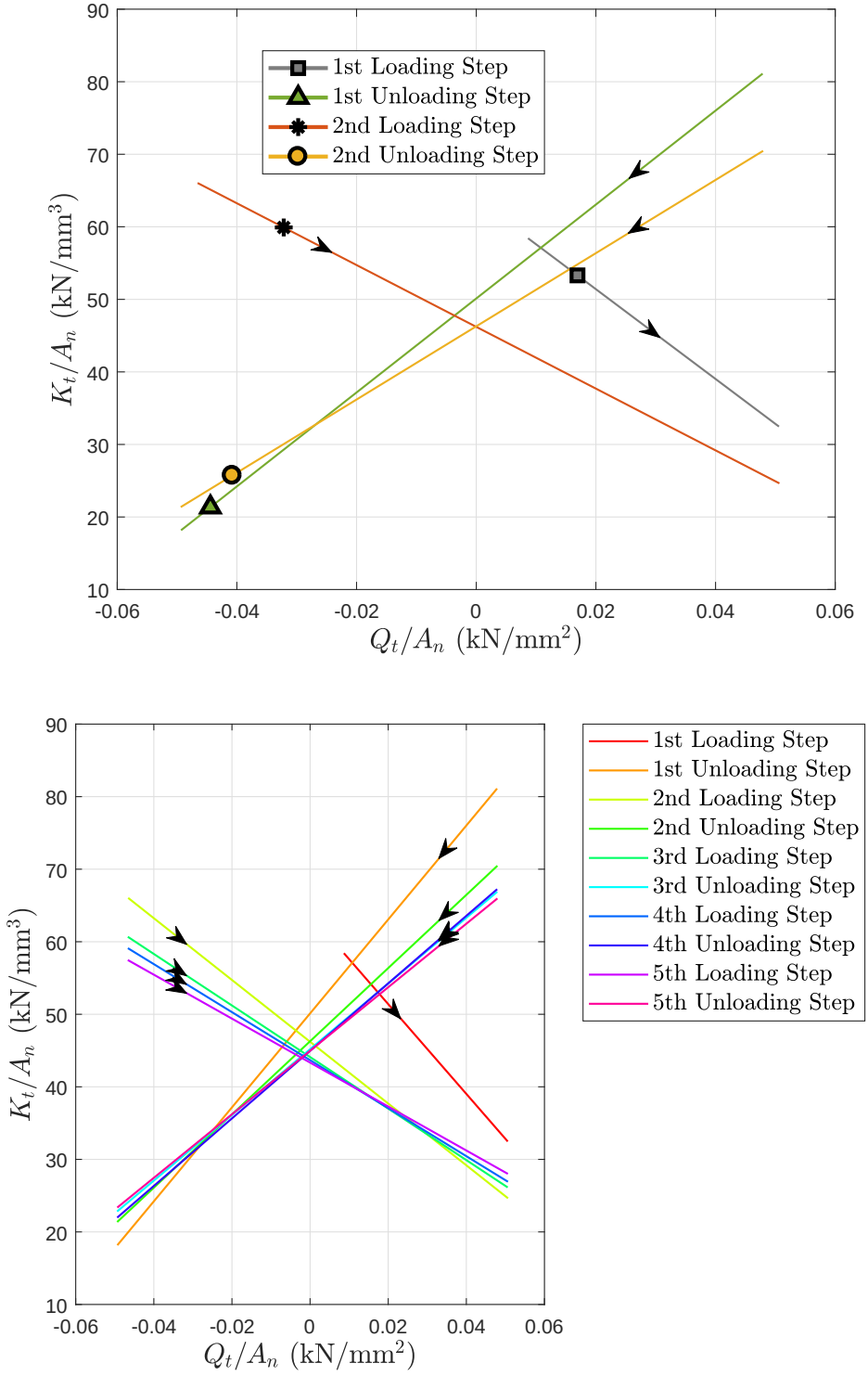

Figure 2.53: Plots of the tangential load and tangential contact stiffness relationship obtained. **Top**: Plots for the first two loading and unloading steps. **Bottom**: Plots for all loading steps. The results are from the S2 test for the tangential loading steps with normal load of $-P_n = 8$ kN.

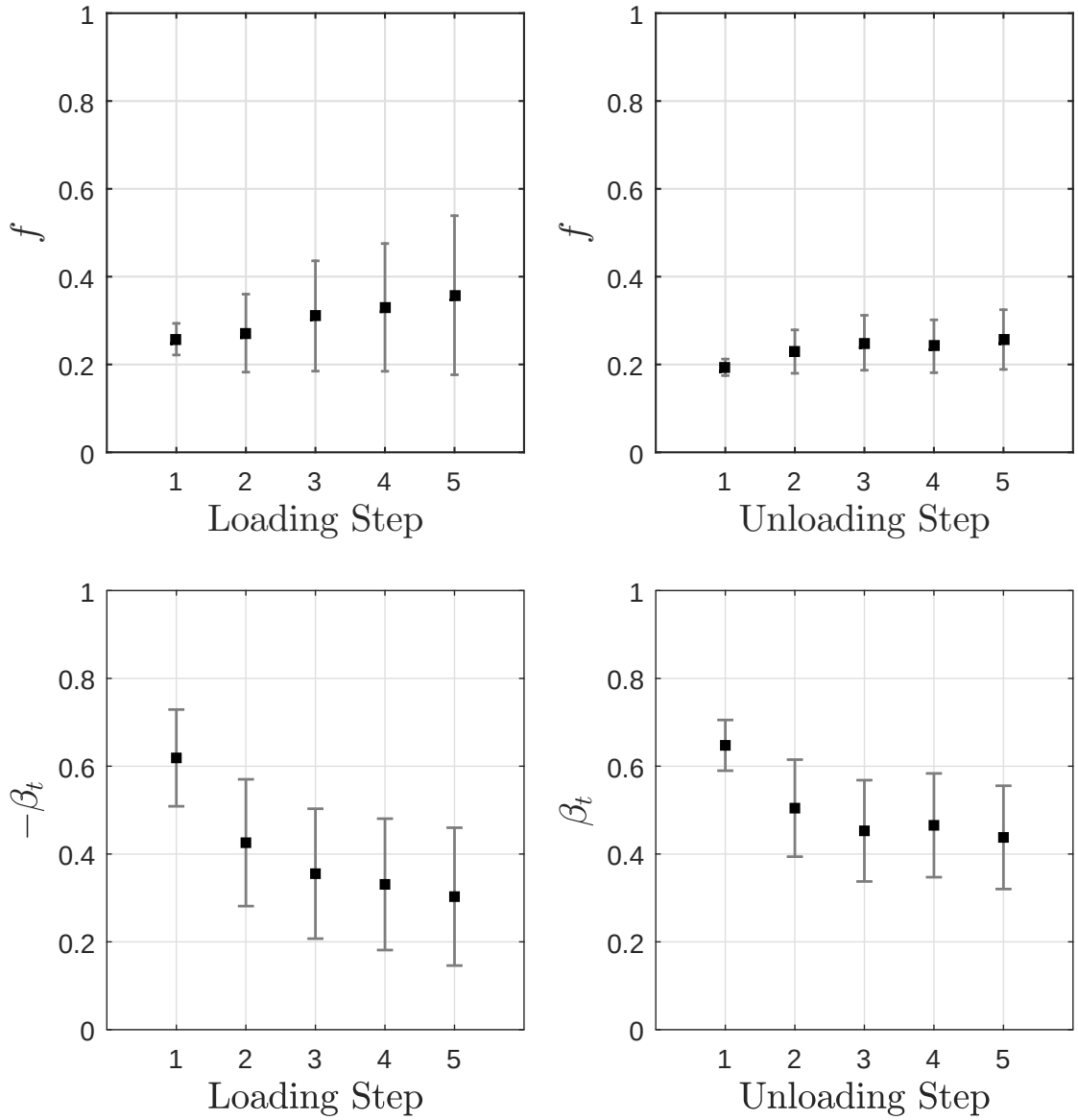

Figure 2.54: **Top**: Coefficient of friction deduced from the derived tangential contact stiffness and tangential load relationship with error bars due to fitting uncertainties for 95% confidence. **Bottom**: The slope of the tangential contact stiffness and tangential load relationship derived for each step with error bars due to fitting uncertainties for 95% confidence. **Left**: Results for the loading steps. **Right**: Results for the unloading steps. The results are from the S2 test for the tangential loading steps with normal load of $-P_n = 8$ kN.

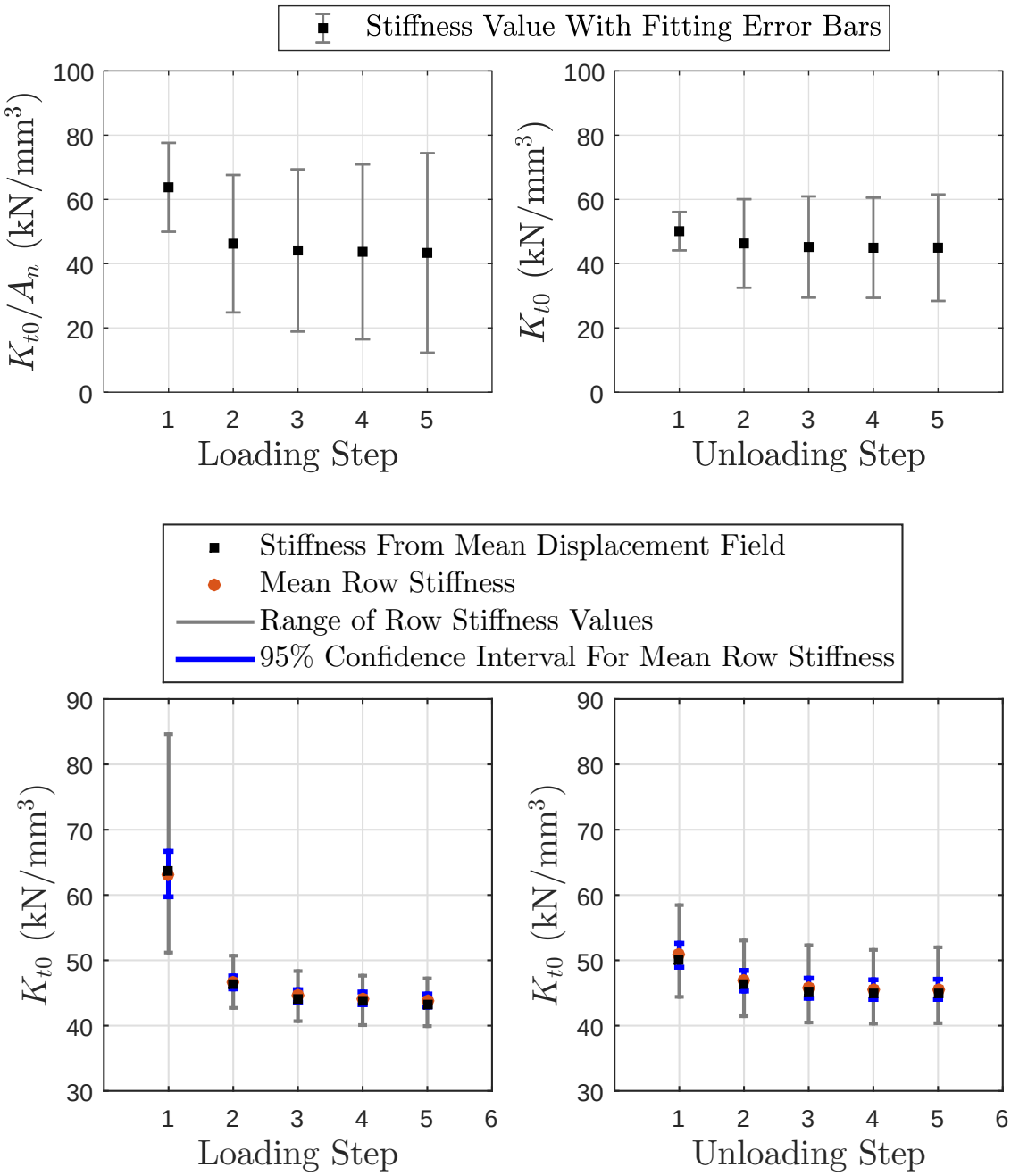

Figure 2.55: **Top**: The tangential contact stiffness at zero tangential load deduced from the derived tangential contact stiffness and tangential load relationship with error bars due to fitting uncertainties for 95% confidence. **Bottom**: The mean row tangential contact stiffness at zero tangential load with error bars from the Student's t-distribution for 95% confidence along with the maximum and minimum values for all the rows. The K_{t0} obtained from the mean displacement field (the values in the top figures) is plotted as well. **Left**: Results for the loading steps. **Right**: Results for the unloading steps. The results are from the S2 test for the tangential loading steps with normal load of $-P_n = 8$ kN.

Test S3 2μm wavelength surface

The exponential model fitted well the data from both loading and unloading steps, though the coefficients of friction derived from the unloading steps were twice as high as that for the loading steps. The K_{t0} values were similar for all steps.

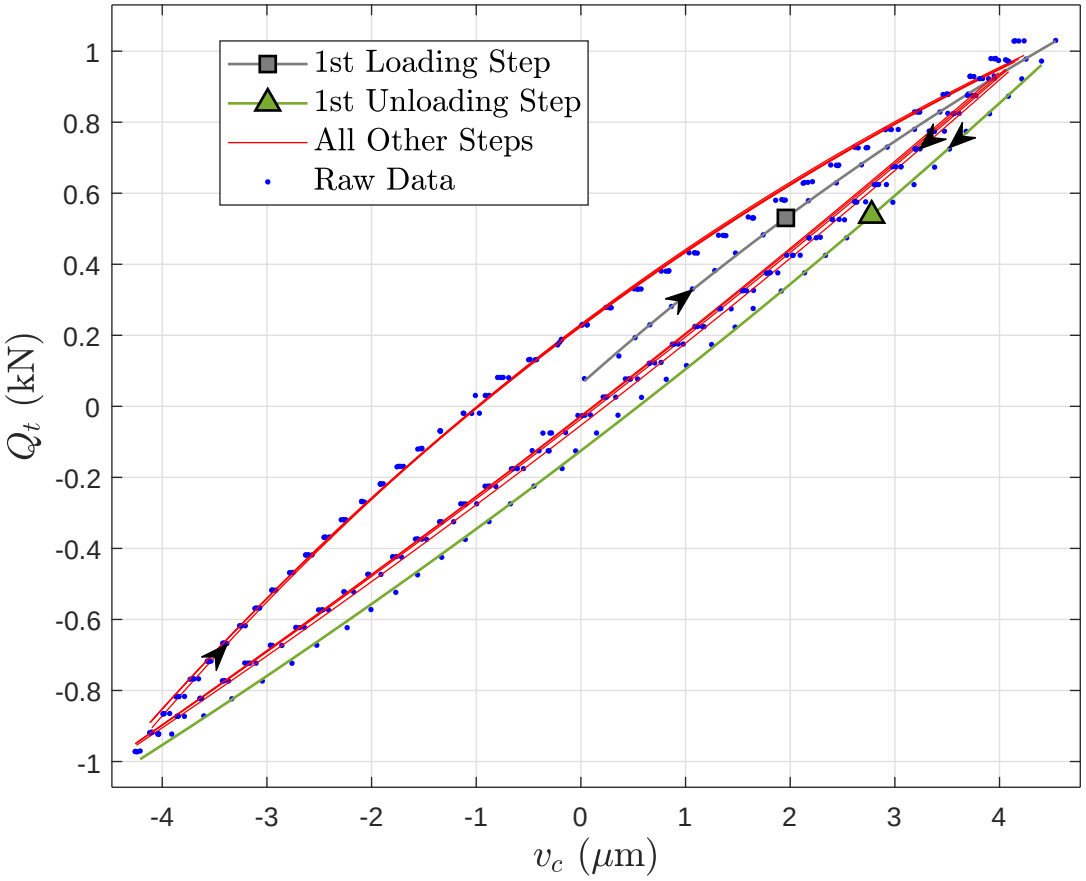

Figure 2.56: Plot of the tangential load and tangential contact displacement relationship, with fitted curves using exponential functions. The result is from the S3 test for the tangential loading steps with normal load of $-P_n = 8$ kN.

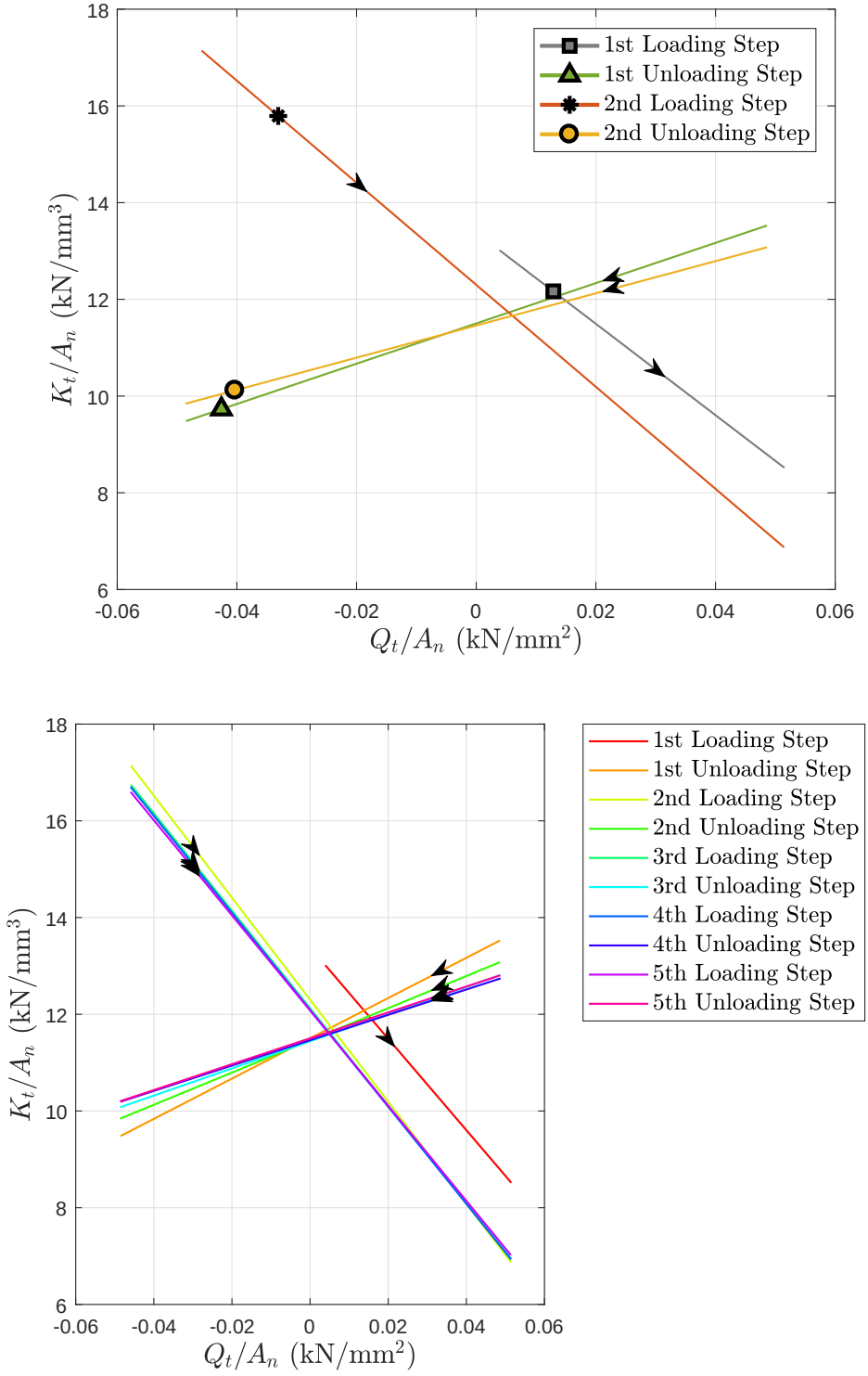

Figure 2.57: Plots of the tangential load and tangential contact stiffness relationship obtained. **Top**: Plots for the first two loading and unloading steps. **Bottom**: Plots for all loading steps. The results are from the S3 test for the tangential loading steps with normal load of $-P_n = 8$ kN.

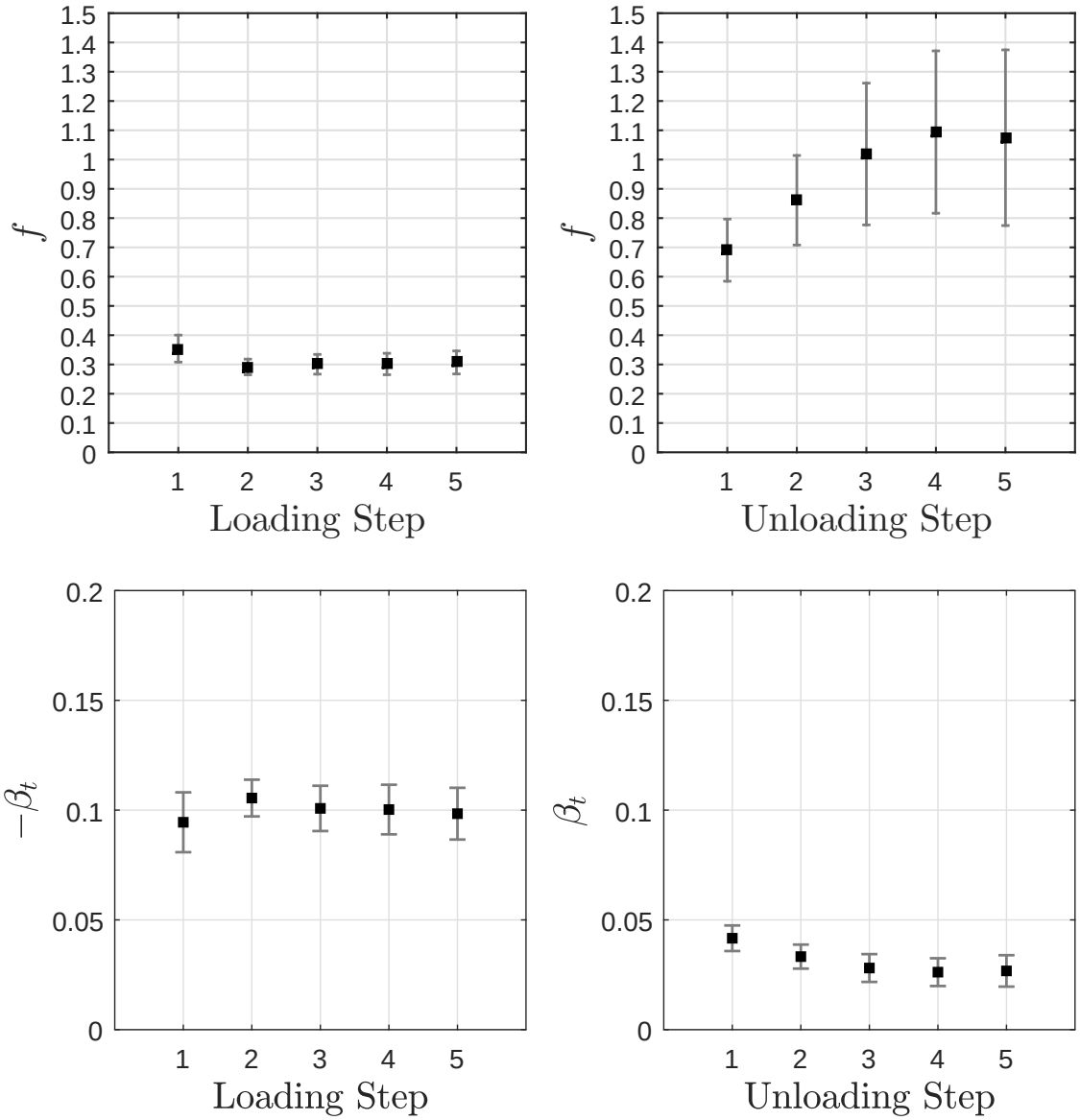

Figure 2.58: **Top**: Coefficient of friction deduced from the derived tangential contact stiffness and tangential load relationship with error bars due to fitting uncertainties for 95% confidence. **Bottom**: The slope of the tangential contact stiffness and tangential load relationship derived for each step with error bars due to fitting uncertainties for 95% confidence. **Left**: Results for the loading steps. **Right**: Results for the unloading steps. The results are from the S3 test for the tangential loading steps with normal load of $-P_n = 8$ kN.

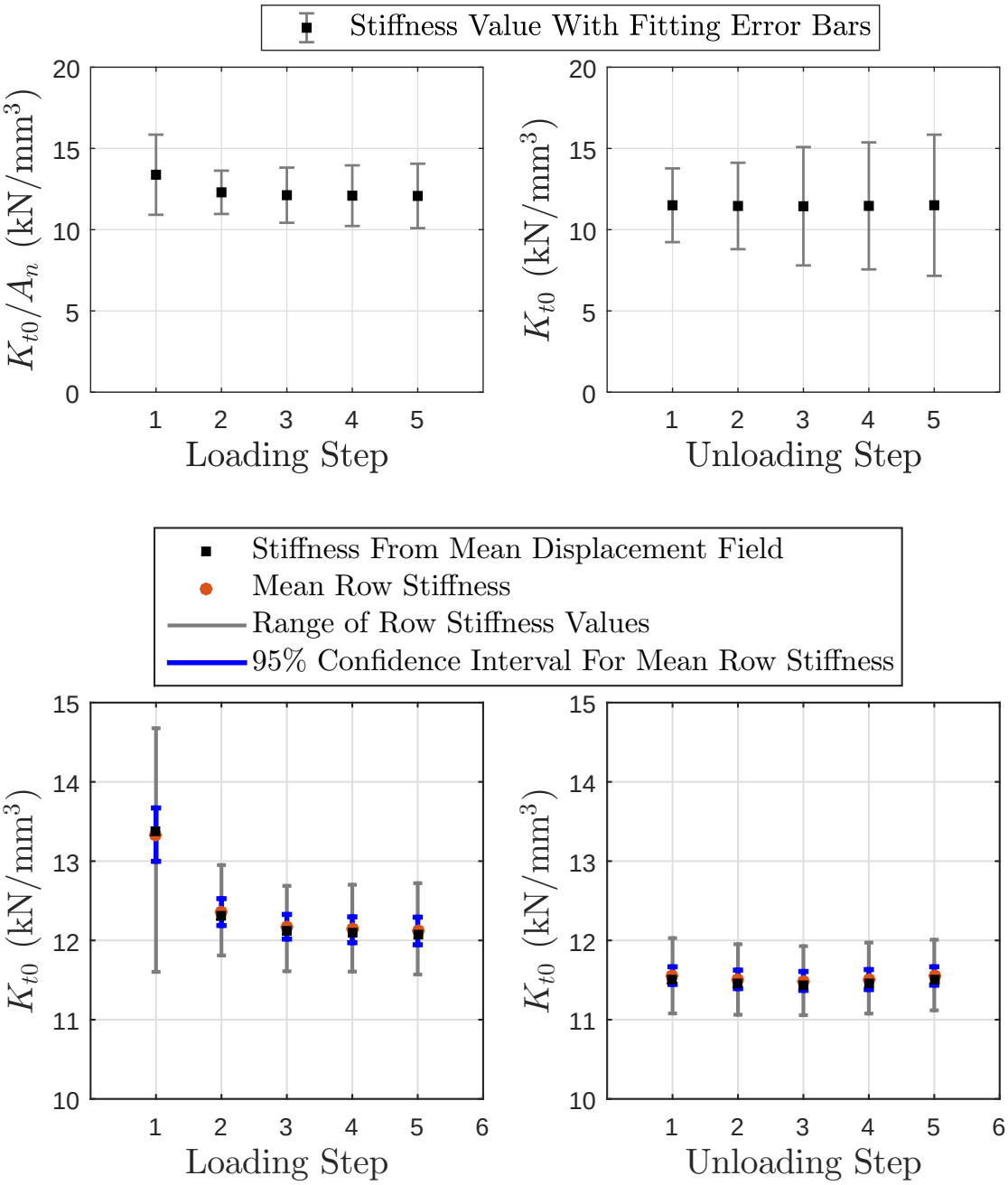

Figure 2.59: **Top**: The tangential contact stiffness at zero tangential load deduced from the derived tangential contact stiffness and tangential load relationship with error bars due to fitting uncertainties for 95% confidence. **Bottom**: The mean row tangential contact stiffness at zero tangential load with error bars from the Student's t-distribution for 95% confidence along with the maximum and minimum values for all the rows. The K_{t0} obtained from the mean displacement field (the values in the top figures) is plotted as well. **Left**: Results for the loading steps. **Right**: Results for the unloading steps. The results are from the S3 test for the tangential loading steps with normal load of $-P_n = 8$ kN.

2.8.3 Note on the quality of the data obtained

Similar observations regarding the quality of the data obtained from the tests with the ground surfaces can be made. The error bars for most of the data for the normal loading versus normal contact displacement measurements were generally small and the data scatter was minimal. Further the margin of error values for the fit parameters for many of the tangential loading and unloading steps were low, though like the results from the tests with ground specimens, significant error was seen in some loading and unloading steps. Further, as noted before the shape of the tangential loading and tangential contact displacement data for some of the tests deviated from the shape implied by the exponential curves. This is particularly the case for the data with the S1 specimen.

The parameter K_{t0} determined as the mean value of the values computed from each row of displacement data had small margins of error, as in the tests with the ground interfaces. See the plots at the bottom of Figures 2.51, 2.55 and 2.59.

2.9 Discussion of Test Results with Structured Surfaces

As seen with the tests with the ground specimens the exponential relationship between normal load and normal contact displacement fit the experimental data well. See Figures 2.45 to 2.59 and Table 2.7. The adjusted R-square goodness of fit for the normal loading and unloading steps for all three tests is above 0.98. The normal contact stiffness at maximum normal load (8 kN) for each test is plotted against the structured pattern wavelength in Figure 2.60. The slope of the normal contact stiffness and normal load relationship is also plotted. The values for both loading and unloading steps are very similar. The results show that the wavelength of the grooves do not have significant effect on the normal contact stiffness values measured.

Figures 2.49 to 2.59 and Tables A.28 to A.39 in Appendix A provide the results from the tangential loading steps. While the change in the contact displacement values with each loading step (from around 2 μm to 8 μm) was significantly greater than those seen in the tests with ground surfaces, the fitted curves did not match the raw data as well for many loading and unloading steps, particularly in comparison with the tests with the ground 'rough specimen' (S_q of 1.422 μm). Furthermore, significant asymmetry was seen between the data for the loading and unloading steps, and for some loading and unloading steps the shape of the raw data profile did not match the exponential relationship expected and used to fit the data. These observations suggest misalignment between the pads and specimens may have been significant. Unlike the ground specimens, which can be considered to have reasonable flat surfaces due to the grinding processes, the structured surface specimens were polished before the patterns were applied. The polishing process could have lead to an uneven surface that resulted in misaligned interfaces during testing.

Nonetheless, decent fits were obtained for some of the loading and unloading steps, and values of mean values of K_{t0}, β_t and f were found using the results from those loading and unloading steps for which the margin of error on the K_{t0} value was less than 50%. The mean C_c value was found by dividing the mean K_{t0} value with the normal contact stiffness, K_n, at the normal load at which the tangential tests were conducted (the average value from the loading and unloading steps was used). These values are plotted in Figure 2.61 and given in Tables 2.8 and 2.9.

As with the tests with the ground specimens, the coefficient of friction values for most loading and unloading steps with relatively small margin of error values were around 0.2. The exception is for the unloading steps from test S3, which on average implied an unrealistic coefficient of friction value of 0.948. The mean coefficient of friction derived from the loading steps was 0.311 and is more consistent with all the other measurements made in this study. The dubiously high coefficient of friction values from the unloading steps therefore skewed the mean coefficient of friction value calculated from test S3 with the 2 μm wavelength specimen.

The C_c values computed may suggest the surface texture pattern has an effect on the tangential contact stiffness values. However, the values for the specimen in test S2 and S3 are near half the Mindlin ratio, though a bit smaller than the values seen for the tests with ground specimens. Also it is not clear whether the laser diffraction process changed significantly the material properties. Furthermore, the patterning was done in tiled sections and raised features at the junctions of the tiles could have affected the measurements.

While the structured surfaces and the pads used were not significantly rougher than the specimens and the pads used in the tests with ground interfaces, both the normal and tangential contact stiffness values are significantly lower. This may due to the nature of structured surfaces, though there is some doubt whether an uneven contact surface (due to polishing) had an excessive effect. Rounding near the edges of the specimen could lead to greater normal contact displacement values being measured from the images taken at the sides of the specimen and pad surfaces, and therefore normal contact stiffness values may be underestimated.

The profile roughness parameters and the areal properties for the structured surfaces and the pads used in the measurement are given in Tables A.26 and A.27 in Appendix A. The surface roughness (both profile and areal) parameters for the pads used in the measurements are similar for all three tests (The S_q values are between 1.016 and 1.057 μm). The specimen used in test S2 (with surface wavelength of 5 μm) is considerably smoother than the those used in the other two tests. S_q values for specimen from S3 test (2 μm wavelength surface) and the specimen for the S1 test (10 μm wavelength surface) are 0.752 and 0.761 μm while the S_q value for the specimen in S2 test (with surface wavelength of 5 μm) is 0.432 μm.

This supports the conclusion found from the tests with the ground specimens, that rougher

surfaces have lower normal contact stiffness and variations in the β_n values are at least in part due to surface texture. However from Table 2.10 the relationship between the equivalent roughness for both surfaces in contact, S_q^e, with the $\beta_n S_q^e$ is not seen to be near linear as in the case with the ground surfaces, nor is $\beta_n S_q^e$ parameter near 1 as per the Medina et al. model (equation (1.4)). While this may be due to the nature of the textured surfaces, it is possible that the results were affected by the rounding of the corners due to polishing.

As in the case with the tests with the ground specimens, the tangential contact stiffness measurement results from first tangential loading step were slightly different from that from other steps. No significant change in the results were observed for the subsequent steps, other than those from loading steps with significant error as indicated by large uncertainty bounds on the fitting parameters. Table 2.11 provides the values of the surface roughness of the pads before and after each test. It is noted as in the tests with the ground surfaces there is a reduction in surface roughness. For these tests the reduction is by 6-11 %. This is consistent with the slight increase in the normal contact stiffness observed at the end of each test.

In short, the results from the measurement of the textured surfaces, confirm many of the observations made from the testing of the ground surfaces. The results indicate that the directional nature of the textured surfaces may have an impact on the tangential contact stiffness, though there is some concern that the measurements were affected by misalignment of the surfaces due to uneven surface profiles and due to rounding of the specimen surface near the edges due to polishing. The results seem to indicate the tangential contact stiffness is greater for the surfaces with larger grooves.

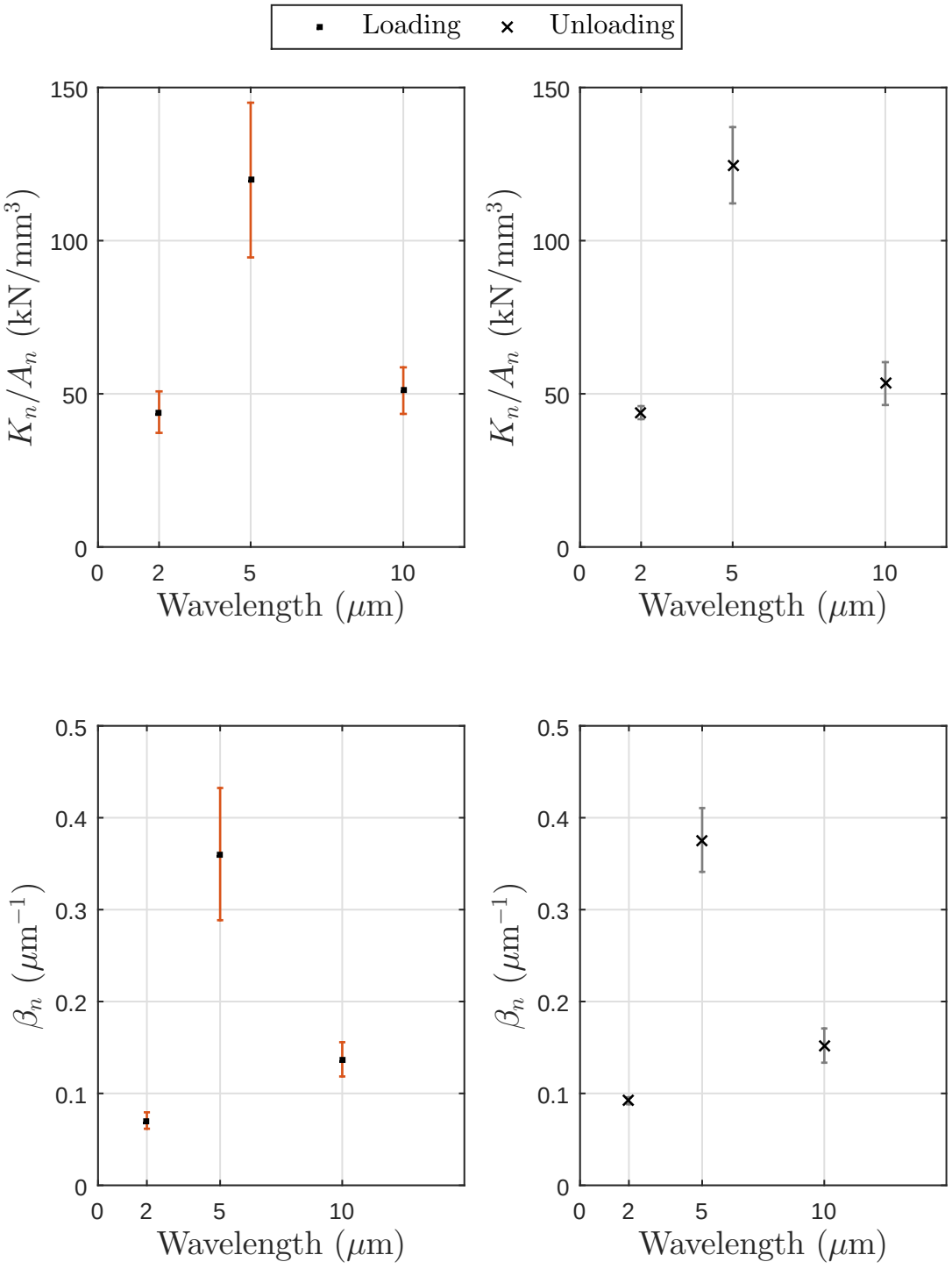

Figure 2.60: Results of the normal contact stiffness measurement. **Top**: The normal contact stiffness by nominal area at the highest normal load applied in the test, $-P_{nmax}$. **Bottom**: the slope of the normal load and normal contact stiffness relationship plotted against structured surface feature wavelength for the test. **Left**: results from the loading step. **Right**: results from the unloading step.

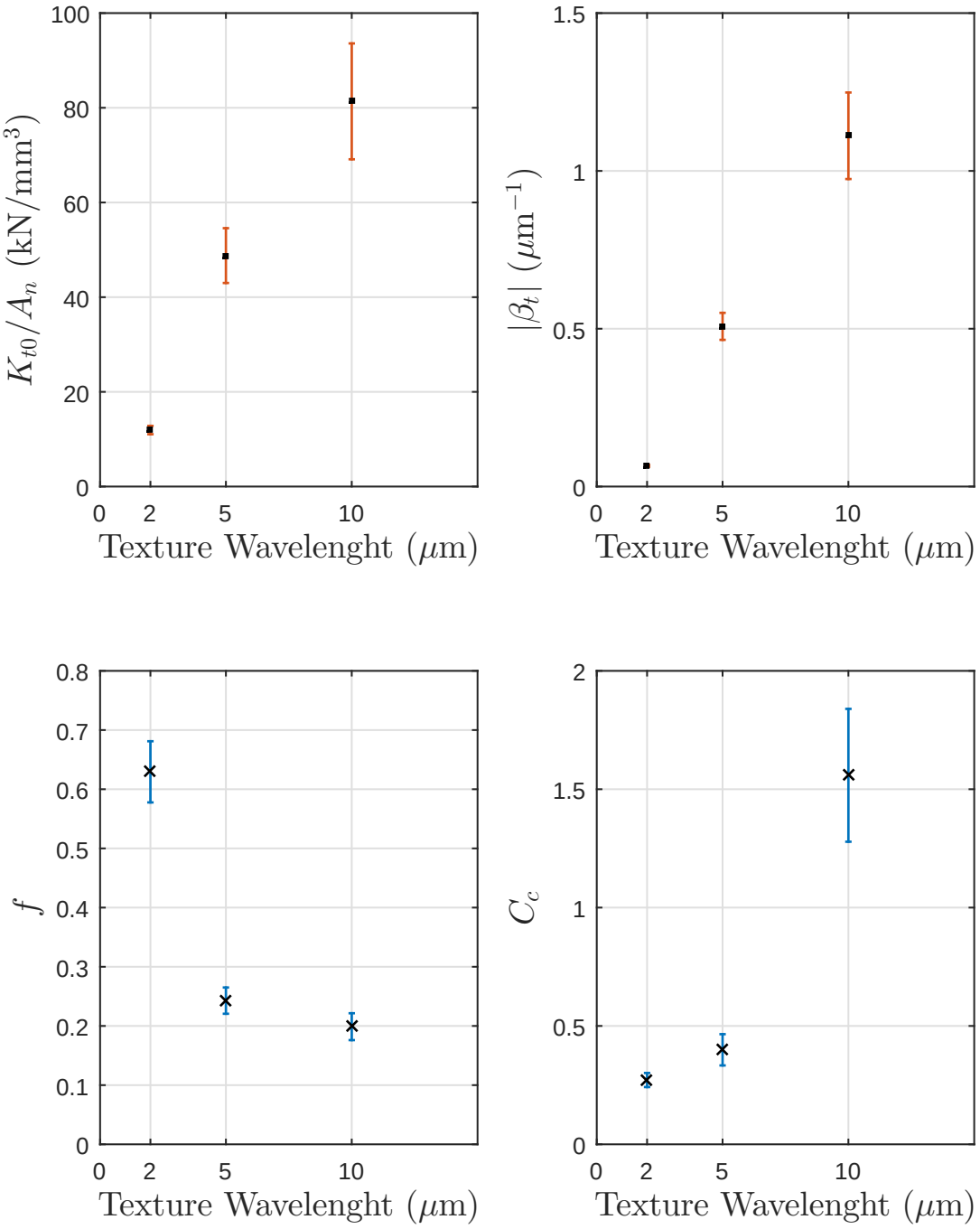

Figure 2.61: Results from the tangential contact stiffness measurements. **Top Left**: The mean tangential contact stiffness at zero tangential load by nominal area plotted against the texture wavelength of the specimen. **Top Right**: the mean absolute slope of the tangential load and tangential contact stiffness relationship plotted against the texture wavelength of the specimen. **Bottom Left**: mean coefficient of friction derived from each test with the 'rough specimen' (S_q of 1.422 μm) plotted against the texture wavelength of the specimen. **Bottom Right**: mean coefficient of friction found from each test with the 'rough specimen' (S_q of 1.422 μm) plotted against the normal loading. Mean values were calculated only for those loading steps for which the fit error margin for the K_{t0} value was less than 50%.

Test No.	Texture Wave-lenght	GOF	K_n/A_n (kN/mm^3)	K_n/A_n (kN/mm^3), margin of error	β_n (μm^{-1})	β_n (μm^{-1}), margin of error	α_n (kN)	α_n (kN), margin of error	P_0 (kN)	P_0 (kN), margin of error
Loading										
S1	10 μm	0.995	51.044	7.579	0.137	0.019	0.343	0.157	0.553	0.436
S2	5 μm	0.982	119.785	25.254	0.360	0.072	0.002	0.004	1.353	0.423
S3	2 μm	0.999	44.025	6.770	0.070	0.009	3.737	0.874	-4.490	1.076
Unloading										
S1	10 μm	0.998	53.339	6.986	0.152	0.019	6.312	0.248	0.985	0.305
S2	5 μm	0.997	124.620	12.450	0.376	0.035	-0.376	6.333	1.368	0.198
S3	2 μm	0.989	43.858	2.124	0.092	0.004	9.214	0.166	-1.532	0.189
Mean										
S1	10 μm		52.191	5.161	0.145	0.013				
S2	5 μm		122.203	14.078	0.368	0.040				
S3	2 μm		43.941	3.548	0.081	0.005				

Table 2.7: Data obtained from the normal loading and unloading steps for each test as well as the mean values are provided here. K_n/A_n value is the normal contact stiffness by nominal area at the normal load used in that tangential loading steps, 8 kN. The margin of error due to fitting uncertainties for a confidence interval of 95% are provided as well as the adjusted R-square goodness of fit value (GOF) for the fitted curves.

Test No.	Texture Wavelength	K_{t0}/A_n (kN/mm^3)	K_{t0}/A_n (kN/mm^3), margin of error	β_t (μm^{-1})	β_t (μm^{-1}), margin of error	f	f, margin of error	Steps Used
Loading								
S1	10 μm	133.721	34.253	-2.478	0.590	0.135	0.015	1
S2	5 μm	54.997	12.739	-0.522	0.091	0.264	0.048	1,2
S3	2 μm	12.395	0.852	-0.100	0.005	0.311	0.017	1,2,3,4,5
Unloading								
S1	10 μm	70.884	12.986	0.838	0.114	0.212	0.027	1,2,3,4,5
S2	5 μm	46.300	6.297	0.502	0.048	0.234	0.024	1,2,3,4,5
S3	2 μm	11.474	1.545	0.031	0.003	0.948	0.102	1,2,3,4,5
Combined				$\lvert\beta_t\rvert$				
S1	10 μm	81.357	12.235	1.111	0.137	0.199	0.023	
S2	5 μm	48.785	5.786	0.508	0.043	0.243	0.022	
S3	2 μm	11.935	0.882	0.066	0.003	0.629	0.052	

Table 2.8: The mean values for stiffness at zero tangential load by nominal area, K_{t0}/A_n, the slope of the tangential contact stiffness and tangential load relationship, β_t, and the deduced coefficient of friction values are provided here for each test for the loading and unloading steps separately and combined. Only those steps for which the margin of error due to fitting for the K_{t0} value was less than 50% were used to calculate the mean values. The steps used are listed. The margin of error values due to fitting uncertainties for the mean values are provided.

Test No.	Texture Wavelength	C_c	Margin of error
S1	10 μm	1.559	0.281
S2	5 μm	0.399	0.066
S3	2 μm	0.272	0.030

Table 2.9: The ratio, C_c, between the mean tangential contact stiffness at zero tangential load from all the tangential loading steps (loading and unloading) and the mean normal contact stiffness at the same normal load.

Test No.	Equivalent S_q^e (μm)	$\beta_n S_q^e$
S1	1.269	0.174
S2	1.092	0.393
S3	1.298	0.091

Table 2.10: The equivalent roughness parameter, S_q^e, for the interfaces in the tests with the structures surfaces and the $\beta_n S_q^e$. The β_n values from the loading steps are used.

Test No.	S_q(nm) before test	S_q(nm) after test	Percent reduction
S1	1057	942	11%
S2	1003	908	9%
S3	1016	951	6%

Table 2.11: Roughness of the pad interface before and after each test.

2.10 Conclusion

The experimental results of the tests with the ground interfaces showed agreement with theoretical models that posited a linear relationship between normal contact stiffness and normal load. Further a linear relationship between tangential contact stiffness and tangential load was observed. Both normal and tangential contact stiffness are seen to be inversely related to the interface roughness, characterised by the equivalent root mean square roughness of both surfaces. The results indicate that the normal and tangential contact stiffness values for similar ground interfaces may be estimated straightforwardly for a range of normal and tangential loads on the basis of three parameters: β_n, C_c and f.

Experimental measurements obtained here, and in many other published studies, suggest half of the value of the Mindlin ratio may be a suitable estimate of the C_c parameter for many interfaces. In addition, the coefficient of friction is a standard parameter and there are numerous resources to assist in the selection of a suitable value. The results imply, consistent with the Medina model [4], that β_n for ground interfaces can be estimated to be near to $1/S_q^e$, where S_q^e is the equivalent root mean square roughness parameter for both rough surfaces in contact as defined in the present study.

The tests with the structured surfaces confirmed many of the observations made from the tests with ground surfaces. Furthermore, they indicated that directional patterns may have an effect

on the tangential contact stiffness value for the tested interfaces, though there are some concerns regarding the accuracy of the measured values due to possible misalignment of the interfaces and rounding of the edges of the specimen surfaces due to polishing, which is likely to have affected measurement of the normal contact stiffness particularly, and may have contributed to misalignment issues in the measurement of tangential contact stiffness.

Future investigation of contact stiffness properties could look at the effect cyclic loading on both normal and tangential contact stiffness as the surface textures change with repeated loading. The tests conducted with the 'rough specimen' (S_q of 1.422 μm) did show a small but not very significant change in the contact stiffness properties. However the tests conducted with the 'smooth specimen' (S_q of 0.687μm) showed, though with greater error margins, a significant change may have occurred. In addition, further testing of different surfaces and loading could test the applicability of the key findings in this study to other surfaces, particularly the linear relationship between tangential contact stiffness and tangential load.

Chapter 3

Modelling of Asperity Contact

3.1 Introduction

As noted in Chapter 1, models of rough interfaces, such as to investigate contact stiffness properties, often involve asperity modelling. Further there is a dearth of asperity modelling of the tangential displacement behaviour of rough interfaces. Therefore, a need exists to understand the physics of asperity contacts, particularly when subject to tangential loading. In the first half of this chapter, details are provided of the modelling of single asperity contacts to find the basic relations for asperity interfaces which are governed by different friction laws and for when plasticity is taken into account. Asperity models such as that by Medina et al. which investigate normal contact stiffness properties assume the asperity material is purely elastic [4]. Also, while the behaviour of an elastic asperity contact with a Coulomb friction law is known, it is not clear how a different friction law will affect the analysis.

The first model compares the tangential load and tangential displacement relationship for a single elastic asperity interface for different friction laws. The second model investigates the tangential behaviour of a fully stuck asperity contact, when the asperity material is elastic and when the material is elastic perfectly plastic. Both of these single asperity models use the results of finite element modelling and known closed form elasticity solutions for spherical contacts (using half-space approximation).

In the second half of this chapter, two multi-asperity models are described. To explore the effect of different normal asperity load distribution for a multi-asperity interface subject to tangential loading, a multi-asperity model was constructed that involves independent asperities, which can be viewed as elastic asperities on a rigid base in contact with similar elastic asperities on a rigid base, with a Coulomb friction interface law. The effect of different asperity load distributions on the tangential load and tangential displacement relationship for the multi-asperity interface is explored. It will be shown that for a range of tangential loads, the relationship can be approximated by a

simple expression for a single asperity contact modified with an appropriate multiplier.

Also, many asperity models, such as Medina et al., assume the asperities are sufficiently spaced such that the loading on one asperity does not affect the loading or the displacement at another, i.e. asperity interactions are neglected. A second multi-asperity model has been constructed that involves elastic asperities on an elastic half space in an organised grid in contact with elastic asperities, perfectly aligned, on a similar elastic half-space. This model can be used to estimate the normal contact stiffness for an elastic contact at given loads and asperity concentrations when asperity interaction is permitted.

3.2 Single Asperity Modelling

3.2.1 Elastic Asperity Contact with Different Friction Laws

A spherical linear elastic asperity in contact with a half-space of the same material is modelled. The asperity and half-space are brought into contact by the application of normal load, $-P$. Then tangential load is applied. See Figure 3.1. The relationship between the displacement of a remote point and centre point of the contact area and the tangential load is found for different contact laws. Three contact laws are compared, namely

1. Fully stuck: no restrictions on shear traction component $q(r, \theta)$ and no slip
2. Frictional contact law: $q(r, \theta) \leq fp(r, \theta)$
3. Shear limit contact law: $q(r, \theta) \leq \tau_{max}$

Here r is the radial coordinate and θ is the angular coordinate of a point on the contact area, with the centre point of the contact area taken as the origin. $p(r, \theta)$ and $q(r, \theta)$ are the normal and shear traction components for the point (r, θ) respectively. f is the coefficient of friction and τ_{max} is the maximum allowed shear traction value. Analytical solutions for the fully stuck case and when the contact is modelled using a Coloumb friction law are found in normalised form. 3D finite element analysis is used to model the asperity on a half-space, approximated as a block of finite dimensions, with a contact law that prescribes the maximum shear traction.

The relationship between the tangential displacement of a remote point with respect to the centre of the contact region, Δ_x, and shear load Q applied is given by Mindlin for the fully stuck case [3, p 261], as

$$\Delta_x = \frac{Q(2-\nu)}{8\mu r_c}, \tag{3.1}$$

where r_c is the contact area and μ and ν are the modulus of rigidity and the Poisson's ratio respectively. It should be noted that Δ_x is half of the total compliance, when there are two elastic asperities in contact (this definition is used throughout this chapter). The relationship in the Coulomb friction case is given by [3, p. 263]

$$\Delta_x = \frac{3fP}{16r_c}\left(\frac{2-\nu}{\mu}\right)\left(1-\left(1-\frac{Q}{fP}\right)^{2/3}\right). \tag{3.2}$$

For normalisation purposes, Δ_n is defined as the tangential displacement of remote point due to reference load of Q_n if the contact was fully stuck, i.e.

$$\Delta_n = \frac{Q_n(2-\nu)}{8\mu r_c}. \tag{3.3}$$

The shear loading at slip is taken as the reference load, i.e.

$$Q_n = fP. \tag{3.4}$$

Equation (3.2) can now be normalised to give

$$\frac{\Delta_x}{\Delta_n} = \frac{3}{2}\left(1-\left(1-\frac{Q}{Q_n}\right)^{2/3}\right). \tag{3.5}$$

The asperity in contact with a half-space loaded normally and tangentially with a shear limit contact law was modelled using finite elements with Abaqus CAE software, as a spherical asperity in contact with a block of finite dimensions. See Figure 3.2 for a side-view schematic representation of the model dimensions. The spherical asperity is of radius 100 mm, where 1 mm is the radius of the contact area after the application of normal load. The spherical section protrudes from a cuboid of dimensions 100 mm × 100 mm × 80 mm. The spherical section has a width of 20 mm. The block has similar dimensions: 100 mm × 100 mm × 80 mm. Encastre boundary condition is enforced on the bottom surface of the block. The model dimensions were chosen to be sufficiently large with respect to the expected contact radius after normal loading so that the contact behaviour can be described by Hertzian equations during the normal loading step but not too large that the computational cost of the analysis would be excessive. Quadratic elements C3D10I and C3D20R were used to mesh the asperity and the block respectively. Tetrahedral elements, C3D10I, were

used to mesh the asperity since brick elements, C3D20R, that were used for the block are unsuitable for a spherical geometry. Dense mesh was applied over a square region of 4.5 mm by 4.5 mm on both the surface of the block and spherical asperity. Average element size of 0.1 mm were used in this region. Initially models were constructed with coarser mesh and the mesh was refined until no significant difference was seen in the surface tractions, and the normal pressure during the normal loading step matched that given by Hertz equations. In total 55,561 elements and 48,960 elements were used to discretize the asperity and block respectively. See Figure 3.3 for images of the mesh.

Normal loading is applied as a downward displacement of 0.01 mm to the top surface (this is the required relative approach, δ, for a contact radius of 1 unit for a spherical asperity of radius of 100 mm, since for a Hertz contact $\delta = r_c^2/R$ [49]). During application of normal loading, 'rough' friction formulation for tangential behaviour, and 'Hard-contact' setting for pressure-overclosure with 'Direct' constraint-enforcement method for normal contact behaviour were used. The bodies were modelled with material properties of Young's modulus of 2×10^6 N/mm^2 and Poisson's ratio of $\nu = 0.3$, though with appropriate normalisation results independent of material properties can be obtained.

After the application of normal loading, tangential loading was applied in the form of tangential displacement increments of up to 0.01 mm of the top surface of the asperity. Lagrangian multiplier friction formulation was used with coefficient of friction of 1 (chosen to be high so it would not act as a significant limitation) with shear limits of 4000, 5000 and 6000 N/mm^2, which correspond to $0.86p_o$, $0.71p_o$, and $0.57p_o$ respectively, where p_o is the maximum normal Hertzian pressure on the half-space due to the normal loading. For the material properties and the asperity dimension used, $p_o = 6995.82$ N/mm^2. The results are normalised so they are load and material property independent. 'Rough' or infinite friction was not enforced, since this led to convergence issues. A coefficient of friction of 1 would lead to some frictional slip, but this was minimal, particularly at higher tangential loads.

The normal contact traction and the normal displacements after the application of normal load (before the application of tangential loading) are compared with the Hertz solution. The pressure distribution as per Hertz along the contact area is given by

$$\frac{P(\check{r})}{p_o} = \sqrt{1 - \check{r}^2} \tag{3.6}$$

Here $\check{r} \equiv /r_c$ where r is the radial distance of a point on the contact area from the origin. With cylindrical coordinates, $\check{r}$,θ and $\check{z}$, (with $\check{z} \equiv z/r_c$) the stress components along the $\check{r} = 0$ axis are given by equations 7.71 and 7.72 in [3, p. 204]

$$\sigma_{\check{r}\check{r}}(\check{z}) = \sigma_{\theta\theta}(\check{z}) = p_o \left((\nu+1) \left(1 - \check{z} \tan^{-1}\left(\frac{1}{\check{z}}\right)\right) - \frac{1}{2\left(\check{z}^2+1\right)} \right),$$

$$\sigma_{\check{z}\check{z}}(\check{z}) = \frac{p_o}{\check{z}^2+1}.$$

Strain $\epsilon_{\check{z}\check{z}}(\check{z})$ is found by Hooke's law

$$\epsilon_{\check{z}\check{z}}(\check{z}) = \frac{1}{2\mu(\nu+1)} \Big(\sigma_{\check{z}\check{z}}(\check{z}) - \nu(\sigma_{\theta\theta}(\check{z}) + \sigma_{\check{r}\check{r}}(\check{z})) \Big).$$

Displacement in the direction of the $\check{z}$ axis, $w(\check{z})/r_c$, is hence

$$\begin{aligned} \frac{w(\check{z})}{r_c} &= \int_0^{\check{z}} \epsilon_{\check{z}\check{z}}(\zeta) d\zeta \\ &= \frac{p_o \left(\check{z}\nu \left(\check{z} \cot^{-1}(\check{z}) - 1 \right) - (\nu-1) \tan^{-1}(\check{z}) \right)}{2\mu} + C_z, \end{aligned}$$

where C_z is a constant and is 0 if the displacement is taken relative to the centre point of the contact area. When non-dimensionalised, this equation becomes

$$\frac{\mu}{p_o} \frac{w(\check{z})}{r_c} = \frac{\check{z}\nu \left(\check{z} \cot^{-1}(\check{z}) - 1 \right) - (\nu-1) \tan^{-1}(\check{z})}{2}. \tag{3.7}$$

At $\check{z} \to \infty$,

$$\frac{\mu}{p_o} \frac{w(\check{z})}{r_c} = \frac{\pi(1-\nu)}{4}.$$

After the application of normal load (before the application of the tangential loading) the normal displacement of points on the asperity along the vertical $\check{z}$ axis from the finite element model correspond to the displacements given by equation (3.7), as seen in Figure 3.4. Further the normal contact traction distribution over the contact area from the finite element model shows good agreement with the Hertzian distribution given in equation (3.6), as seen in Figure 3.5. This suggests the model under normal load is consistent with Hertz theory.

The relationship of normalised tangential displacement of a remote point on the asperity with the normalised tangential load applied for the three different shear limit laws are compared with the relationship for the case when a Coloumb friction is used to model the contact, as given in

Equation (3.5). See Figure 3.6. For the models with shear limits, reference load Q_n is defined as the total shear load applied when the whole contact area has a shear traction equal to the shear limit, i.e.

$$Q_n = \pi r_c^2 \tau_{max} \tag{3.8}$$

where τ_{max} is the maximum shear permitted. Δ_n, the reference displacement for the shear limit interface models, is defined by equation (3.3) with the reference load Q_n defined above. Notably, the relationship between normalised tangential load and tangential displacement for the asperity contact with the shear limit contact laws is very similar to the relationship for a purely frictional contact. This suggests equation (3.5) can provide an approximate relationship for contact interfaces defined by shear limit contact laws, provided the tangential load and tangential displacement are normalised as described in this section.

$$Q_n = \pi r_c^2 \tau_{max} \tag{3.9}$$

where τ_{max} is the maximum shear permitted. Δ_n, the reference displacement for the shear limit interface models, is defined by equation (3.3) with the reference load Q_n defined above. Notably, the relationship between normalised tangential load and tangential displacement for the asperity contact with the shear limit contact laws is very similar to the relationship for a purely frictional contact. This suggests equation (3.5) can provide an approximate relationship for contact interfaces defined by shear limit contact laws, provided the tangential load and tangential displacement are normalised as described in this section.

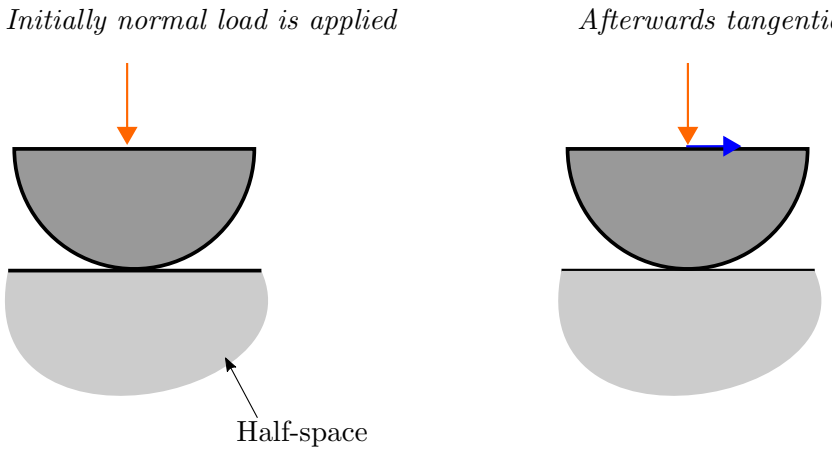

Figure 3.1: Schematic diagram showing the loading applied in the asperity models.

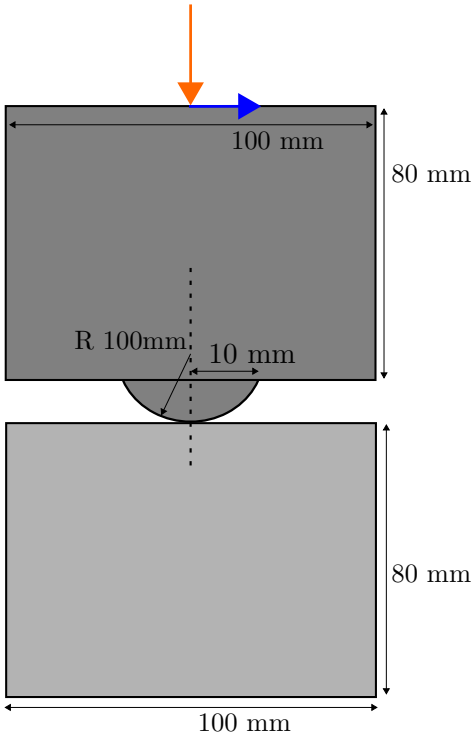

Figure 3.2: Side view of a schematic representation of the asperity (top) in contact with a block (below) in the finite element model. The asperity part is composed of a spherical section protruding from a cuboid of dimensions 100 mm × 100 mm × 80 mm. The radius of the spherical section is 100 mm. Loading is applied on the top surface of the asperity, by means of displacements. The block (below) is of dimensions 100 mm × 100 mm mm × 80 mm. The bottom surface of the block is constrained by encastre boundary condition.

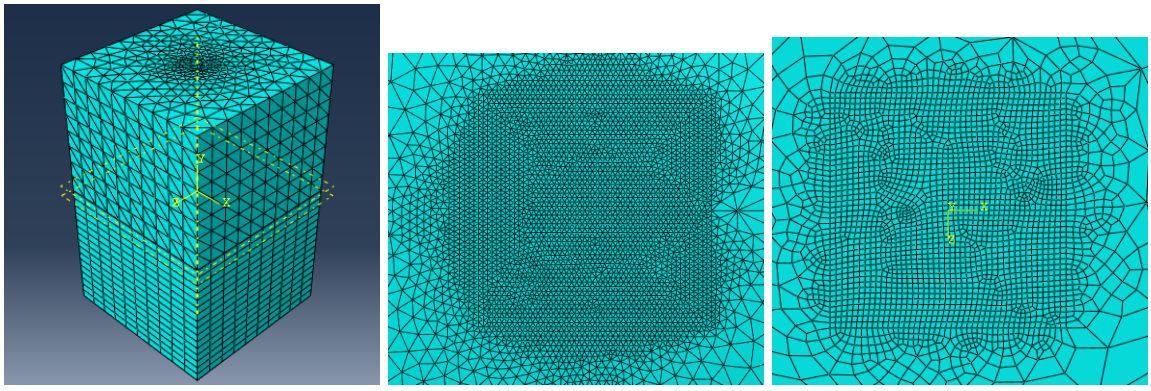

Figure 3.3: The mesh applied in the models. Left: Asperity on top of block. Centre: Top view of dense mesh at centre of the asperity interface. Right: Top view of the dense mesh at the centre of the block interface.

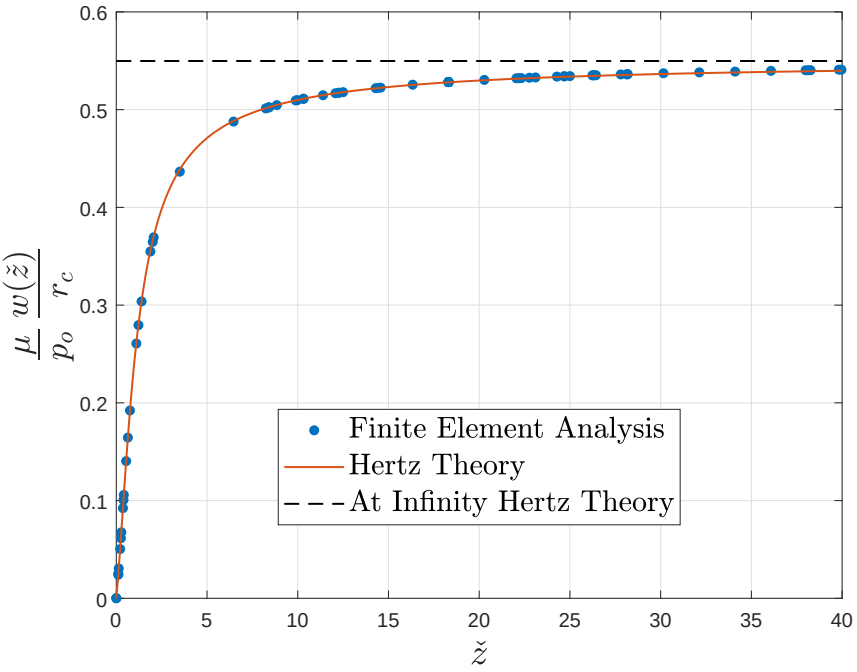

Figure 3.4: Normal displacement, $w(\check{z})$, of points along the central normal axis (perpendicular to the interface).

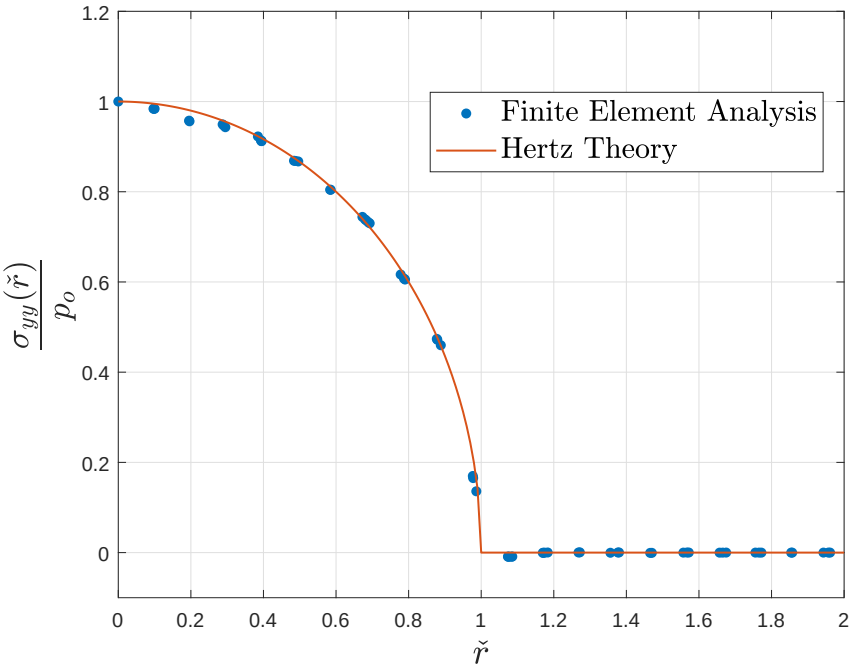

Figure 3.5: Normal contact traction for points along the contact interface from the finite element model after the application of normal load and according to Hertz theory.

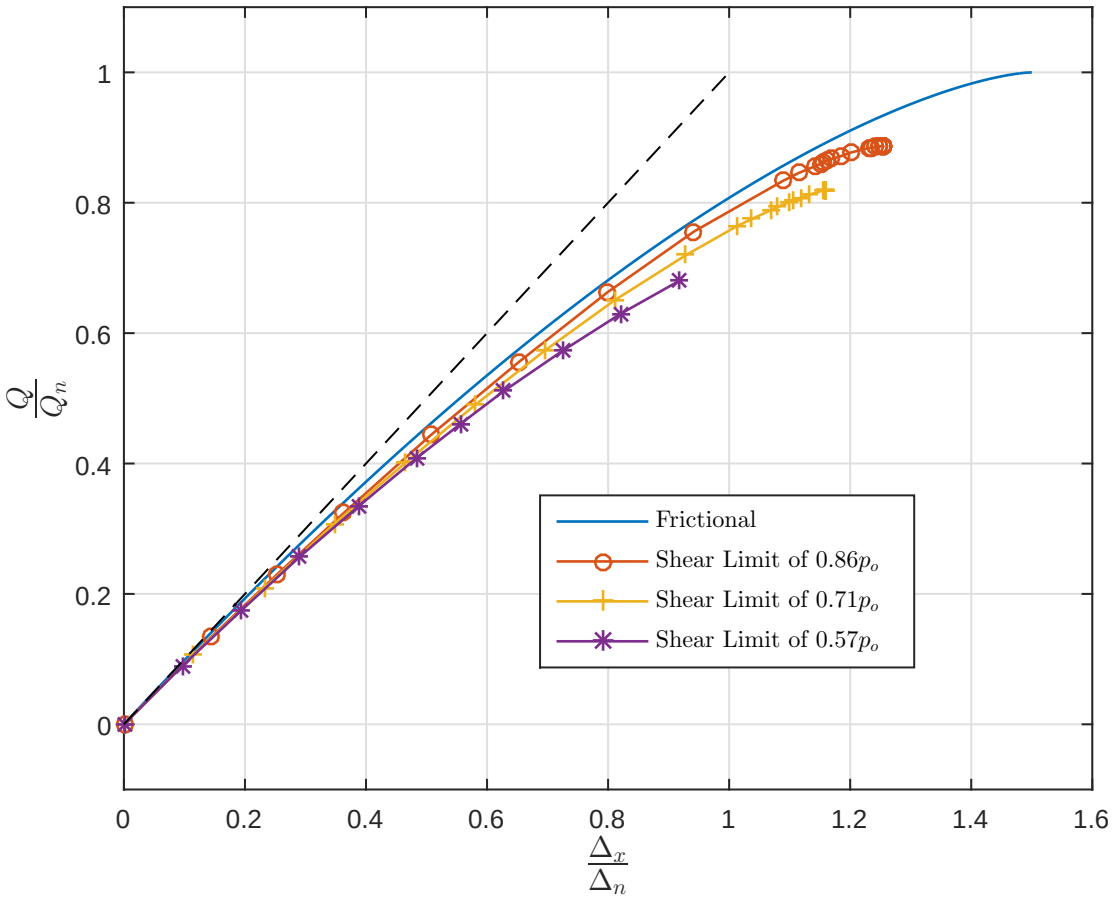

Figure 3.6: Normalised tangential load and normalised tangential relationship for the models with shear limit contact laws with different shear limits and the relationship for the frictional contact. The reference load, Q_n, for the frictional case is given by equation (3.4) and in the shear limit cases are given by equation (3.9). The reference displacement, Δ_n, for both cases are given by using the reference load in equation (3.3).

3.2.2 Elastic Perfectly Plastic Asperity Modelling

The asperity and the block of same dimensions and boundary conditions as in the elasticity models (see Figure 3.2) with an elastic perfectly plastic material law are modelled with displacement loading. The contact is taken to be fully stuck. Both the asperity and the block have a Young's modulus of 2×10^6 N/mm^2 and Poisson's ratio of $\nu = 0.3$. Models were run for different yield limits (von Mises criteria), σ_y, of 5000, 4000, 3000, and 2000 N/mm^2. The stress strain relationship for an elastic perfectly plastic material law is given schematically in Figure 3.7. A mesh of similar density near the contact interface as used in the elastic models was used. Both the asperity and the block were discretized quadratic tetrahedral C3D10I elements. A total of 102,939 elements were used. Initial models with less dense mesh were constructed. Mesh density was increased till convergence in the results was observed.

A normal displacement of 0.015 mm is applied to the top surface of the asperity and then tangential displacements are applied of up to 0.01 mm. The contact during the application of both normal loading and tangential loading is modelled as 'rough', i.e. fully stuck. $p_o = 8568.1$ N/mm^2, where p_o is defined as the Hertzian maximum normal pressure after the application of the remote normal displacement for a purely elastic model of the same geometry and boundary conditions.

For a Hertzian (i.e. purely elastic) model of the sphere indenting on a half-space, on the basis of either the Tresca or von Mises yield yield criterion, the first point of yielding will lie on the z-axis at $z/r_c = \pm 0.48$, when $\nu = 0.3$. The maximum shear stress is found to be $0.31p_0$, and therefore the maximum Tresca stress is $0.62p_0$. The maximum von Mises stress, σ_v, is also found to be $0.62p_0$. Yielding will occur during the normal loading step in the elastic perfectly plastic models if $\sigma_y < \sigma_v$. The yield limits can be expressed in terms of σ_v, to give an indication of the extent of yielding that has occurred before tangential loading has been applied. The yield limits expressed this way are $0.93\sigma_v$, $0.74\sigma_v$, $0.56\sigma_v$, and $0.37\sigma_v$. In all four cases, yielding has occurred before the application of tangential loading.

To normalise the tangential load applied to the asperity, reference load, Q_n, for the elastic perfectly plastic models is defined as

$$Q_n = \sigma_y \pi r_c^2, \tag{3.10}$$

where r_c is the Hertzian contact radius after the application of the normal displacement for a purely elastic model with the same dimensions. As in the previous models, Δ_n, the reference displacement, is defined using Q_n in equation (3.1).

The relationship between $\frac{\Delta_x}{\Delta_n}$ and normalised tangential load for the elastic perfectly plastic

models is given in Figure 3.8. The relationship for the theoretical Mindlin frictional elastic model is shown in Figure 3.8, as is the relationship for a fully stuck elastic model. The reference tangential load, Q_n, and reference displacement, Δ_n, for the frictional model is given by equations (3.4) and (3.3). (In the fully stuck case, Q_n is any arbitrary load such that reference tangential displacement, Δ_n, is the tangential displacement at Q_n. It can be shown, by equation (3.1), that $Q/Q_n = \Delta_x/\Delta_n$ for a fully stuck elastic contact.)

Of interest, the expression for the fully stuck elastic model is seen to be a reasonable approximation of the normalised relationship for the plastic models with the normalisation used here (which depends on contact radius). The normalised relationship for frictional elastic contacts given in equation (3.5) is also seen to be a reasonable approximation for the the normalised relationship for elastic perfectly plastic interfaces, i.e provided the Q_n and Δ_n values used in the expression are the reference values defined here for elastic perfectly plastic interfaces.

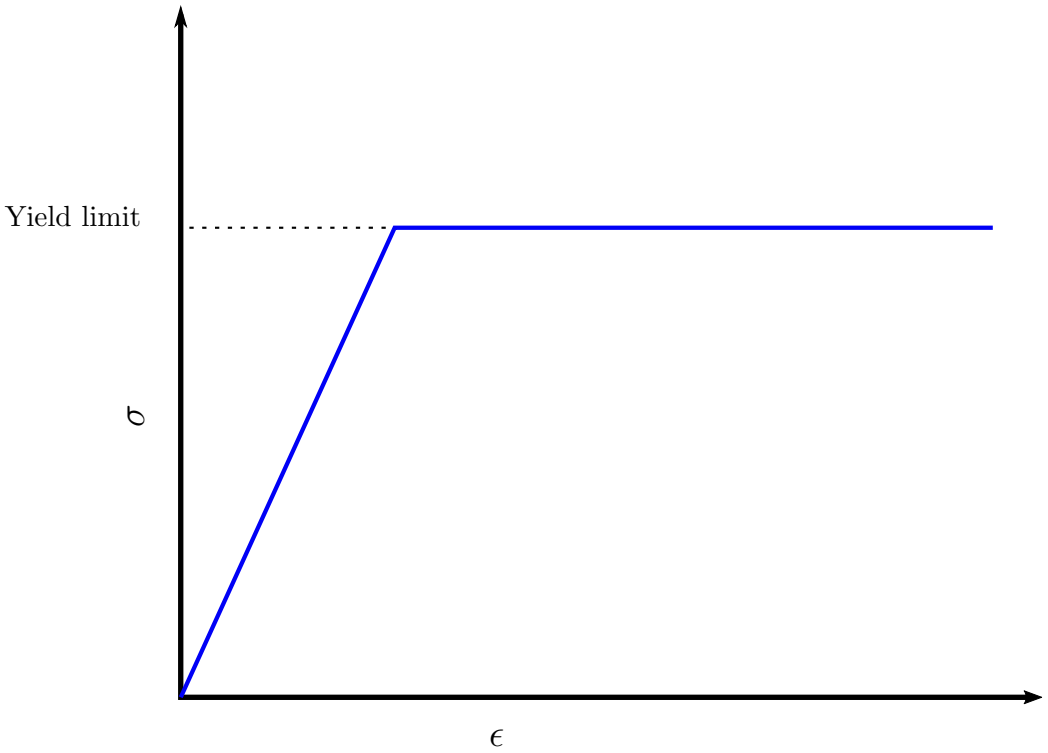

Figure 3.7: The stress strain curve for an elastic perfectly plastic material.

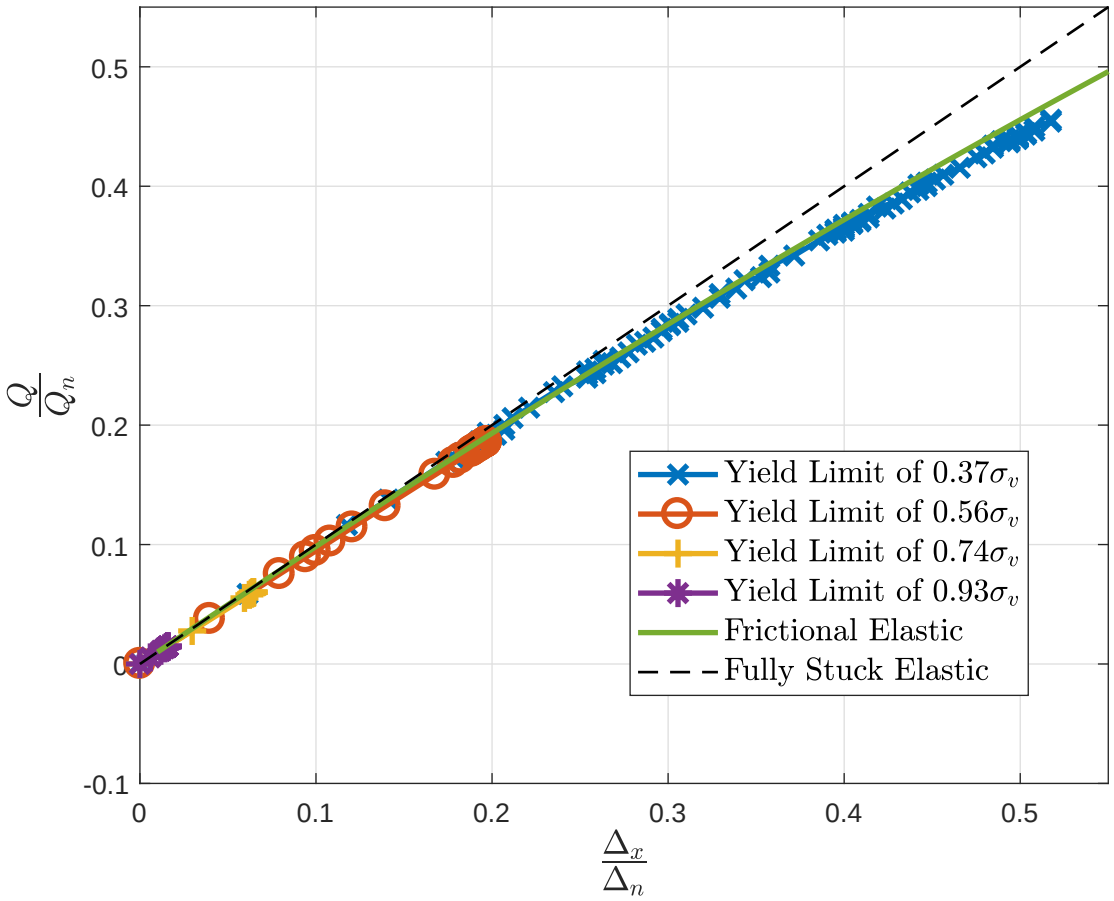

Figure 3.8: Normalised tangential load and normalised tangential displacement for an elastic stuck contact interface, an elastic perfectly plastic stuck interfaces with different yield limits, and a frictional elastic interface. The reference load, Q_n, for stuck elastic contacts can be any arbitrary load. The reference loads for elastic perfectly plastic models are given by equation (3.10) and for the frictional elastic contact is given by equation (3.4). The reference displacement, Δ_n, values for all models are given by equation (3.3) using the values for the respective reference load, Q_n.

3.3 Multi-asperity Models

3.3.1 Tangential Behaviour due to Different Asperity Load Distributions

The relationship between tangential load and tangential remote displacement is modelled for multiple asperities in contact for different normal asperity load distributions. In real interfaces due to asperity height differences, the interpenetration at the asperity contacts vary and so does the normal load carried by each asperity. There is hence a need to explore the effect of different asperity load distributions on the tangential behaviour of contact interfaces.

Consider a rigid body with several independent spherical elastic asperities, all with the same radii of curvature, in contact with a similar body with elastic asperities, perfectly aligned, on a fixed rigid base with Coulomb frictional interfaces. See Figure 3.9. The normal load on each asperity is $-P_i$ where

$$i = 1, 2, ...m.$$

If n_i is the number of asperities with $-P_i$ normal loading, the total normal load, $-P_t$ is given by

$$P_t = \sum_{1}^{m} n_i P_i.$$

Further, r_i is the contact radius of the asperity under a load of $-P_i$. From equation 4.22 of [49, p. 93],

$$\frac{r_i}{r_m} = \left(\frac{P_i}{P_m}\right)^{1/3}. \tag{3.11}$$

The rigid base of one of the bodies is displaced tangentially by Δ_x with respect to the contact interface by the application of tangential load of Q_t (say the base of the other body is kept fixed). The reference displacement, Δ_n, is defined as

$$\Delta_n = \frac{fP_m}{8r_m}\left(\frac{2-\nu}{\mu}\right). \tag{3.12}$$

It is the relative tangential displacement of a remote point away from the contact interface of an asperity subject to the highest normal load, $-P_m$, if the contact is fully stuck and subject to a tangential load of fP_m. Asperities that were loaded with normal load of $-P_i$ experience shear loads of Q_i magnitude. For asperities in partial slip, from equation (3.2)

$$\frac{\Delta_x}{\Delta_n} = \frac{3}{2}\left(\frac{P_i}{P_m}\right)\left(\frac{r_m}{r_i}\right)\left(1-\left(1-\frac{Q_i}{fP_i}\right)^{2/3}\right), \tag{3.13}$$

which gives using equation (3.11)

$$\frac{Q_i}{f} = P_i \left[1 - \left(1 - \frac{\Delta_x}{\Delta_n} \frac{2}{3} \left(\frac{P_m}{P_i} \right)^{\frac{2}{3}} \right)^{\frac{3}{2}} \right]. \tag{3.14}$$

For asperities that have fully slipped

$$\frac{Q_i}{f} = P_i. \tag{3.15}$$

It can be shown from equation (3.14) that for a given Δ_x displacement, slip occurs on asperities with normal loads $-P_i$ such that

$$\frac{\Delta_x}{\Delta_n} \frac{2}{3} \left(\frac{P_m}{P_i} \right)^{\frac{2}{3}} \geq 1.$$

This criteria is used to determine whether to use equation (3.14) or (3.15) to determine the $\frac{Q_i}{f}$ value for the asperities with $-P_i$ normal loading. The total shear load applied will be given by

$$Q_t = \sum_{1}^{m} n_i Q_i.$$

This implies the normalised total shear load (normalised with respect to load for full slip, fP_t,) is then given by

$$\frac{Q_t}{fP_t} = \frac{\sum_{1}^{m} n_i \frac{Q_i}{f}}{\sum_{1}^{m} n_i P_i}. \tag{3.16}$$

From equations (3.14) (3.15) and (3.16), it can be seen that for a given $\frac{\Delta_x}{\Delta_n}$ the normalised shear load is friction independent and varies only with the P_i and n_i values.

The relationship between tangential displacement Δ_x and Q_t are found for different distributions of asperity normal loads, P_i. The loads used are

$$P_i = \frac{i}{m} P_m$$

In each model the number of asperities, n_i, with a load P_i is varied according to a distribution law of this form

$$n_i = Cg(i),$$

where C is a constant. The number of asperities are determined so that the total normal load is the same for each model, i.e. $\frac{P_t}{P_m}$ is fixed. To ensure this, C varies for each model and can be shown

to given by

$$C = m\frac{P_t}{P_m}\left(\frac{1}{\sum_i^m g(i)i}\right).$$

Table 3.1 shows the asperity load distribution laws used in each model. The slopes of the normalised

	Model Distribution Law	n_i	$g(i)$
1	Uniform	$n_i = C$	$g(i) = 1$
2	Linearly Increasing Distribution	$n_i = Ci$	$g(i) = i$
3	Linearly Decreasing Distribution	$n_i = C(m+1-i)$	$g(i) = m+1-i$
4	Exponentially Increasing Distribution	$n_i = Ci^2$	$g(i) = i^2$
5	Exponentially Decreasing Distribution	$n_i = C(m+1-i)^2$	$g(i) = (m+1-i)^2$

Table 3.1: The asperity load distributions used.

shear load and normalised displacement relationships at low loads for each model can be found noting that as $\frac{\Delta_x}{\Delta_n} \to 0$, $Q_t \to Q_{st}$, where Q_{st} is the shear load applied for a tangential displacement of Δ_x when all the asperities are stuck. From equation (3.1)

$$\Delta_x = \frac{Q_{st}^i(2-\nu)}{8\mu r_i}, \tag{3.17}$$

where Q_{st}^i is the shear load applied to asperities with normal load of $-P_i$ when fully stuck. Keeping the definition of the reference displacement, Δ_n, the same, using equation (3.12) with the above equation

$$\frac{\Delta_x}{\Delta_n} = \frac{Q_{st}^i}{fP_m}\frac{r_m}{r_i}. \tag{3.18}$$

This leads to (with equation (3.11))

$$\frac{Q_{st}^i}{f} = \frac{\Delta_x}{\Delta_n}P_m\left(\frac{P_i}{P_m}\right)^{\frac{1}{3}}. \tag{3.19}$$

The total shear load applied is therefore given by

$$\frac{Q_{st}}{f} = \frac{\Delta_x}{\Delta_n}P_m\sum_i^m\left(\frac{P_i}{P_m}\right)^{\frac{1}{3}}n_i. \tag{3.20}$$

When normalised with respect to P_t, this becomes

$$\frac{Q_{st}}{fP_t} = \frac{\Delta_x}{\Delta_n}\left(\frac{P_m}{P_t}\sum_i^m\left(\frac{P_i}{P_m}\right)^{\frac{1}{3}}n_i\right). \tag{3.21}$$

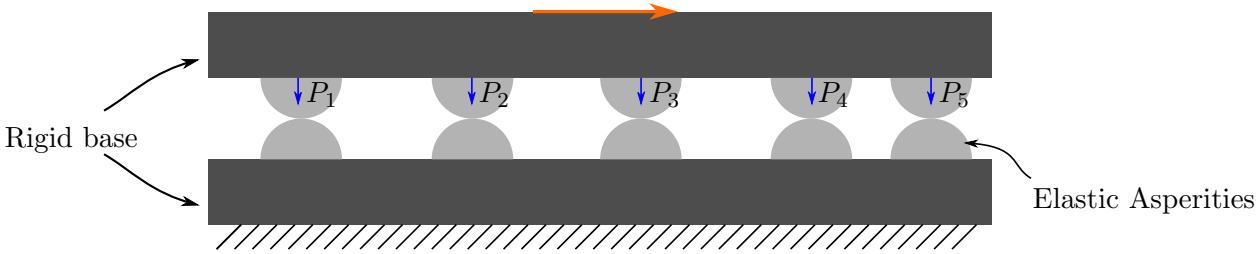

Figure 3.9: Schematic representation of the model. Elastic asperities on a rigid base are in contact with similar elastic asperities on a rigid base. Different normal loads are applied to different asperities. Base of one of the surfaces is fixed, while tangential displacement is applied to the rigid base of the other surface.

Since, $Q_t \to Q_{st}$ at low shear loads in the frictional case, for low loads

$$\frac{Q_t}{fP_t} \approx \frac{\Delta_x}{\Delta_n}\left(\frac{P_m}{P_t}\sum_i^m \left(\frac{P_i}{P_m}\right)^{\frac{1}{3}} n_i\right). \tag{3.22}$$

Therefore the initial slope of the load-displacement relationship for each model is given by

$$S(n) = \left(\frac{P_m}{P_t}\sum_i^m \left(\frac{P_i}{P_m}\right)^{\frac{1}{3}} n_i\right). \tag{3.23}$$

To plot the relationship between shear load and displacement so that the curves all have the same initial slope, $\frac{Q_t}{fP_t}$ is plotted with $\frac{\Delta_x}{\Delta_n}S(n)$. See Figure 3.10. For each model, $\frac{Q_t}{fP_t}$ relationship with $\frac{\Delta_x}{\Delta_n}$ value is found from equations (3.14) (3.15) and (3.16), and the $S(n)$ value is found from equation (3.23). For the models plotted, $m = 100$ and $\frac{P_t}{P_m} = 100$. Further in Figure 3.10 the relationship is plotted for a single asperity subjected to the total normal load, $-P_t$, and total shear load, Q_t, using equation (3.5) with $Q_n = fP_t$. ($S(n)$ for a single asperity is equal to 1.). The relationship for a single stuck asperity is plotted as well, which gives the initial slope for all the curves.

The curves found for all the models with different asperity distributions are seen to be similar to that for the single asperity. This implies for low loads, an approximate relationship between the normalised shear load and normalised tangential displacement relationship for multi-asperity interface for a variety of asperity load distributions can be found with equations (3.5) and (3.23).

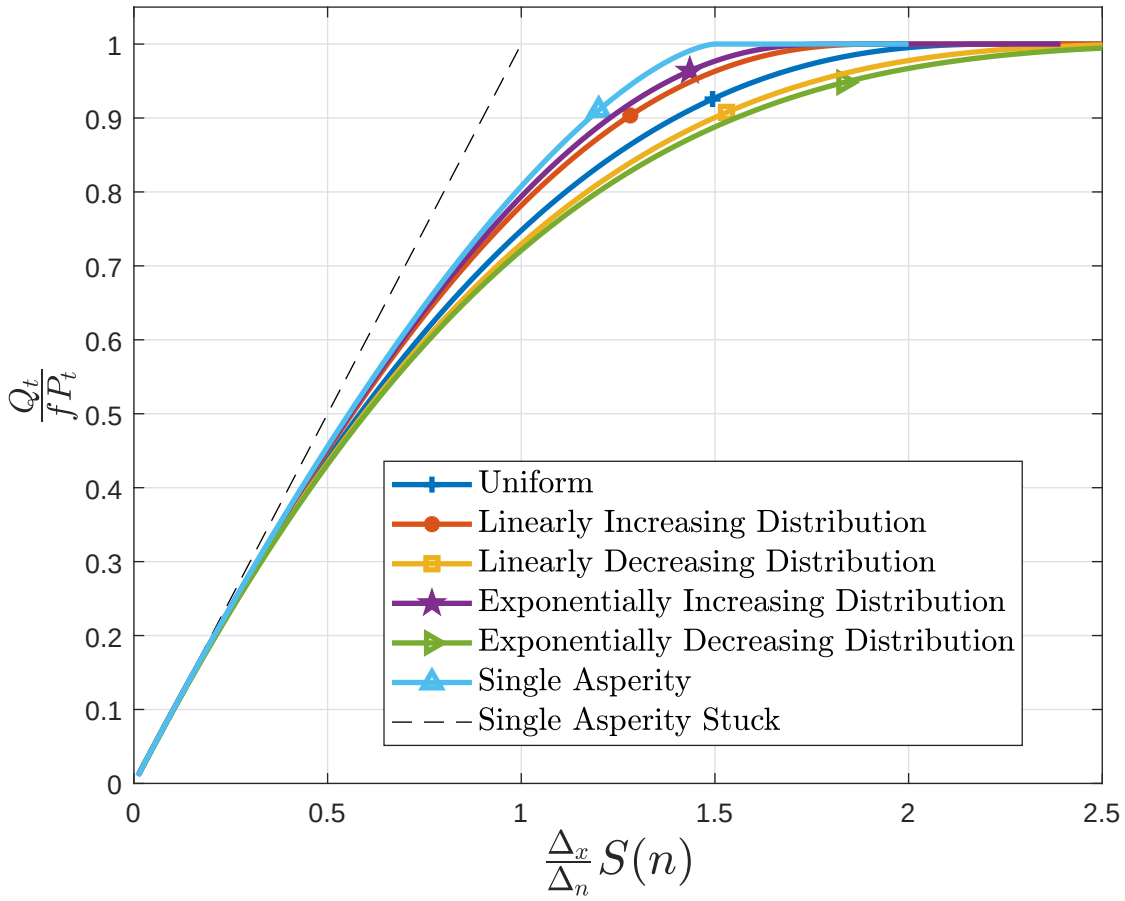

Figure 3.10: Normalised tangential load, given for each model by equation (3.23), versus normalised tangential displacement multiplied by the $S(n)$ parameter. Plots are for different asperity load distributions. The relationship for a single asperity is also plotted using equation (3.5) and is seen to be similar to that for the different multi-asperity models. This implies equations (3.5) and (3.23) can be used to estimate this relationship for a variety of asperity load distributions for multi-asperity interfaces.

3.3.2 Multi-asperity Model with Asperity Interaction for Normal Stiffness Calculation

In §3.3.1, the asperities were modelled as if they were on a rigid substrate and independent of each other. The displacement of one asperity is not affected by the loading on other asperities. Further, published asperity models to study contact stiffness properties, such as Medina et al., do not take into account asperity interaction [4]. There is hence a need to understand contact stiffness properties when asperity interaction is permitted. In this section elastic asperities on an elastic half-space interfacing with other elastic asperities on a half-space are modelled to calculate the normal stiffness properties of the interface. The effect of loading on other asperities is taken into account when calculating the displacement at each asperity. However, the change in loading due to the displacement at different asperities is neglected– the loading at each asperity is assumed to remain Hertzian. A basic model is derived, and the approach can be used as the basis for more comprehensive models.

Normal displacement components due to loading at an asperity

In this subsection, an expression for the normal displacement component of the centre of an asperity due to loading on that asperity is found, as well as an expression for the normal displacement component due to loading elsewhere on the half-space, such as at another asperity location. The total displacement of the centre point of an elastic asperity due to loading at several different asperity locations can be determined from these expressions.

When two elastic asperities are in contact and loaded by normal load, $-P$, the displacement of points within the contact area with respect to a remote point deep inside the half space is given by Hertz [49, p 61]

$$u_z(r) = \left(\frac{1-\nu^2}{E}\right)\frac{\pi p_0}{4r_c}(2r_c^2 - r^2) \qquad r \leq r_c \tag{3.24}$$

where r_c the contact radius, which depends on the relative curvature, the normal load and the elastic material properties. The displacement of the centre point ($r = 0$) of the contact area, taking $p_0 = \frac{3P}{2\pi r_c^2}$, is hence

$$u_z(0) = \left(\frac{1-\nu^2}{E}\right)\frac{3P}{4r_c}. \tag{3.25}$$

Reference load P_d and reference length D are defined such that $-P_d$ is the load required for a contact radius $r_c = D$. From Hertz's equations

$$r_c = D\left(\frac{P}{P_d}\right)^{\frac{1}{3}}.$$

Equation (3.25) becomes

$$u_z(0) = \left(\frac{1-\nu^2}{E}\right)\frac{3P}{4D\left(\frac{P}{P_d}\right)^{\frac{1}{3}}},$$

$$u_z(0)\left(\frac{E}{1-\nu^2}\right)\left(\frac{D}{P_d}\right) = \frac{3}{4}\left(\frac{P}{P_d}\right)^{\frac{2}{3}}. \tag{3.26}$$

The displacement of a point external to the contact area on the surface with respect to the remote point due to the normal pressure transmitted through the contact interface is given by [49, p 61]

$$u_z(r) = \left(\frac{1-\nu^2}{E}\right)\frac{p_0}{2r_c}r^2\left[\left(\frac{2r_c^2}{r^2}-1\right)\arcsin\left(\frac{r_c}{r}\right)+\left(\frac{r_c}{r}\right)\left(1-\frac{r_c^2}{r^2}\right)^{\frac{1}{2}}\right].$$

Using reference variables and putting $p_0 = \frac{3P}{2\pi r_c^2}$,

$$u_z(r)\left(\frac{E}{1-\nu^2}\right)\left(\frac{D}{P_d}\right) = \frac{3}{4\pi}\frac{r^2}{D^2}\left[\begin{array}{c}\left(\frac{2D^2}{r^2}\left(\frac{P}{P_d}\right)^{2/3}-1\right)\arcsin\left(\frac{D}{r}\left(\frac{P}{P_d}\right)^{1/3}\right)+\\ \left(\frac{D}{r}\left(\frac{P}{P_d}\right)^{1/3}\right)\left(1-\left(\frac{D^2}{r^2}\left(\frac{P}{P_d}\right)^{2/3}\right)\right)^{1/2}\end{array}\right]. \tag{3.27}$$

Equations (3.26) and (3.27) hence give displacement of points on the contact interface due the normal load transmitted via a single asperity.

Fixed grid model

A square array of asperities on an elastic half-space are in contact with a similar grid of elastic asperities on a half-space (the analysis is the same if the second surface is rigid or an elastic half space). There are N by N asperities in the grid of length of D, which shall be used as the reference length. See Figure 3.11 for a sample grid with $N = 3$. The total force, $-P_t$, is taken to be evenly distributed among N^2 asperities. In this model, the relationship between the total normal load applied and the displacement of the the centre of the square grid contact interface is found, for different asperity concentrations. Taking N as an odd number ensures there is an asperity at the centre of the grid, implying the relative displacement of the centre-point is a measure of the compliance across the interface.

$-P_a$, the load acting on each asperity is given by $P_a = \frac{P_t}{N^2}$. The total displacement of the centre point of the centre asperity is found by summing the displacement component due to its

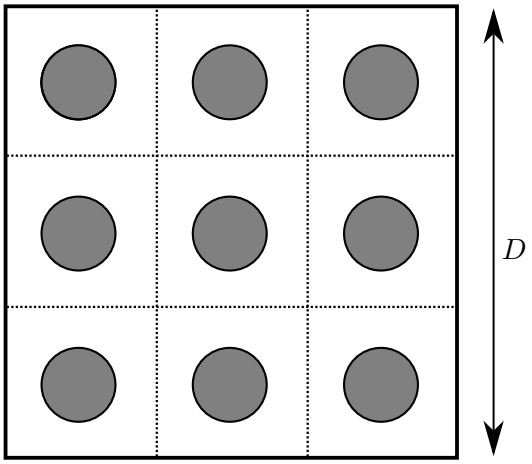

Figure 3.11: A square grid of N by N asperities with $N = 3$. Total length of the grid is D.

own loading, using equation (3.26), and the displacement components due to loading at the other asperities in the grid, using equation (3.27).

The contact radius for each asperity is given by

$$\frac{r_c}{D} = \left(\frac{P_t}{P_d}\right)^{1/3} \frac{1}{N^{2/3}}.$$

(The contact radius is taken to remain Hertzian on all the asperities). The total real contact area to the apparent contact area is therefore

$$\frac{A_{real}}{A_{apparent}} = \pi \left(N \frac{P_t}{P_d}\right)^{2/3}. \tag{3.28}$$

(The area of the grid is D^2). To ensure the asperities don't overalap

$$\frac{2r_c}{D/N} = \frac{2r_c N}{D} \leq 1,$$

implying

$$\frac{2r_c N}{D} = 2N^{1/3} \left(\frac{P_t}{P_d}\right)^{1/3} \leq 1,$$

or

$$\frac{P_t}{P_d} \leq \frac{1}{8N}.$$

It can be shown from above equations that to avoid overlap

$$\frac{A_{real}}{A_{apparent}} \leq \frac{\pi}{4} \approx 0.79.$$

When $N \to \infty$, it is expected that the normal displacement of the centre point of the centre asperity, u_{cen}, will approach the displacement of the centre point of square grid of dimensions D by D loaded by uniform pressure, $p_o = P_t/D^2$. The displacement of the centre of a square patch of pressure distribution, u_r, is given (equation 11.20 in [3]) by

$$u_r \frac{2\pi\mu}{(1-v)p_0} = 2B \ln\left(\frac{\tilde{R}+A}{\tilde{R}-A}\right) + 2A \ln\left(\frac{\tilde{R}+B}{\tilde{R}-B}\right),$$

where $\tilde{R}^2 = A^2 + B^2$. In this case, $A = B = D/2$ and $\mu = \frac{E}{2(1+\nu)}$. So

$$u_r \left(\frac{E}{1-\nu^2}\right) D = \frac{2}{\pi} P_t, \ln\left(\frac{\sqrt{2}+1}{\sqrt{2}-1}\right),$$

which leads to

$$\begin{aligned} u_r \left(\frac{E}{1-\nu^2}\right) \frac{D}{P_d} &= \frac{2}{\pi} \frac{P_t}{P_d} \ln\left(\frac{\sqrt{2}+1}{\sqrt{2}-1}\right) \\ &\approx 1.1222 \frac{P_t}{P_d}. \end{aligned} \tag{3.29}$$

Figure 3.12 shows normalised displacement of the centre point of the grid, $\frac{u_{cen}}{u_r}$, for normalised loads $\frac{P_t}{P_d}$ of 0.00125 and 0.025, for different N. It is seen that for both values of normal load, the displacement $\frac{u_{cen}}{u_r}$ approaches 1 for $N > 9$. The relationship between normalised load to normalised displacement of the centre point of the grid is given in Figure 3.13 for grids with different N. For a given N and loading $\frac{P_t}{P_d}$, the real area to apparent contact area ratio can be found from Figure 3.14, which was constructed using Equation (3.28). The stiffness of the interface across the centre point for a given contact area to apparent area ratio for grids with different N can be found using Figure 3.15. The slope ($\frac{dP_t}{du_{cen}}$ values) of the curves in Figure 3.13 were used to determine the normal contact stiffness values. (In this study, contact displacement is defined as half the relative approach of the two bodies in contact).

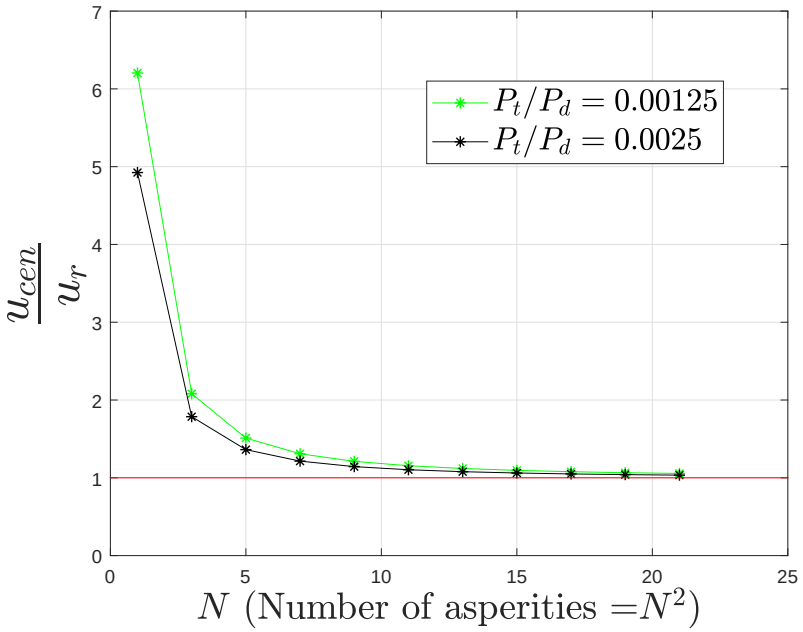

Figure 3.12: Ratio of the displacement of centre point of the grid with asperities to that for a smooth contact with constant pressure, with increasing number of asperities, for two different total normal load values. For the chosen loads it is seen that centre point displacement approaches that for the constant pressure patch for when $N > 9$.

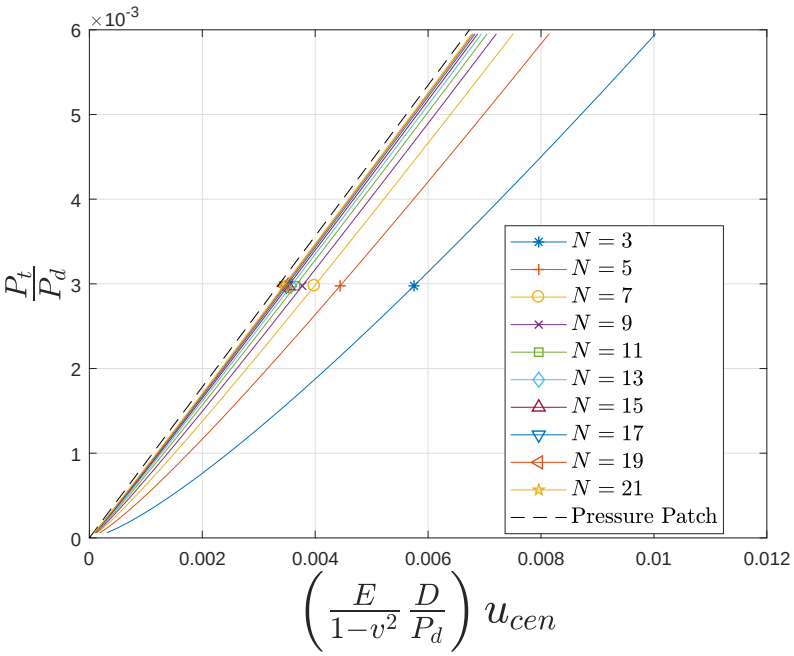

Figure 3.13: The relation between applied normalised normal load and normalised displacement of the centre point of the grid, for different N. The relationship approaches that for uniform pressure applied in the grid area for large N.

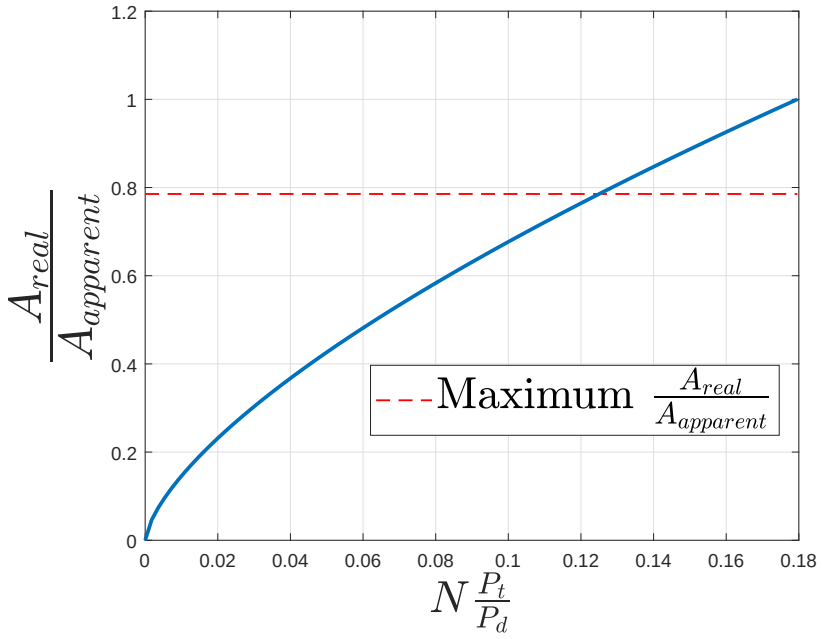

Figure 3.14: The ratio of the real contact area to the nominal contact area for given normalised normal load and N value for the fixed grid model. Dotted line represents the maximum area ratio permitted, before contact spots overlap.

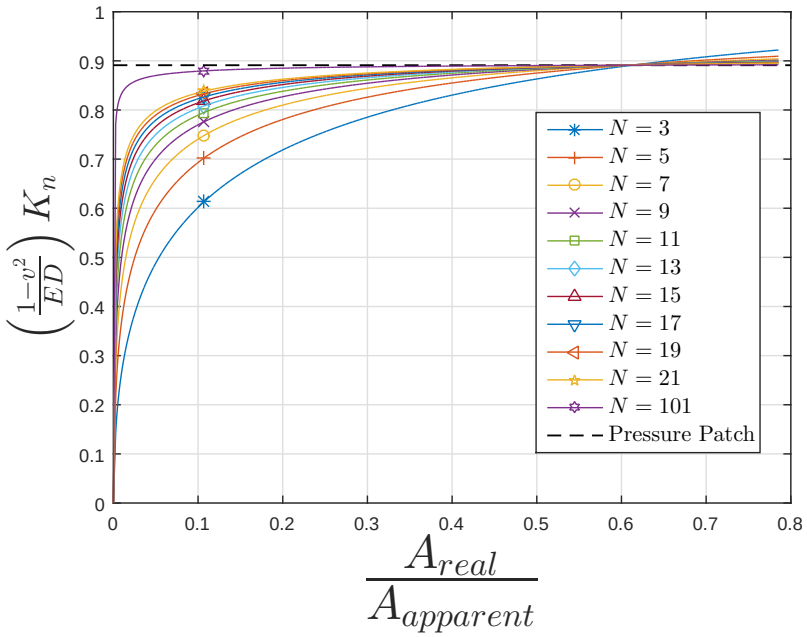

Figure 3.15: Normal contact stiffness for a given real to apparent area ratio and different N. This plot can be used to estimate the normal contact stiffness when the number of asperity contacts and the real to apparent area ratio is known.

Expanding Grid Model

In §3.3.2, the grid dimensions were kept constant for all N. Alternatively a similar model can be constructed with the dimensions of the grid are taken proportional to N. In this model the width of the unit cell, $2C_u$, is fixed. Further the load on each asperity is $-P_a$. The total load, $-P_t$, is hence given by

$$P_t = N^2 P_a$$

C_u is the reference length. And $-P_c$ is defined as the load for contact radius of the asperity $r_c = C_u$. So

$$r_c = C_u \left(\frac{P_a}{P_c}\right)^{\frac{1}{3}}.$$

C_u is related to the length of the grid, D, the reference length used in the fixed grid model, by $C_u = D/2N$. Also, reference load P_c is related to P_d by

$$P_c = \frac{P_d}{8N^3}.$$

It can be shown that (in a similar process as provided in §3.3.2)

$$\frac{A_{real}}{A_{apparent}} = \frac{\pi}{4}\left(\frac{P_a}{P_c}\right)^{2/3}$$

Displacement of the centre point of the grid, u_{cen}, is found as before with Equations (3.26) and (3.27), modified with new reference parameters, for different real contact area to apparent contact area ratios for different N. The slope of the total load and the displacement of the centre point u_{cen} relationship is found and plotted in normalised form in Figure 3.16. The curves in Figure 3.16 are identical to the curves in Figure 3.15, with $D = 2C_u N$, indicating both approaches provide the same relationship for normal contact stiffness with the number of asperity points and the real to apparent area ratio.

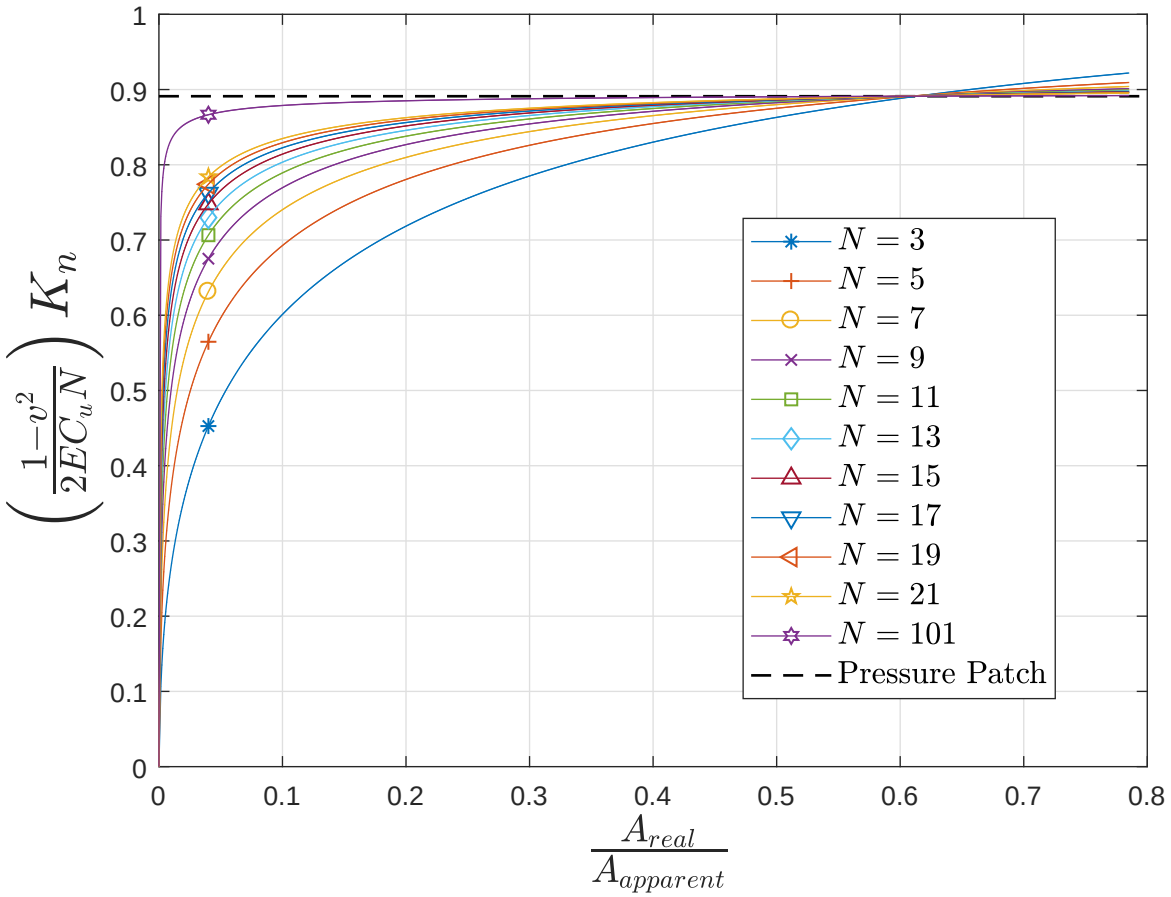

Figure 3.16: Normal contact stiffness relationships with real to apparent contact area ratio for different N, derived from the expanding grid model. The plot is identical to that derived from the fixed grid model and presented in Figure 3.15.

Discussion

The first grid model kept the grid length fixed irrespective of the number of asperity contact points, and the second grid model expanded the size of the grid in proportion with increasing number of asperities. Both approaches yielded the same relation between normal contact stiffness and real to apparent contact area ratio.

The results provide a means to estimate the contact stiffness for a given number of asperity contacts and normal load for contact between two elastic surfaces in contact, such as by using Figures 3.14 and 3.15 from the fixed grid model. For real surfaces N can be taken to be the square root of the number of asperity contacts. Alternatively, if N is unknown, the normal contact stiffness can be found provided the real to apparent contact ratio and the normal load values are known. The normal contact stiffness is seen therefore to depend on the length of the grid, the number of asperity contacts, and the normal load. For a high number of asperity points, the stiffness across the contact approaches that of smooth contact with uniform pressure. Figure 3.14 shows that real contact area increases with N for a given normal load. Values for contact stiffness in Figure 3.15 are only plotted for real to apparent contact area ratio of 0.79 since at that ratio the asperities overlap and the assumptions of the model break down. Models with higher values of N approached the smooth contact stiffness value for lower values of real contact area as seen in Figure 3.15.

Interestingly, according to Figure 3.15, the normal contact stiffness of the central asperity becomes greater than that for the central point of a smooth contact with equivalent constant pressure applied over the nominal area of the grid, when the real to nominal contact area of the rough interface is around 0.6. This is when the real to nominal contact area ratio at which an interface involving a grid of only 9 asperities ($N = 3$) becomes stiffer at the central point than a smooth interface with constant pressure. The plot indicates that with greater number of asperities the stiffness of the central asperity reduces for real to nominal contact ratios greater than 0.6, and, given the observed trend, it is expected for when $N \to \infty$, it will approach that for the central point of the smooth interface with constant pressure loading.

While the model can be used to estimate normal contact stiffness for a given load and number of asperity points (or the real to apparent contact area ratio), the model however can not directly predict the evolution of contact stiffness for real rough surfaces with normal load. This is because for real contacts with the application of normal load the number of asperity points will increase. Furthermore in real interfaces the loading on the asperities may not be equally distributed as it is assumed in this model. In addition, while the displacements of the asperity contacts in the z direction were permitted to be affected by the loading on all asperities, the contact radius and the loading at each asperity was taken to remain Hertzian, i.e. unaffected by the loading at other

asperity locations.

The limitations of this model (and of the results plotted in Figure 3.15) are therefore as follows

1. The model breaks down as the asperities move closer to each other, i.e. as the real to nominal contact area becomes large. This is because the loading at each asperity can no longer be assumed Hertzian, when the asperities are not sufficiently spaced.

2. The model assumes each asperity has similar radius of curvature and height and that the asperities are organised in a regular grid.

3. Effects due to plasticity are neglected, since this is an elastic model.

A more refined model could take into account asperity loads that are distributed according to an appropriate probability function (such as on the basis of the height distribution of asperities found in real surfaces), and the change in the number of asperity points with normal loading. A future analysis could also investigate the effect of loading on all asperity points on the load distribution at each asperity (i.e. non-Hertzian pressure distributions at each asperity contact will need to be used), and the effect of plasticity.

3.4 Conclusion

The two single asperity models showed that the normalised relation for a frictional elastic asperity contact between tangential load and tangential displacement, given in equation (3.5), can be used to approximate the relationship when the asperity contact law is changed and when plasticity is allowed, provided the reference parameters as defined in this chapter are used. This suggests a model of a rough interface with frictional elastic asperities can be modified straightforwardly, with simple multipliers on some terms, to take into account effects due to plasticity and non-Coulomb contact behaviours.

The first multi-asperity model, of §3.3.1, demonstrated that the normalised tangential load and tangential displacement relationship for multi-asperity elastic frictional interfaces for different asperity load distributions can be estimated with the relationship for a single asperity modified by a simple multiplier term that depends on the load distribution function. Future work can use this result to find the relationship for real interfaces, when real asperity load distributions are known.

The second multi-asperity model, of §3.3.2, modelled elastic rough contacts when asperity interaction is allowed. The basic model provides a means to estimate the normal contact stiffness values for elastic surfaces in contact for a given normal load when the number of asperity contact points are known.

Part III

Analysis of Receding Contacts

Chapter 4

Introduction to Receding Contact Analysis

4.1 Introduction

Receding contacts are an important class of contacts found in many components, including bolted joints, for which the contact area reduces with the application of any finite normal load. The reduction in many cases is non-continuous, — with the application of any finite normal load, however small, the contact surfaces snap into a new configuration with a reduced contact area. This was shown to be the case for frictionless elastic receding contacts by Dundurs and Strippes [50] and the result is valid for frictional elastic interfaces when the loading is monotonic [51].

Some receding contact analysis was conducted by Keer et al and Tsai et al [52] [53] in the 1970s for smooth or frictionless interfaces. Since then though solutions for receding contacts problems with complex geometries and material properties, such as functionally graded materials, have been obtained, most studies assume frictionless interfaces or fully sliding contacts [54, 55, 56, 57, 58, 59, 60]. Only a few studies have looked at the fundamental quasi-static behaviour of frictional receding contacts taking into account slip, stick and separation. One study was by Ahn and Barber, in which a frictional receding contact between an elastic block pressed against a rigid plane by cyclic normal loading was modelled with finite elements [51]. This study showed the contact area in elastic frictional receding contacts is independent of load only during monotonic loading.

Further, Chaise et al. studied the most fundamental two dimensional frictional receding contact problem of that of an infinitely long layer pressed on a half-plane of the same linear elastic material by a line load [61]. While finite elements may be suitable for modelling some receding contact situations, convergence difficulties due to the instantaneous separation of a large number contact nodes with the application of any finite normal load, however small, makes modelling of many receding

contacts situations cumbersome and difficult to implement, particularly when the dimensions of the contacting surfaces are relatively large (such as to approximate semi-infinite interfaces), and the results when obtained may be of questionable reliability. Probably to circumvent this, Chaise et al. resorted to the distributed dislocations technique to model this contact problem. See §4.2 for a detailed explanation of this method.

The standard methods for solving the integral equations that arise from this technique require the distributed dislocations inserted to be either square-root bounded to zero or square-root singular at the end points of the region of application [62][63]. However in many receding contact problems, including the problem solved by Chaise et al., there is separation of interfaces at remote points and the required climb dislocation density should be neither square-root bounded nor square root singular at the remote end point. In the Chaise solution, square root bounded-bounded dislocation densities were inserted regardless of this limitation and the solution implied an unrealistic form of separation of surfaces at remote points.

Fundamental receding contact problems involving an infinitely long linear elastic layer of thickness c pressed on a half-plane $y \leq 0$ of the same material with a frictional interface are solved in this thesis using the distributed dislocation technique. In Chapter 5, the distributed dislocations technique is used to solve a receding contact problem for which square root bounded-bounded dislocation density distributions would be consistent with the interface displacements. The loading in this problem was contrived to ensure this. In this receding contact problem the layer is pressed onto a half-plane by constant pressure applied everywhere on the layer free surface except over a finite patch. This study demonstrated the applicability of the distributed dislocation technique to solve a receding contact problem. In Chapter 6 the problem studied by Chaise et al. is revisited and solved with a new procedure involving the insertion of a 'preformed' climb dislocation distribution with the form appropriate for remote points and by superimposing corrective bounded-bounded glide and climb dislocation distributions. This procedure ensures the contact tractions satisfy the contact conditions and the remote displacements of the interface are of the correct form and are consistent with the contact tractions. In Chapter 7, this general procedure is refined and applied to solve three further problems involving a the layer pressed on a half-plane with three different pressure distributions, thus demonstrating the robustness of the new procedure to analyse receding contact problems hitherto difficult to solve. In Chapter 8 finite element analysis is used with Abaqus CAE to solve similar problems but with finite dimensions and the results are compared with solutions obtained with the insertion of distributions of dislocations.

4.2 Distributed Dislocations Technique

One powerful method for analysing contact and crack behaviour is with distributions of dislocations. In contact problems, the two bodies are modelled as one homogeneous body with distributions of dislocations inserted at the location of the contact interface. These dislocations are not lattice defects but represent displacement discontinuities in a homogeneous material. For plane problems, two kinds of dislocations are used: climb dislocations are inserted at the location of the interface where separation occurs and glide dislocations are inserted at the locations of slip. The magnitude of the climb dislocation density inserted at a point equals the differential of the separation of the interface with distance along the interface. Similarly, the magnitude of the glide dislocation density inserted at a point equals the differential of the relative slip with distance along the interface. Integration of Green's functions for unit dislocations of both types in the homogeneous body provide the stress-fields due to the presence of distributions of dislocations. The stress components along the location of the interface due to the external loading applied to the augmented body are refered to as the bilateral stress components. The total stress components at the location of the contact (i.e. the traction components) are given, by superposition principle, as the sum of the bilateral stress components and the stress components due to the distribution of dislocations applied. See Figure 4.1. Distribution of dislocations are found such that the resulting tractions and displacements satisfy the required conditions. Hills et al. provide a detailed explanation of the method [62].

For the case of a layer of thickness c in contact with a half-plane $y \leq 0$, the two bodies are modelled as an augmented half-plane $y \leq c$ with the contact interface at $y = 0$. The normal and shear stress components at a point $(x, 0)$ in the half-plane $y \leq c$ due to a dislocation with a Burgers vector (b_x, b_y) at point $(\xi, 0)$ were derived by Dundurs [64] and are given by

$$\begin{Bmatrix} \sigma_{xyd}(x,0) \\ \sigma_{yyd}(x,0) \end{Bmatrix} = \begin{bmatrix} H_{xxy}(\hat{x},\hat{\xi}) & H_{yxy}(\hat{x},\hat{\xi}) \\ H_{xyy}(\hat{x},\hat{\xi}) & H_{yyy}(\hat{x},\hat{\xi}) \end{bmatrix} \begin{Bmatrix} b_x/c \\ b_y/c \end{Bmatrix} \times \frac{2\mu}{\pi(\kappa+1)}, \tag{4.1}$$

($\hat{x} \equiv x/c$ and $\hat{\xi} \equiv \xi/c$). Here μ is the modulus of rigidity and κ is Kolosov's constant. $\kappa = 3 - 4\nu$ for plane strain and $\kappa = \frac{3-\nu}{1+\nu}$ for plane stress, where ν is Poisson's ratio. Expressions for $H_{xxy}(\cdot)$, $H_{yxy}(\cdot)$, $H_{xyy}(\cdot)$ and $H_{yyy}(\cdot)$ Green's functions are given in Appendix B.1. Note shorthand $\hat{v}$ is used in this thesis for the expression v/c, where v is any variable. The Burgers vector, b_i, at a point is related to the dislocation density, $B_i(x)$, at that point by $B_i(x)\delta x = b_i$. The stress components due to any distribution of dislocations of either type inserted along $y = 0$ can be found by integration

using equation (4.1). The distribution of dislocations of both types to be inserted are found such that the required conditions are satisfied. For frictional interfaces these conditions include the contact conditions (Signorini conditions):

1. $N(x) = S(x) = 0$, at location of separation.
2. $S(x) = \pm fN(x)$, at locations of slip.
3. $\left|S(x)\right| < \left|fN(x)\right|$, at locations of stick.

Here $N(x)$ and $S(x)$ are the total normal and shear traction components along the contact interface $y = 0$ for a point $(x, 0)$. f is the coefficient of friction. Additional conditions are determined for different problems as needed.

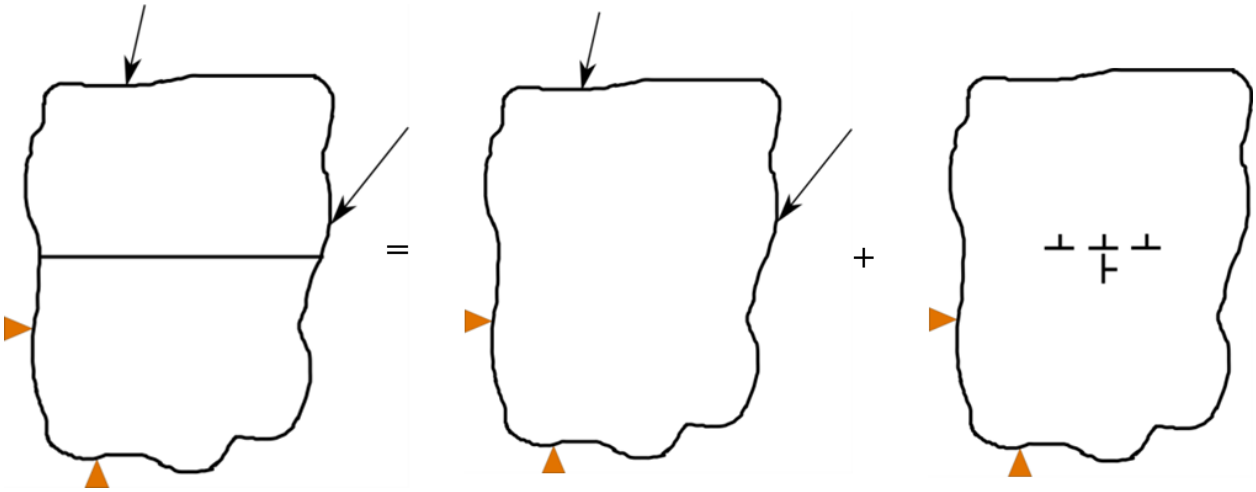

Figure 4.1: Principle of the distributed dislocations technique: the stress field due to external loading on elastic bodies in contact is equal to the sum of the bilateral stress field (that due to the external loading on the bodies if they were fused) and the stress field due to a distribution of dislocations inserted into the fused body that ensure the contact conditions are met.

4.3 Assumptions, Limitations and a Note on Validation

4.3.1 Assumptions

The solutions presented in this part of the thesis takes place in an idealised theoretical framework. The layer and the half-plane have infinite dimensions. Both the layer and the half-plane are linearly elastic and homogeneous. The interface is perfectly smooth and behaves with a Coulomb friction law and Signorini's contact conditions apply. Further the coefficient of friction is the same at all locations along the contact. Body forces are not present.

4.3.2 Limitations

The analysis of these problems proceed from first principles. Using well established linear elastic relations for the stresses and the displacements due to the external loading and the insertion of

dislocations, which model the effect of the contact, equations are written to satisfy the boundary conditions, particularly the contact conditions given above. These equations are difficult to solve analytically and solutions are found using numerical methods, such as numerical integration and some approximations are made, particularly in Chapters 6 and 7, to insert distribution of dislocations along semi-infinite regions. Numerical solutions are found using MATLAB with tools such as 'fminsearch', a built in non-linear programming solver.

Furthermore, the problem geometries studied are idealised. Real bodies in contact are finite and real interfaces are rough. In addition, real bodies in contact may be subject to body forces, such as gravity, and the material properties may not be linearly elastic nor homogeneous, particularly when significant deformations are present.

4.3.3 Note on Validation

Following the general approach of prior studies, such as the pioneering investigation by Keer et al. [52] on receding contacts[1], the analysis is presented as standalone derivations from first principles and well established formulations of linear elasticity theory. The solutions are checked whether they satisfy the boundary conditions, and in the case of Chapters 6 and 7, the remote displacements and the dislocation densities are checked to be of the expected forms.

Receding contacts are notoriously difficult to model with finite elements, due to the instantaneous separation of contact nodes even with the smallest application of normal load. Further, finite element analysis of these problems is of limited validity itself, since it is an approximate method. Some finite element modelling has been conducted for analogous loading situations for a finite strip pressed on a block. Convergence difficulties limited the geometry of the strip and the block and results were obtained only for relatively small dimensions. Nonetheless these results are compared with those from from the semi-infinite analysis, and they are provided in Chapter 8.

Given the problems studied here are semi-infinite (and not subject to body forces such as gravity), experimental validation of the analysis is not straightforward. This is not to say that the solutions or insights obtained here may not be found to be relevant in practical finite situations, which a future experimental programme could explore.

[1] See also a previous attempt of the problem studied in Chapter 6 by Chaise et al. [61]

Chapter 5

Receding Contact Analysis with Semi-Infinite Pressure Loading

5.1 Introduction

In this Chapter[1], a contact problem with a semi-infinite layer, of thickness c, in contact with a half-plane, $y \leq 0$, subject to surface pressure is solved, as shown in Figure 5.1. Both the layer and half-plane are of the same linear elastic homogeneous isotropic material.

Normal pressure, $\sigma_{yy}(x, c)$, is applied to the points (x, c) on the surface of the layer, $y = c$,

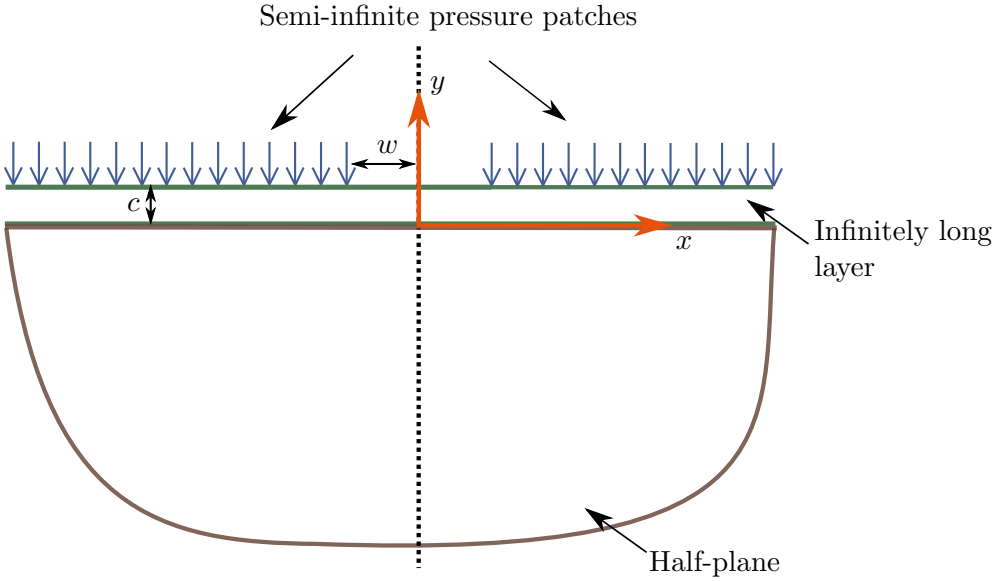

Figure 5.1: The problem geometry and loading

[1]Contents of this chapter were published in an article in the *International Journal of Mechanical Sciences*, 2016 [65].

everywhere except over a region of width $2w$, such that

$$\begin{aligned} \sigma_{yy}(x,c) &= -p, & |x| \geq w, \\ &= 0, & |x| < w. \end{aligned}$$

The origin is taken to be at the contact interface, equidistant from the two pressure patches. This problem is particularly attractive since only two parameters are involved in the problem definition — $\hat{w}$, which defines the geometry and the loading of the problem, and the coefficient of friction, f. ($\hat{w} \equiv w/c$). Further unlike the problem solved by Chaise et al. separation of points at infinite distances from the contact region do not occur and hence additional complexities required in the solution of the integral equations are avoided, i.e. bounded-bounded distributions [2] of both glide and climb dislocation densities can be inserted at the location of the contact interface to model this problem with the distributed dislocation technique. One of the primary aims in solving this problem is to demonstrate the applicability of the distributed dislocation technique to solve a frictional receding contact problem.

5.2 Solution Using Distributed Dislocations

The layer and the half-plane in contact are modelled as though they are fused as one augmented half plane, $y \leq c$, with distributions of dislocations inserted at the location of the contact interface. For values of f and $\hat{w}$ for which the tractions determined by the bilateral solution are found not to correspond to stick throughout the contact surface, a distributions of glide and if required climb dislocations are applied to regions along the $y = 0$ surface.

The bilateral solution for the traction components along the contact interface, $y = 0$, is found by the appropriate integration of the Flamant's solution for a normal line load on the half plane, $y \leq c$, over the area to which the pressure is applied in this problem. The bilateral normal and shear traction components, $\sigma_{yyb}(x)$ and $\sigma_{xyb}(x)$, that act at points $(x, 0)$ along the contact surface were thus found to be given by

[2] A bounded-bounded distribution is one which tends to zero at both end points of the area of application. Standard methods are available to find dislocation distributions that are square root singular or bounded to zero at the end points. See Hills et al. for further details [62].

$$\frac{\sigma_{yyb}(x)}{p} = \frac{1}{\pi\left((\hat{w}+\hat{x})^2+1\right)}\left[(\hat{w}+\hat{x}) - \left((\hat{w}+\hat{x})^2+1\right)\arctan\left(\frac{1}{\hat{w}+\hat{x}}\right)\right] + \frac{1}{\pi\left((\hat{w}-\hat{x})^2+1\right)}\left[(\hat{w}-\hat{x}) - \left((\hat{w}-\hat{x})^2+1\right)\arctan\left(\frac{1}{\hat{w}-\hat{x}}\right)\right], \tag{5.1}$$

$$\frac{\sigma_{xyb}(x)}{p} = \frac{1}{\pi\left((\hat{w}+\hat{x})^2+1\right)} - \frac{1}{\pi\left((\hat{w}-\hat{x})^2+1\right)}. \tag{5.2}$$

($\hat{x} \equiv x/c$ and $\hat{w} \equiv w/c$).

It is expected that the normal traction will be symmetrical and the shear traction will be anti-symmetrical with respect to the y-axis. Depending on the coefficient of friction and the $\hat{w}$ value, three possible outcomes are envisioned

1. Stick occurs everywhere along the contact interface. In this case the bilateral solution wholly satisfies the condition for stick at every point along the contact interface.

2. Slip occurs along portions of the contact interface, but separation does not occur anywhere at the interface: It is expected that there will be two regions of slip,— two on either side of the y-axis, with a stick zone at the centre. See Figure 5.2. In modelling this case, a distribution of glide dislocations is applied to portions of the contact area to satisfy the conditions for slip and stick along the interface.

3. Both slip and separation occur along portions of the contact interface: It is expected that separation and stick zones will occur at the central area of the contact interface. See Figure 5.3. In modelling this case, both climb and glide dislocations are applied along portions of the contact area to satisfy the conditions for slip, separation, and stick at points along the interface.

Equations (5.1) and (5.2) are used to find the values of $\hat{w}$ and f for which stick occurs throughout the contact interface. For the other values of $\hat{w}$ and f, expressions for the traction components due to the inserted distributions of the dislocations are found.

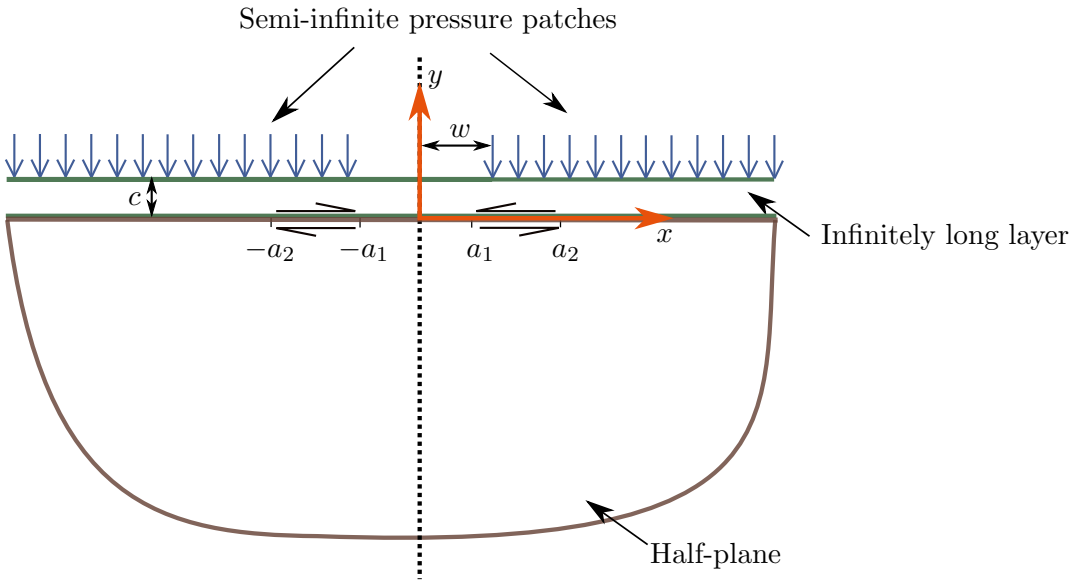

Figure 5.2: Solution in which slip but no separation occurs. Slip is expected to occur in two regions along the contact interface.

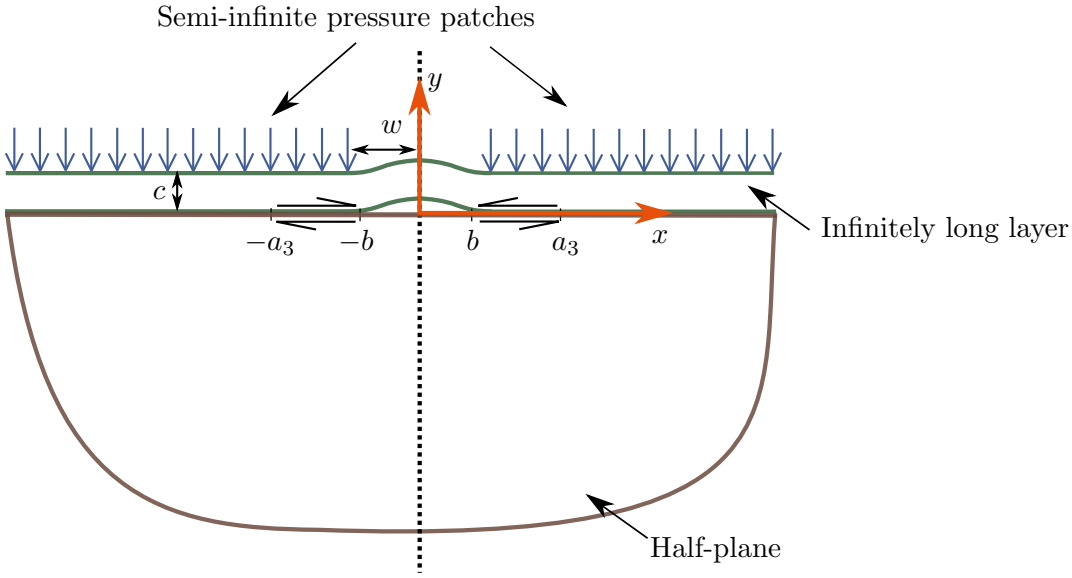

Figure 5.3: Solution in which both slip and separation occur. Separation is expected to occur at the central region of the contact interface along the interval $[-b \quad b]$ and slip is expected to occur along the contact interface along the interval $[-a_3 \quad a_3]$.

5.2.1 Slip but No Separation Case

Formulation

If the coefficient of friction is lower than that needed to maintain stick through-out, but not by a large margin, it is anticipated that there will be two slip regions, occupying the regions $-a_2 < x < -a_1$ and $a_2 < x < a_1$, as shown in Figure 5.2. The shear traction $S(x)$ and the normal traction $N(x)$ along the contact surface $y = 0$ are given by (making use of equation (4.1))

$$S(x) = \sigma_{xyb}(x) + \frac{2\mu}{\pi(\kappa+1)}\left\{\int_{-a_2}^{-a_1} H_{xxy}\left(\hat{x},\hat{\xi}\right)\frac{B_x(\xi)}{c}d\xi + \int_{a_1}^{a_2} H_{xxy}(\hat{x},\hat{\xi})\frac{B_x(\xi)}{c}d\xi\right\}, \tag{5.3}$$

$$N(x) = \sigma_{yyb}(x) + \frac{2\mu}{\pi(\kappa+1)}\left\{\int_{-a_2}^{-a_1} H_{xyy}\left(\hat{x},\hat{\xi}\right)\frac{B_x(\xi)}{c}d\xi + \int_{a_1}^{a_2} H_{xyy}(\hat{x},\hat{\xi})\frac{B_x(\xi)}{c}d\xi\right\}, \tag{5.4}$$

where $B_x(\xi)$ is the glide dislocation density ($db_x/d\xi$) applied at the point (ξ,0).

From symmetry considerations it is noted that

$$B_x(\xi) = B_x(-\xi).$$

Therefore on simplification the equations give

$$\begin{aligned} S(x) &= \sigma_{xyb}(x) + \frac{2\mu}{\pi(\kappa+1)}\int_{\hat{a_1}}^{\hat{a_2}} F_{xxy}\left(\hat{x},\hat{\xi}\right)B_x(\xi)\,d\hat{\xi}, \\ N(x) &= \sigma_{yyb}(x) + \frac{2\mu}{\pi(\kappa+1)}\int_{\hat{a_1}}^{\hat{a_2}} F_{xyy}\left(\hat{x},\hat{\xi}\right)B_x(\xi)\,d\hat{\xi}. \end{aligned}$$

($\hat{\xi} \equiv \xi/c$, $\hat{a_1} \equiv a_1/c$, and $\hat{a_2} \equiv a_2/c$). Here

$$\begin{aligned} F_{xyy} &\equiv H_{xyy}(\hat{x},\hat{\xi}) + H_{xyy}(\hat{x},-\hat{\xi}), \\ F_{xxy} &\equiv H_{xxy}(\hat{x},\hat{\xi}) + H_{xxy}(\hat{x},-\hat{\xi}), \end{aligned}$$

The contact condition for slip is now applied

$$S(x) = +fN(x), \qquad a_1 \le x \le a_2. \tag{5.5}$$

For positive x, $\sigma_{xyb}(x)$ is negative and therefore $S(x)$ is expected to be negative. Since $N(x) < 0$

for positive x as well, the above equation has a '+' sign. Expanding equation (5.5)

$$\frac{2\mu}{\pi(\kappa+1)}\int_{\hat{a_1}}^{\hat{a_2}}\left[F_{xxy}(\hat{x},\hat{\xi})-fF_{xyy}(\hat{x},\hat{\xi})\right]B_x(\xi)\,d\hat{\xi}= \\ -\sigma_{xyb}(x)+f\sigma_{yyb}(x),$$

$$a_1\le x\le a_2. \tag{5.6}$$

This is a Cauchy singular integral equation of the first kind with a generalised Cauchy kernel. A 'bounded both ends' solution for the primary unknown, the dislocation density $B_x(\xi)$, together with the location of the slip zone end points, $\hat{a_1}$ and $\hat{a_2}$, is required.

The solution for $B_x(\xi)$ will also have to satisfy a side condition, which ensures that the surfaces return to the stick state at the end of the slip zone, given by

$$\int_{a_1}^{a_2}B_x(\xi)d\xi=\int_{\hat{a_1}}^{\hat{a_2}}B_x(\xi)d\hat{\xi}=0. \tag{5.7}$$

Discretization of the equations in the slip but no separation case

The equations (5.6) and (5.7) are normalised with respect to the reference length by defining the parameters

$$\begin{aligned}\Delta &= \frac{1}{2}(\hat{a_2}-\hat{a_1}),\\ \Psi &= \frac{1}{2}(\hat{a_1}+\hat{a_2}).\end{aligned}$$

So

$$\begin{aligned}\hat{\xi} &= \Psi+\Delta s,\\ \hat{x} &= \Psi+\Delta t.\end{aligned}$$

Further

$$\begin{aligned}\hat{x}-\hat{\xi} &= \Delta(t-s),\\ d\hat{\xi} &= \Delta ds.\end{aligned}$$

To solve the integral equations numerically, a Gauss-Chebyshev quadrature is used for a dislocation density function bounded at both ends. Further details of this numerical solution procedure can

be found from Erdogan et al. [63]. It is hence posited that

$$B_x(\xi) = \phi_x(s)\sqrt{1-s^2}.$$

In this quadrature, the positions of the integration points, collocation points and the weight functions are given by

$$s_i = \cos\left(\frac{\pi i}{N+1}\right), \quad i = 1..N, \tag{5.8}$$

$$t_k = \cos\left(\pi\frac{2k-1}{2(N+1)}\right), \quad k = 1..N+1, \tag{5.9}$$

$$w_i = \pi\frac{1-s_i^2}{N+1}. \tag{5.10}$$

Here, N is the number of integration points used in the quadrature. The discretized version of equation (5.6) is hence written as

$$\frac{2\mu}{\pi(\kappa+1)}\sum_{i=1}^{N}\begin{bmatrix}\left(\frac{1}{t_k-s_i}+\right.\\ \Delta F_{xxy}(\Psi+\Delta t_k,\Psi+\Delta s_i)-\\ \left.f\Delta F_{xyy}(\Psi+\Delta t_k,\Psi+\Delta s_i)\right)\\ \times w_i(s_i)\,\phi_x(s_i)\end{bmatrix} = \begin{bmatrix}-\sigma_{xyb}\left(c(\Psi+\Delta t_k)\right)\\ +f\sigma_{yyb}\left(c(\Psi+\Delta t_k)\right)\end{bmatrix},$$

$$k = 1..N+1. \tag{5.11}$$

The discretization and further simplification of equation (5.7) leads to the side condition in discretized form

$$\sum_{i=1}^{N} w_i(s_i)\phi_x(s_i) = 0. \tag{5.12}$$

Values for Δ, Ψ and $\phi_x(s_i)$ are found to satisfy the equations (5.11) and the equation (5.12), for different combinations of f and $\hat{w}$ for which slip but no separation occur. The solution procedure involves first discarding any one equation from the $N+1$ equations given by (5.11). The choice of which equation to discard does not affect the analysis. For each combination of Δ and Ψ, the N $\phi_x(s_i)$ values can be computed from the remaining N equations. The values of the $\phi_x(s_i)$ computed for each combination of Δ and Ψ are checked with respect to the equation initially discarded and the side condition given by equation (5.12). The error values associated with both of these equations are computed. Δ and Ψ are found to minimise these error values.

5.2.2 Slip and Separation Case

Formulation

The third possibility is that the normal contact pressure becomes zero over a region, leading to the separation of the two surfaces. Since the zone of separation will have to be symmetrical about the y-axis, it is assumed that the separation spans the interval $[-b \quad b]$. It is also be assumed that the slip interval is larger and spans the range $[-a_3 \quad a_3]$. See Figure 5.3. A distribution of climb dislocations is applied to the region between the interval $[-b \quad b]$ and a distribution of glide dislocations applied between the interval $[-a_3 \quad a_3]$.

The expressions for the shear traction, $S(x)$, and the normal traction, $N(x)$, along the contact surface $y = 0$, due to the bilateral components and the applied distribution of dislocations can be hence written to be given by

$$S(x) = \sigma_{xyb}(x) + \frac{2\mu}{\pi(\kappa+1)}\left\{\int_{-b}^{b} H_{yxy}\left(\hat{x},\hat{\xi}\right)\frac{B_y(\xi)}{c}d\xi + \int_{-a_3}^{a_3} H_{xxy}\left(\hat{x},\hat{\xi}\right)\frac{B_x(\xi)}{c}d\xi\right\}, \tag{5.13}$$

$$N(x) = \sigma_{yyb}(x) + \frac{2\mu}{\pi(\kappa+1)}\left\{\int_{-b}^{b} H_{yyy}\left(\hat{x},\hat{\xi}\right)\frac{B_y(\xi)}{c}d\xi + \int_{-a_3}^{a_3} H_{xyy}\left(\hat{x},\hat{\xi}\right)\frac{B_x(\xi)}{c}d\xi\right\}. \tag{5.14}$$

where $B_x(\xi)$ and $B_y(\xi)$ are the glide and climb dislocation densities ($db_x/d\xi$ and $db_y/d\xi$) applied at the point (ξ,0).

The contact conditions at the slip and separation regions in this model are given by

$$N(x) = 0, \qquad -b \le x \le b, \tag{5.15}$$

$$S(x) = +sign(x)\, fN(x), \qquad -a_3 \le x \le a_3, \tag{5.16}$$

$$\Leftrightarrow S(x) = +H\left(\mid x \mid -b\right) sign(x)\, fN(x), \qquad -a_3 \le x \le a_3. \tag{5.17}$$

The Heavisde function is used above with $H(x) = 1$ for $x > 0$ and $H(x) = 0$ for $x \le 0$. For positive x, $\sigma_{xyb}(x)$ is negative and therefore $S(x)$ is expected to be negative. Since $N(x) \le 0$ for positive x as well, the above equations (5.16) and (5.17) have '+' signs. The contact conditions therefore

imply

$$\frac{2\mu}{\pi(\kappa+1)}\begin{bmatrix}\int_{-\hat{b}}^{\hat{b}} H_{yyy}\left(\hat{x},\hat{\xi}\right)B_y(\xi)\,d\hat{\xi}\\ +\int_{-\hat{a_3}}^{\hat{a_3}} H_{xyy}\left(\hat{x},\hat{\xi}\right)B_x(\xi)\,d\hat{\xi}\end{bmatrix} = -\sigma_{yyb}(x),$$

$$-b \le x \le b. \tag{5.18}$$

and

$$\frac{2\mu}{\pi(\kappa+1)}\begin{bmatrix}\int_{-\hat{b}}^{\hat{b}} J\left(\hat{x},\hat{\xi}\right)B_y(\xi)\,d\hat{\xi}\\ +\int_{-\hat{a_3}}^{\hat{a_3}} K\left(\hat{x},\hat{\xi}\right)B_x(\xi)\,d\hat{\xi}\end{bmatrix} = \begin{bmatrix}-\sigma_{xyb}(x)\\ +H\left(\mid x \mid -b\right)sign(x)\,f\sigma_{yyb}(x)\end{bmatrix},$$

$$-a_3 \le x \le a_3, \tag{5.19}$$

where

$$\begin{aligned} J\left(\hat{x},\hat{\xi}\right) &= H_{yxy}\left(\hat{x},\hat{\xi}\right) - H\left(\mid \hat{x} \mid -\hat{b}\right)sign(x)\,fH_{yyy}\left(\hat{x},\hat{\xi}\right),\\ K\left(\hat{x},\hat{\xi}\right) &= H_{xxy}\left(\hat{x},\hat{\xi}\right) - H\left(\mid \hat{x} \mid -\hat{b}\right)sign(x)\,fH_{xyy}\left(\hat{x},\hat{\xi}\right). \end{aligned}$$

Further, similar to the case of slip but no separation (see equation (5.7)), the dislocation densities, $B_x(\xi)$ and $B_y(\xi)$, must be such that the surfaces return smoothly to the stick state at the end of the slip region and that the surfaces close smoothly at the end of the separation region, i.e.

$$\int_{-a_3}^{a_3} B_x(\xi)d\xi = \int_{-\hat{a_3}}^{\hat{a_3}} B_x(\xi)d\hat{\xi} = 0, \tag{5.20}$$

$$\int_{-b}^{b} B_y(\xi)d\xi = \int_{-\hat{b}}^{\hat{b}} B_y(\xi)d\hat{\xi} = 0. \tag{5.21}$$

Values of $\hat{b}$ and $\hat{a_3}$, and the distribution densities $B_y(\xi)$ and $B_x(\xi)$ need to be found to satisfy equations (5.18) ,(5.19) ,(5.20) and (5.21), for the values of $\hat{w}$ and f for which both slip and separation occur.

Discretization of the equations in the slip and separation case

As in the slip and no separation case, the Guass-Chebysev quadrature was used to discretize and solve equations (5.18) and (5.19) and the side conditions stated in equations (5.20) and (5.21). In equation (5.18), the integral term with limits $[-\hat{b} \quad \hat{b}]$ is Cauchy over the whole interval and the other integral term is regular. In equation (5.19), the integral term with the kernel $K(\hat{x},\hat{\xi})$ is

Cauchy and while the the integral term with the kernel $J(\hat{x},\hat{\xi})$ is regular within its limits, $[-\hat{b} \quad \hat{b}]$. Hence in each of these two integral equations, only one integral term is Cauchy within its limits, so there is no conflict in the choice of appropriate collocation points required to discretize both equations with the quadrature. For each integral equation, the collocation points will be selected to be compatible with the requirements of the quadrature for the Cauchy integral term.

The first step in the solution is to normalise the intervals of integration by defining

$$\begin{aligned}\hat{\xi} &= \hat{b}s = \hat{a_3}\ddot{u},\\ \hat{x} &= \hat{b}t = \hat{a_3}\ddot{v}.\end{aligned}$$

So

$$d\hat{\xi} = \hat{b}ds = \hat{a_3}d\ddot{u}.$$

A 'bounded both ends' behaviour for each distribution of dislocations is expected and it is posited that

$$\begin{aligned}B_x(\xi) &= \phi_x(\ddot{u})\sqrt{1-\ddot{u}^2},\\ B_y(\xi) &= \phi_y(s)\sqrt{1-s^2}.\end{aligned}$$

The numerical quadrature scheme used is the same as before, with

$$\ddot{u}_i = s_i = cos\left(\frac{\pi i}{N+1}\right), \quad i = 1\ldots N, \tag{5.22}$$

$$\ddot{v}_k = t_k = cos\left(\pi\frac{2k-1}{2(N+1)}\right), \quad k = 1\ldots N+1, \tag{5.23}$$

$$w_i = \pi\frac{1-s_i^2}{N+1} = \pi\frac{1-\ddot{u}_i^2}{N+1}. \tag{5.24}$$

The two integral equations (5.18) and (5.19) discretized thus become

$$\left[\begin{array}{l}\displaystyle\sum_{i=1}^{N}\hat{b}H_{yyy}\left(\hat{b}t_k,\hat{b}s_i\right)w_i(s_i)\,\phi_y(s_i)\\ \displaystyle+\sum_{i=1}^{N}\hat{a_3}H_{xyy}\left(\hat{b}t_k,\hat{a_3}\ddot{u}_i\right)w_i(\ddot{u}_i)\,\phi_x(\ddot{u}_i)\end{array}\right] = -\frac{\pi(\kappa+1)}{2\mu}\sigma_{yyb}\left(\hat{b}t_k\right),$$

$$k = 1\ldots N+1, \tag{5.25}$$

$$\begin{bmatrix} \sum_{i=1}^{N} \hat{b} J\left(\hat{a_3}\ddot{v}_k, \hat{b}s_i\right) w_i\left(s_i\right) \phi_y(s_i) \\ + \sum_{i=1}^{N} \hat{a_3} K\left(\hat{a_3}\ddot{v}_k, \hat{a_3}\ddot{u}_i\right) w_i\left(s_i\right) \phi_x(\ddot{u}_i) \end{bmatrix} = \frac{\pi\left(\kappa+1\right)}{2\mu} \times \begin{bmatrix} -\sigma_{xyb}\left(\hat{a_3}\ddot{v}_k\right) + H\left(\mid \hat{a_3}\ddot{v}_k \mid -\hat{b}\right) \\ \times sign\left(\hat{a_3}\ddot{v}_k\right) f\sigma_{yyb}\left(\hat{a_3}\ddot{v}_k\right) \end{bmatrix},$$

$$k = 1 \ldots N+1. \tag{5.26}$$

And the two side conditions, equations (5.20) and (5.21), become

$$\sum_{i=1}^{N} w_i\left(\ddot{u}_i\right) \phi_x(\ddot{u}_i) = 0, \tag{5.27}$$

$$\sum_{i=1}^{N} w_i\left(s_i\right) \phi_y(s_i) = 0. \tag{5.28}$$

Equations (5.25) and (5.26) provide $2N+2$ equations— one equation for each collocation point, t_k and $\ddot{v}_k$ respectively. A similar method of solution is employed as in the slip but no separation case. One equation from (5.25) and one equation from (5.26) are initially discarded. The choice of which equations to discard does not affect the results. For each combination of $\hat{b}$ and $\hat{a_3}$, $\phi_x(\ddot{u}_i)$ and $\phi_y(s_i)$ values are computed from the remaining $2N$ equations. The $\phi_x(\ddot{u}_i)$ and $\phi_y(s_i)$ values computed are checked with respect to the two omitted equations and the two side conditions, and the associated error values with respect to these equations are computed. Values of $\hat{b}$ and $\hat{a_3}$ are found to minimise these error values.

Though there seems to be four equations to find two unknowns, the results show that two equations are redundant— when the values $\hat{b}$ and $\hat{a_3}$ are found to satisfy the side condition equation (5.27) and one of the initially discarded equations, the side condition equation (5.28) and the other omitted equation are found to be also satisfied.

5.3 Results

The bilateral equations (5.1) and (5.2) were used to determine the minimum coefficient of friction required to maintain stick throughout the contact area for a range of $\hat{w}$ values. It was expected for a given $\hat{w}$ value that a reduction in the coefficient of friction would lead initially to slip but no separation and further reduction would lead to both slip and separation. It was found, however, for values of $\hat{w} \leq 1.5$ separation does not occur for any value of coefficient of friction.

The results from the distributed dislocation technique were used to find the highest value of

coefficient of friction, in steps of 0.01, for which separation occurs for a given $\hat{w}$ value. The values found are plotted in Figure 5.4.

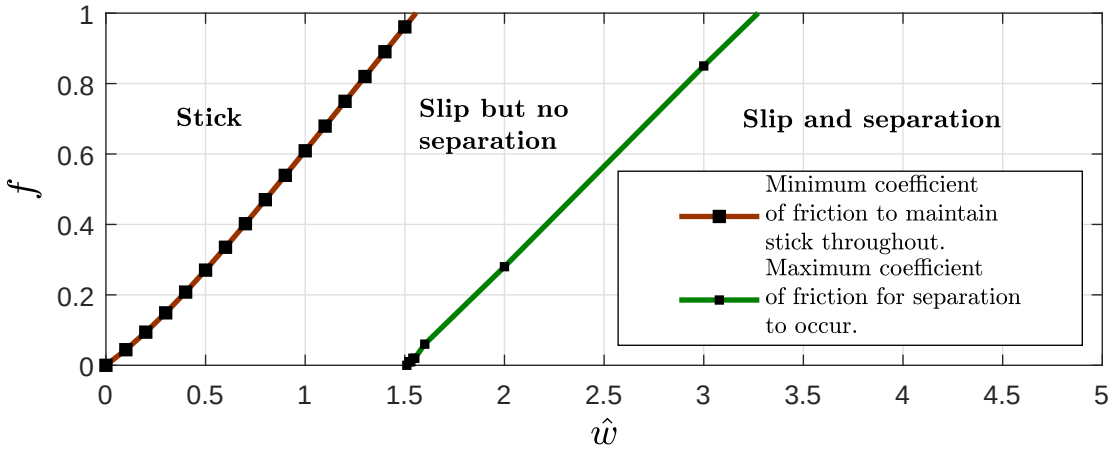

Figure 5.4: The solution regimes depending on f and the $\hat{w}$ value.

Figure 5.4 shows the solution regimes corresponding to different combinations of $\hat{w}$ and coefficient of friction values, as deduced from the results of the bilateral equations and by application of the distributed dislocations. Top diagram of Figure 5.5 shows the slip and separation parameters—$\hat{a_1}$, $\hat{a_2}$, $\hat{b}$ and $\hat{a_3}$—determined when the coefficient of friction is fixed at 0.5 for different $\hat{w}$ values. When the $\hat{w}$ value is small the surfaces stick throughout. With an increase in the $\hat{w}$ value, two areas of slip emerge, which with further increase in the $\hat{w}$ value enlarge and progress towards the centre.

It is interesting to note that once the slip region has reached near the centre, the size of the slip zone expands almost linearly with an increase in the $\hat{w}$ parameter. Once the $\hat{w}$ value is large enough for separation to occur, the extent of separation also increases with the $\hat{w}$ parameter, and once $\hat{w}$ value is sufficiently high, such as $\hat{w} > 3.5$ in this case with $f = 0.5$, the separation zone expands with $\hat{w}$ almost linearly and almost at the identical the rate as the expansion of the slip zone with the $\hat{w}$ value.

Bottom diagram of Figure 5.5 shows the slip and separation parameters computed similarly when $\hat{w} = 2.5$ and the coefficient of friction is varied. Similar values for the slip and separation parameters were obtained with the number of integration points $N = 10$ as with $N = 100$. The calculation becomes computationally most difficult and demanding when the $\hat{a_1}$ parameter approaches 0, i.e. the central stick region becomes very small, and the number of integration points required for accurate solutions is found to increase significantly. With $N = 10$, values of $\hat{a_1}$ and $\hat{a_2}$ were found to satisfy the equations, but the $\hat{a_1}$ values were found at times to be negative, though very small in magnitude. More realistic solutions were found when $N = 100$.

For $\hat{w} = 2.5$ and $f = 0.5$, the required distributions of glide and climb dislocation densities along the contact surface are plotted in Figure 5.6. The tractions along the contact surface are

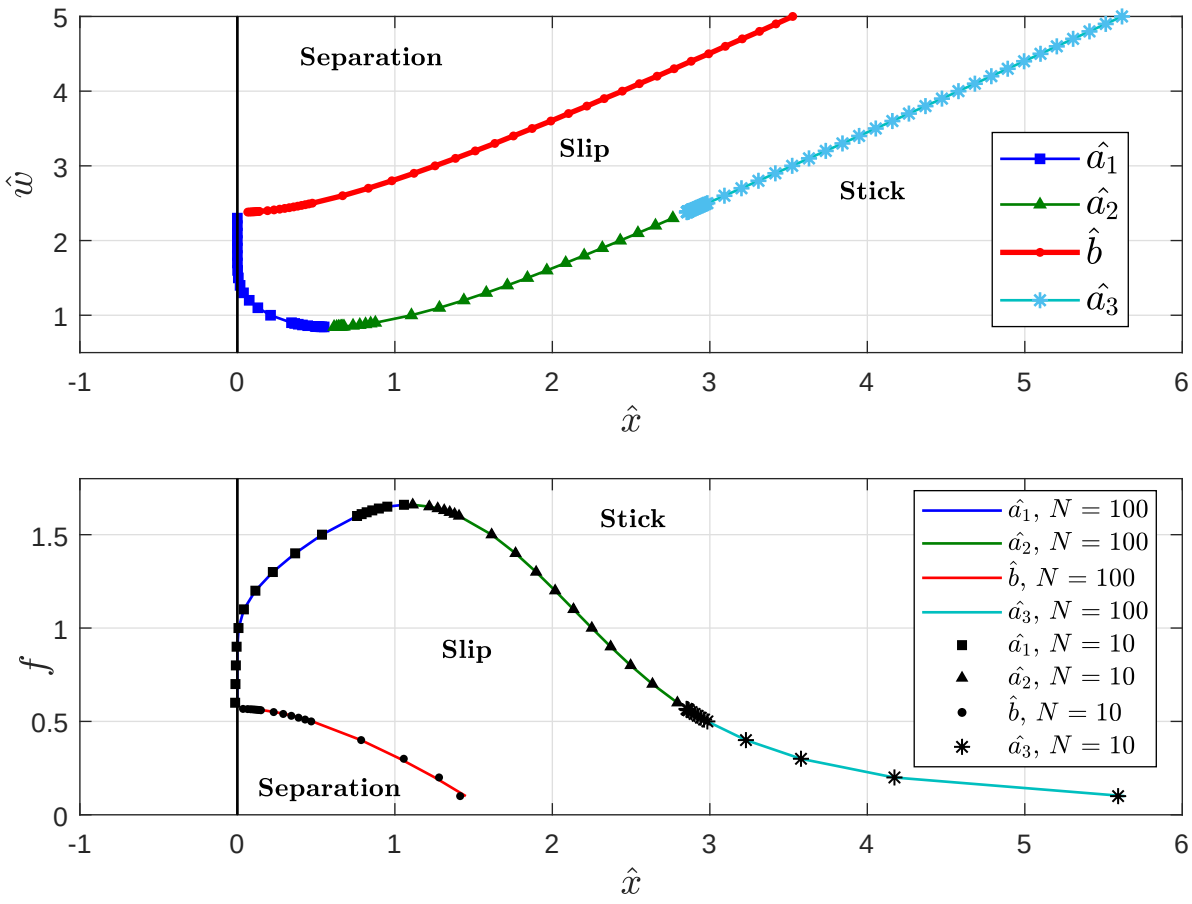

Figure 5.5: **Top**: For $f = 0.5$, the parameters, $\hat{a_1}$, $\hat{a_2}$, $\hat{a_3}$, $\hat{b}$ that determine areas of slip and separation along the contact surface for different values of $\hat{w}$. $N = 100$. **Bottom**: For $\hat{w} = 2.5$, the same parameters for different f, found with $N = 100$ and $N = 10$.

determined using equations (5.14) and (5.13) and plotted in Figure 5.7. Similarly, the extent of tangential slip and separation along the contact area determined are given in Figure 5.8. These are computed by numerical integration of the computed glide and climb dislocation densities. $u_1(x)$ and $v_1(x)$ are the tangential and normal displacement components of the half-plane surface and $u_2(x)$ and $v_2(x)$ are the tangential and normal displacement components of the layer interface.

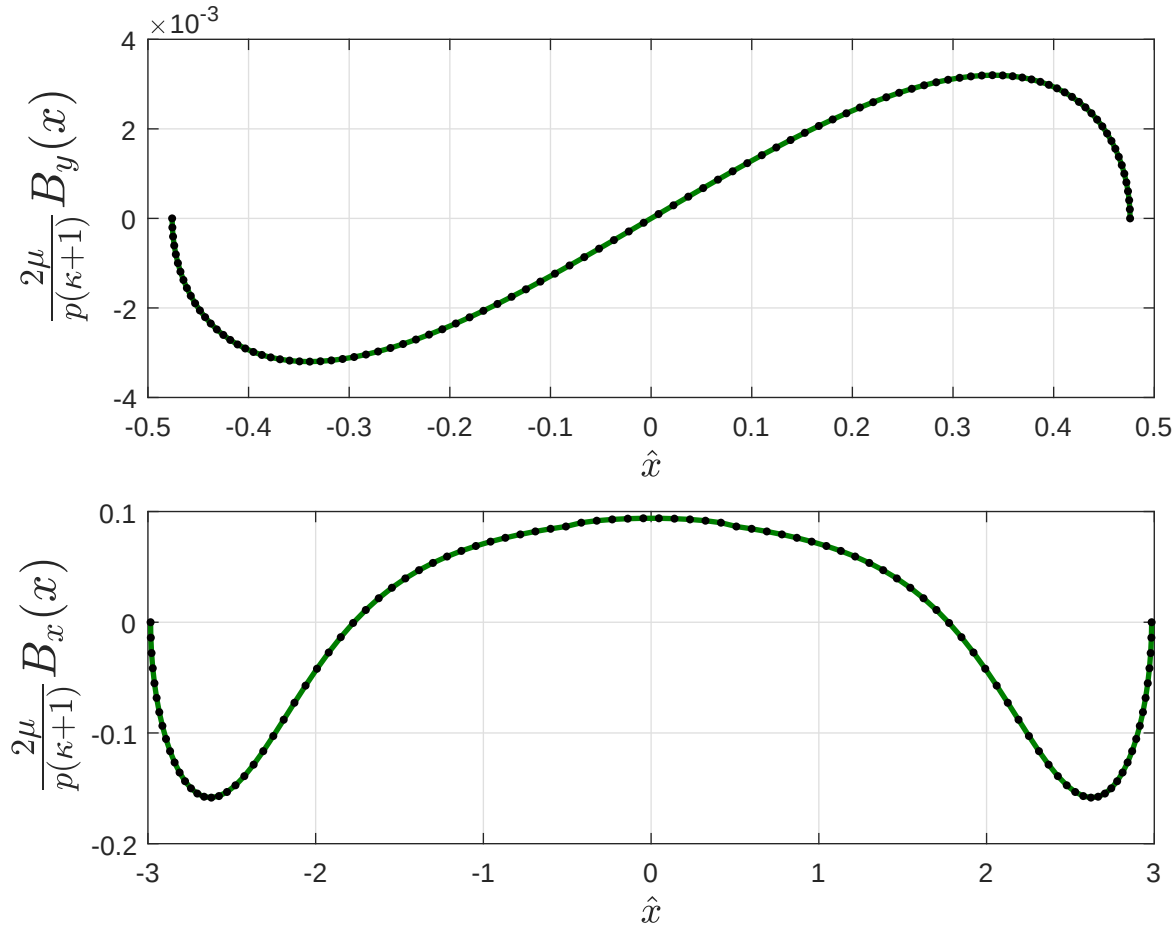

Figure 5.6: For $\hat{w} = 2.5$ and $f = 0.5$. **Top:** The climb dislocation density inserted along the location of the contact interface. **Bottom:** The glide dislocation density inserted along the location of the contact interface.

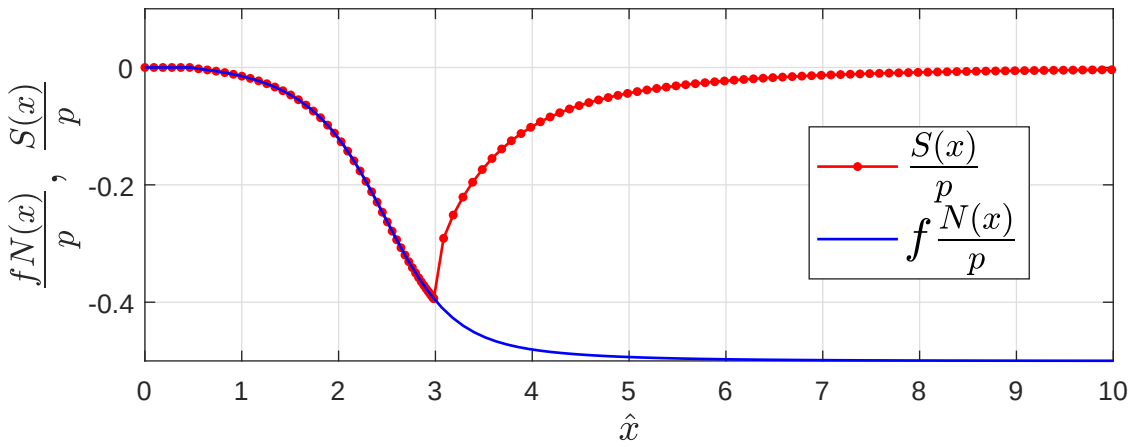

Figure 5.7: The normal and shear tractions along the contact interface when $\hat{w} = 2.5$ and $f = 0.5$.

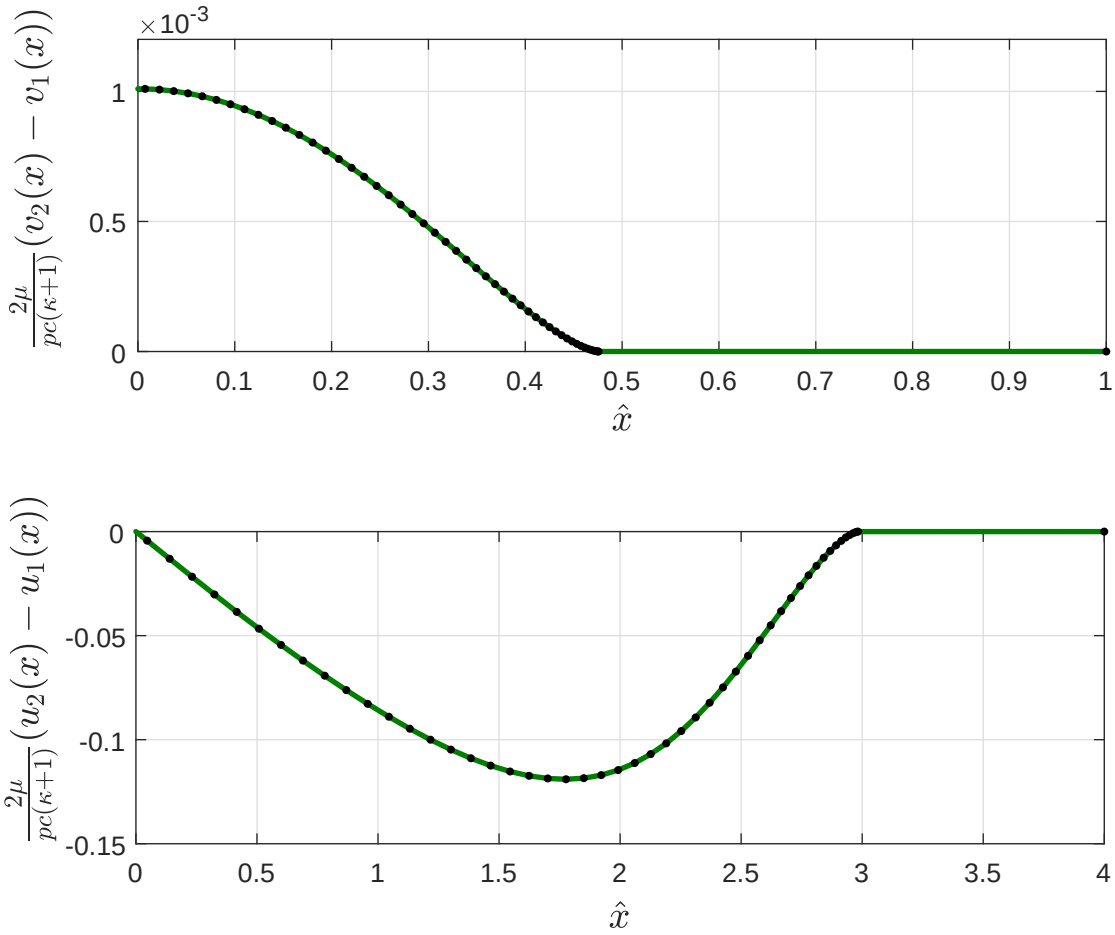

Figure 5.8: For $\hat{w} = 2.5$ and $f = 0.5$. **Top:** Separation of the surfaces along the interface. **Bottom:** The tangential slip along the contact interface. $\hat{w} = 2.5$ and $f = 0.5$.

5.4 Conclusion

A 2D linear elastic receding contact problem has been solved by applying distributions of dislocations and solving numerically the integral equations that arise with a Gauss-Chebyshev quadrature. The solution demonstrates the applicability of the distributed dislocation technique to solve a receding contact problem and the results of this problem has provided useful insights regarding the behaviour of receding contacts. Like other receding contact problems, the locations of slip and separation portions along the contact area are seen to be load and material properties independent. Further it is seen, as is with other receding contacts, with any finite load the layer snaps into slip and separation, for values of coefficient of friction and $\hat{w}$ for which separation occur.

The results show that there are three possible solution regimes depending on the coefficient of friction, f, and the $\hat{w}$ value— stick along all of the contact interface, some slip but no separation along portions of the contact, both slip and separation along portions of the contact. See Figure 5.4.

Interestingly, the results indicate that the surfaces do not separate for any value of coefficient of friction for $\hat{w} \leq 1.5$. In addition, for sufficiently high values of $\hat{w}$, such as $\hat{w} > 4$, for all practical values of coefficient of friction both slip and separation will occur along the contact. In addition, from Figure 5.5, it is significant to note the near linear relationship between the $\hat{w}$ value and the extent of the slip and separation regions for sufficiently high $\hat{w}$ values.

Chapter 6

Receding Contact Analysis with Separation of Surfaces at Remote Points

6.1 Introduction

The fundamental plane receding contact problem of an infinitely long linear elastic layer pressed by a line load onto a half-plane with a frictional interface is revisited in this Chapter. The problem geometry and loading is given in Figure 6.1. An infinitely long layer of thickness c is in contact with a half-plane $y \leq 0$ of the same homogeneous linear elastic material. A line load of $-P$ is applied at the point $(0, c)$ on the layer. The origin is taken directly below the point of application of the line load at the contact interface.

As discussed in Chapter 4, Chaise et al. attempted a solution to this problem by using distributions of dislocations of only the 'bounded-bounded' form which implied a physically unrealistic lift-off the layer [61]. A bounded-bounded distribution of climb dislocations implies that the separation of the layer and the half-plane approaches a constant value at remote points. In actuality the layer should lift-off and its slope should approach a constant value, as the layer becomes straight. This problem is revisited taking into account the behaviour of the layer and half-plane at remote points. The general procedure described can be used to model other contact problems, particularly receding contacts with separation of surfaces at all remote points. Chapter 7 will demonstrate the applicability of this method to other loading conditions.

6.2 Outline of the Method

As in the previous chapter (and as in Chaise et al.), the layer and half-plane are modelled *together* as an augmented half plane, $y \leq c$, with distributions of dislocations along the surface $y = 0$, at the location of the contact interface. It is expected that with the application of the load, the layer will lift off, with a stick region at the centre, slip along the contact interface in the region of $x \in [a \quad \infty]$ and $x \in [-\infty \quad -a]$ and separation at the regions of $x \in [b \quad \infty]$ and $x \in [-\infty \quad -b]$, as in Figure 6.1.

The general procedure is as follows.

1. Closed form expressions for the displacement of the lower surface of the layer, $u_2(x)$ and $v_2(x)$, and the half-plane interface surface, $u_1(x)$ and $v_1(x)$, at remote points, $x >> c$, are written. From these, expressions for the gap between the surfaces, $V(x)$ and the relative slip, $U(x)$, at remote points are found.

2. The required forms of climb and glide dislocation densities at remote points, $x >> c$, are now given by

$$B_{yl}(x) = -\frac{dV(x)}{dx}, \quad x >> c$$

$$B_{xl}(x) = -\frac{dU(x)}{dx}, \quad x >> c.$$

   Symmetry and anti-symmetry properties of the expected glide and climb distributions, respectively, are used to determine similar expressions at $x << -c$.

3. When the density of either dislocation type is not bounded to zero or singular at infinity, a 'preformed' smooth and continuous distribution of dislocations, with the correct form at remote points, is inserted along the contact interface, $y = 0$. In the problem studied here, the required glide dislocation density at remote points will be shown to be bounded to zero, but not the required climb dislocation density. Therefore, a preformed climb dislocation distribution, $A_y(x)$, is inserted such that at $x \geq e$, $A_y(x) = B_{yl}(x)$. e is a point sufficiently far away (say $e = 5c$). $A_y(x)$ has non-zero values only for points along the location of the contact surface where separation occurs. A simple polynomial function is used to define $A_y(x)$ for $x \in [b \quad e]$. The preformed dislocation distribution, $A_y(x)$ needs to be anti-symmetric about the y-axis, and is inserted along the interface for negative x accordingly.

4. The bilateral traction components, due to the external load, are found for points at the location of the interface, using Flamant's solution. Further the expressions for the traction

components due to the preformed distribution of dislocations are written by appropriate integration of the Green's functions for the stress components due to the presence of a dislocations using equation (4.1).

5. Bounded-bounded corrective distributions of dislocations of both types, $B_{yc}(x)$ and $B_x(x)$, are now inserted along the location of the contact interface, $y = 0$, so the resultant tractions satisfy the contact conditions for stick, slip and separation, which are given by

   (a) $N(x) = S(x) = 0, \qquad \text{for } |x| \geq b$

   (b) $S(x) = -sign(x) f N(x), \qquad \text{for } a \leq |x| \leq b$

   (c) $S(x) < -fN(x), \qquad \text{for } 0 < x < a$

   (d) $S(x) > fN(x), \qquad \text{for } 0 > x > -a$

   where $N(x)$, and $S(x)$ are the total normal and shear traction components at the point $(x, 0)$ at the location of the contact interface. The total traction components are the sum of the bilateral stress components, the stress components due to the preformed dislocation distribution (the $A_y(x)$ distribution) and the stress components due to the corrective dislocation distributions.

6. An additional condition is obtained by ensuring that the dislocation densities approach the required values at remote points. This means that at $x = e$, $B_{yc}(x) \to 0$. See Figure 6.2. The total climb dislocation density, $B_y(x)$, inserted at the location of the interface is given by

$$B_y(x) = A_y(x) + B_{yc}(x),$$

   and this condition requires $B_y(x) \to A_y(x)$ for $x \geq e$.

The standard Gauss-Chebyshev quadrature is used to solve the integral equations that arise from the above process to find the primary unknowns— a and b values, the $B_{yc}(x)$, $B_x(x)$ distributions, and other variables that determine far-field behaviour of the layer and half-plane (the slope of the layer, k_l, at remote points is a primary unknown).

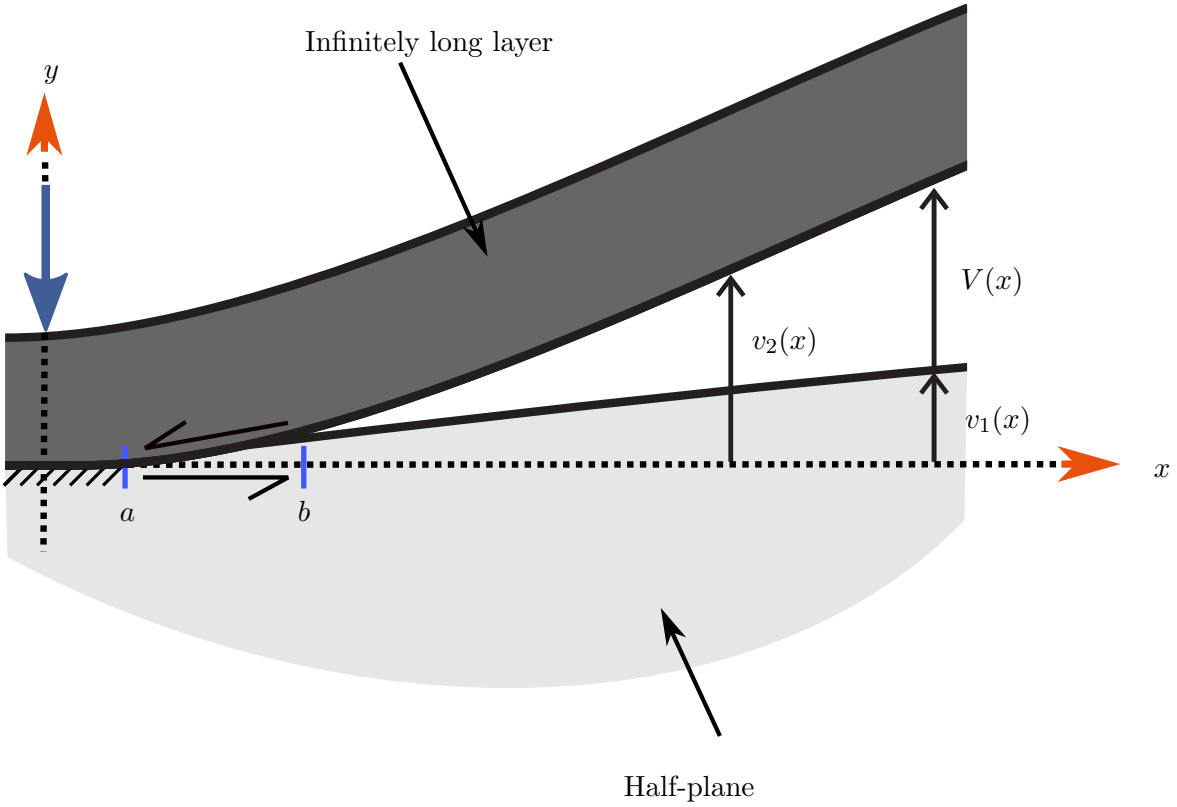

Figure 6.1: The problem geometry.

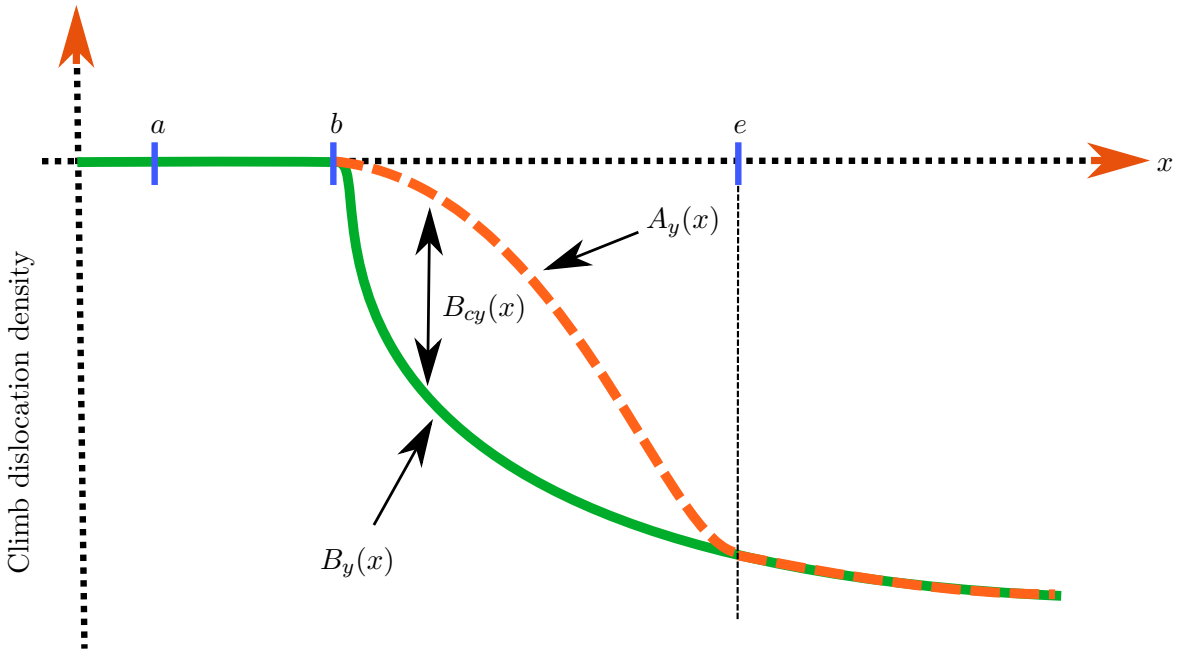

Figure 6.2: Schematic plots of the preformed climb dislocation distribution, $A_y(x)$, and the total climb dislocation distribution, $B_y(x)$, inserted. The corrective bounded-bounded climb dislocation distribution, $B_{cy}(x)$, is the difference between the total climb dislocation density and the preformed dislocation density.

6.3 Formulation

Expressions for remote glide and climb dislocation densities are derived from the expected displacements of the contact surface of the layer and contact surface of $y \leq 0$ half-plane. The formulation is written in detail here for the behaviour of the layer and the half-plane on right hand side of the y-axis. The behaviour on the left hand side when not stated can be inferred from symmetry. It is deduced that the half-plane, $y \leq 0$, will be loaded by a normal traction with a resultant normal force of $-P$, i.e.

$$\int_{-\infty}^{\infty} N(x) = -P.$$

Further, due to symmetry, the half-plane will be subject to an anti-symmetric shear traction, such that

$$\int_{0}^{\infty} S(x) = F, \tag{6.1}$$

and

$$\int_{-\infty}^{0} S(x) = -F,$$

where F is *a priori* of unknown magnitude. The half-plane surface, $y = 0$, at $|x| >> c$, can be said, by St Venant's principle, to displace as if it were loaded by a point load $-P$ at the origin, and by two tangential forces, of magnitude F and $-F$ applied at either side of the origin at points $(d, 0)$ and $(-d, 0)$. d is also *a priori* of unknown magnitude and is related to the shear traction and the F parameter by

$$\int_{0}^{\infty} xS(x)dx = Fd. \tag{6.2}$$

This use of the St Venant's principle is justified mathematically in Appendix B.2.

It is assumed the y-displacement of layer interface has a constant slope at remote points, $x >> c$, and is given by $k_l x + D_c$ (D_c is an unknown constant). Using Flamant's solution to find the normal displacement of the half-plane ($y \leq 0$) surface, the gap, $V(x)$, between the layer and the half plane is given by

$$V(x) = k_l x + D_c - \left[\begin{array}{r} \dfrac{P(\kappa+1)\ln(x)}{4\pi\mu} - \dfrac{F(\kappa-1)sign(x-d)}{8\mu} \\ + \dfrac{F(\kappa-1)sign(x+d)}{8\mu} \end{array} \right], \qquad x >> c \tag{6.3}$$

This implies,

$$B_{yl}(x) = -\frac{dV(x)}{dx} = -k_l + \frac{k_2}{\hat{x}}, \qquad x >> c, \tag{6.4}$$

where $k_2 \equiv \frac{P(\kappa+1)}{4\pi\mu c}$ and $\hat{x} \equiv x/c$. As $V(x)$ is symmetric about the y-axis

$$B_{yl}(x) = -k_l + \frac{k_2}{\hat{x}}, \quad x << -c.$$

Flamant's solution for the x-displacement of the half-plane surface is given by

$$u_1(x) = \frac{-P(\kappa-1)}{8\mu} + \frac{F(\kappa+1)}{4\pi\mu} \ln\left(\frac{|x+d|}{|x-d|}\right), \qquad x >> c.$$

Anticipating no strain within the layer, i.e. $\frac{du_2(x)}{dx} = 0$ at remote points, where $u_2(x)$ is the x-displacement of the layer, we see that

$$B_{xl}(x) = -\frac{U(x)}{dx} = \frac{du_1(x)}{dx} = \frac{F^*}{\hat{d}^2 - \hat{x}^2}, \qquad x >> c. \tag{6.5}$$

where $U(x)$ is the relative slip between the layer interface and the half-plane interface and $F^* \equiv \frac{F\hat{d}(1+\kappa)}{2\mu\pi c}$, and $\hat{d} \equiv d/c$. It should be noted that the above expression implies that the glide distribution is bounded to zero at $x \to \infty$, and therefore insertion of a preformed glide dislocation distribution is not required, which is convenient since the variables F and d are unknown.

Since the required climb dislocation density, $B_y(x)$, is not bounded to zero at infinity, two bounded-bounded dislocation densities, $B_x(x)$ and $B_{yc}(x)$, and a preformed climb dislocation distribution, $A_y(x)$, is inserted at the location of the contact interface, $y = 0$, with the total climb

dislocation density given by $B_y(x) = A_y(x) + B_{yc}(x)$, as represented schematically in Figure 6.2. The $B_x(x)$ distribution should approach the $B_{xl}(x)$ value at remote points.

The bilateral stress components are given by Flamant's solution for a normal line load of magnitude $-P$ acting at the point (0,c) on the augmented half plane $y \leq c$. For points along the location of contact interface these components are given by

$$\frac{\sigma_{yyb}(x)}{P/c} = \frac{-2}{\pi(1^2 + (\hat{x})^2)^2}, \tag{6.6}$$

$$\frac{\sigma_{xyb}(x)}{P/c} = \frac{2(\hat{x})}{\pi(1^2 + (\hat{x})^2)^2}. \tag{6.7}$$

In order to avoid singularities in the stress field, the preformed distribution of climb dislocations, $A_y(x)$, should be continuous and smooth. As shown in Figure 6.2, for $x \in [b \quad e]$ $A_y(x)$ should be such that required corrective distribution $B_{yc}(x)$ is smooth and bounded-bounded. A function of the following form is used

$$A_y(x) = \begin{cases} 0, & |x| < b, \\ R(x), & b \leq |x| \leq e, \\ B_{yl}(x) = -sign(\hat{x})k_l + \frac{k_2}{\hat{x}} & |x| > e, \end{cases} \tag{6.8}$$

where $e > b$. To ensure the function $A_y(x)$ is continuous and smooth, for the interval $[b \quad e]$

$$\begin{aligned} R_y(e) &= -k_l + \frac{k_2}{\hat{e}} \\ R'_y(e) &= \frac{d}{d\hat{x}}\left(-k_l + \frac{k_2}{\hat{x}}\right)\Bigg|_{\hat{x}=\hat{e}} = -\frac{k_2}{(\hat{e})^2} \\ R_y(b) &= 0 \\ R'_y(b) &= 0 \end{aligned}$$

($\hat{e} \equiv e/c$). Similar conditions are written for the interval $[-b \quad -e]$. A third order polynomial that satisfies the necessary conditions is given by

$$R_y(x) = \begin{cases} R_{1y}(\hat{x} - \hat{b})^2 + R_{2y}(\hat{x} - \hat{b})^3 & b \leq x \leq e \\ -R_{1y}(\hat{x} + \hat{b})^2 + R_{2y}(\hat{x} + \hat{b})^3 & -b \geq x \geq -e \end{cases} \tag{6.9}$$

with

$$R_{1y} = -\frac{\hat{b}k_2 - 4\hat{e}k_2 + 3\hat{e}^2 k_l}{\hat{e}^2(\hat{b}-\hat{e})^2}$$
$$R_{2y} = -\frac{-\hat{b}k_2 - 3\hat{e}k_2 + 2\hat{e}^2 k_l}{\hat{e}^2(\hat{e}-\hat{b})^3}.$$

($\hat{b} \equiv b/c$). The stress components at a point $(x, 0)$ due to the distribution of climb dislocations $A_y(x)$ are given by, from equation (4.1)

$$\frac{\sigma_{yyA}(x)}{P/c} = M\int_{-\infty}^{\infty} A_y(\xi)H_{yyy}(\hat{x},\hat{\xi})d\hat{\xi}, \tag{6.10}$$
$$\frac{\sigma_{xyA}(x)}{P/c} = M\int_{-\infty}^{\infty} A_y(\xi)H_{yxy}(\hat{x},\hat{\xi})d\hat{\xi}. \tag{6.11}$$

Here $M \equiv \frac{2\mu c}{\pi(\kappa+1)P}$ and $\hat{\xi} \equiv \xi/c$. Closed formed solutions of the above integrals are obtained and the right hand sides can be reduced to an expression involving only $\hat{x}$, $\hat{b}$, $\hat{e}$, and K terms, which are too long to print. $K \equiv k_l \frac{2\mu c}{(\kappa+1)P}$.

The traction components along the contact interface at a point (x,0) are given by superposition of the traction components due to the bilateral loading, the applied dislocation density, $A_y(x)$, and the two unknown bounded-bounded dislocation densities, $B_x(x)$ and $B_{yc}(x)$, by

$$\frac{N(x)}{P/c} = \frac{\sigma_{yyb}(x)}{P/c} + \frac{\sigma_{yyA}(x)}{P/c} + M\begin{bmatrix} \int_{\hat{a}}^{\infty} B_x(\xi)H_{xyy}(\hat{x},\hat{\xi})d\hat{\xi} \\ +\int_{\hat{b}}^{\infty} B_{yc}(\xi)H_{yyy}(\hat{x},\hat{\xi})d\hat{\xi} \\ +\int_{-\infty}^{-\hat{a}} B_x(\xi)H_{xyy}(\hat{x},\hat{\xi})d\hat{\xi} \\ +\int_{-\infty}^{-\hat{b}} B_{yc}(\xi)H_{yyy}(\hat{x},\hat{\xi})d\hat{\xi} \end{bmatrix}, \tag{6.12}$$

$$\frac{S(x)}{P/c} = \frac{\sigma_{xyb}(x)}{P/c} + \frac{\sigma_{xyA}(x)}{P/c} + M\begin{bmatrix} \int_{\hat{a}}^{\infty} B_x(\xi)H_{xxy}(\hat{x},\hat{\xi})d\hat{\xi} \\ +\int_{\hat{b}}^{\infty} B_{yc}(\xi)H_{yxy}(\hat{x},\hat{\xi})d\hat{\xi} \\ +\int_{-\infty}^{-\hat{a}} B_x(\xi)H_{xxy}(\hat{x},\hat{\xi})d\hat{\xi} \\ +\int_{-\infty}^{-\hat{b}} B_{yc}(\xi)H_{yxy}(\hat{x},\hat{\xi})d\hat{\xi} \end{bmatrix}. \tag{6.13}$$

($\hat{a} \equiv a/c$, $\hat{b} \equiv b/c$, and $\hat{\xi} \equiv \xi/c$). Making use of symmetry and anti-symmetry

$$B_x(\xi) = B_x(-\xi),$$

$$B_{yc}(\xi) = -B_{yc}(-\xi),$$

the above equations, after changing the intervals of some of the integral terms, reduce to

$$\frac{N(x)}{P/c} = \frac{\sigma_{yyb}(x)}{P/c} + \frac{\sigma_{yyA}(x)}{P/c} + M \begin{bmatrix} \int_{\hat{a}}^{\infty} B_x(\xi) F_{xyy}(\hat{x}, \hat{\xi}) d\hat{\xi} \\ + \int_{\hat{b}}^{\infty} B_{yc}(\xi) F_{yyy}(\hat{x}, \hat{\xi}) \hat{\xi} \end{bmatrix}, \tag{6.14}$$

$$\frac{S(x)}{P/c} = \frac{\sigma_{xyb}(x)}{P/c} + \frac{\sigma_{xyA}(x)}{P/c} + M \begin{bmatrix} \int_{\hat{a}}^{\infty} B_x(\xi) F_{xxy}(\hat{x}, \hat{\xi}) d\hat{\xi} \\ + \int_{\hat{b}}^{\infty} B_{yc}(\xi) F_{yxy}(\hat{x}, \hat{\xi}) d\hat{\xi} \end{bmatrix}, \tag{6.15}$$

where

$$\begin{aligned} F_{xyy} &\equiv H_{xyy}(\hat{x}, \hat{\xi}) + H_{xyy}(\hat{x}, -\hat{\xi}), \\ F_{yyy} &\equiv H_{yyy}(\hat{x}, \hat{\xi}) - H_{yyy}(\hat{x}, -\hat{\xi}), \\ F_{xxy} &\equiv H_{xxy}(\hat{x}, \hat{\xi}) + H_{xxy}(\hat{x}, -\hat{\xi}), \\ F_{yxy} &\equiv H_{yxy}(\hat{x}, \hat{\xi}) - H_{yxy}(\hat{x}, -\hat{\xi}). \end{aligned}$$

The contact conditions require

1. When $|x| \geq b$

$$N(x) = 0. \tag{6.16}$$

2. When $|x| \geq a$

$$S(x) = -sign(x) f N(x) = -sign(x) H(\hat{b} - \hat{x}) f N(x). \tag{6.17}$$

Where $H(\cdot)$ is the Heaviside function. There is a negative sign in equation (6.17) as it is inferred from the bilateral tractions that the shear and normal tractions are of opposite sign for positive x and of the same sign for negative x.

Equations (6.12) and (6.16) provide the first integral equation

$$M\begin{bmatrix}\int_{\hat{a}}^{\infty} B_x(\xi)F_{xyy}(\hat{x},\hat{\xi})d\hat{\xi}\\ +\int_{\hat{b}}^{\infty} B_{yc}(\xi)F_{yyy}(\hat{x},\hat{\xi})d\hat{\xi}\end{bmatrix} = \frac{\sigma_{yyb}(x)}{P/c}+\frac{\sigma_{yyA}(x)}{P/c},$$

$$x \geq b. \tag{6.18}$$

Equations (6.13) and (6.17) provide the second integral equation

$$M\begin{bmatrix}\int_{\hat{a}}^{\infty} B_x(\xi)L_x(\hat{x},\hat{\xi})d\hat{\xi}\\ +\int_{\hat{b}}^{\infty} B_{yc}(\xi)L_y(\hat{x},\hat{\xi})d\hat{\xi}\end{bmatrix} = \begin{bmatrix}-\left(\frac{\sigma_{xyb}(x)}{P/c}+\frac{\sigma_{xyA}(x)}{P/c}\right)\\ -H(\hat{b}-\hat{x})f\left(\frac{\sigma_{yyb}(x)}{P/c}+\frac{\sigma_{yyA}(x)}{P/c}\right)\end{bmatrix},$$

$$x \geq a, \tag{6.19}$$

where

$$L_x(\hat{x},\hat{\xi}) \equiv F_{xxy}(\hat{x},\hat{\xi}) + H(\hat{b}-\hat{x})fF_{xxy}(\hat{x},\hat{\xi}),$$
$$L_y(\hat{x},\hat{\xi}) \equiv F_{yxy}(\hat{x},\hat{\xi}) + H(\hat{b}-\hat{x})fF_{yyy}(\hat{x},\hat{\xi}).$$

6.4 Discretization and Solution

Equations (6.18) and (6.19) are now discretized and solved using the standard Gauss-Chebyshev quadratures in the form employed by Chaise et al [61]. Following Chaise et al., the integral terms in both equations need to be first written within the $[-1 \quad 1]$ intervals. A transform function $T_\gamma(s_j)$ is defined

$$T_\gamma(s_j) = \gamma + \lambda \log\left(\frac{2}{1-s_j}\right),$$

where λ is a parameter. For the integral terms over the interval $[\hat{a} \quad \infty]$, a variable $s_{\hat{a}}$ is defined such that

$$\hat{\xi} = T_{\hat{a}}(s_{\hat{a}}) = \hat{a} + \lambda \log\left(\frac{2}{1-s_{\hat{a}}}\right),$$
$$\frac{d\hat{\xi}}{ds_{\hat{a}}} = \frac{\lambda}{1-s_{\hat{a}}}.$$

Similarly for the integral terms over the interval $[\hat{b} \quad \infty]$, a variable $s_{\hat{b}}$ is defined such that

$$\hat{\xi} = T_{\hat{b}}(s_{\hat{b}}) = \hat{b} + \lambda \log\left(\frac{2}{1 - s_{\hat{b}}}\right),$$
$$\frac{d\hat{\xi}}{ds_{\hat{b}}} = \frac{\lambda}{1 - s_{\hat{b}}}.$$

Gauss-Chebyshev quadratures for bounded-bounded unknown functions, $B_x(\xi)$ and $B_{yc}(\xi)$, are now used to discretize the integral equations. It is posited these corrective distributions are of the form

$$B_x(\xi) = \phi_x(s_{\hat{a}})\sqrt{1 - s_{\hat{a}}^2},$$
$$B_{yc}(\xi) = \phi_{yc}(s_{\hat{b}})\sqrt{1 - s_{\hat{b}}^2}.$$

The locations of the integration points, collocation points and the weight function are given by

$$s_{ji} = \cos\left(\frac{\pi i}{N_j + 1}\right), \quad i = 1, ..., N_j, \quad j = \hat{a}, \hat{b},$$
$$t_{jk} = \cos\left(\pi \frac{2k - 1}{2(N_j + 1)}\right), \quad k = 1, ..., N_j + 1, \quad j = \hat{a}, \hat{b},$$
$$w_j(s_{ji}) = \pi \frac{1 - s_{ij}^2}{N_j + 1}, \quad j = \hat{a}, \hat{b}.$$

Cauchy integrals are evaluated at collocation points associated with the integration points used to evaluate the integral. Note

$$\hat{x} = T_j(t_{jk}), \quad j = \hat{a}, \hat{b},$$

where t_{jk} is a collocation point, associated with integration points s_{ji}.

It should be noted that in equation (6.18) the kernel $F_{yyy}(\hat{x}, \hat{\xi})$ is Cauchy but not the kernel $F_{xyy}(\hat{x}, \hat{\xi})$. Therefore in the discretization of this equation, collocation points that are suitable for the Cauchy integral term with the $F_{yyy}(\hat{x}, \hat{\xi})$ kernel are used. Similarly in equation (6.19), the kernel $L_x(\hat{x}, \hat{\xi})$ is Cauchy but not the kernel $L_y(\hat{x}, \hat{\xi})$, and so to discretize this equation collocation points suitable for the Cauchy integral term with $L_x(\hat{x}, \hat{\xi})$ kernel are used. Equations (6.18) and

(6.19) thus discretized give

$$M\begin{bmatrix}\sum_{i}^{N_{\hat{a}}} F_{xyy}(T_{\hat{b}}(t_{\hat{b}k}),T_{\hat{a}}(s_{\hat{a}i}))w_a(s_{\hat{a}i})\phi_x(s_{\hat{a}i})\dfrac{\lambda}{1-s_{\hat{a}i}}+\\ \sum_{i}^{N_{\hat{b}}} F_{yyy}(T_{\hat{b}}(t_{\hat{b}k}),T_{\hat{b}}(s_{\hat{b}i}))w_b(s_{\hat{b}i})\phi_{yc}(s_{\hat{b}i})\dfrac{\lambda}{1-s_{\hat{b}i}}\end{bmatrix}=$$
$$-\frac{1}{P/c}\left[\sigma_{yyb}(T_{\hat{b}}(t_{\hat{b}k})c)+\sigma_{yyA}(T_{\hat{b}}(t_{\hat{b}k})c)\right],$$
$$\hat{x}\geq\hat{b}, \tag{6.20}$$

$$M\begin{bmatrix}\sum_{i}^{N_{\hat{a}}} L_x(T_{\hat{a}}(t_{\hat{a}k}),T_{\hat{a}}(s_{\hat{a}i}))w_a(s_{\hat{a}i})\phi_x(s_{\hat{a}i})\dfrac{\lambda}{1-s_{\hat{a}i}}+\\ \sum_{i}^{N_{\hat{b}}} L_y(T_{\hat{a}}(t_{\hat{a}k}),T_{\hat{b}}(s_{\hat{b}i}))w_b(s_{\hat{b}i})\phi_{yc}(s_{\hat{b}i})\dfrac{\lambda}{1-s_{\hat{b}i}}\end{bmatrix}=$$
$$\frac{1}{P/c}\begin{bmatrix}-\left(\sigma_{xyb}(T_{\hat{a}}(t_{\hat{a}k})c)+\sigma_{xyA}(T_{\hat{a}}(t_{ak})c)\right)\\ -H(b-(T_{\hat{a}}(t_{\hat{a}k})f\left(\sigma_{yyb}(T_{\hat{a}}(t_{\hat{a}k})c)+\sigma_{yyA}(T_{\hat{a}}(t_{\hat{a}k})c)\right)\end{bmatrix},$$
$$\hat{x}\geq\hat{a}. \tag{6.21}$$

The above equations provide $(N_{\hat{a}}+N_{\hat{b}})+2$ equations for $(N_{\hat{a}}+N_{\hat{b}})$ unknown $\phi_x(s_{\hat{a}i})$ and $\phi_{yc}(s_{\hat{b}i})$ values, and $\hat{a}$, $\hat{b}$, and K unknown parameters, for a given coefficient of friction, f. As shown in Figure 6.2, to provide an extra condition the $B_{yc}(x)$ distribution evaluated at the the integration point nearest to $\hat{e}$ is made to approach zero, i.e.

$$B_{yc}(cT_{\hat{b}}(s_e))=\phi_{yc}(s_e)\sqrt{1-s_e^2}\to 0 \tag{6.22}$$

where s_e is the integration point such that $T_{\hat{b}}(s_e)\approx\hat{e}$. $\hat{e}$ is taken as 5.

In solving, $N_{\hat{a}}$ and $N_{\hat{a}}$ were both taken as 500, and $\hat{e}$ was taken as 5, though similar results can be obtained for different values of $N_{\hat{a}}$, $N_{\hat{a}}$, and $\hat{e}$. λ, the numerical parameter in the transform function, was taken as 3.5. While results can be obtained for different values of λ, numerical difficulties are encountered for larger values such as $\lambda\geq 5$.

6.5 Expected Slip at Remote Points

The formulation written till this point is complete and is used to obtain a full solution. The problem is analysed afresh to obtain an expression relating the expected total slip at remote points with the shear traction and the remote slope of the layer. The expression derived here is compared with the

results obtained from §6.4. Consider again the half-plane and layer fused as one half-plane, $y \leq c$. In the interval $x \in [-\infty \quad \infty]$, at the location of the contact interface, the following preformed climb dislocation distribution is inserted

$$B_{yl}(x) = -sign(\hat{x})k_l + \frac{k_2}{\hat{x}},$$

as well as a preformed glide dislocation distribution of the following form (from equation (6.5))

$$B_{xl}(x) = \frac{F^*}{\hat{d}^2 - \hat{x}^2}.$$

Corrective distributions are required for points nearer the origin since these preformed distributions only accurately describe the interface behaviour at remote points. If $B_{rcx}(x)$ is the corrective glide dislocation density and $B_{rcy}(x)$ is the corrective climb dislocation density applied along the interface, then for all x

$$B_{rcx}(x) = B_x(x) - B_{xl}(x) \tag{6.23}$$

$$B_{rcy}(x) = B_y(x) - B_{yl}(x) \tag{6.24}$$

where $B_x(x)$ and $B_y(x)$ is the total glide and climb dislocation densities applied at a point x. Since $B_{rcx}(x)$ and $B_{rcy}(x)$ approach 0 for $x >> c$, the stress at remote points due to them can be approximated by that due to a pair of discrete glide dislocations each of magnitude b_x applied on either side of the origin and a pair of discrete climb dislocations of magnitude $-b_y$ and b_y also inserted on either side of the origin. This is taking into account the symmetry and the anti-symmetry of the required glide and climb dislocation distributions. The magnitude of the discrete dislocations are related to the corrective distributions by

$$b_x = \int_0^\infty B_{rcx}(x)dx, \tag{6.25}$$

$$b_y = \int_0^\infty B_{rcy}(x)dx. \tag{6.26}$$

The key assumption made here is that the stress field at remote points due to a distribution of dislocations near the origin can be approximated by that due to a discrete dislocation.

The total stress component at a remote point, x, can be said to be the sum of the components due to the bilateral loading, the pair of glide dislocations, the pair of climb dislocations, and the $B_{yl}(x)$ and $B_{xl}(x)$ dislocation distributions applied at all points along the interface. Table 6.1 shows the slowest decaying term in the expressions for the stress components at the remote point $(x, 0)$, where $x >> c$, due the bilateral loading and the different terms of the glide and climb dislocation

distributions and discrete dislocations inserted along the contact interface. Higher order terms are neglected. At remote point $(x,0)$ to satisfy the contact condition for separation

$$\frac{N(x)}{P/c} = \frac{-2}{\pi\hat{x}^4} - \frac{48M\hat{b_x}}{\hat{x}^4} + \frac{12\pi MF^*}{\hat{x}^4} - \frac{24Mk_l}{\hat{x}^4} - \frac{8Mk_2\pi}{\hat{x}^4} = 0, \tag{6.27}$$

$$\frac{S(x)}{P/c} = \frac{2}{\pi\hat{x}^3} + \frac{32M\hat{b_x}}{\hat{x}^3} - \frac{8\pi MF^*}{\hat{x}^3} + \frac{16Mk_l}{\hat{x}^3} + \frac{4M\pi k_2}{\hat{x}^3} = 0 \tag{6.28}$$

($F^* \equiv \frac{Fd(1+\kappa)}{2\mu\pi c}$, $\hat{x} \equiv x/c$ and $\hat{b_x} \equiv b_x/c$). It should be noted that the pair of corrective discrete climb dislocations, of magnitude b_y, has no significant effect on the contact tractions at remote points (the stress components due to it involve only higher order terms). From the above equations, it is deduced that

$$\hat{b_x} = \frac{-P(1+\kappa)}{16\mu c} - \frac{k_l}{2} + \frac{F\hat{d}(1+\kappa)}{8\mu c}. \tag{6.29}$$

($\hat{d} \equiv d/c$). $F\hat{d}/c$ parameter can be computed from the shear traction field from

$$\frac{F\hat{d}}{c} = \int_0^{\hat{b}} \hat{\xi} S(\xi) d\hat{\xi}. \tag{6.30}$$

Equation (6.24) leads to

$$\begin{aligned}\int_0^\infty B_x(x)dx &= \int_0^\infty B_{xl}(x)dx + \int_0^\infty B_{rxc}(x)dx \\ &= b_x + \int_0^\infty B_{xl}(x)dx\end{aligned}$$

On integration it is found that $\int_0^\infty B_{xl}(x)dx = 0$. So

$$\hat{b_x} = \int_0^\infty B_x(x)d\hat{x}. \tag{6.31}$$

Equations (6.30) and (6.31) in (6.29) give

$$M\int_0^\infty B_x(\xi)d\hat{\xi} = \frac{-1}{8\pi} + \frac{K}{2\pi} + \frac{1}{4\pi}\int_0^{\hat{b}} \hat{\xi}\frac{S(\xi)}{P/c}d\hat{\xi}. \tag{6.32}$$

($K \equiv k_l \frac{2\mu c}{(\kappa+1)P}$). This is a relationship between for the value of the total slip at remote points, the final slope of the layer and the shear traction when the contact conditions are met.

	Location	$\frac{\sigma_{yy}(x)}{P/c}$	$\frac{\sigma_{xy}(x)}{P/c}$
Line Load $-P$	$(0,1)$	$\frac{-2}{\pi\hat{x}^4}$	$\frac{2}{\pi\hat{x}^3}$
Discrete glide dislocations of magnitude b_x	$(\xi_1,0)$, $(-\xi_1,0)$	$\frac{-48M\hat{b_x}}{\hat{x}^4}$	$\frac{32M\hat{b_x}}{\hat{x}^3}$
Discrete climb dislocations of magnitude b_y and $-b_y$	$(\xi_2,0)$, $(-\xi_2,0)$	$\frac{-480M\hat{b_y}}{\hat{x}^6}$	$\frac{192M\hat{b_y}}{\hat{x}^5}$
Distribution of climb dislocations of density $sign(x)k_l$	$x \in [-\infty \quad \infty]$, $y=0$	$\frac{24Mk_l}{\hat{x}^4}$	$\frac{-16Mk_l}{\hat{x}^3}$
Distribution of climb dislocations of density $\frac{k_2}{\hat{x}}$	$x \in [-\infty \quad \infty]$, $y=0$	$\frac{-8Mk_2\pi}{\hat{x}^4}$	$\frac{4Mk_2\pi}{\hat{x}^3}$
Distribution of glide dislocations of density $\frac{F^*}{\hat{d}^2-\hat{x}^2}$	$x \in [-\infty \quad \infty]$, $y=0$	$\frac{12\pi MF^*}{\hat{x}^4}$	$\frac{-8\pi MF^*}{\hat{x}^3}$

Table 6.1: The slowest decaying terms of the normalised normal traction component and the normalised shear traction components at a remote point, $(x,0)$, due to the external loading, the discrete dislocations and the components of the preformed distributions of dislocations. ($F^* \equiv \frac{F\hat{d}(1+\kappa)}{2\mu\pi c}$, $M \equiv \frac{2\mu c}{\pi(\kappa+1)P}$, $\hat{b_x} \equiv b_x/c$ and $\hat{b_y} \equiv b_y/c$).

6.6 Results and Discussion

The normalised values of the location of the slip-stick transition point, $\hat{a}$, the slip-separation transition point, $\hat{b}$, and the final slope of the layer at remote points, k_l, have been obtained for different coefficients of friction from 0 to 1. See Figure 6.3. The results obtained here are compared with the those obtained by the Chaise model [61].[1] The location of the slip and separation regions are found to be independent of load. The slope of the layer at remote points as well as the relative slip and separation between the interfaces are found proportional to the applied normal load.

Top of figure 6.4 shows the climb dislocation density distribution, $B_y(x)$, for the case when $f = 0.5$, along with the applied distribution, $A_y(x)$, and the corrective bounded-bounded climb dislocation density, $B_{yc}(x)$. It is seen that the total climb dislocation density approaches the expected distribution for remote points. Bottom of figure 6.4 shows the glide dislocation density inserted, which also approaches the expected form at remote points, as given by equation (6.5). The parameter F is determined by numerical integration of the shear traction determined (with equation (6.1)), and the parameter d is determined similarly with equation (6.2).

Figure 6.5 shows the tractions along the contact surface obtained by the current model and those obtained by the simpler Chaise model are similar, except for points near the start of separation. This is most likely since the behaviour of the interface at remote points in this problem geometry had only a small affect on the stress field near the application of the load.

However significant differences are seen in the values obtained for the separation and slip along the interface for the two models. At the top of Figure 6.6, the separation between the layer and the half-plane according to the current model is seen to increase with x, and the increase becomes linear for large x. The expected slip at infinity is computed using the shear traction found from the current model and equation (6.32). The slip between the surfaces obtained from the current model approach this value, implying the displacements obtained with this model are physically consistent with the contact tractions found.

[1] Those values found by the Chaise model were obtained with $\lambda = 3.5$ and $N_{\hat{a}}, N_{\hat{b}} = 500$, – i.e. similar numerical parameters to that used in the model described in this chapter. The original published results from the Chaise model used a more unstable value of $\lambda = 5$, which was found not to provide adequate solutions when the coefficient friction was lower than 0.3. Acknowledgement to Thibaut Chaise for making available the code used in the Chaise model.

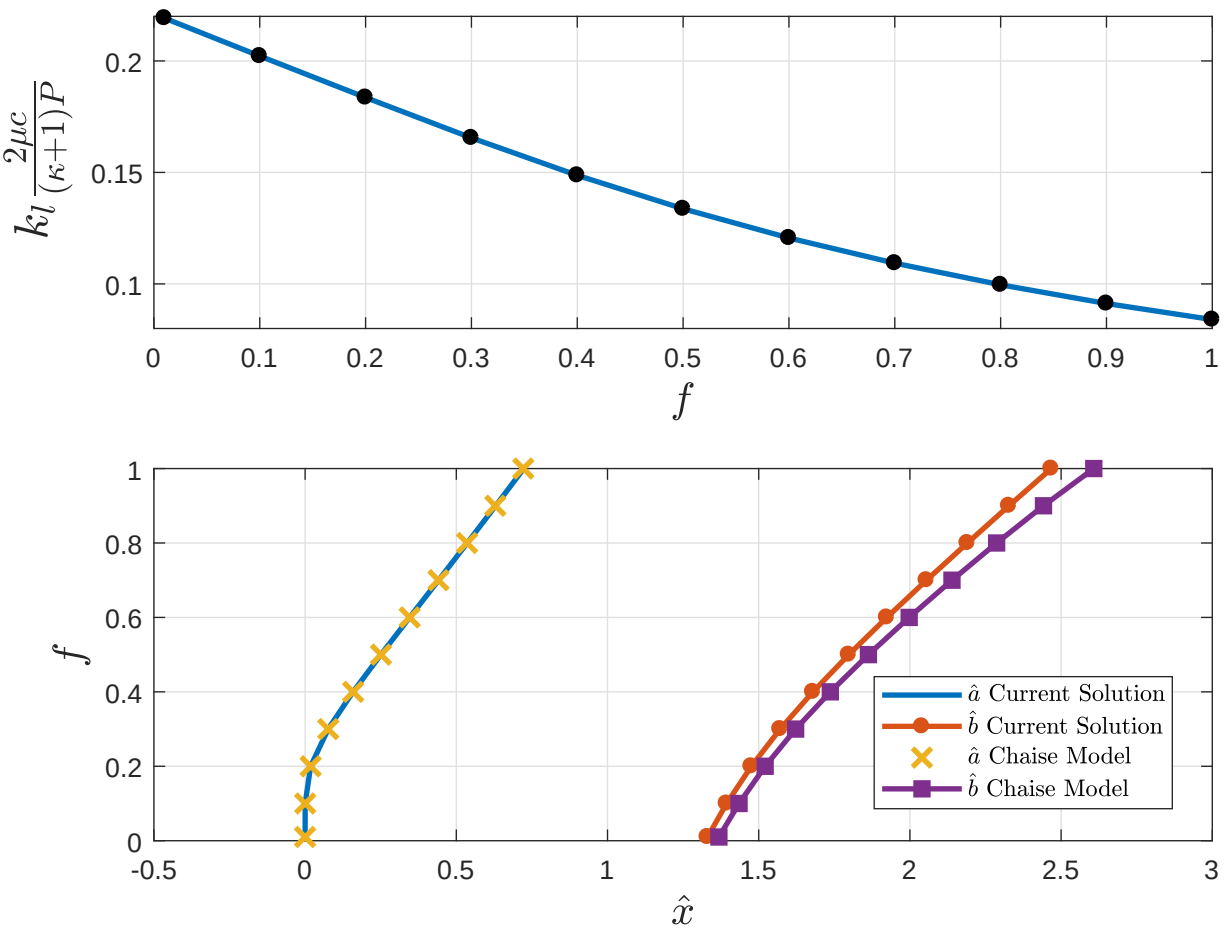

Figure 6.3: **Top**: Normalised slope of the layer at remote points. **Bottom**: Location of first points of slip and separation, $\hat{a}$ and $\hat{b}$, for different coefficients of friction.

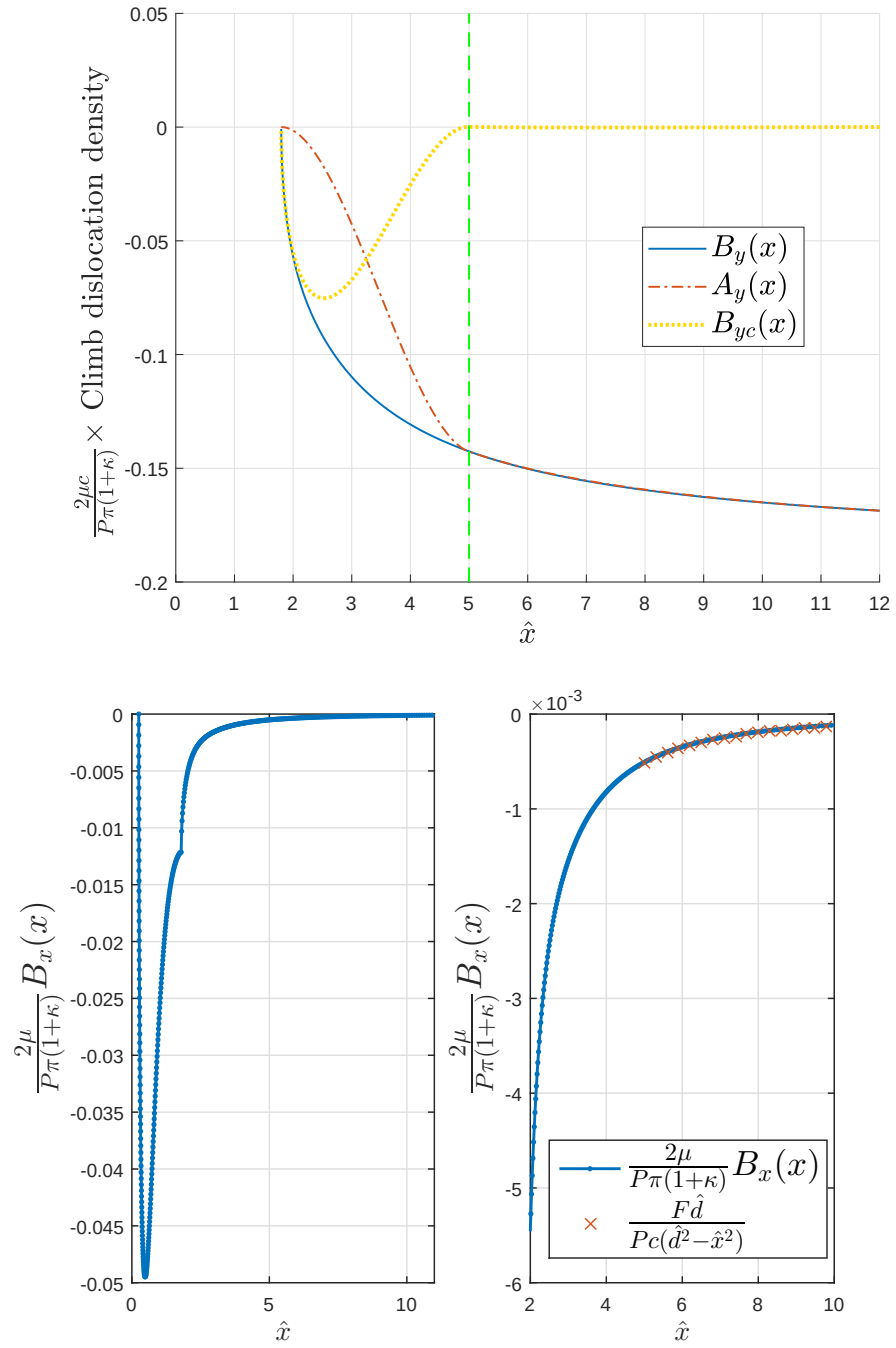

Figure 6.4: For $f = 0.5$. **Top**: The total climb dislocation density, $B_y(x)$, plotted with the preformed climb dislocation density, $A_y(x)$ and the corrective $B_{yc}(x)$ density. **Bottom left**: the normalised glide dislocation density. **Bottom right:** close up of the normalised glide density plotted with the form of the glide dislocation density at remote points given in equation (6.5).

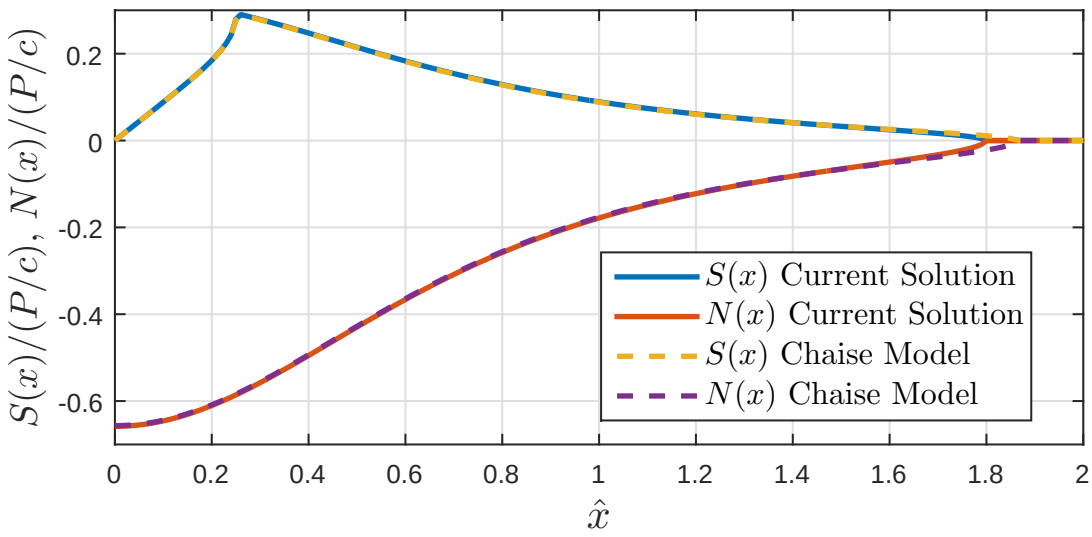

Figure 6.5: The shear and normal tractions from the current model compared with those from the Chaise model, for coefficient of friction, $f = 0.5$.

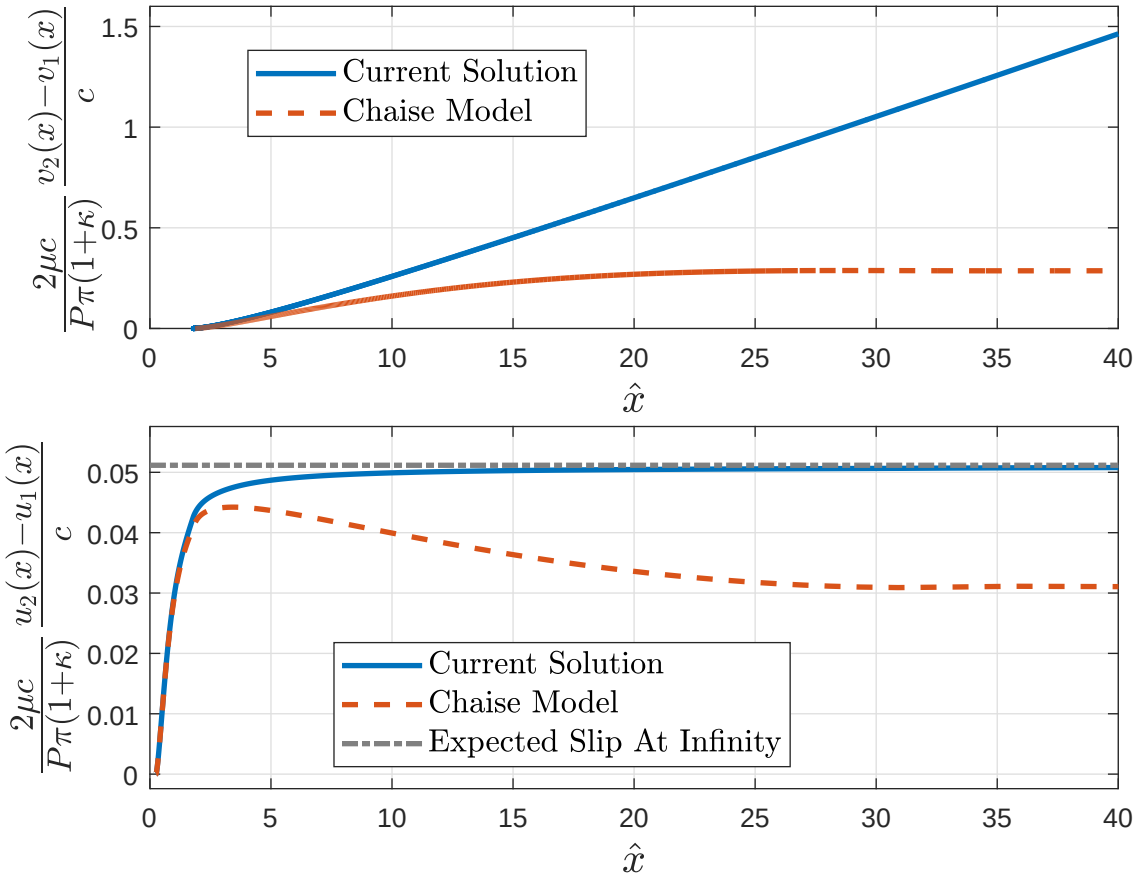

Figure 6.6: For $f = 0.5$, **Top**: Separation along the contact interface. **Bottom**: Relative slip along the interface. Results from the current model are compared with the results from the Chaise model.

6.7 Conclusions

A fundamental limitation in the conventional formulation employing 'distributed dislocations' to model a contact interface when separation extends to infinity has been overcome. This has been achieved by the insertion of preformed dislocation densities that ensures the correct form of interface displacements at remote points, and then superimposing a corrective 'bounded-bounded' distribution of dislocations to satisfy the conditions at near points. This method has been successfully applied to solve a basic frictional receding contact problem of a layer pressed onto an elastically similar half-plane by a line load. The method may be applied, *mutatis mutandis*, to other contact problems in which regions of slip and separation extend to infinity. In Chapter 7 the general solution process is applied to solve problems with different loading.

Chapter 7

Receding Contact Analysis with Pressure Loading Over a Finite Width

7.1 Introduction

In this Chapter, to demonstrate the applicability of the method derived in the previous Chapter, it is applied to solve three further receding contact problems, involving an infinity long layer pressed on a half-plane with similar linear elastic homogeneous material properties. The layer is of thickness c and is in contact with the half-plane $y \leq 0$. The problem loading and geometry for all three problems are as shown in Figure 7.1, and are as follows

1. Constant pressure patch problem: a constant pressure, $p(x) = -A_1$, applied over $x \in [-w \quad w]$ on the layer surface at $y = c$. A_1 is a constant.

2. Square root bounded (Hertzian) pressure patch problem: a pressure, $p(x)$, applied over $x \in [-w \quad w]$ on the layer surface at $y = c$ with the form

$$p(x) = -A_2\sqrt{w^2 - x^2}$$

   or,

$$\frac{p(x)}{A_2 c} = -\sqrt{\hat{w}^2 - \hat{x}^2}$$

   ($\hat{w} \equiv w/c$ and $\hat{x} \equiv x/c$). A_2 is a constant of dimensions FL^{-3}.

3. The square root singular pressure patch problem: a pressure, $p(x)$, applied over $x \in [-w \quad w]$ on the layer surface at $y = c$ with the form

$$p(x) = -\frac{A_3}{\sqrt{w^2 - x^2}}$$

or

$$\frac{p(x)}{A_3/c} = -\frac{1}{\sqrt{\hat{w}^2 - \hat{x}^2}}.$$

A_3 is a constant of dimensions FL^{-1}.

The constant pressure patch problem is the natural extension of the solution for the layer loaded by a line load. It is the solution for the simplest pressure distribution. While the constant pressure patch problem may be of theoretical interest, the square root bounded (Hertzian) pressure patch problem and the square root singular pressure patch problems have greater practical significance, since constant pressure never occurs in practice. The Hertzian pressure loading would approximately occur if the layer is loaded by, say, an elastic rod of circular cross-section, and the square root singular pressure loading would occur when the layer is loaded by a flat-faced frictionless rigid punch. The solutions to these problems contribute to the understanding of the fundamental properties of frictional receding contacts, and demonstrate the applicability of the method developed in Chapter 6 to other problems.

7.2 Outline of the Solution

All three problems will be solved by the application of distributions of dislocations. The layer and the half-plane will be modelled as a fused augmented half-plane $y \leq c$, with distributions of glide and climb dislocations applied at the location of the interface, $y = 0$. The problem for all three loading cases is symmetric. It is expected along the contact interface, as in the case of the problem studied in the last chapter, that there will be a region of stick at the centre, slip will occur in a region $x \in [a \quad \infty]$ and $x \in [-\infty \quad -a]$, and separation will occur in a region $x \in [b \quad \infty]$ and $x \in [-\infty \quad -b]$, with $a < b$.

The form of the glide and climb dislocation densities at remote points, $x/c >> 1$, will be derived for each problem as described in Chapter 6. The remote glide dislocation density will be shown to be bounded to zero in all three cases. Preformed climb dislocation densities of the appropriate form for remote points will be inserted. The stress components due to the external loading, the bilateral stress components, are derived as well as the stress components due to the preformed climb distribution. Corrective bounded-bounded climb dislocation density and bounded-bounded glide dislocation density distributions are found using Gauss-Chebyshev quadrature to satisfy the contact conditions and are superimposed. The tractions, the locations of slip and separation, the extent of slip and separation, and the slope of the layer at remote points are found for different widths of the area of pressure loading (w) and for different coefficients of friction (f).

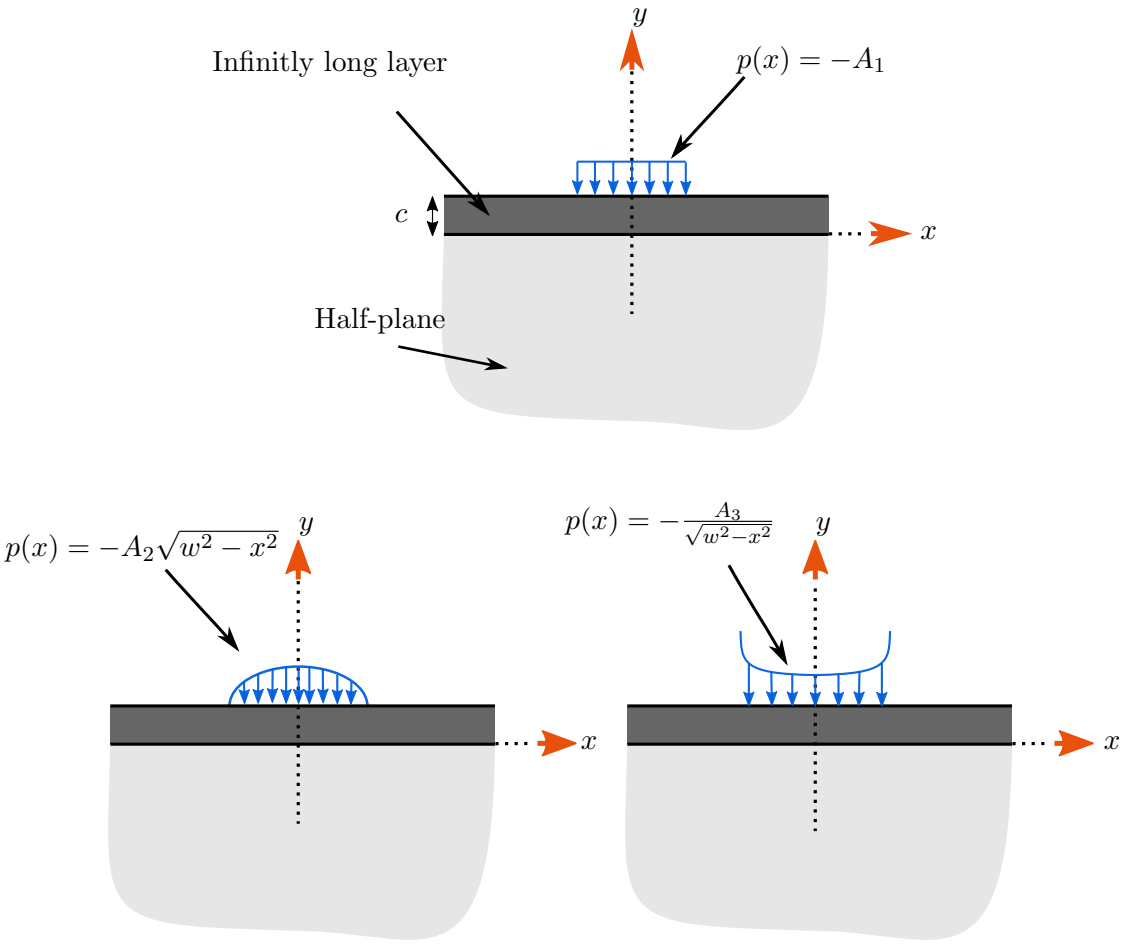

Figure 7.1: Schematic representation of the loading and geometry used in three receding contact problems. Pressure is applied along region of width $2w$. **Top**: the constant pressure patch problem. **Bottom left**: The square root bounded (Hertzian) pressure patch problem. **Bottom right**: The square root singular pressure patch problem.

7.3 Formulation

7.3.1 Bilateral Solutions

The bilateral solution for the half-plane, $y \leq c$, loaded by a finite patch of constant pressure was found from the Airy's function $\phi = -\frac{A_1}{2\pi}(r_1^2\theta_1 + r_2^2\theta_2)$ where r_1 and θ_1 are the radial and angular coordinates with the origin at $(-w, c)$ and r_2 and θ_2 are the radial and angular coordinates with the origin at (w, c). θ_1 is zero for points perpendicularly below $(-w, c)$ and is positive anti-clockwise. θ_2 is zero for points perpendicularly below (w, c) and is positive clockwise. See solution to problem 4 in [66, p. 167]. The normal and shear bilateral components at the location of the the interface, $y = 0$, for the constant pressure patch problem are given by

$$\frac{\sigma_{yyb1}(x)}{A_1} = \frac{-1}{\pi}\begin{pmatrix} -\tan^{-1}((\hat{x}-\hat{w})/1) + \tan^{-1}((\hat{w}+\hat{x}),1) + \\ \dfrac{2(\hat{w}-\hat{x})}{(\hat{x}-\hat{w})^2+1} + \dfrac{\left((\hat{w}-\hat{x})^2+1\right)(\hat{x}-\hat{w})}{\left((\hat{x}-\hat{w})^2+1\right)^2} + \\ \dfrac{(\hat{w}+\hat{x})}{(\hat{w}+\hat{x})^2+1} \end{pmatrix}, \tag{7.1}$$

$$\frac{\sigma_{xyb1}(x)}{A_1} = \frac{-1}{2\pi}\begin{pmatrix} \dfrac{2(\hat{w}-\hat{x})^2}{(\hat{x}-\hat{w})^2+1} - \dfrac{(\hat{w}-\hat{x})^2+1}{(\hat{x}-\hat{w})^2+1} \\ -\dfrac{2}{(\hat{x}-\hat{w})^2+1} + \dfrac{2\left((\hat{w}-\hat{x})^2+1\right)}{\left((\hat{x}-\hat{w})^2+1\right)^2} \\ + \dfrac{2(-\hat{w}-\hat{x})(\hat{w}+\hat{x})}{(\hat{w}+\hat{x})^2+1} + 1 \end{pmatrix}. \tag{7.2}$$

($\hat{x} \equiv x/c$ and $\hat{w} \equiv w/c$). $\tan^{-1}(x, y)$ is defined as the arctangent of a point with coordinate (x, y), i.e. taking into account the quadrant it is in.

For the Hertzian and square root singular pressure patch problems, the traction components at $y = 0$ were found by integrating the solution for a line load. From from equations (6.6) and (6.7) of Chapter 6, the bilateral normal and shear stress components, $\sigma_{yybPF}(x)$ and $\sigma_{xybPF}(x)$, at $y = 0$ due to a line load $-P$ applied at $(0, c)$ on the augmented half-plane $y \leq c$ are given by

$$\sigma_{yybPF}(x) = \frac{-2(P/c)}{\pi(1^2 + (\hat{x})^2)^2} \tag{7.3}$$

$$\sigma_{xybPF}(x) = \frac{2(\hat{x})(P/c)}{\pi(1^2 + (\hat{x})^2)^2}. \tag{7.4}$$

The bilateral components for a square root bounded pressure distribution are therefore

$$\sigma_{yyb2}(x) = \int_{-w}^{w} \left[\frac{-2}{\pi(1^2 + (x/c - \xi/c)^2)^2}\right] \left[(A_2/c)\sqrt{w^2 - \xi^2}\right] d\xi$$
$$\sigma_{xyb2}(x) = \int_{-w}^{w} \left[\frac{2(x/c - \xi/c)}{\pi(1^2 + (x/c - \xi/c)^2)^2}\right] \left[(A_2/c)\sqrt{w^2 - \xi^2}\right] d\xi.$$

Non dimensionalising with $x/c = \hat{x}$, $\xi/c = \hat{\xi}$, and $z/c = \hat{x}$ (with $d\xi = cd\hat{\xi}$), this becomes

$$\frac{\sigma_{yyb2}(x)}{A_2 c} = \int_{-\hat{w}}^{\hat{w}} \left[\frac{-2}{\pi(1^2 + (\hat{x} - \hat{\xi})^2)^2}\right] \left[\sqrt{\hat{w}^2 - \hat{\xi}^2}\right] d\hat{\xi} \tag{7.5}$$
$$\frac{\sigma_{xyb2}(x)}{A_2 c} = \int_{-\hat{w}}^{\hat{w}} \left[\frac{2(\hat{x} - \hat{\xi})}{\pi(1^2 + (\hat{x} - \hat{\xi})^2)^2}\right] \left[\sqrt{\hat{w}^2 - \hat{\xi}^2}\right] d\hat{\xi}. \tag{7.6}$$

Closed form expressions of these integrals in terms of $\hat{x}$ and $\hat{w}$ were obtained, but are too long to print.

Similarly, the bilateral components for the square root singular case can be written as

$$\sigma_{yyb3}(x) = \int_{-w}^{w} \left[\frac{-2}{\pi(1^2 + (x/c - \xi/c)^2)^2}\right] \left[\frac{A_3/c}{\sqrt{w^2 - x^2}}\right] d\xi,$$
$$\sigma_{xyb3}(x) = \int_{-w}^{w} \left[\frac{2(x/c - \xi/c)}{\pi(1^2 + (x/c - \xi/c)^2)^2}\right] \left[\frac{A_3/c}{\sqrt{w^2 - x^2}}\right] d\xi.$$

which on normalisation give

$$\frac{\sigma_{yyb3}(x)}{A_3/c} = \int_{-\hat{w}}^{\hat{w}} \left[\frac{-2}{\pi(1^2 + (\hat{x} - \hat{\xi})^2)^2}\right] \left[\frac{1}{\sqrt{\hat{w}^2 - \hat{\xi}^2}}\right] d\hat{\xi}, \tag{7.7}$$
$$\frac{\sigma_{xyb3}(x)}{A_3/c} = \int_{-\hat{w}}^{\hat{w}} \left[\frac{2(\hat{x} - \hat{\xi})}{\pi(1^2 + (\hat{x} - \hat{\xi})^2)^2}\right] \left[\frac{1}{\sqrt{\hat{w}^2 - \hat{\xi}^2}}\right] d\hat{\xi}. \tag{7.8}$$

Closed form expressions for these integrals were also obtained in terms of $\hat{x}$ and $\hat{w}$ but are also too long to print.

7.3.2 Dislocation Densities at Remote Points

In all three problems, as in Chapter 6, the layer is assumed to have straightened at remote points at $x >> c$, so

$$v_2(x) = k_l x + D_c$$

where $v_2(x)$ is the normal displacement of the layer interface with respect to the displacement of the point at the centre $(0, 0)$, and D_c is a constant. The normal surface displacement gradient of

the layer interface is therefore, at $x >> c$,

$$\frac{dv_2(x)}{dx} = k_l.$$

Further, it is assumed that, at $x >> c$, the layer is strain free, or

$$\frac{du_2(x)}{dx} = 0,$$

where $u_2(x)$ is the tangential displacement of the layer interface. The surface, $y = 0$ of the half-plane, $y \leq 0$, will deform due to the normal and shear tractions. As before, we assume the effect of the shear traction on remote displacement gradient can be modelled by a pair of line forces, F and $-F$, applied at point $(0, d)$ and $(0, -d)$, where

$$\int_0^\infty S(x) = F, \tag{7.9}$$

and

$$\int_0^\infty xS(x)dx = Fd. \tag{7.10}$$

Both F and d are not known *a priori*. In Chapter 6, the normal traction was modelled as an equivalent line force. However, so that the displacement gradients approach the form derived here nearer the origin (i.e. for smaller $\hat{x}$ values), the effect of the normal traction shall be modelled as the external pressure distribution, $p(x)$, applied directly on the half-plane ($y \leq 0$) surface ($y = 0$). Intuitively, this makes sense, since for $x >> c$, the thickness of the layer becomes negligible, and the half-plane ($y \leq 0$) can be visualised as being loaded normally by the external pressure loading[1].

The remote glide dislocation density for all three problems can now be shown in the same process as in Chapter 6 to have a form at remote points of

$$B_{xl}(x) = \frac{F^*}{\hat{d}^2 - \hat{x}^2}, \qquad x >> c, \tag{7.11}$$

where $F^* \equiv \frac{F\hat{d}(1+\kappa)}{2\mu\pi c}$, and $\hat{d} \equiv d/c$. The remote form of the glide dislocation density is therefore bounded at infinity, and the slip behaviour at remote points can be captured, as in Chapter 6, by a bounded-bounded glide dislocation density distribution.

[1] In Appendix B.2, it was shown mathematically that a normal traction can be modelled as a statically equivalent line load to find the remote displacement gradients of the half-plane ($y \leq 0$) surface. It should not be difficult to show in a similar manner that a normal traction can be modelled as a statically equivalent pressure.

The normal displacement of remote points of the surface of the half-plane, $y \leq 0$, loaded by a constant pressure distribution, in the constant pressure patch problem, is given by (derived from the Airy's Stress Function [2]), for $x > w$

$$v_2(x) = -\frac{A_1(1+\kappa)}{4\pi\mu}\bigg((x-w)\ln(x-w) - (w+x)\ln(w+x)\bigg).$$

Applying the shear force pair, F and $-F$, does not affect the above expression for $x >> c$, since the normal surface displacement due to a shear line load is a step function, and the contributions from each shear line load cancel out. The remote form of the climb dislocation density for the constant pressure patch problem is now derived for $x >> c$

$$\begin{aligned} B_{yl1}(x) &= -\frac{dV(x)}{dx} = -\bigg(\frac{dv_1(x)}{dx} - \frac{dv_2(x)}{dx}\bigg), \\ &= \frac{A_1(\kappa+1)}{4\pi\mu}\bigg(\ln(x+w) - \ln(w-x) - K_1\bigg), \\ &= \frac{A_1(\kappa+1)}{4\pi\mu}\bigg(\ln(\hat{x}+\hat{w}) - \ln(\hat{w}-\hat{x}) - K_1\bigg), \end{aligned} \tag{7.12}$$

where

$$K_1 = k_l\frac{4\pi\mu}{A_1(1+\kappa)}. \tag{7.13}$$

For the square root bounded pressure problem and the square root singular pressure problems, the remote normal displacement gradient of the half-plane ($y \leq 0$) surface ($y = 0$) is found by (from equation 12.27 of [66])

$$\frac{dv_2(x)}{dx} = -\frac{\kappa+1}{4\pi\mu}\int_{-w}^{w}\frac{p(\xi)}{x-\xi}d\xi. \tag{7.14}$$

Again the shear traction (or the pair of line loads) do not affect the normal surface displacement gradient at remote points. For the square root bounded pressure problem the remote surface displacement gradient of the half-plane ($y \leq 0$) surface ($y = 0$) on integration is seen to be

$$\frac{dv_2(x)}{dx} = A_2\frac{\kappa+1}{4\mu}\left(x - \sqrt{x^2-z^2}\right)$$

[2] See http://www-personal.umich.edu/ jbarber/elasticity/mathematica/catalogue.html [accessed 28/09/2017] for codes prepared by James Barber that deduce the displacement fields from a given Airy's stress function.

which leads to the glide dislocation density at remote points for this problem of this form

$$B_{yl2}(x) = (A_2 c)\frac{\kappa+1}{4\mu}\left(\hat{x} - \sqrt{\hat{x}^2 - \hat{z}^2} - K_2\right) \tag{7.15}$$

where

$$K_2 = k_l \frac{4\mu}{A_2 c(1+\kappa)}. \tag{7.16}$$

Similarly, the remote normal displacement gradient of the half-plane ($y \leq 0$) surface ($y = 0$) for the square root singular pressure problem is derived to be

$$\frac{dv_2(x)}{dx} = A_3 \frac{\kappa+1}{4\mu}\frac{1}{\sqrt{x^2 - z^2}}$$

which corresponds to a remote climb dislocation density of the following form

$$B_{yl3}(x) = (A_3/c)\frac{\kappa+1}{4\mu}\left(\frac{1}{\sqrt{\hat{x}^2 - \hat{z}^2}} - K_3\right) \tag{7.17}$$

where

$$K_3 = k_l \frac{4\mu}{(A_3/c)(1+\kappa)}. \tag{7.18}$$

7.3.3 The Preformed Climb Dislocation Distribution

A preformed climb dislocation density $A_y(x)$ distribution is inserted at the location of the contact interface, $y = 0$, for all three problems. As in Chapter 6, the function $A_y(x)$ is defined for positive x as follows

$$A_y(x) = \begin{cases} 0, & x < b, \\ R(x), & b \leq x \leq e, \\ B_{yl}(x) & x > e. \end{cases} \tag{7.19}$$

The function $A_y(x)$ should be anti-symmetric about the y axis and is defined accordingly for negative x. Here $B_{yl}(x)$ is the remote climb dislocation density distribution for each problem– given by the $B_{yl1}(x)$, $B_{yl2}(x)$, and $B_{yl3}(x)$ functions for the constant pressure problem, the square root bounded pressure problem and the square root singular pressure problem respectively, defined in equations (7.12), (7.15) and (7.17). e is a value sufficiently large such that at $x = e$, the

separation of the interfaces correspond to a climb dislocation density that would have approached the expected remote climb dislocation form ($e = 5c+w$ is found to be an appropriate value). $R_y(x)$ function is defined so that the $A_y(x)$ distribution is smooth and continuous and $R_y(b)$ is equal to 0. $R_y(x)$ function is defined here with a third order polynomial function, as was done in Chapter 6. For positive x it is given by

$$\begin{aligned} R_y(x) &= \frac{A_N(\kappa+1)}{4\mu}\left[R_{1y}(\hat{x}-\hat{b})^2 + R_{2y}(\hat{x}-\hat{b})^3\right] \\ &= \frac{A_N(\kappa+1)}{4\mu} r_y(x) \qquad\qquad b \le x \le e \end{aligned} \tag{7.20}$$

($\hat{b} \equiv b/c$). A_N is A_1 for the constant pressure problem, $A_2 c$ for the square root bounded pressure problem, and A_3/c for the square root singular problem. The coefficients $R_1 y$ and $R_2 y$ are found for each problem, as in Chapter 6, to ensure the continuity and the smoothness of the $A_y(x)$ function.

The stress components due to the preformed climb dislocation distribution are given by

$$\sigma_{yyA}(x) = \frac{2\mu}{\pi(1+\kappa)} \int_{-\infty}^{\infty} A_y(\xi) H_{yyy}(\hat{x},\hat{\xi}) d\hat{\xi} \tag{7.21}$$

$$\sigma_{xyA}(x) = \frac{2\mu}{\pi(1+\kappa)} \int_{-\infty}^{\infty} A_y(\xi) H_{yxy}(\hat{x},\hat{\xi}) d\hat{\xi}. \tag{7.22}$$

If

$$A_y(x) = \frac{A_N(\kappa+1)}{4\mu} a_y(x) \tag{7.23}$$

where $a_y(x)$ is a function involving $\hat{x}$, $\hat{\xi}$, $\hat{w}$, $\hat{b}$, $\hat{e}$ and K_N variables (K_N equals K_1, K_2 and K_3, for the constant pressure problem, the square root bounded pressure problem, and the square root singular problem, respectively), the above equations reduce to

$$\frac{\sigma_{yyA}(x)}{A_N} = \frac{1}{2\pi} \int_{-\infty}^{\infty} a_y(\xi) H_{yyy}(\hat{x},\hat{\xi}) d\hat{\xi}, \tag{7.24}$$

$$\frac{\sigma_{xyA}(x)}{A_N} = \frac{1}{2\pi} \int_{-\infty}^{\infty} a_y(\xi) H_{yxy}(\hat{x},\hat{\xi}) d\hat{\xi}, \tag{7.25}$$

The integral in equation (7.24) is singular and is evaluated in a Cauchy principal value sense. Closed form expressions for both stress components were obtained for the constant pressure patch problem (but are too long to print). A closed-form solution for the integral in equation (7.25) was also obtained for the square root bounded pressure problem. Solutions to the integral in equation (7.24) for the square root bounded pressure problem and the integrals in both equations for the

square root singular problem were obtained using a combination of closed-form expressions and numerical integration (the solutions are too long to print as well).

Obtaining values for these integrals poses the greatest difficulty in the solution process. The solution process is long and tedious. Particularly for complicated forms of remote climb dislocation density, it is suggested the solution of these integrals are attempted with a mix of closed form expressions and numerical integration. The general procedure is to write the integral as the sum of several integral terms. The solutions for the component terms can be re-used in problems with similar terms. Numerical integration was used for some component terms when they were regular. Closed form solutions for all the singular component integral terms were however required. Strategies to simplify and solve these integrals are discussed in Appendix B.3, particularly in reference to the square root singular problem.

7.3.4 The Integral Equations

The augmented half-plane ($y \leq c$) is subjected to external pressure loading, with the preformed climb dislocation density $A_y(x)$ applied at the location of the interface, $y = 0$, and two bounded-bounded dislocation densities $B_{yc}(x)$ and $B_x(x)$ superimposed at the location of the interface. The stress components along the interface are given by the superposition of the stress components due to the external loading (the bilateral components), the stress components due to the preformed distribution and the stress components due to the two bounded-bounded dislocation densities. The equations for the normal and shear traction components, $N(x)$ and $S(x)$, at a point $(x, 0)$ on the location of the interface are written (as in Chapter 6)

$$\frac{N(x)}{A_N} = \frac{\sigma_{yyb}(x)}{A_N} + \frac{\sigma_{yyA}(x)}{A_N} + M_n \left[\begin{array}{l} \displaystyle\int_{\hat{a}}^{\infty} B_x(\xi) H_{xyy}(\hat{x}, \hat{\xi}) d\hat{\xi} \\ + \displaystyle\int_{\hat{b}}^{\infty} B_{yc}(\xi) H_{yyy}(\hat{x}, \hat{\xi}) d\hat{\xi} \\ + \displaystyle\int_{-\infty}^{-\hat{a}} B_x(\xi) H_{xyy}(\hat{x}, \hat{\xi}) d\hat{\xi} \\ + \displaystyle\int_{-\infty}^{-\hat{b}} B_{yc}(\xi) H_{yyy}(\hat{x}, \hat{\xi}) d\hat{\xi} \end{array} \right], \tag{7.26}$$

$$\frac{S(x)}{A_N} = \frac{\sigma_{xyb}(x)}{A_N} + \frac{\sigma_{xyA}(x)}{A_N} + M_n \begin{bmatrix} \int_{\hat{a}}^{\infty} B_x(\xi) H_{xxy}(\hat{x},\hat{\xi}) d\hat{\xi} \\ + \int_{\hat{b}}^{\infty} B_{yc}(\xi) H_{yxy}(\hat{x},\hat{\xi}) d\hat{\xi} \\ + \int_{-\infty}^{-\hat{a}} B_x(\xi) H_{xxy}(\hat{x},\hat{\xi}) d\hat{\xi} \\ + \int_{-\infty}^{-\hat{b}} B_{yc}(\xi) H_{yxy}(\hat{x},\hat{\xi}) d\hat{\xi} \end{bmatrix}. \tag{7.27}$$

($\hat{a} \equiv a/c$, $\hat{b} \equiv b/c$, and $\hat{\xi} \equiv \xi/c$). Here

$$M_n = \frac{2\mu}{\pi(\kappa+1)A_N}.$$

$\sigma_{yyb}(x)$ and $\sigma_{xyb}(x)$ are the normal and shear bilateral stress components for each problem. $\sigma_{yyb}(x)$ is equal to $\sigma_{yyb1}(x)$, $\sigma_{yyb2}(x)$, and $\sigma_{yyb3}(x)$, for the constant pressure patch, square root bounded pressure, and square root singular problems, respectively, given by equations (7.1), (7.5) and (7.7); and $\sigma_{xyb}(x)$ is equal to $\sigma_{xyb1}(x)$, $\sigma_{xyb2}(x)$, and $\sigma_{xyb3}(x)$, for the constant pressure patch, square root bounded pressure, and square root singular problems, respectively, given by equations (7.2), (7.6) and (7.8).

Applying the contact conditions for slip and separation as in Chapter 6 (equations (6.16) and (6.17)), and changing the intervals of the integrals in equations (7.26) and (7.27) by making use of symmetry and anti-symmetry properties of the distributions, two integral equations are obtained

$$M_n \begin{bmatrix} \int_{\hat{a}}^{\infty} B_x(\xi) F_{xyy}(\hat{x},\hat{\xi}) d\hat{\xi} \\ + \int_{\hat{b}}^{\infty} B_{yc}(\xi) F_{yyy}(\hat{x},\hat{\xi}) d\hat{\xi} \end{bmatrix} = \frac{\sigma_{yyb}(x)}{A_N} + \frac{\sigma_{yyA}(x)}{A_N},$$

$$x \geq b, \tag{7.28}$$

$$M_n \begin{bmatrix} \int_{\hat{a}}^{\infty} B_x(\xi) L_x(\hat{x},\hat{\xi}) d\hat{\xi} \\ + \int_{\hat{b}}^{\infty} B_{yc}(\xi) L_y(\hat{x},\hat{\xi}) d\hat{\xi} \end{bmatrix} = \begin{bmatrix} -\left(\frac{\sigma_{xyb}(x)}{A_N} + \frac{\sigma_{xyA}(x)}{A_N}\right) \\ -H(\hat{b}-\hat{x}) f \left(\frac{\sigma_{yyb}(x)}{A_N} + \frac{\sigma_{yyA}(x)}{A_N}\right) \end{bmatrix},$$

$$x \geq a, \tag{7.29}$$

where

$$L_x(\hat{x},\hat{\xi}) \equiv F_{xxy}(\hat{x},\hat{\xi}) + H(\hat{b}-\hat{x})fF_{xxy}(\hat{x},\hat{\xi}),$$
$$L_y(\hat{x},\hat{\xi}) \equiv F_{yxy}(\hat{x},\hat{\xi}) + H(\hat{b}-\hat{x})fF_{yyy}(\hat{x},\hat{\xi}),$$

where

$$F_{xyy} \equiv H_{xyy}(\hat{x},\hat{\xi}) + H_{xyy}(\hat{x},-\hat{\xi}),$$
$$F_{yyy} \equiv H_{yyy}(\hat{x},\hat{\xi}) - H_{yyy}(\hat{x},-\hat{\xi}),$$
$$F_{xxy} \equiv H_{xxy}(\hat{x},\hat{\xi}) + H_{xxy}(\hat{x},-\hat{\xi}),$$
$$F_{yxy} \equiv H_{yxy}(\hat{x},\hat{\xi}) - H_{yxy}(\hat{x},-\hat{\xi}).$$

7.4 Discretization and Solution

The two integrals are discretized and solved as described in Chapter 6 but with some minor changes. Variable $s_{\hat{a}}$ is defined such that

$$\hat{\xi} = T_{\hat{a}}(s_{\hat{a}}) = \hat{a} + \lambda_{\hat{a}} \log\left(\frac{2}{1-s_{\hat{a}}}\right),$$
$$\frac{d\hat{\xi}}{ds_{\hat{a}}} = \frac{\lambda_{\hat{a}}}{1-s_{\hat{a}}},$$

and variable $s_{\hat{b}}$ is defined so

$$\hat{\xi} = T_{\hat{b}}(s_{\hat{b}}) = \hat{b} + \lambda_{\hat{b}} \log\left(\frac{2}{1-s_{\hat{b}}}\right),$$
$$\frac{d\hat{\xi}}{ds_{\hat{b}}} = \frac{\lambda_{\hat{b}}}{1-s_{\hat{b}}}.$$

The unknown functions, $B_x(\xi)$ and $B_{yc}(\xi)$, are assumed to be of the form

$$B_x(\xi) = \phi_x(s_{\hat{a}})\sqrt{1-s_{\hat{a}}^2},$$
$$B_{yc}(\xi) = \phi_{yc}(s_{\hat{b}})\sqrt{1-s_{\hat{b}}^2}.$$

The locations of the integration points, collocation points and the weight function in the Gauss-

Chebyshev quadrature to discretize of the integral equations are given as before by

$$s_{ji} = \cos\left(\frac{\pi i}{N_j+1}\right), \quad i = 1, ..., N_j, \quad j = \hat{a}, \hat{b},$$
$$t_{jk} = \cos\left(\pi\frac{2k-1}{2(N_j+1)}\right), \quad k = 1, ..., N_j+1, \quad j = \hat{a}, \hat{b},$$
$$w_j(s_{ji}) = \pi\frac{1-s_{ij}^2}{N_j+1}, \quad j = \hat{a}, \hat{b}.$$

In equations (7.28) and (7.29) the integral terms with the $F_{yyy}(\hat{x}, \hat{\xi})$ and $L_x(\hat{x}, \hat{\xi})$ kernals are Cauchy, respectively. Both these equations are evaluated at collocation points appropriate for these two integral terms. Note

$$\hat{x} = T_j(t_{jk}), \quad j = \hat{a}, \hat{b},$$

where t_{jk} is a collocation point, associated with integration points s_{ji}. The two integral equations discretized give

$$M_n \begin{bmatrix} \sum_i^{N_{\hat{a}}} F_{xyy}(T_{\hat{b}}(t_{\hat{b}k}), T_{\hat{a}}(s_{\hat{a}i}))w_a(s_{\hat{a}i})\phi_x(s_{\hat{a}i})\dfrac{\lambda_{\hat{a}}}{1-s_{\hat{a}i}} + \\ \sum_i^{N_{\hat{b}}} F_{yyy}(T_{\hat{b}}(t_{\hat{b}k}), T_{\hat{b}}(s_{\hat{b}i}))w_b(s_{\hat{b}i})\phi_{yc}(s_{\hat{b}i})\dfrac{\lambda_{\hat{b}}}{1-s_{\hat{b}i}} \end{bmatrix} =$$
$$-\frac{1}{A_N}\left[\sigma_{yyb}(T_{\hat{b}}(t_{\hat{b}k})c) + \sigma_{yyA}(T_{\hat{b}}(t_{\hat{b}k})c)\right],$$
$$\hat{x} \geq \hat{b}, \tag{7.30}$$

$$M_n \begin{bmatrix} \sum_i^{N_{\hat{a}}} L_x(T_{\hat{a}}(t_{\hat{a}k}), T_{\hat{a}}(s_{\hat{a}i}))w_a(s_{\hat{a}i})\phi_x(s_{\hat{a}i})\dfrac{\lambda_{\hat{a}}}{1-s_{\hat{a}i}} + \\ \sum_i^{N_{\hat{b}}} L_y(T_{\hat{a}}(t_{\hat{a}k}), T_{\hat{b}}(s_{\hat{b}i}))w_b(s_{\hat{b}i})\phi_{yc}(s_{\hat{b}i})\dfrac{\lambda_{\hat{b}}}{1-s_{\hat{b}i}} \end{bmatrix} =$$
$$\frac{1}{A_N}\begin{bmatrix} -\left(\sigma_{xyb}(T_{\hat{a}}(t_{\hat{a}k})c) + \sigma_{xyA}(T_{\hat{a}}(t_{ak})c)\right) \\ -H(b - (T_{\hat{a}}(t_{\hat{a}k})f\left(\sigma_{yyb}(T_{\hat{a}}(t_{\hat{a}k})c) + \sigma_{yyA}(T_{\hat{a}}(t_{\hat{a}k})c)\right) \end{bmatrix},$$
$$\hat{x} \geq \hat{a}. \tag{7.31}$$

These two equations provide $(N_{\hat{a}} + N_{\hat{b}})+2$ equations for $(N_{\hat{a}} + N_{\hat{b}})$ unknown $\phi_x(s_{\hat{a}i})$ and $\phi_{yc}(s_{\hat{b}i})$ values, and $\hat{a}$, $\hat{b}$, and K_N unknown parameters, for a given coefficient of friction, f, and the width of pressure distribution, w. A further condition is obtained by requiring the corrective climb dislocation density at the integration point nearest to $\hat{e}$ to approach zero, as in equation (6.22) in

Chapter 6.

In solving, $N_{\hat{a}}$ and $N_{\hat{a}}$ were both taken as 100, and $\hat{e}$ was taken as $5+\hat{w}$, though similar results can be obtained for different values of $N_{\hat{a}}$, $N_{\hat{a}}$ and $\hat{e}$. $\lambda_{\hat{a}}$ and $\lambda_{\hat{b}}$ the numerical parameter in the transform function, were taken as 2 for problems with $\hat{w} \leq 1$, though different values can be used, but solutions can become unstable when $\lambda_{\hat{b}} > 3$. For larger values of $\hat{w}$, λ_b was kept as 2, but $\lambda_{\hat{a}}$ was increased to 5 and in some cases for $\hat{w} > 10$, $\lambda_{\hat{a}}$ was taken as 10.[3]

7.5 Expected Slip at Remote Points

As in Chapter 6, the relationship between the total slip at infinity, the slope of the layer and the shear-traction can be found by modelling *afresh* the augmented half-plane with the dislocation distributions of the form appropriate for remote points inserted at the location of the interface at all remote points and all or some near points, and applying corrective pairs of discrete dislocations of both types near the origin. The slowest decaying normal and shear stress components at remote points due to the bilateral loading, the glide and climb dislocation densities, and the discrete dislocations are summed and equated to zero for remote points.

See Appendix B.4 for derivation of this relationship for the constant pressure patch problem. An identical process can be used to derive similar relationship for the square root bounded and square root singular pressure patch problems. The relationship for all three cases can be generalised to

$$\frac{\tilde{M}\int_0^\infty B_x(\xi)d\hat{\xi}}{T} = \frac{-1}{8\pi} + \frac{\tilde{M}k_l}{2T} + \frac{1}{4\pi}\int_0^{\hat{b}} \hat{\xi}\frac{S(\xi)}{T}d\hat{\xi}. \tag{7.32}$$

where

$$\tilde{M} = \frac{2\mu}{\pi(1+\kappa)}, \quad T = \left(\int_{-w}^{w} p(x)dx\right)/c. \tag{7.33}$$

For the constant pressure patch

$$T = 2A_1\hat{w}, \tag{7.34}$$

for the square root bounded pressure patch problem

$$T = \frac{\pi(A_2 c)\hat{w}^2}{2}, \tag{7.35}$$

[3]Larger $\lambda_{\hat{a}}$ is used when w is large to ensure the $B_x(x)$ distribution is evaluated at points relatively away from the origin, where it may have significant magnitude.

and for the square root singular pressure patch problem

$$T = \pi(A_3/c). \tag{7.36}$$

This is the exact same relationship for the layer loaded by a line load of magnitude Tc. This relationship is expected to be universal for all receding contacts involving a similar layer and half-plane loaded by symmetric finite pressure distributions.[4]

7.6 Results

Solutions were obtained for a variety of coefficients of friction and pressure patch widths for all three problems. Once the bounded-bounded glide dislocation density distribution and the corrective climb dislocation density are found, by numerical integration the traction components along the interface are determined by equations (7.26) and (7.27). The normalised normal and shear traction for positive $\hat{x}$ along the contact interface are plotted for all three problems for $f = 0.3$ and $\hat{w} = 1$ in Figure 7.2. It is seen from these plots that the contact conditions for stick, slip and separation are met.

The climb and glide dislocation distributions for positive $\hat{x}$ along the contact interface are shown in Figure 7.3 for the square root bounded pressure probblem for $f = 0.3$ and $\hat{w} = 1$. As seen in this figure, the climb dislocation density applied along the contact interface has approached the remote form given by the preformed distribution of dislocations, $A_y(x)$. It is seen that the corrective climb dislocation is near zero for all points $\hat{x} > \hat{e}$, where $\hat{e} = 6$ in this case. The glide dislocation density is seen to approach zero for large $\hat{x}$, as was deduced in the formulation, and approaches the form given in equation (7.11) for large $\hat{x}$. Numerical integration of the shear traction was used to evaluate the integrals in equations (7.9) and (7.10) to determine the parameters F and $\hat{d}$.

Furthermore, the normalised relative slip between the interfaces and normalised separation is given in Figure 7.4, for the square root bounded pressure patch problem with $f = 0.3$ and $\hat{w} = 1$. These values are found from numerical integration of the glide dislocation density, $B_x(x)$ and the total climb dislocation density, $B_y(x)$, inserted along the interface. For large $\hat{x}$, the normalised slip is seen to approach the value found from equation (7.32), on the basis of the normalised slope of the layer and the shear traction. This again confirms the relative displacements at the interface are of the required form.

Similar plots of the dislocation densities, interface slip and separation were obtained for all three problems for different coefficients of friction and $\hat{w}$ values. The locations of the stick-slip transition

[4] A short explanation is provided on why this relationship should be universal for similar problems with symmetric finite pressure loading in Appendix B.4.

point, $\hat{a}$, and the point of separation, $\hat{b}$, for $\hat{w} = 1$, is provided in Figure 7.5, for all three problems for different values of the coefficient of friction. For $\hat{w} = 1$, the normalised slope of the layer at remote points is plotted against coefficient of friction for the three different problems as well as for the line load problem of Chapter 6 in Figure 7.6. The slope of the layer is normalised with respect to the parameter, T, which is the total normal load divided by the thickness of the layer, c, as defined in equation (7.33). The value of T in terms of constants used to define the pressure loading in each finite pressure problem is given by equations (7.34), (7.35) and (7.36). It should be noted that the slope of the layer in all four loading situations decrease with the coefficient of friction and should approach zero at infinite friction.

Solutions were obtained for all three finite pressure patch problems for increasing values of $\hat{w}$. The solution process is seen to be robust and stable solutions were obtained even for very large values of $\hat{w}$. Figure 7.8 provides the climb and glide dislocation densities inserted for the constant pressure patch problem for $f = 0.3$ and $\hat{w} = 20$. The solution appears as neat as for the problems with smaller values of $\hat{w}$.

When $\hat{w}$ is made very big, the solution to the finite patch problems can be said to approach that of three semi-infinite loading problems. A coordinate x_e is defined from the edge of the pressure loading, i.e. $x_e = x - w$. The three semi-infinite pressure loading problems involve the top surface of the layer loaded along $x_e \in [-\infty \quad 0]$, as explained in Appendix B.5, with pressure distributions of the following forms:

1. Constant pressure loading, $\frac{p(x_e)}{B_1} = -1$
2. Square-root bounded pressure loading, $\frac{p(x_e)}{B_2\sqrt{c}} = -\sqrt{-\hat{x_e}}$
3. Square-root singular pressure loading, $\frac{p(x_e)}{(B_3/\sqrt{c})} = -\sqrt{-\hat{x_e}}$.

See Figure 7.7. The constants B_1, B_2, and B_3 are related to the parameters that define the finite loading problems (see Appendix B.5 for derivation) by

$$B_1 \approx A_1 \tag{7.37}$$

$$B_2\sqrt{c} \approx (A_2 c\sqrt{2\hat{w}}) \tag{7.38}$$

$$B_3/\sqrt{c} \approx \left(\frac{A_3}{c\sqrt{2\hat{w}}}\right). \tag{7.39}$$

The normalised slope of the layer at remote points for $f = 0.3$ for increasing $\hat{w}$ is plotted in Figure 7.9. The slope is normalised using the parameters B_1, B_2 and B_3. The normalised slope is seen to increase logarithmically with $\hat{w}$ for the constant pressure patch problem. For the square

root bounded problem, the normalised slope relationship with $\hat{w}$ is fitted with a curve of the form $\alpha_h\sqrt{\hat{w}} + \beta_h$, where α_h and β_h are fit parameters. Only for the square root singular problem does the normalised slope value seems to reach an asymptotic value for large $\hat{w}$. The locations of the stick-slip transition point, $\hat{a}$, and the point of separation, $\hat{b}$, for different $\hat{w}$, are provided in Figure 7.10 for $f = 0.3$. The values are plotted relative to the location of the edge of the pressure patches. For the constant pressure patch problem and the square root singular problem, the locations of slip and separation with respect to the edge of loading appear to approach a constant value with increasing $\hat{w}$. For the square root bounded problem, the location of the stick-slip transition point with respect to the edge of loading moves deeper into the area of the interface directly below the application of loading with greater $\hat{w}$, suggesting there might not be an asymptotic distance from the edge of loading towards which the location of the stick-slip transition point would approach. These results suggest that finite valued solutions for the slope of the layer may not be obtained for the semi-infinite problems with a constant pressure loading or a square root bounded loading.

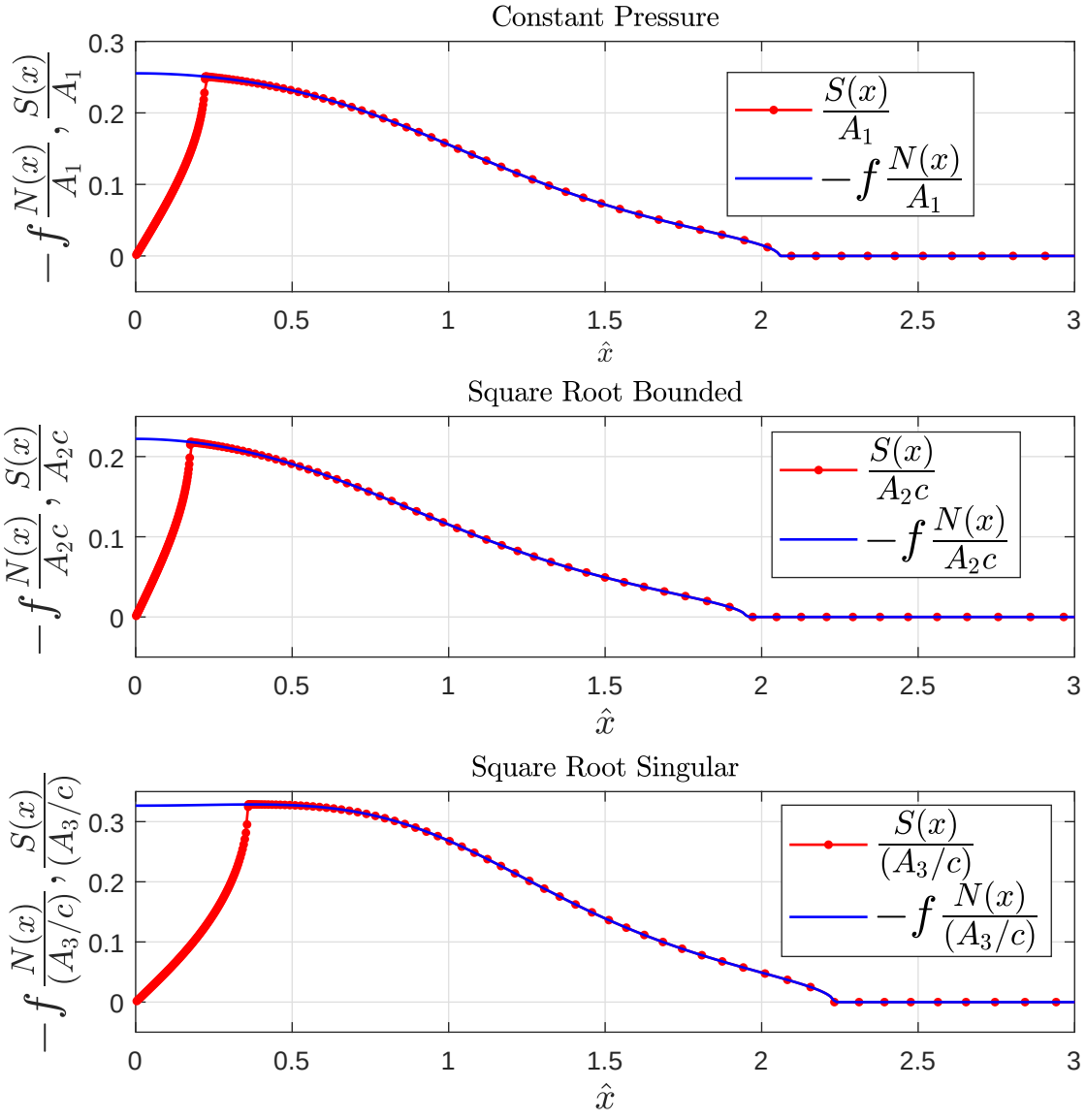

Figure 7.2: Normalised normal and shear traction along the contact interface plotted against $\hat{x}$ for the three problems for $f = 0.3$ and $\hat{w} = 1$.

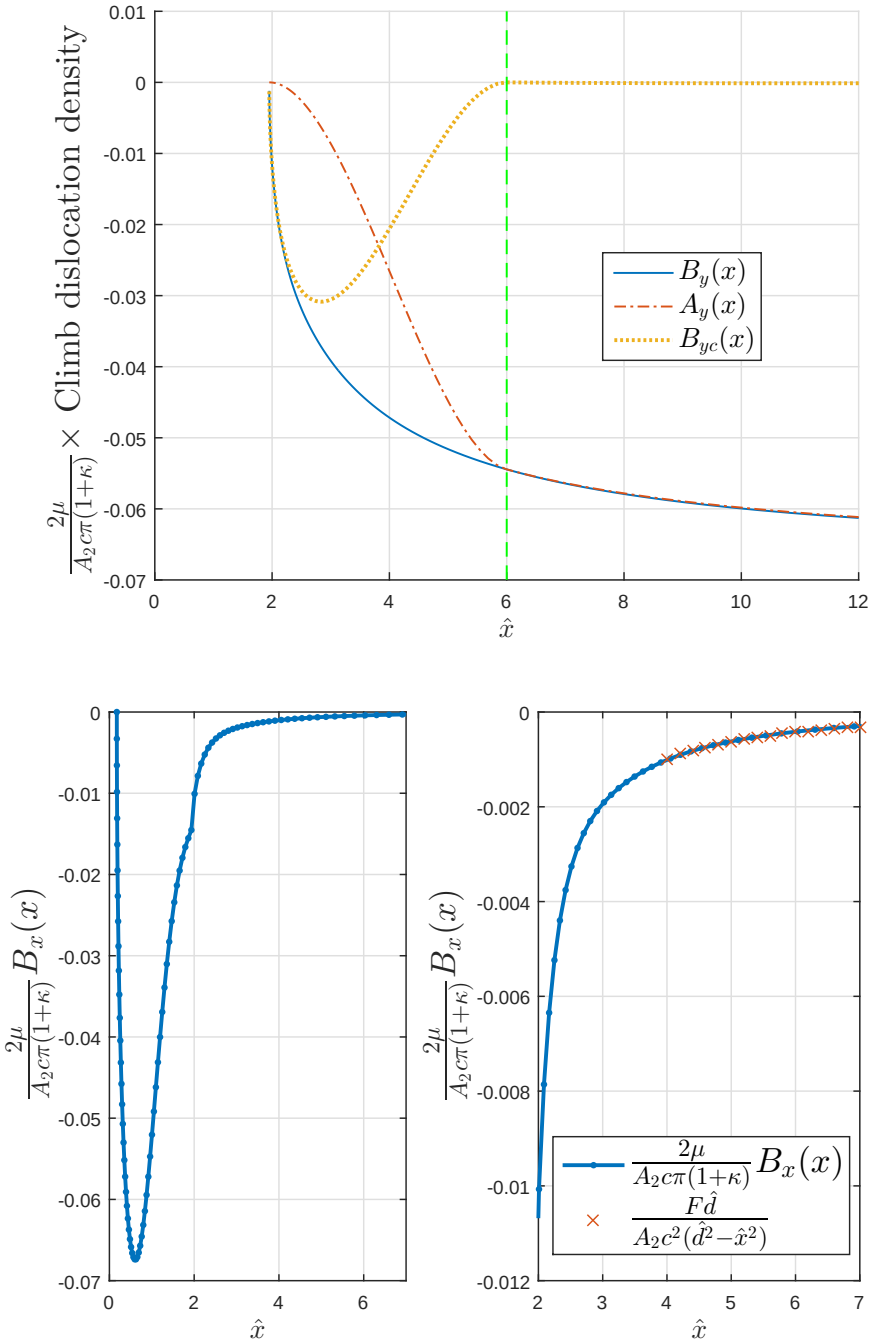

Figure 7.3: All plots are for the square root bounded pressure patch problem for $f = 0.3$ and $\hat{w} = 1$. **Top:** The total climb dislocation density, $B_y(x)$, plotted with the preformed climb dislocation density, $A_y(x)$, and the corrective $B_{yc}(x)$ density. **Bottom left**: the normalised glide dislocation density. **Bottom right:** close up of the normalised glide density plotted with the form of the glide dislocation density at remote points given in equation (7.11).

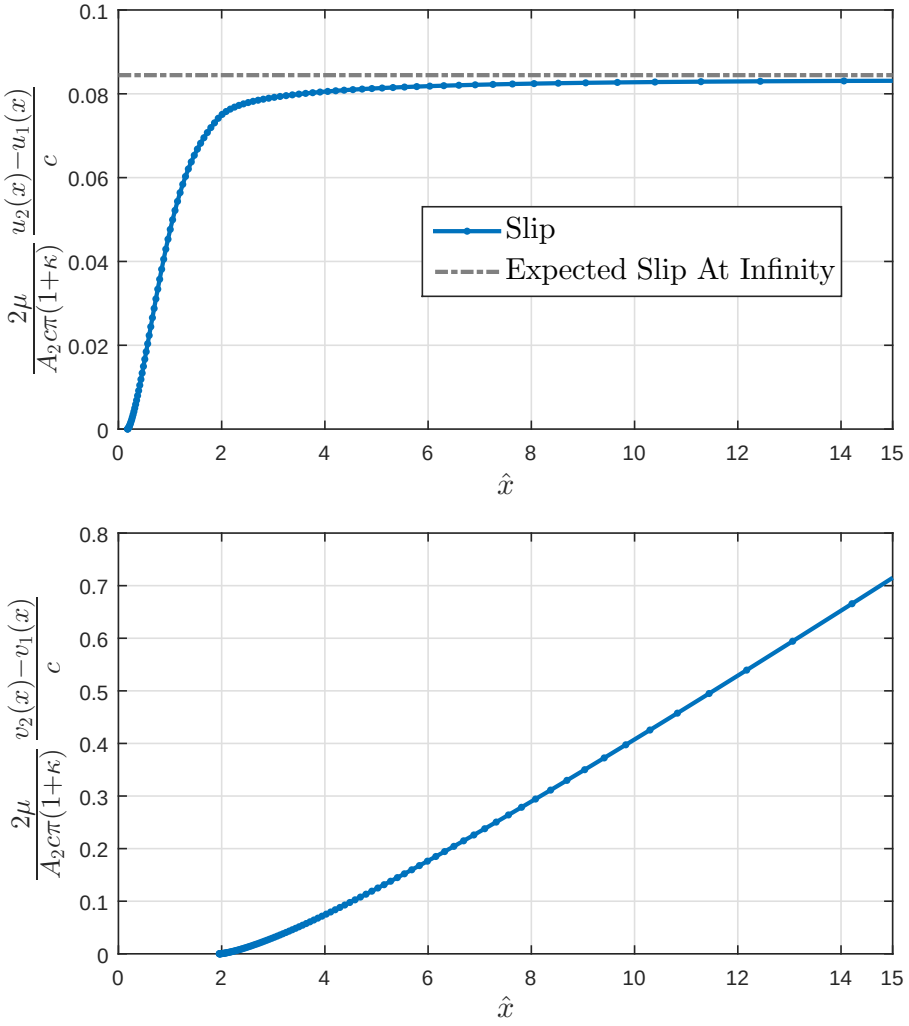

Figure 7.4: All plots are for the square root bounded pressure patch problem for $f = 0.3$ and $\hat{w} = 1$. **Top**: The normalised relative slip along the interface, plotted against $\hat{x}$, with the expected slip at infinity computed using equation (7.32). **Bottom**: the normalised separation of the surfaces along the contact interface, plotted against $\hat{x}$.

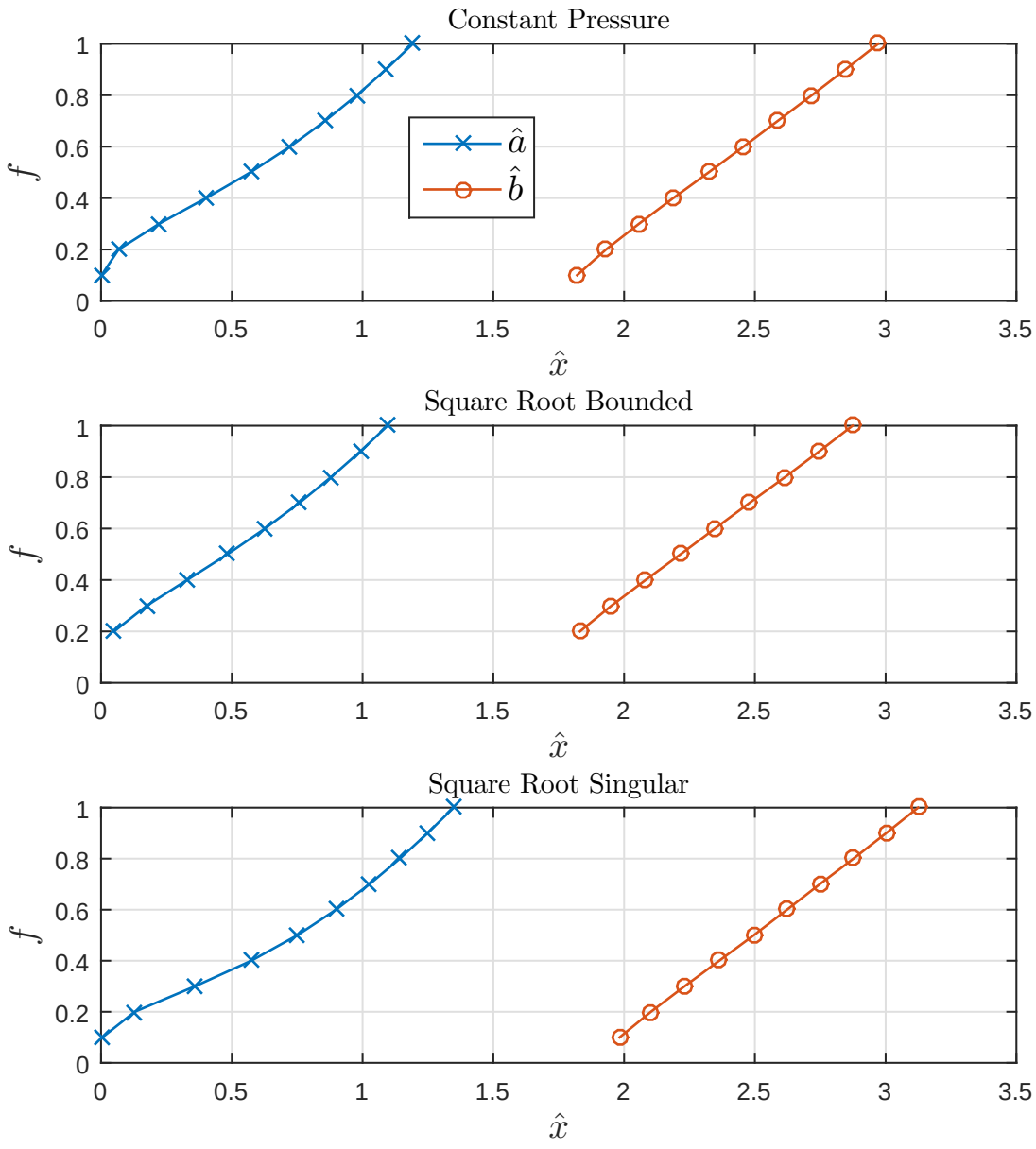

Figure 7.5: Location of slip-stick transition point, $\hat{a}$, and the point of separation, $\hat{b}$, along the contact interface, for different coefficients of friction, when $\hat{w} = 1$, for the three different problems.

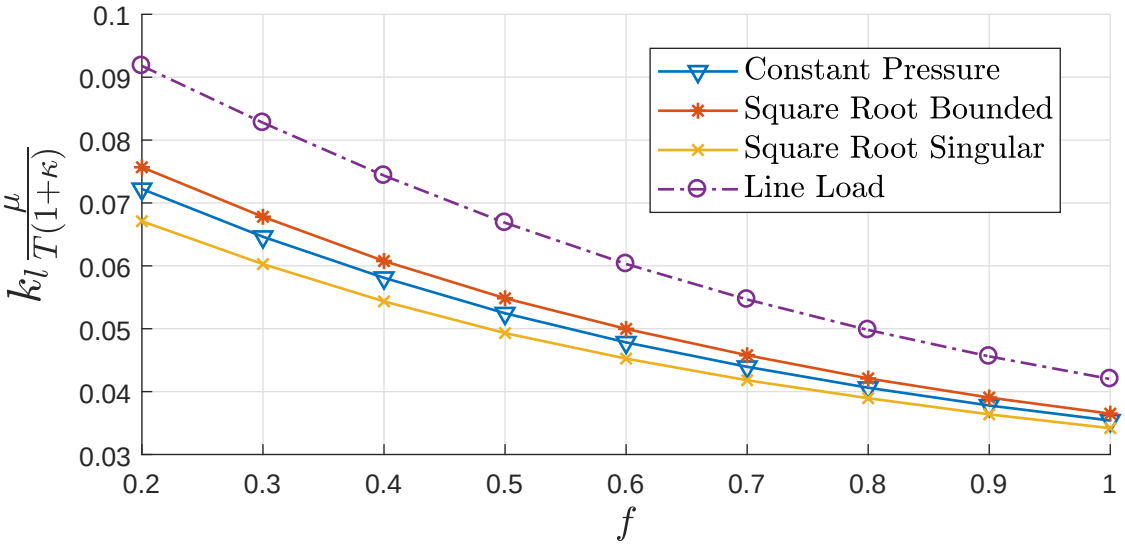

Figure 7.6: Normalised value of the slope of the layer ($k_l = \frac{dv_2(x)}{dx}$) at remote points for different coefficients of friction for $\hat{w} = 1$. The equivalent values for the line load problem (Chapter 6) are plotted. The slope of the layer is normalised with respect to the parameter, T, defined in equation (7.32).

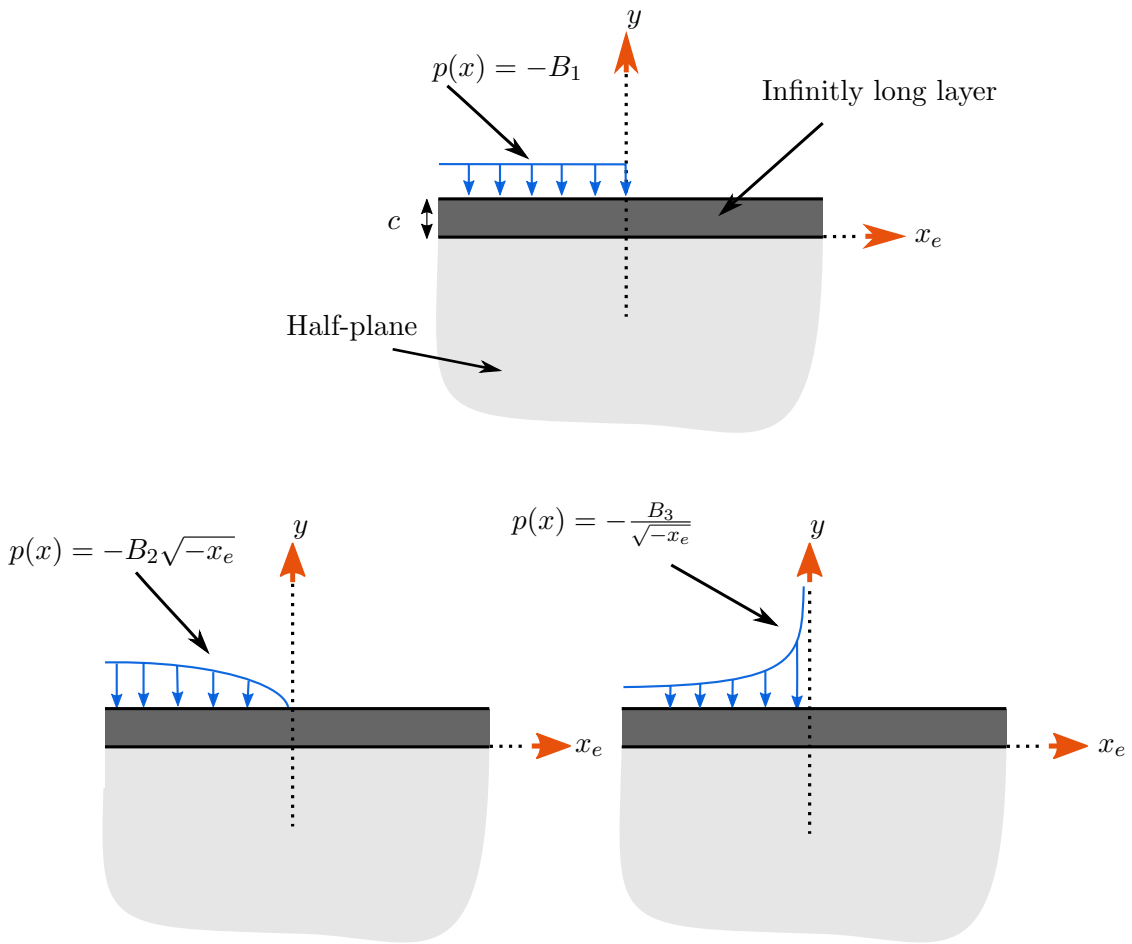

Figure 7.7: Schematic representation of the loading and geometry for the three semi-infinite pressure loading problems. Pressure is applied along region $x_e \in [-\infty \quad 0]$ on the free surface of layer. **Top**: the semi-infinite constant pressure problem. **Bottom left**: The semi-infinite square root singular pressure problem. **Bottom right**: The semi-infinite square root singular pressure problem.

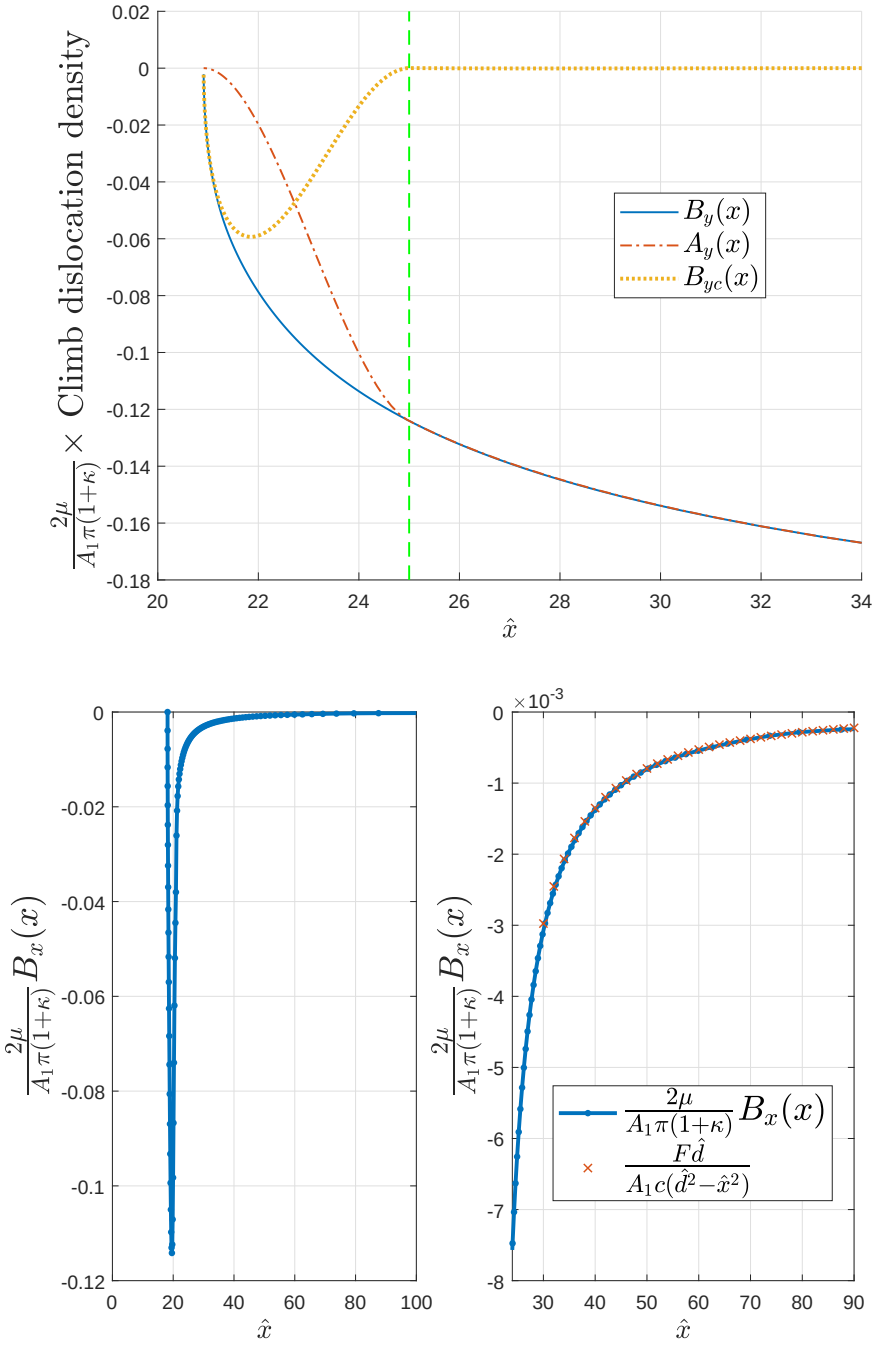

Figure 7.8: All plots are for the constant pressure problem for $f = 0.3$ and $\hat{w} = 20$. **Top**: The total climb dislocation density, $B_y(x)$, plotted with the preformed climb dislocation density, $A_y(x)$ and the corrective $B_{yc}(x)$ density. **Bottom left**: the normalised glide dislocation density. **Bottom right:** Close up of the normalised glide density plotted with the form of the glide dislocation density at remote points given in equation (7.11).

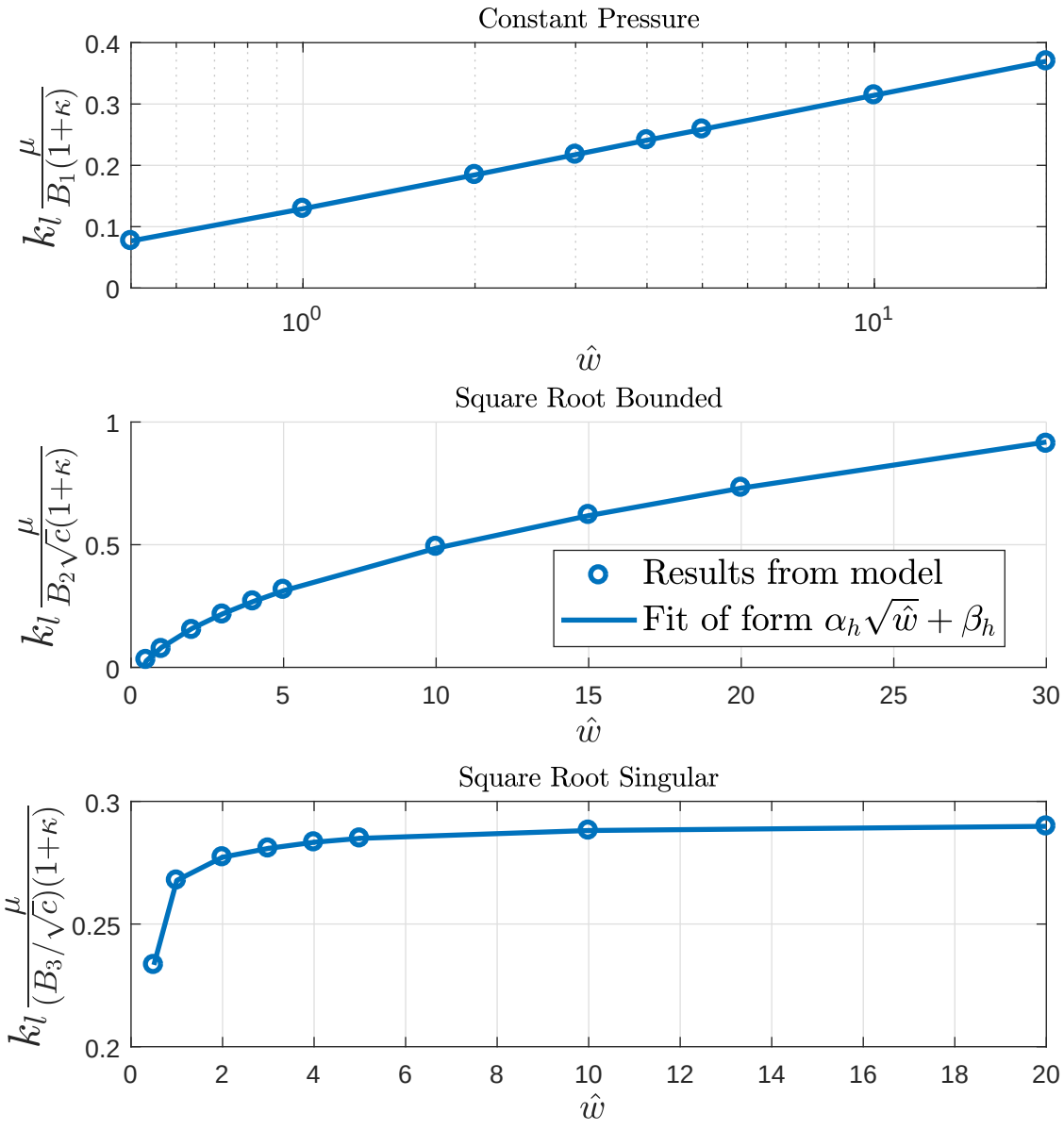

Figure 7.9: For $f = 0.3$, the normalised slope of the layer with increasing pressure patch half-width, $\hat{w}$, for the three problems. The slope is normalised using the parameters B_1, B_2 and B_3 defined in equations (7.37), (7.38) and (7.39).

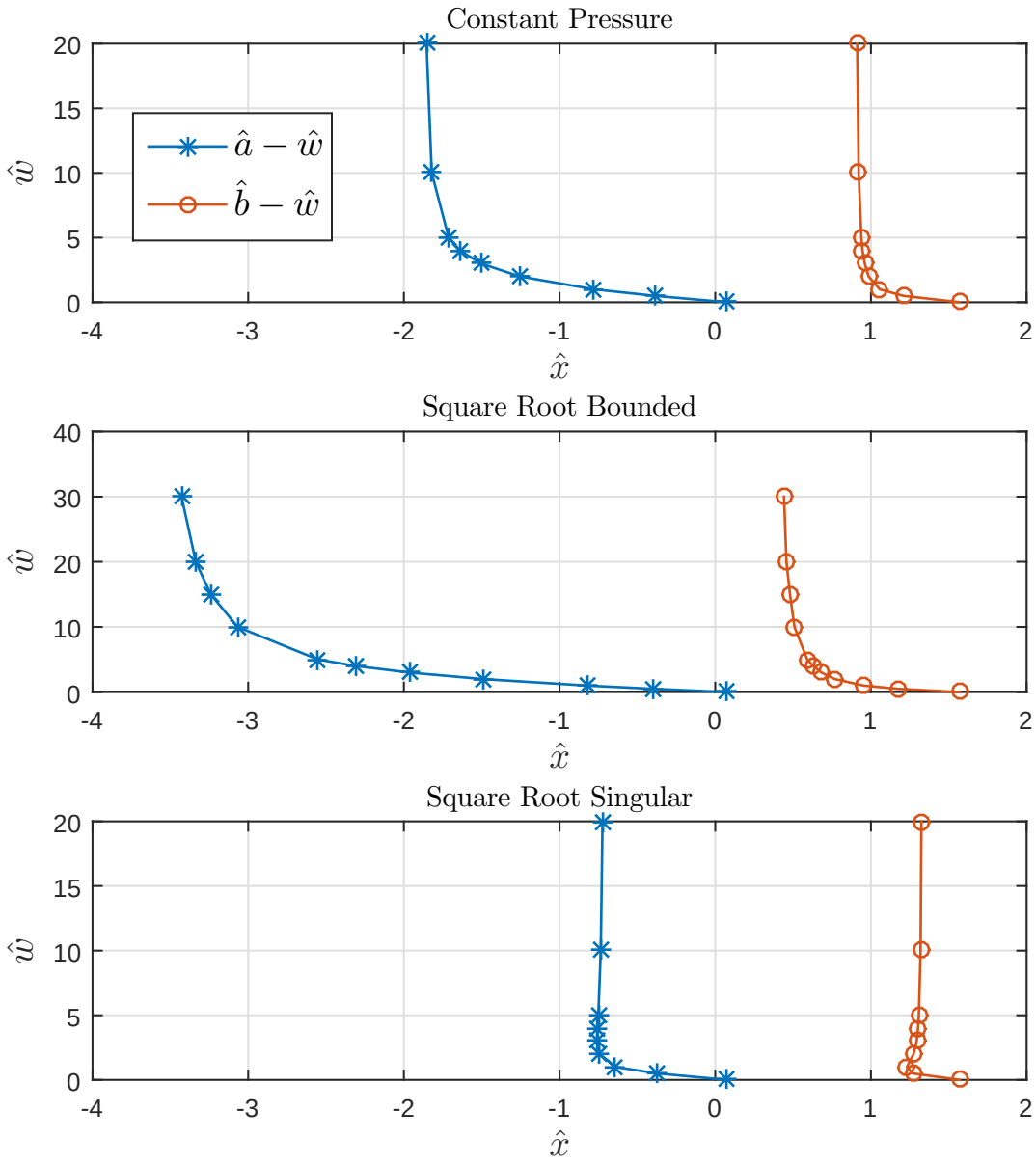

Figure 7.10: Location of slip-stick transition point, $\hat{a}$, and the point of separation, $\hat{b}$, along the contact interface, for different pressure patch half-widths, when $f = 0.3$, for the three different problems. Solution for the line load problem (Chapter 6) is used to provide the values at $\hat{w} = 0$.

7.7 Discussion and Concluding Remarks

The method developed in Chapter 6 has been applied to solve three receding contact problems with symmetrical pressure loading. High fidelity solutions for the contact tractions, locations and extent of slip and separation, as well as the slope of the layer at remote points have been obtained for a variety of coefficients of friction and pressure widths.

Various difficulties in implementing this method have been overcome. The first difficulty was to determine solutions for the bilateral stress components along the location of the interface. In the case of the constant pressure problem, the bilateral solution was found through the Airy's stress function for a half-plane surface loaded by a patch of constant pressure. Fortunately, this is a well known solution. For other pressure loading situations, particularly those that involve continuous distribution of pressure, integration of Flamant's solution, as was done for the square root bounded and square root singular problems, is identified as a straightforward means to obtain the bilateral solutions.

The second difficulty was to find the form of the glide and climb dislocation densities at remote points along the interface. For any problem involving symmetric normal loading, the glide dislocation density can be assumed to be bounded at infinity and of the form given in equation (7.11) for large $\hat{x}$. The form of the remote climb dislocation density is found from the gradient at remote points of the layer interface, which is assumed to be given by an unknown constant value, and the gradient of the half-plane interface at remote points. The gradient of the half-plane surface at remote points in the case of the constant pressure patch was found by differentiation of the vertical displacement of the half-plane surface with respect to x. In the case of more complex pressure loading situations, the gradient of the half-plane surface can be obtained directly from equation (7.14), as was done for the other two problems.

The third and probably the most tedious and time consuming difficulty in the solution process was to find the stress components along the interface due to the preformed dislocation density distribution inserted. As shown in Appendix B.3, symmetry and anti-symmetry was used to simplify the solution process, and some component integral terms for some intervals can be solved numerically.

The final difficulty that has been overcome was to solve for situations when the width of the pressure patch is made very large. High fidelity solutions were obtained by using larger values of $\lambda_{\hat{a}}$. This ensures the glide dislocation distribution, $B_x(x)$, is computed at integration points relatively far away from the origin, where its value is not negligible when the pressure patch is made wide.

In addition, a universal relationship for all receding contacts with the similar layer and half-plane interface loaded by symmetrical pressure distirbution has been identified, and is given in equation

(7.32). This equation stipulates a relationship between the total slip at infinity, the normalised slope of the layer at remote points and the shear traction. The results from all three problems for different coefficients of friction and pressure widths satisfy this relationship.

The results from all three problems show that the location of slip and separation are load independent, though the slope of the layer is inversely proportional to the parameters A_1, $A_2 c$ and A_3/c for the three problems, for a given f and $\hat{w}$. By solving the problems with increasing pressure patch widths, it is concluded that a finite solution for the slope of the layer will not be obtained for a constant semi-infinite pressure distribution or a semi-infinite square root bounded distribution. Further for the square root bounded pressure problem, the location of slip with respect to the edge of loading is not seen asymptotic.

Chapter 8

Finite Element Analysis of Frictional Receding Contacts

8.1 Introduction

Finite element analysis (FEA) modelling is a powerful means of solving a large variety of solid-mechanics problems. It is, however, currently not very adept at solving receding contact problems. The separation of interfaces on the application of infinitesimally small normal load makes obtaining convergence of finite element models difficult. Furthermore, finite element models require boundary conditions, which are *a priori* unknown, to be applied to the edges of the finite bodies modelled, such as when solutions are sought for interfaces between semi-infinite bodies. The results, when obtained, are of questionable accuracy since the finite element method itself has not been validated in the study of receding contacts. Part of the reason for solving the semi-infinite receding contact problems in this thesis by the distributed dislocations technique (DDT) was because of the difficulty in modelling these contacts currently with finite element methods.

Nonetheless 2D finite element models were constructed with the commercial software Abaqus CAE (static analysis) to see how the results from finite models compare with the solutions for the semi-infinite problems by the insertion of dislocations, as described in Part III of this thesis. The models, limitations, convergence analysis and the results are described in this chapter. Further, some discussion is provided on possible means to develop more advanced models.

In all of the finite element models presented here, the infinitely long layer is modelled as a finite strip and the half-plane as a finite block. Both the strip and the block are homogeneous solids. Linear elastic plane strain elements were used[1]. The interface is modelled with a Coulomb friction law modelled with a Lagrangian multiplier friction formulation to avoid the interpenetration of

[1]Models were also run with plane stress elements and the results when normalised with respect to the appropriate Kolosov's constant match those from the plain strain models.

contact nodes (as in the penalty formulation). The surface of the half-plane is assigned as the 'master' and the surface of the layer is assigned 'slave' in the interaction properties.

8.2 The finite element models and results

8.2.1 Finite element modelling of semi-infinite pressure distribution problem

Of the receding contact problems studied in this thesis, the problem addressed in Chapter 5 is by far the easiest to model with finite elements. The problem loading and geometry was chosen to avoid large areas of the interface moving out of contact, and hence avoids the complications of the more fundamental problems of Chapters 6 and 7. Consequently obtaining convergence was relatively straightforward. Since the loading is symmetric only half of this problem needed to be modelled.

See Figure 8.1 for the problem loading, and boundary conditions. The left edge of both the layer and the block are constrained with symmetry boundary conditions about the y-axis. (The x axis is parallel to the interface and the y axis in parallel with loading applied. In presenting the results the origin is taken to be on the interface at the left edge of the model). The pressure loading of 1 N/mm^2 is applied everywhere on the free surface of the layer except over a region of finite width– 2.5 mm next to the left edge. The right side edge of the block is unconstrained and the bottom edge is constrained to not move in the y-direction. The layer is 20 mm x 1 mm and the block has dimensions 20 mm x 20 mm. The loading is similar to the semi-infinite problem of Chapter 5 with $\hat{w} = 2.5$.

Linear elements of CPE4R and CPE3 kind were used with a total of 303,571 elements[2]. A dense structured mesh (with quadrilateral elements) was generated near the contact in the areas of interest, i.e. near regions of expected slip and separation. The mesh is shown in Figure 8.2. The average element size applied in the region of interest along interface is 0.01 mm, this was next to 7 mm of the contact interface adjacent to the left edge. Material properties of Young's modules of 200,000 N/mm^2 and Poisson's ratio of 0.3 were assigned (chosen arbitrarily, since the results are normalised). Models of smaller dimensions and coarser mesh had been constructed initially. As with the modelling of the other problems, both the model dimensions and the mesh density were increased until the results obtained were seen not to be affected significantly by any further refinement of the mesh or increase in length of the strip and the block. Since the region of separation of surfaces is relatively small (< 10 mm), there was no difficulty in obtaining results for models of larger dimensions (unlike the models for the other problems).

See Figures 8.3, 8.4, 8.5 and 8.6 for the tractions, separation and relative slip along the interface

[2]300,735 linear quadrilateral elements CPE4R and 2,836 linear triangular elements CPE3 were used.

obtained from this model for a coefficient of friction of 0.5. The results are compared with the results obtained from Chapter 5 for the semi-infinite case with $N = 100$. (The origin is at the interface directly below the centre of the no pressure zone, – in the finite element model it is at left edge.) There are two key implications of the results. First, the tractions and the interface behaviour for a finite model are well approximated by the solution for an infinitely long layer pressed on a half-plane. This implies the semi-infinite solutions provide accurate estimation for the interface behaviour of some contacts of finite lengths. Secondly, both methods have led to similar results, and therefore support the conclusions from each other.

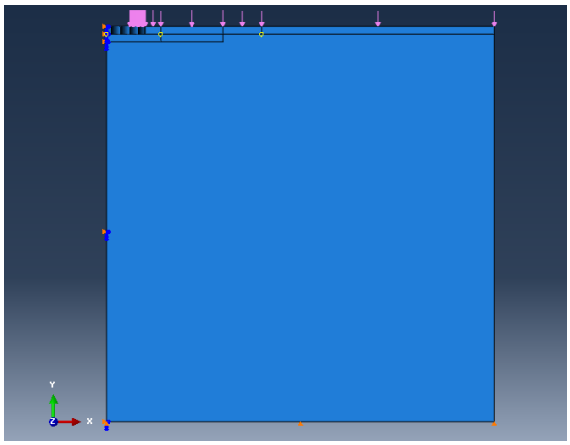

Figure 8.1: The finite element model of the two semi-infinite pressure patch problem. Symmetry boundary conditions are applied to the layer and block left edge. The base edge of the block is restricted in the normal direction.

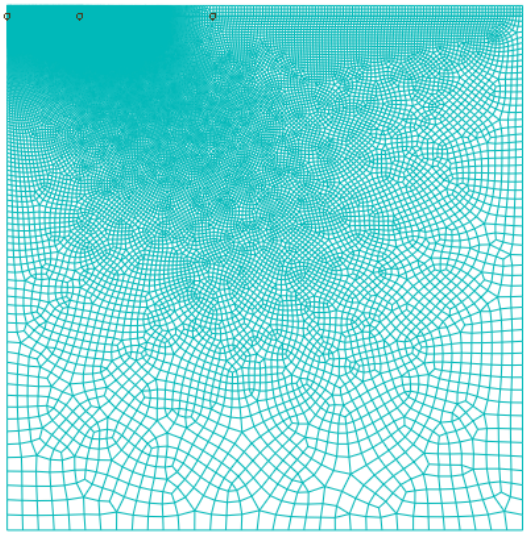

Figure 8.2: The mesh applied to discretize the problem. Dense structured mesh is applied near the interface adjacent to the left edge where locations of slip and separation are expected.

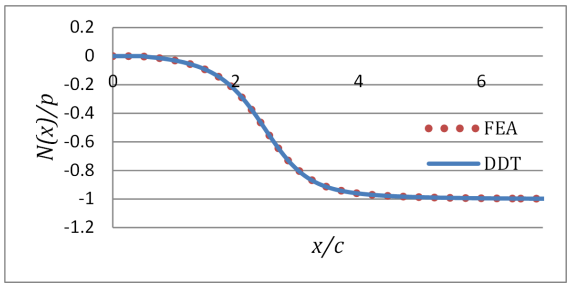

Figure 8.3: Normal traction along the interface obtained from the finite element model compared with results of the distributed dislocations technique with $N = 100$. $\hat{w} = 2.5$ and $f = 0.5$.

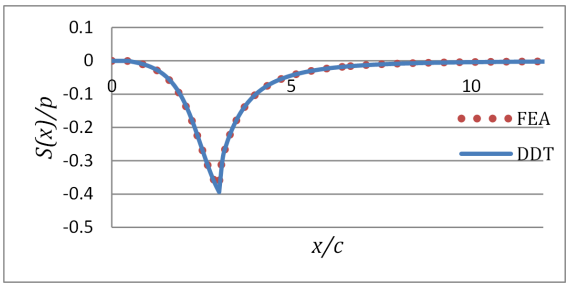

Figure 8.4: Shear traction along the interface obtained from the finite element model compared with results of the distributed dislocations technique with $N = 100$. $\hat{w} = 2.5$ and $f = 0.5$.

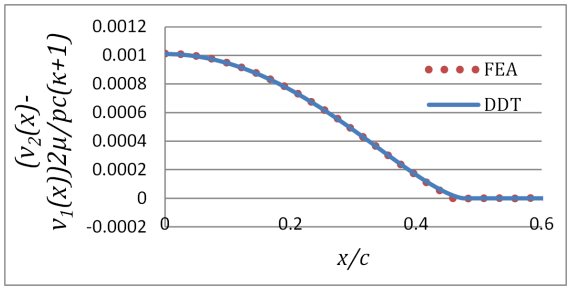

Figure 8.5: Separation along the interface obtained from the finite element model compared with results of the distributed dislocations technique with $N = 100$. $\hat{w} = 2.5$ and $f = 0.5$.

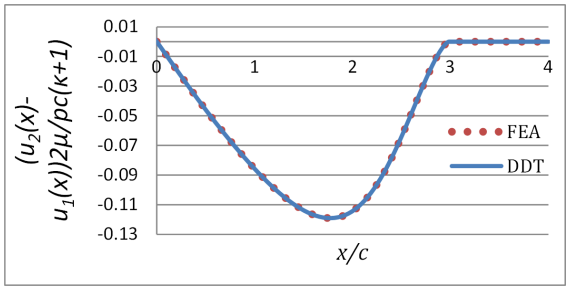

Figure 8.6: Relative slip along the interface obtained from the finite element model compared with results of the distributed dislocations technique with $N = 100$. $\hat{w} = 2.5$ and $f = 0.5$.

8.2.2 Finite Element Modelling of the Layer Pressed by a Line Load

A finite strip on a block is loaded by a line load at the centre of the free surface of the layer to study a similar problem to that studied in Chapter 6. The full geometry was modelled, to avoid applying a singular force at the edge of a model with symmetry conditions[3][4]. See loading and the boundary conditions in Figure 8.7. The strip has dimensions 20 mm x 1mm and the block dimensions of 20 mm x 20 mm. A line load of 1 N/mm is applied at the centre point of the free surface of the strip. The dimensions and the boundary conditions were restricted by the difficulties of obtaining solutions for models with larger dimensions and different boundary conditions. Figure 8.8 shows the mesh generated. Material properties of Young's modulus of 20,000 N/mm^2 and Poisson's ratio of 0.3 were assigned to both the strip and the block. Linear plane strain elements of type CPE4R and CPE3 were used. A finely structured mesh (quadrilateral) was generated throughout the layer and region of the block near the interface (to depth of 1 mm from the interface). The average element size of these elements is 0.01 mm. In total 637,133 elements were used[5]. Solution was obtained with encastre boundary conditions on the side edges. A solution was not obtained for this geometry when the side edges of the half-plane were unconstrained or constrained only in the y-direction.

Figures 8.9 and 8.10 show the contact tractions obtained from this model along the interface for a coefficient of friction of 0.5. As seen both the normal and tangential contact tractions match the results from the distributed dislocation technique obtained in Chapter 6. (The origin is at the centre point of the interface directly below the point of loading). Figures 8.11 and 8.12 show the interface separation and the relative slip along the interface. The separation predicted by the finite element analysis and the analysis with distributed dislocations are almost identical, and so

[3]Solutions were not obtained for a model of equivalent dimensions constructed using a symmetry boundary condition.

[4]Application of cyclic tangential load was applied to this model in subsequent steps for a separate study published in *Tribology International* [67]

[5]633,659 linear quadrilateral plane strain CPE4R elements and 3,474 linear triangular plane strain CPE3 elements.

is the relative slip for locations along the interface near the area of loading ($\hat{x} \leq 1.5$). There is some significant discrepancy in the slip at remote points. This is due to the encastre boundary condition applied in the finite element model that forced the half-plane surface displacement to zero at the edges of the finite model. Abaqus was not able to solve this problem when the model dimensions were made significantly larger or with the encastre boundary condition removed from the side edges. The results nonetheless support the theoretical analysis of Chapter 6.

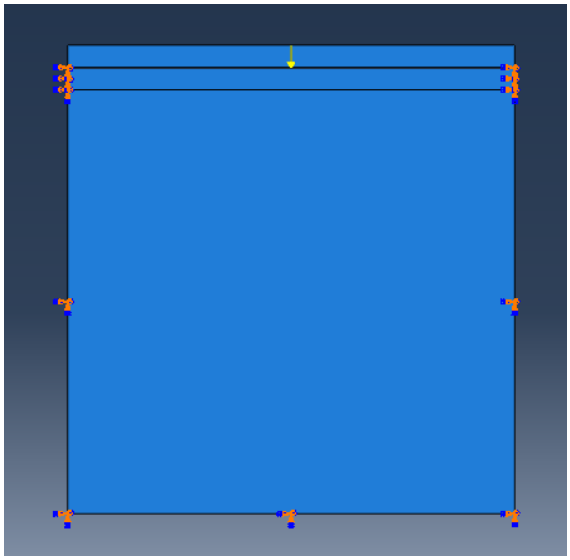

Figure 8.7: The finite element model of layer and half-plane pressed by a line load problem. Encastre boundary conditions are applied to the side edges and the base of the block.

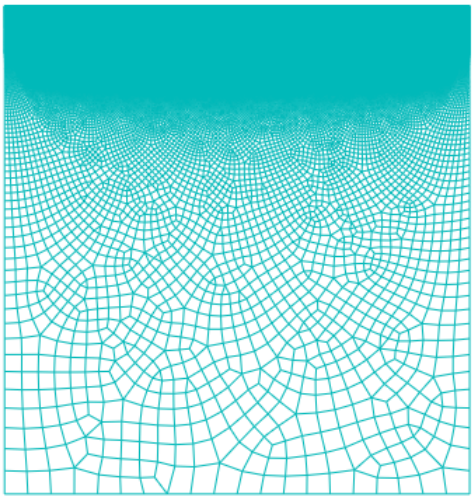

Figure 8.8: The mesh used in the finite element model of the layer and half-plane pressed by a line load problem.

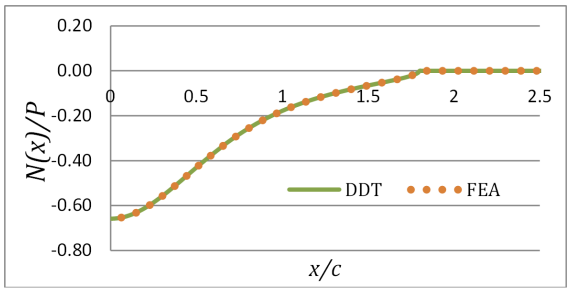

Figure 8.9: Normal traction along the interface obtained from the finite element model compared with results of the distributed dislocations technique obtained with $\lambda = 3.5$ and $N_{\hat{a}}, N_{\hat{b}} = 500$. $f = 0.5$

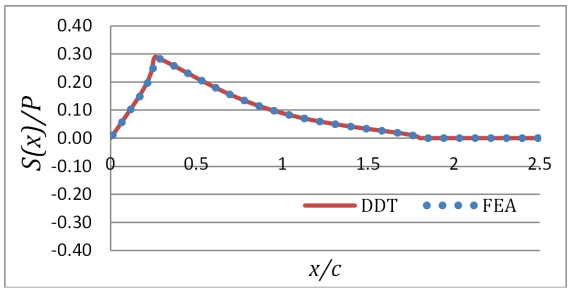

Figure 8.10: Shear traction along the interface obtained from the finite element model compared with results of the distributed dislocations technique obtained with $\lambda = 3.5$ and $N_{\hat{a}}, N_{\hat{b}} = 500$. $f = 0.5$

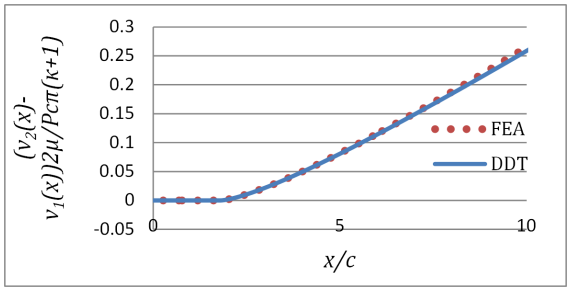

Figure 8.11: Separation along the interface obtained from the finite element model compared with results of the distributed dislocations technique obtained with $\lambda = 3.5$ and $N_{\hat{a}}, N_{\hat{b}} = 500$. $f = 0.5$.

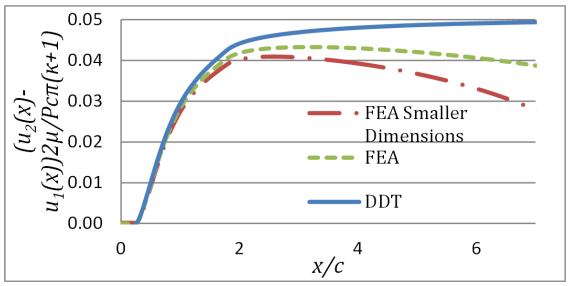

Figure 8.12: Relative slip along the interface obtained from the finite element model compared with results of the distributed dislocations technique obtained with $\lambda = 3.5$ and $N_{\hat{a}}, N_{\hat{b}} = 500$. $f = 0.5$. The results from a finite element model with smaller dimensions is plotted as well. In this model the layer is 15 mm by 1 mm and block of 15 mm by 15 mm.

8.2.3 Finite Element Modelling of the Layer Pressed by Pressure Over a Finite Width

The limitations of the finite element method become apparent when it is applied to solve problems involving finite loading, when the width of the region of pressure application becomes greater than the thickness of the layer, as increasing the dimensions of the layer and the half-plane causes convergence difficulties in the model. Adequate finite element solutions were not obtained when the layer and the block had the dimensions used in the finite element model in the line load problem (due to edge effects) described above. A larger model with the layer of dimensions 25 mm by 1 mm and block of dimensions 25 mm by 25 mm was constructed. Solutions could not be obtained with this geometry for the line load problem but solutions were obtained for the finite pressure patch problem when the layer was pressed by a constant pressure of 1 N/mm^2 over a width of 5 mm on the layer free surface. The loading is similar to that for the constant pressure patch problem of Chapter 7 with $\hat{w} = 2.5$. See Figure 8.13 for the model loading and boundary conditions. As in the model of the line load problem the block bottom edge and the side edges have encastre boundary conditions.

Images of the mesh applied is provided in Figures 8.14 and 8.15. A structured mesh of approximate element size of 0.0025 mm was generated next to the central 7.5 mm of the interface. As in the other models linear plane strain elements of the type CPE4R and CPE3 were used. In total there were 1,580,858 elements in this model[6]. Material properties of Young's modulus of 20,000 N/mm^2 and Poisson's ratio of 0.3 were assigned to both the strip and the block.

Figures 8.16, 8.17, 8.18 and 8.19 provide the tractions, the separation and the relative slip along the interface obtained from this model for $f = 0.3$ compared with the solutions with distributed

[6] 1,573,662 CPE4R and 7196 CPE3 elements.

dislocations described in Chapter 7. (The origin is at the centre point on the interface directly below the centre point of the area of loading). The tractions and separation from both models match as does the slip along the interface for points near the location of loading $\hat{x} \leq 2$. Interestingly the discrepancy between the finite element result for slip at remote points and that from distributed dislocations technique is lower in this model than for the model for with line loading. This is because this model has larger dimensions and the effect of the encastre boundary conditions is hence reduced for points near the centre.

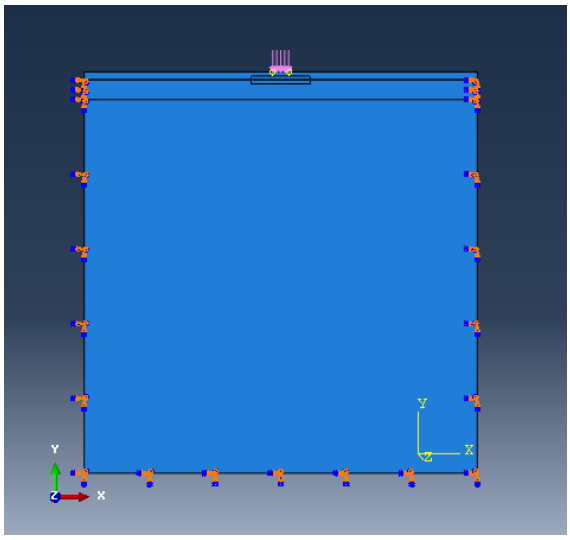

Figure 8.13: The finite element model of layer and half-plane pressed by a line load problem. Encastre boundary conditions are applied to the side edges and the base of the block.

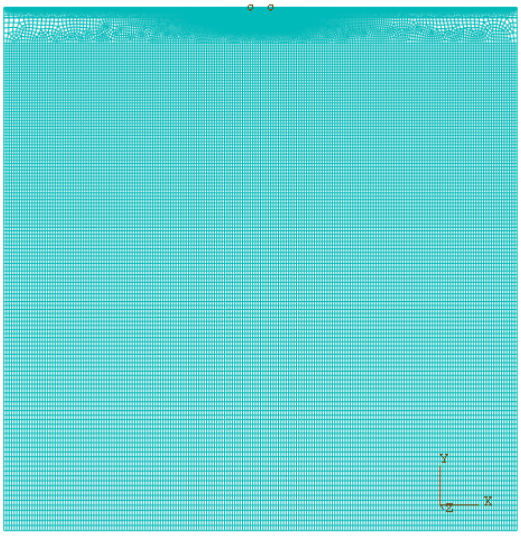

Figure 8.14: The mesh used in the finite element model of the layer and half-plane pressed by a line load problem.

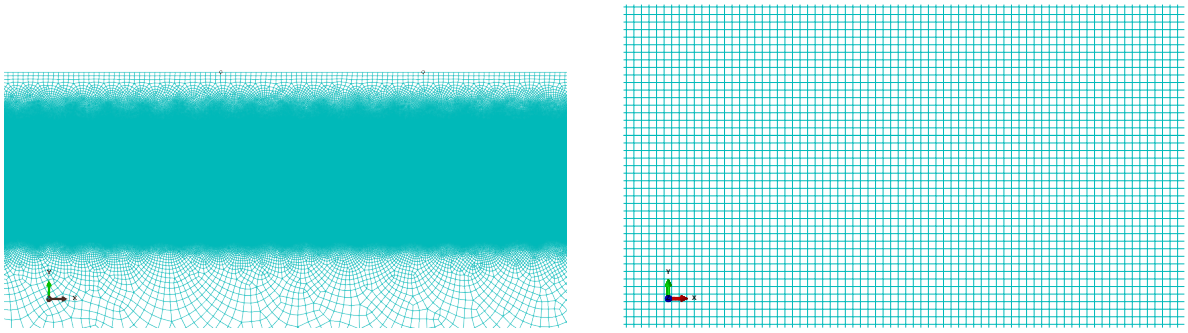

Figure 8.15: Close-up of the structured mesh applied near the region of interest next to the contact interface.

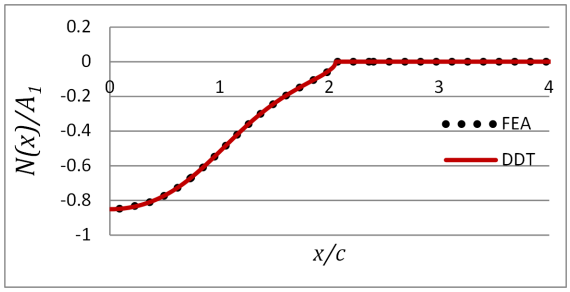

Figure 8.16: Normal traction along the interface obtained from the finite element model compared with results of the distributed dislocations technique obtained with with $N_{\hat{a}}, N_{\hat{b}} = 100$ and $\lambda_{\hat{a}}, \lambda_{\hat{b}} = 2$.

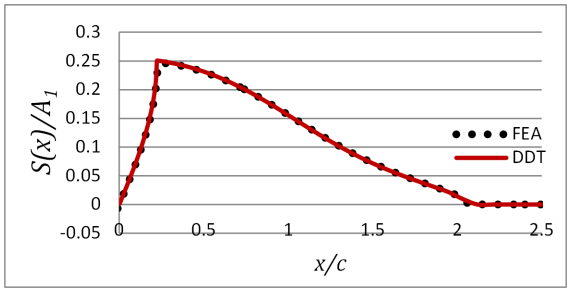

Figure 8.17: Shear traction along the interface obtained from the finite element model compared with results of the distributed dislocations technique obtained with $N_{\hat{a}}, N_{\hat{b}} = 100$ and $\lambda_{\hat{a}}, \lambda_{\hat{b}} = 2$.

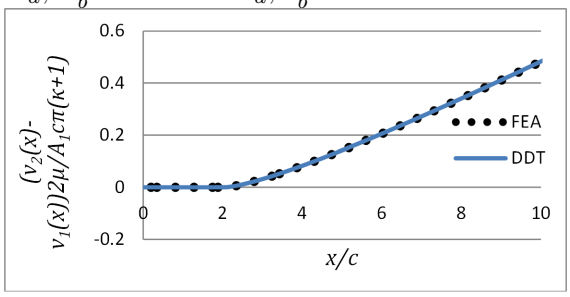

Figure 8.18: Separation along the interface obtained from the finite element model compared with results of the distributed dislocations technique obtained with with $N_{\hat{a}}, N_{\hat{b}} = 100$ and $\lambda_{\hat{a}}, \lambda_{\hat{b}} = 2$.

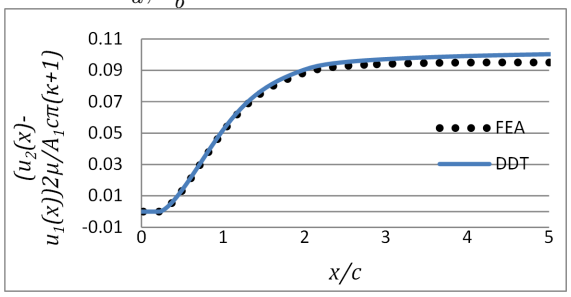

Figure 8.19: Relative slip along the interface obtained from the finite element model compared with results of the distributed dislocations technique obtained with with $N_{\hat{a}}, N_{\hat{b}} = 100$ and $\lambda_{\hat{a}}, \lambda_{\hat{b}} = 2$.

8.3 Convergence Study

As described above, the mesh density and the dimensions of the finite element models were increased until no significant change in the results were observed, and the results of the finite element model were seen to match those from the theoretical analysis with distributed dislocations. Increasing the dimensions of the models with finite pressure distribution and line load however proved difficult and there is a discrepancy in the magnitude of slip at remote points along the interface from that predicted by the analysis in Chapters 6 and 7. Figures 8.20, 8.21, 8.22 and 8.23 compare the results from a coarser finite element model for the line load problem with those obtained the from the more refined model described in section 8.2.2. The coarser model has a layer of smaller dimensions of 15 mm by 1 mm and block of 15 mm by 15 mm. The coarser model also had a mesh half as dense near the contact interface with the average element length of the elements near the interface of 0.02 mm (as opposed to 0.01 mm for the more refined model) with a total of 118,666 elements[7] (the more refined model has 637,133 element of similar kind as described in Section 8.2.2). As seen from these figures the results for the tractions and the separation along the interface from the two finite element models match well, as well as the relative slip for points near the area of application of

[7]There were 118,003 linear quadrilateral CPE4R elements and 663 linear triangular CPE3 elements.

load. This implies convergence has been achieved for both mesh density and for model dimensions (except for slip at remote points). Similarly, convergence of results was noted for the other two problems. (Convergence was also tested by comparing results from models of same dimensions with increasing mesh density and for models of similar mesh density with increasing dimensions.)

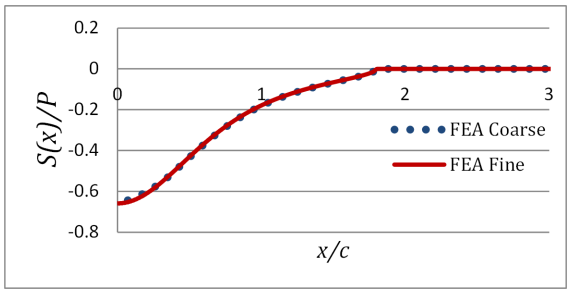

Figure 8.20: Normal traction obtained for the line load problem from the finite element model compared with that from a model with coarser mesh and smaller dimensions. The coarser mesh had element size of 0.02 mm near the interface, while the finer mesh had element size of 0.01 mm near the interface.

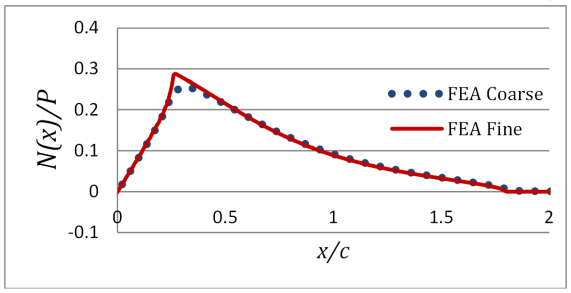

Figure 8.21: Shear traction obtained for the line load problem from the finite element model compared with that from a model with coarser mesh and smaller dimensions. The coarser mesh had element size of 0.02 mm near the interface, while the finer mesh had element size of 0.01 mm near the interface.

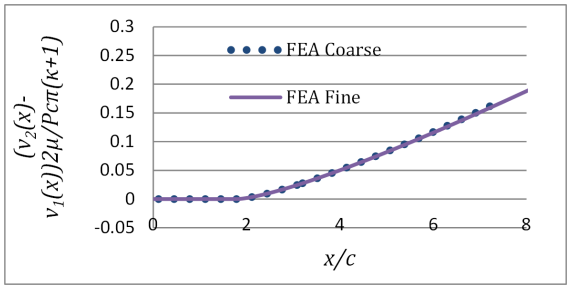

Figure 8.22: Separation along the interface obtained for the line load problem from the finite element model compared with that from a model with coarser mesh and smaller dimensions. The coarser mesh had element size of 0.02 mm near the interface, while the finer mesh had element size of 0.01 mm near the interface.

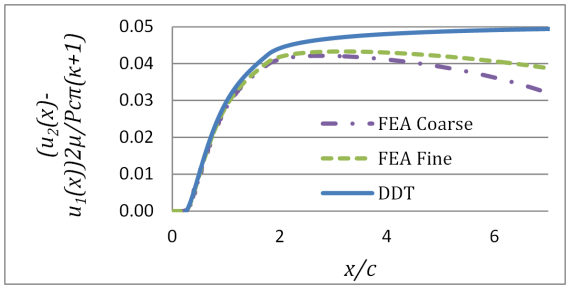

Figure 8.23: Relative slip along the interface obtained for the line load problem from the finite element model compared with that from a model with coarser mesh and smaller dimensions. The coarser mesh had element size of 0.02 mm near the interface, while the finer mesh had element size of 0.01 mm near the interface.

8.4 Discussion and Conclusions

Finite element modelling of the receding contact problems showed good agreement with solutions obtained by the insertion of distribution of dislocations. Both methods predict similar surface tractions, areas of slip, stick and separation, as well as the inter-facial gap between the layer and the half-plane. Further, the extent of slip along the interface determined by both methods was identical for the problem with the two semi-infinite pressure patches. The extent of slip along the interface in the problems with the line load and finite pressure obtained from both methods was the same for locations along the interface near the area of loading application ($\hat{x} < 1.5$) but not

at remote points. This is due to the encastre boundary condition applied to the finite block used to model the half-plane in the finite element models. This forced the tangential displacements of points along the surface of block to become zero at the far edge. Difficulties were encountered in obtaining solutions with other boundary conditions. The finite element modelling presented in this chapter therefore provides support for the analysis of receding contacts with the insertion of dislocations. Further, since the results are seen to match, they indicate the solutions for the semi-infinite situations are a good approximation for some problems with finite dimensions.

The difficulties in obtaining solutions for problems that look straightforward by finite element analysis illustrate some of challenges and limitations of modelling receding contact behaviour with finite elements. It is not straightforward to predict whether a finite element model with a particular dimension, mesh or boundary conditions will converge, and the models described here were developed by trial and error. In general, convergence of a model was limited when a zone of separation extended over 10 times the thickness of the layer. Furthermore, for models that required relatively large areas of separation, convergence was obtained only when the side edges of the block were encastred. Mesh density is also important, and convergence in some models was only obtained when the mesh was sufficiently dense.

Future work can investigate the construction of more advanced methods to model these contacts with finite elements. These could involve the use of more sophisticated boundary conditions that are not only more appropriate but also may help with obtaining convergence. Two possible approaches are suggested here (the implementation may not be straightforward):

1. One approach would be to use analytical formulations (such as the bilateral solution) to determine displacement boundary conditions to be applied to the edges of the block that models the half-plane. Though the bilateral solution would be an approximate estimate, it is more accurate than forcing an encastre boundary condition on the edges of the block.

2. Another approach would be to solve the problem iteratively. The tractions obtained from an initial model can be applied to a half-plane surface to determine the displacement field in the half-plane due to them. On the basis of this displacement field, the displacement boundary conditions for the edges of the block that models the half-plane are determined for the next iteration. Boundary conditions for subsequent models can be determined by the same process until the boundary conditions converge.

Part IV

Conclusion

Conclusion

Contact stiffness is an important contact parameter. It determines the relationship between the relative displacement at the contact interface with load. Indeed, frictional force can be defined as the tangential load at which the tangential contact stiffness becomes zero. A key finding is that for the Ti-6Al-4V ground surfaces investigated here, at different normal loads, a linear relationship exists between tangential contact stiffness and tangential load. Further for ground interfaces, the tangential contact stiffness at the start of application of tangential load is seen proportional to the normal contact stiffness, and the ratio between tangential and normal contact stiffness is given by roughly half the Mindlin ratio ($\frac{2(1-\nu)}{2-\nu}$), consistent with numerous other measurements in the literature. In addition, for ground surfaces the normal contact stiffness was seen to be inversely proportional to the equivalent surface roughness parameter. These results imply a straightforward means of estimating both the normal and tangential contact stiffness values from the surface roughness, coefficient of friction and the Mindlin ratio.

The second part of the thesis demonstrates the applicability of a new method with distributed dislocations to model receding contacts. The general principle of applying preformed distributions and superimposing corrective bounded-bounded distributions using the standard methods is novel and can be applied to a variety situations in which the end behaviour of the required distributions are neither square root singular nor square root bounded. The implementation of this method represents a significant step in the modelling of frictional receding contacts.

The key findings from this thesis are the following. They are presented here with a critical assessment and a discussion of the limitations.

1. For ground Ti-6Al-4V interfaces studied the tangential contact stiffness linearly decreases with tangential load as slip approaches. The exponential relationship between tangential loading and tangential contact displacement is seen to describe the observed experimental data well, quite consistently, for many loading steps. The fitting parameters for many of the loading steps have reasonably low uncertainty error bounds. Furthermore the fitted curves suggest a coefficient of friction for the interfaces of around 0.2, which is well within the expected value for these interfaces. Furthermore K_{t0}/K_n ratio measured on the basis of these fits are seen to

be normal load independent and hence are consistent with asperity models of contact stiffness such as the Medina model. Furthermore the ratio measured for ground interfaces was seen to be around half the Mindlin ratio and is consistent with numerous other measurements of this ratio (though according to the Medina model it should be given by the Mindlin ratio). However experimental evidence for this relationship is limited to the interfaces studied here and for the loading applied. Also, it should be noted the fitting parameters from the data from some loading steps, particularly for tests with the ground 'smooth specimen' (S_q of 0.687μm), had very large uncertainties. While it is argued that this is due to significant experimental scatter in measured displacements that varied by only a few hundred nanometres during a whole loading step, it cannot be ruled out the underlying model may not be appropriate for some loading steps. The strongest support for the observed relationship comes from the tests with the 'rough specimen' (S_q of 1.422 μm) which consistently implied lower uncertainties in the fitting parameters measured. The linear relationship between tangential contact stiffness and tangential load provides support to the model of Paggi et al [28] using Boundary Element Method with Greenwood and Williamson type interfaces.

2. The normal contact stiffness is observed to be linearly related to normal loading. This provides experimental support for both asperity based models such as Medina et al and fractal surface based models such those based on the Persson contact theory. Though there are numerous models of normal contact stiffness, as described in Chapter 1, that predict a linear relationship between normal loading, there are not many published experimental measurements of this relationship. However the validity of experimental evidence provided for this relationship is limited to the range of loading applied and to the nature of the surfaces tested.

3. The measurements of the normal contact stiffness relationship with the equivalent surface roughness parameter for the ground interfaces is seen to be consistent with that predicted by the Medina model, which indicates a linearly inverse relationship given by equation (1.4)

$$K_n = \frac{P_n}{\sigma_{rms}}.$$

   The measurements therefore provide some support to the Medina model, as the model relates to ground surfaces studied here. The results from the structured surfaces, however, did not show a similar relationship. This could be due to effects of polishing and other features on the surface, such as raised areas, that affected the measurements. Further they may indicate a limitation of the Medina model's applicability to these surfaces.

4. Asperity modelling led to the following observations

- The tangential displacement and tangential load relationship for a single spherical asperity contact with a shear limit law has a similar form to that with a Coulomb friction law, provided appropriate normalisation is used. This observation is limited to linear elastic asperity contacts and is valid only for the range of shear limit values investigated.
- This relationship for stuck, elastic perfectly-plastic spherical asperities in contact has a similar form to that for a spherical elastic contact with a Coulomb friction interface law, provided appropriate normalisation is used. This result is however limited to the range of tangential loading applied in the models, and the range of yield limits used to define the material properties.

These results regarding the behaviour of asperity contacts are relevant for constructing asperity models of rough surfaces that involve shear limit interface laws and elastic-perfectly plastic behaviour.

5. Multi-asperity modelling of rough interfaces with each surface consisting of elastic asperities on a rigid base with the asperities loaded normally by different load distribution laws showed that the initial slope of the tangential load and tangential displacement relationship of the interface can be given by equation (3.22). Furthermore, the tangential load and tangential displacement of the interface relationship can be approximated by the relationship of a single asperity contact with a Coulomb interface law, with the use of appropriate multipliers. The application and validity of this model for real contacts is however limited due to the assumptions made: the bulk material is assumed to be rigid, the contact asperities have the same spherical shape and radius, they are perfectly aligned and deform only elastically, and each asperity contact obeys a Coulomb friction law.

6. Multi-asperity modelling with elastic asperity contacts arranged in organised grids on half-spaces provide estimates of the normal contact stiffness for interfaces when the number of asperity contacts and the real to nominal contact area is known. This model is limited since the loading on each asperity point is taken as Hertzian, which will break down for large real to nominal contact areas. This model cannot be used to estimate the evolution of normal contact stiffness with load since the number of asperity contacts will increase with loading for real interfaces. The model is also limited by the many simplifying assumptions made: the asperities are organised in regular grids, have the same normal loading, have the same radius of curvature, and only deform elastically.

7. The applicability of the distributed of dislocation technique was demonstrated in the solution of a receding contact problem in Chapter 5. The chief limitation of this solution is that

the problem loading and geometry was contrived, and is not related to any obvious practical application. Receding contact analysis described in this thesis is limited by the assumptions of linear elasticity, perfectly smooth interfaces (infinite contact stiffness), uniform coefficient of friction, a Coulomb friction interface law, and the accuracy of numerical solutions of integral equation obtained with the Gauss-Cheybyshev quadrature with the aid of a computational software (Matlab).

8. The solution for the receding contact problem involving a semi-infinite layer loaded by a line load presented in Chapter 6 marks a significant step in the theoretical analysis of receding contacts, for the following reasons

    - The problem loading and geometry is the most fundamental 2D receding contact situation. It is the asymptomatic form for other loading conditions involving semi-infinite layer in contact with a half-plane. For example, for problems in which the layer is loaded by a finite pressure patch, when the size of the region over which load is applied becomes significantly smaller than the thickness of the layer, the contact behaviour will approach the solution to the line load problem (this observation was used in presenting the results in Chapter 7).
    - Many receding contact problems involve separation along the interface at remote points. The method of inserting preformed distributions that correspond to the expected displacements at remote points along the interface is new and can be applied to solve other receding contact situations as demonstrated in Chapter 7.

    The chief limitation of this method is that the solution process is long and requires the analytical solution of some complicated integrals. Furthermore, some numerical approximations were used to insert distributions of dislocations over an infinitely large region.

9. The solutions of semi-infinite receding contact problems with finite pressure distributions were obtained in Chapter 7. These solutions demonstrated the method developed in Chapter 6 can be applied to other loading situations. Furthermore, by solving these problems for greater pressure widths, the feasibility of attaining solutions for problems with semi-infinite pressure was investigated. It was shown that finite solutions for the layer loaded by a semi-infinite square-root bounded and semi-infinite constant pressures can not to be obtained. The solution process for these problems are subject to the same limitations as the problem described in Chapter 6.

10. Finite element modelling of a strip pressed on a block with loading analogous to the semi-infinite problems studied in Chapters 5, 6 and 7 showed the results for the semi-infinite

problems found with the distributed dislocation technique match the results obtained by finite element analysis for receding contacts between finite bodies. This is the case for the interface tractions, slip and separation, though there was a discrepency in the magnitude of slip at remote points for some models. Finite element modelling is limited by the dimensions of the models, since convergence was not obtained for receding contacts with relatively large dimensions (when the zone of separation of the interface is greater than around 10 times the thickness of the layer). Also finite element analysis is an approximate numerical technique and the applicability of the method for solving receding contacts has not been validated. Furthermore, the encastre boundary-conditions that were applied to the sides of the block that models the half-plane is not physically realistic and unrealistic values of slip were obtained along the interface away from the region of loading for some of the models.

In light of the above observations the following suggestions are made for future work to further explore the properties of contact stiffness and receding contacts.

1. Future experimental investigation can be conducted to measure both normal and tangential contact stiffness properties for a greater variety of interfaces– for a wider range of surface roughness and surface texture properties – loading and material properties. This is to find the range of surfaces textures, materials and loading for which the observations made in this thesis are applicable (such as the linear relationship between tangential contact stiffness and tangential load).

2. Experimental investigation was restricted in this study to the measurement of the initial tangential contact stiffness properties observed during the first few cycles of tangential loading. Future work can explore the effect of several loading cycles on the contact stiffness properties, when significant changes in the interface profile, such as due to wear, is likely.

3. Future work can explore constructing more detailed asperity models of rough interfaces to explore the tangential contact displacement and tangential load behaviour of interfaces. The basic relationships found in Chapter 3 for asperity contacts with different friction laws and for elastic perfectly plastic material properties can be incorporated into such a model to see how these effects affect the tangential contact stiffness properties of a rough interface.

4. The experimental results for ground interfaces provided in this thesis and from other published studies suggest that the ratio K_{t0}/K_n is around half the theoretical value given by the Mindlin ratio for some interfaces, when theoretical modelling (such as by Medina et al [4]) suggest it should be equal to the Mindlin ratio for elastic interfaces. A theoretical investigation could look into the possible reasons for this discrepancy between experimental results

and modelling. Further refinement of the Medina model can be explored to explain these experimental observations.

5. The major drawback of the new solution process described in Chapter 6 and applied also in Chapter 7 for solving receding contacts is that they require the analytical solutions of some integral terms that are singular. While these solutions have been found for the problems solved in this thesis, the solution process is long and tedious. Therefore a future project can investigate mathematical methods, such as numerical procedures, to evaluate these integrals more straightforwardly.

6. Finite element analysis of receding contacts is currently limited to models with relatively small dimensions. Solution procedures to model receding contacts between bodies of larger dimensions with finite elements is therefore of interest. These may for instance involve applying boundary conditions at the remote edges of the block and layer on the basis of displacements found by analytical methods. Alternatively, an iterative process could be explored to determine suitable boundary conditions.

7. Part III of this thesis aimed to develop theoretical methods to analyse idealised frictional receding contacts. However there is a dearth of experimental studies of receding contact behaviour. A future experimental programme could explore measuring properties of receding contacts. Such a programme could evaluate the extent to which the linear elastic modelling of receding contacts, as was done in this thesis, relates to the behaviour of real contacts. This however is not likely to be straightforward due to the very small relative inter-facial displacements expected for metallic receding contacts. Indirect methods such as measuring the conductivity properties of receding contact interfaces or ultrasound based methods may be viable.

8. It is likely the effects due to the presence of a rough interface (such as due to asperity contacts) will be relevant to receding contact behaviour, particularly in regard to interface displacements. Future work could explore how the results of contact stiffness analysis for rough interfaces of Part II of this thesis can be incorporated into the modelling of receding contacts described in Part III, when the assumption of a perfectly smooth interface is relaxed.

Appendix A

Appendix for Contact Stiffness Measurement

A.1 Pad and Specimen Drawings

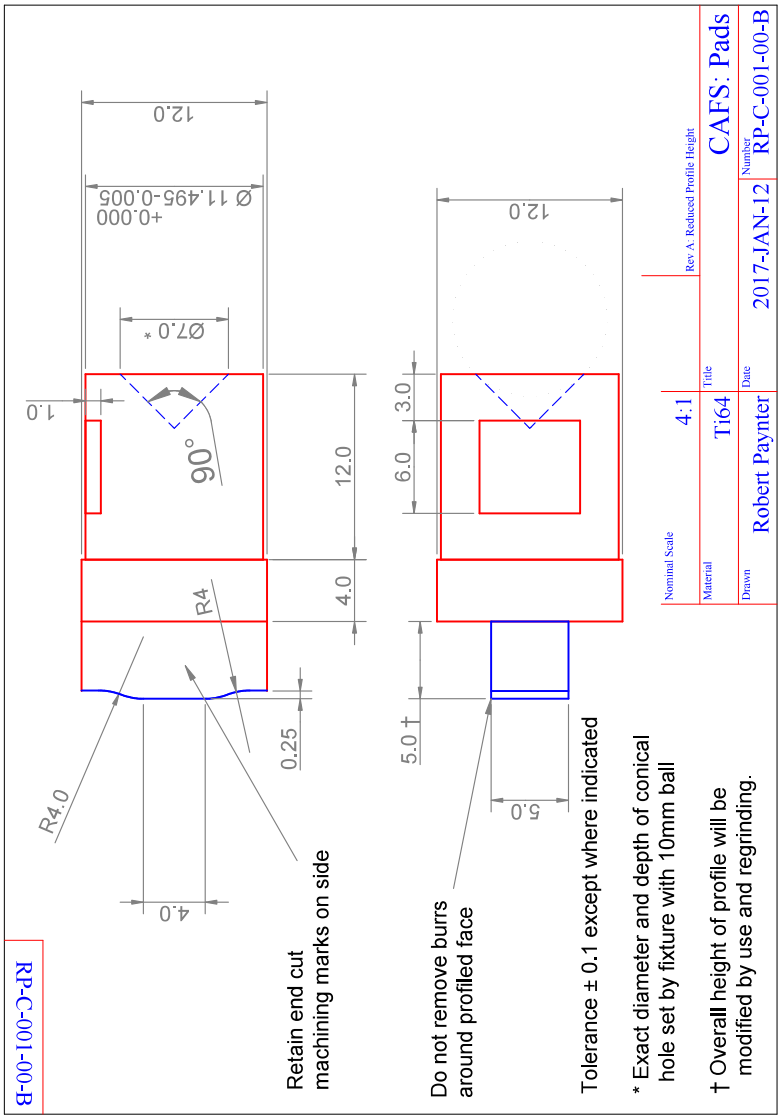

Figure A.1: Scaled down copy of the engineering drawing of the pad, drawn by Robert Paynter.

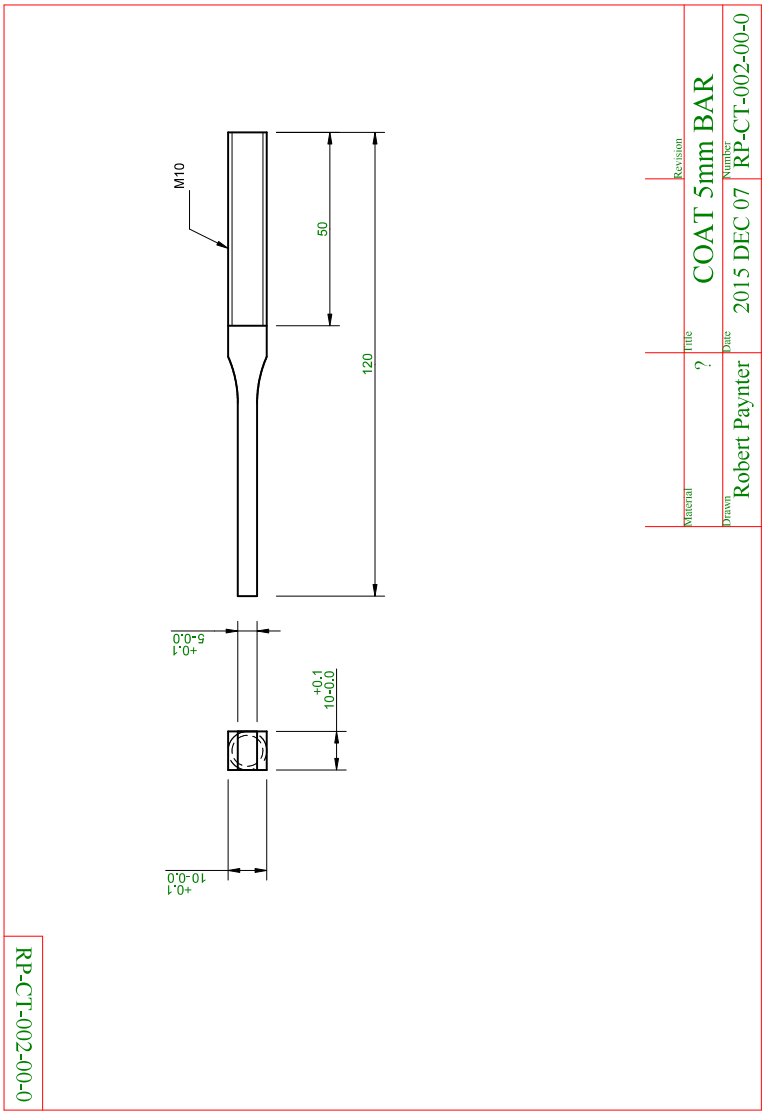

Figure A.2: Scaled down copy of the engineering drawing of the specimen, drawn by Robert Paynter.

A.2 Roughness Parameters for Ground Surfaces

	R_a (nm)	R_q (nm)	R_z (μm)	Profile length (mm)	Profile width (nm)	λ_c (μm)
Rough specimen						
Side A	1280	1499	6.485	5	437	800
Side B	1244	1456	6.978	5	437	800
Test RU1, max $P_n = 4$ kN						
Pad A	1208	1583	8.087	4	437	800
Pad B	1173	1428	7.067	4	437	800
Test RU2, max $P_n = 8$ kN						
Pad A	633	819	4.801	4	670	800
Pad B	629	814	4.614	4	670	800
Test RU3, max $P_n = 12$ kN						
Pad A	605	784	4.537	4	671	800
Pad B	609	792	4.538	4	671	800
Smooth specimen						
Side A	396	524	3.776	5	671	800
Side B	526	708	4.973	5	671	800
Test SU1, max $P_n = 4$kN						
Pad A	490	631	3.829	4	671	800
Pad B	458	593	4.015	4	671	800
Test SU2, max $P_n = 8$kN						
Pad A	521	694	5.252	4	671	800
Pad B	541	723	4.805	4	671	800
Test SU3, max $P_n = 12$kN						
Pad A	492	646	4.404	4	671	800
Pad B	521	693	4.707	4	671	800

	S_a (nm)	S_q (nm)	S_p (μm)	S_{tr}	Fractal Dimension	Sample Area (mm^2)	λ_c (μm)
Rough specimen							
Side A	1247	1470	13.470	0.379	2.002	2	800
Side B	1211	1422	13.715	0.401	2.002	2	800
Test RU1, max $P_n = 4$kN							
Pad A	1225	1585	9.624	0.094	2.008	2	800
Pad B	1188	1460	6.688	0.102	2.006	2	800
Test RU2, max $P_n = 8$kN							
Pad A	630	819	19.808	0.088	2.002	2	800
Pad B	632	822	4.616	0.114	2.002	2	800
Test RU3, max $P_n = 12$kN							
Pad A	591	811	15.056	0.062	2.002	2	800
Pad B	626	814	7.635	0.072	2.002	2	800
Smooth specimen							
Side A	399	533	4.359	0.090	2.001	2	800
Side B	518	687	5.472	0.117	2.002	2	800
Test SU1, max $P_n = 4$kN							
Pad A	510	652	4.050	0.140	2.002	2	800
Pad B	480	623	5.787	0.160	2.002	2	800
Test SU2, max $P_n = 8$kN							
Pad A	525	707	7.572	0.070	2.002	2	800
Pad B	565	760	5.360	0.067	2.003	2	800
Test SU3, max $P_n = 12$kN							
Pad A	504	685	11.428	0.085	2.002	2	800
Pad B	618	821	23.696	0.049	2.003	2	800

Table A.1: Roughness parameters for the ground surfaces (before testing) **Left**:Profile roughness parameters calculated as the average of 5 measurements for the specimen and pad surfaces used in the tests with ground surfaces. **Right**: Areal parameters calculated for the specimen and pad surfaces used in the tests with ground surfaces. Vertical resolution 50 nm, lateral resolution of 2.01 μm, with 20X magnification objective were used for the measurement with the Alicona optical profilometer

A.3 Tangential Stiffness Test Results for Ground Surfaces

Loading Step	1	2	3	4	5
K_{t0}/A_n (kN/mm^3)	45.415	43.689	45.148	44.391	44.214
K_{t0}/A_n (kN/mm^3), margin of error of fit	131.637	24.129	21.009	17.405	15.993
α_t fitting parameter	-1.899	-1.318	-1.217	-1.565	-1.336
α_t, margin of error (±) for 95% confidence level	3.656	0.636	0.511	0.529	0.427
β_t fitting parameter	-0.466	-0.516	-0.565	-0.457	-0.518
β_t, margin of error (±) for 95% confidence level	1.026	0.208	0.189	0.128	0.134
Q_s fitting parameter	1.950	1.695	1.598	1.941	1.707
Q_s, margin of error (±) for 95% confidence level	3.675	0.640	0.518	0.534	0.431
f	0.487	0.424	0.399	0.485	0.427
f, margin of error (±) for 95% confidence level	0.924	0.167	0.136	0.142	0.115
Adjusted R-Square Goodness of Fit	0.966	0.994	0.993	0.997	0.997

Table A.2: Data obtained from the fitted curves to the mean tangential contact displacement and tangential load data for the loading steps from the RU1 test.

Unloading Step	1	2	3	4	5
K_{t0}/A_n (kN/mm^3)	43.138	48.616	49.973	50.520	50.274
K_{t0}/A_n (kN/mm^3), margin of error of fit	6.061	11.554	7.979	8.200	10.290
α_t fitting parameter	0.591	1.163	1.124	1.119	1.221
α_t, margin of error (±) for 95% confidence level	0.069	0.154	0.095	0.094	0.133
β_t fitting parameter	1.234	1.030	1.150	1.176	1.054
β_t, margin of error (±) for 95% confidence level	0.132	0.181	0.136	0.142	0.159
Q_s fitting parameter	-0.699	-0.944	-0.869	-0.859	-0.954
Q_s, margin of error (±) for 95% confidence level	0.064	0.151	0.093	0.093	0.132
f	0.175	0.236	0.217	0.215	0.239
f, margin of error (±) for 95% confidence level	0.021	0.043	0.029	0.029	0.038
Adjusted R-Square Goodness of Fit	0.995	0.993	0.997	0.996	0.995

Table A.3: Data obtained from the fitted curves to the mean tangential contact displacement and tangential load data for the unloading steps from the RU1 test.

Loading Step	1	2	3	4	5	Units
Mean K_{t0}/A_n	44.837	43.045	44.430	43.829	43.726	kN/mm^3
Margin of error (±) for mean row stiffness value for 95% confidence level	1.739	0.522	0.569	0.510	0.547	kN/mm^3
Largest value for K_{t0}/A_n	62.332	45.590	47.148	46.025	46.825	kN/mm^3
Lowest value for K_{t0}/A_n	35.484	38.507	39.378	39.146	38.979	kN/mm^3

Table A.4: Stiffness data obtained by fitting tangential load and tangential contact displacement data for each row in the displacement field for test RU1 for the loading steps.

Unloading Step	1	2	3	4	5	Units
Mean K_{t0}/A_n	42.575	48.297	49.819	50.645	50.405	kN/mm^3
Margin of error (±) for mean row stiffness value for 95% confidence level	0.761	0.905	1.009	1.115	0.985	kN/mm^3
Largest value for K_{t0}/A_n	48.917	54.708	57.047	59.288	57.741	kN/mm^3
Lowest value for K_{t0}/A_n	36.030	40.944	41.768	40.914	41.715	kN/mm^3

Table A.5: Stiffness data obtained by fitting tangential load and tangential contact displacement data for each row in the displacement field for test RU1 for the unloading steps.

Loading Step	1	2	3	4	5
K_{t0}/A_n (kN/mm^3)	98.684	87.026	86.954	82.878	83.768
K_{t0}/A_n (kN/mm^3), margin of error of fit	11.893	18.192	32.678	24.308	18.720
α_t fitting parameter	-1.659	-2.707	-2.784	-2.875	-2.716
α_t, margin of error (±) for 95% confidence level	0.063	0.240	0.420	0.370	0.268
β_t fitting parameter	-1.649	-0.958	-0.955	-0.839	-0.911
β_t, margin of error (±) for 95% confidence level	0.170	0.148	0.266	0.181	0.148
Q_s fitting parameter	1.197	1.817	1.821	1.976	1.839
Q_s, margin of error (±) for 95% confidence level	0.075	0.256	0.460	0.393	0.282
f	0.150	0.227	0.228	0.247	0.230
f, margin of error (±) for 95% confidence level	0.012	0.035	0.060	0.052	0.039
Adjusted R-Square Goodness of Fit	0.996	0.994	0.982	0.991	0.995

Table A.6: Data obtained from the fitted curves to the mean tangential contact displacement and tangential load data for the loading steps from the RU2 test.

Unloading Step	1	2	3	4	5
K_{t0}/A_n (kN/mm^3)	90.650	88.001	85.649	86.108	86.202
K_{t0}/A_n (kN/mm^3), margin of error of fit	8.099	10.249	24.967	17.124	25.753
α_t fitting parameter	0.492	0.529	0.734	0.673	0.705
α_t, margin of error (±) for 95% confidence level	0.068	0.093	0.288	0.185	0.285
β_t fitting parameter	1.203	1.156	0.986	1.033	1.016
β_t, margin of error (±) for 95% confidence level	0.081	0.102	0.214	0.155	0.228
Q_s fitting parameter	-1.507	-1.522	-1.738	-1.668	-1.696
Q_s, margin of error (±) for 95% confidence level	0.088	0.116	0.338	0.218	0.335
f	0.188	0.190	0.217	0.208	0.212
f, margin of error (±) for 95% confidence level	0.015	0.018	0.045	0.030	0.045
Adjusted R-Square Goodness of Fit	0.998	0.998	0.989	0.993	0.987

Table A.7: Data obtained from the fitted curves to the mean tangential contact displacement and tangential load data for the unloading steps from the RU2 test.

Loading Step	1	2	3	4	5	Units
Mean K_{t0}/A_n	97.413	85.670	84.738	80.864	82.163	kN/mm^3
Margin of error (±) for mean row stiffness value for 95% confidence level	2.644	1.957	1.878	1.479	1.854	kN/mm^3
Largest K_{t0}/A_n value	104.867	93.731	91.615	85.940	88.324	kN/mm^3
Lowest K_{t0}/A_n value	81.917	74.028	73.798	72.624	71.731	kN/mm^3

Table A.8: Stiffness data obtained by fitting tangential load and tangential contact displacement data for each row in the displacement field for test RU2 for the loading steps.

Unloading Step	1	2	3	4	5	Units
Mean K_{t0}/A_n	87.884	85.919	84.061	85.672	86.639	kN/mm^3
Margin of error (±) for mean row stiffness value for 95% confidence level	2.240	2.075	1.652	1.697	2.069	kN/mm^3
Largest K_{t0}/A_n value	94.780	96.116	92.216	91.409	99.100	kN/mm^3
Lowest K_{t0}/A_n value	77.201	74.545	74.109	75.422	75.117	kN/mm^3

Table A.9: Stiffness data obtained by fitting tangential load and tangential contact displacement data for each row in the displacement field for test RU2 for the unloading steps.

Loading Step	1	2	3	4	5
K_{t0}/A_n (kN/mm^3)	180.701	205.112	188.074	181.981	170.533
K_{t0}/A_n (kN/mm^3), margin of error of fit	36.036	34.380	36.521	43.473	51.302
α_t fitting parameter	-1.830	-3.546	-3.265	-3.136	-2.954
α_t, margin of error ($\pm$) for 95% confidence level	0.166	0.208	0.254	0.320	0.417
β_t fitting parameter	-1.950	-1.903	-1.777	-1.729	-1.622
β_t, margin of error ($\pm$) for 95% confidence level	0.342	0.242	0.262	0.312	0.368
Q_s fitting parameter	1.853	2.156	2.117	2.106	2.103
Q_s, margin of error ($\pm$) for 95% confidence level	0.177	0.235	0.268	0.329	0.415
f	0.154	0.180	0.176	0.175	0.175
f, margin of error ($\pm$) for 95% confidence level	0.017	0.022	0.025	0.030	0.037
Adjusted R-Square Goodness of Fit	0.989	0.992	0.988	0.984	0.971

Table A.10: Data obtained from the fitted curves to the mean tangential contact displacement and tangential load data for the loading steps from the RU3 test.

Unloading Step	1	2	3	4	5
K_{t0}/A_n (kN/mm^3)	206.268	213.386	174.454	165.473	156.646
K_{t0}/A_n (kN/mm^3), margin of error of fit	32.832	35.378	45.032	77.729	122.327
α_t fitting parameter	0.414	0.592	1.294	1.806	2.816
α_t, margin of error ($\pm$) for 95% confidence level	0.123	0.163	0.419	0.958	2.179
β_t fitting parameter	2.187	2.074	1.281	1.027	0.744
β_t, margin of error ($\pm$) for 95% confidence level	0.270	0.262	0.245	0.353	0.423
Q_s fitting parameter	-1.886	-2.058	-2.725	-3.223	-4.211
Q_s, margin of error ($\pm$) for 95% confidence level	0.189	0.221	0.472	1.031	2.254
f	0.157	0.171	0.227	0.269	0.351
f, margin of error ($\pm$) for 95% confidence level	0.018	0.021	0.042	0.089	0.192
Adjusted R-Square Goodness of Fit	0.989	0.990	0.989	0.974	0.959

Table A.11: Data obtained from the fitted curves to the mean tangential contact displacement and tangential load data for the unloading steps from the RU3 test.

Loading Step	1	2	3	4	5	Units
Mean K_{t0}/A_n	197.803	208.511	192.907	194.124	180.8931	kN/mm^3
Margin of error ($\pm$) for mean row stiffness value for 95% confidence level	37.525	7.762	7.729	8.651	10.3193	kN/mm^3
Largest K_{t0}/A_n value	424.547	239.130	229.656	230.581	232.3593	kN/mm^3
Lowest K_{t0}/A_n value	94.976	170.086	162.220	137.668	127.804	kN/mm^3

Table A.12: Stiffness data obtained by fitting tangential load and tangential contact displacement data for each row in the displacement field for test RU3 for the loading steps.

Unloading Step	1	2	3	4	5	Units
Mean K_{t0}/A_n	215.026	224.847	211.924	180.565	188.350	kN/mm^3
Margin of error (±) for mean row stiffness value for 95% confidence level	30.779	24.374	25.505	11.753	18.209	kN/mm^3
Largest K_{t0}/A_n value	365.727	362.354	343.864	251.881	298.160	kN/mm^3
Lowest K_{t0}/A_n value	129.537	161.780	137.078	121.284	119.548	kN/mm^3

Table A.13: Stiffness data obtained by fitting tangential load and tangential contact displacement data for each row in the displacement field for test RU3 for the unloading steps.

Loading Step	1	2
K_{t0}/A_n (kN/mm^3)	86.882	85.536
K_{t0}/A_n (kN/mm^3), margin of error of fit	134.562	226.734
α_t fitting parameter	-2.110	-3.265
α_t, margin of error (±) for 95% confidence level	2.707	6.862
β_t fitting parameter	-0.694	-0.464
β_t, margin of error (±) for 95% confidence level	0.765	0.873
Q_s fitting parameter	2.504	3.686
Q_s, margin of error (±) for 95% confidence level	2.722	6.888
f	0.626	0.921
f, margin of error (±) for 95% confidence level	0.688	1.732
Adjusted R-Square Goodness of Fit	0.981	0.977

Table A.14: Data obtained from the fitted curves to the mean tangential contact displacement and tangential load data for the loading steps from the SU1 test.

Unloading Step	1	2	3
K_{t0}/A_n (kN/mm^3)	128.018	118.115	108.914
K_{t0}/A_n (kN/mm^3), margin of error of fit	41.804	37.543	48.700
α_t fitting parameter	0.945	0.941	0.945
α_t, margin of error (±) for 95% confidence level	0.082	0.100	0.162
β_t fitting parameter	4.863	4.012	3.484
β_t, margin of error (±) for 95% confidence level	1.310	1.035	1.241
Q_s fitting parameter	-0.526	-0.589	-0.625
Q_s, margin of error (±) for 95% confidence level	0.097	0.109	0.169
f	0.132	0.147	0.156
f, margin of error (±) for 95% confidence level	0.027	0.030	0.045
Adjusted R-Square Goodness of Fit	0.969	0.973	0.963

Table A.15: Data obtained from the fitted curves to the mean tangential contact displacement and tangential load data for the unloading steps from the SU1 test.

Loading Step	1	2	Units
Mean K_{t0}/A_n	86.940	86.518	kN/mm^3
Margin of error (±) for mean row stiffness value for 95% confidence level	2.841	3.230	kN/mm^3
Largest K_{t0}/A_n value	98.023	97.359	kN/mm^3
Lowest K_{t0}/A_n value	74.410	73.725	kN/mm^3

Table A.16: Stiffness data obtained by fitting tangential load and tangential contact displacement data for each row in the displacement field for test SU1 for the loading steps.

Unloading Step	1	2	3	Units
Mean K_{t0}/A_n	122.360	116.670	103.052	kN/mm^3
Margin of error (±) for mean row stiffness value for 95% confidence level	7.477	6.210	4.690	kN/mm^3
Largest K_{t0}/A_n value	152.509	146.702	127.159	kN/mm^3
Lowest K_{t0}/A_n value	81.049	95.930	88.400	kN/mm^3

Table A.17: Stiffness data obtained by fitting tangential load and tangential contact displacement data for each row in the displacement field for test SU1 for the unloading steps.

Loading Step	1	2	3	4	5
K_{t0}/A_n (kN/mm^3)	235.666	342.191	318.397	331.350	326.927
K_{t0}/A_n (kN/mm^3), margin of error of fit	251.897	89.929	105.445	125.041	143.593
α_t fitting parameter	-3.251	-4.648	-5.318	-7.245	-9.546
α_t, margin of error (±) for 95% confidence level	1.844	0.130	0.314	1.072	3.069
β_t fitting parameter	-1.785	-3.630	-3.704	-3.891	-4.425
β_t, margin of error (±) for 95% confidence level	1.414	0.702	0.910	1.091	1.474
Q_s fitting parameter	2.641	1.885	1.719	1.703	1.478
Q_s, margin of error (±) for 95% confidence level	1.896	0.336	0.382	0.430	0.423
f	0.330	0.236	0.215	0.213	0.185
f, margin of error (±) for 95% confidence level	0.241	0.045	0.050	0.056	0.055
Adjusted R-Square Goodness of Fit	0.950	0.994	0.986	0.982	0.967

Table A.18: Data obtained from the fitted curves to the mean tangential contact displacement and tangential load data for the loading steps from the SU2 test.

Unloading Step	1	2	3	4	5
K_{t0}/A_n (kN/mm^3)	375.296	358.746	336.052	320.367	271.614
K_{t0}/A_n (kN/mm^3), margin of error of fit	270.266	491.486	1.93E+04	4.11E+04	3.16E+04
α_t fitting parameter	1.841	2.618	157.384	223.209	166.770
α_t, margin of error (±) for 95% confidence level	1.559	3.948	6508.109	20521.518	13964.826
β_t fitting parameter	2.115	1.575	0.042	0.028	0.032
β_t, margin of error (±) for 95% confidence level	1.093	1.540	1.706	2.572	2.638
Q_s fitting parameter	-3.549	-4.555	-160.142	-226.131	-169.560
Q_s, margin of error (±) for 95% confidence level	1.779	4.371	6509.033	20523.182	13966.709
f	0.444	0.569	20.018	28.266	21.195
f, margin of error (±) for 95% confidence level	0.227	0.552	813.830	2565.681	1746.051
Adjusted R-Square Goodness of Fit	0.983	0.965	0.946	0.896	0.868

Table A.19: Data obtained from the fitted curves to the mean tangential contact displacement and tangential load data for the unloading steps from the SU2 test.

Loading Step	1	2	3	4	5	Units
Mean K_{t0}/A_n	229.552	333.306	318.505	328.865	320.183	kN/mm^3
Margin of error (±) for mean row stiffness value for 95% confidence level	4.539	11.006	11.775	9.599	14.952	kN/mm^3
Largest K_{t0}/A_n value	238.483	354.415	341.807	350.790	339.689	kN/mm^3
Lowest K_{t0}/A_n value	219.705	313.973	298.018	313.380	290.821	kN/mm^3

Table A.20: Stiffness data obtained by fitting tangential load and tangential contact displacement data for each row in the displacement field for test SU2 for the loading steps.

Unloading Step	1	2	3	4	5	Units
Mean K_{t0}/A_n	380.163	351.683	340.175	345.275	316.322	kN/mm^3
Margin of error (±) for mean row stiffness value for 95% confidence level	21.180	11.429	20.941	20.056	34.692	kN/mm^3
Largest K_{t0}/A_n value	420.854	373.390	383.087	380.385	377.159	kN/mm^3
Lowest K_{t0}/A_n value	350.758	330.936	310.144	309.920	256.018	kN/mm^3

Table A.21: Stiffness data obtained by fitting tangential load and tangential contact displacement data for each row in the displacement field for test SU2 for the unloading steps.

Loading Step	1	2	3	4	5
K_{t0}/A_n (kN/mm^3)	400.362	352.892	335.920	314.682	326.287
K_{t0}/A_n (kN/mm^3), margin of error of fit	42.121	63.083	82.282	125.344	132.433
α_t fitting parameter	-2.180	-3.623	-4.395	-5.272	-5.876
α_t, margin of error (±) for 95% confidence level	0.089	0.257	0.383	0.674	0.307
β_t fitting parameter	-4.469	-3.012	-2.487	-2.050	-2.683
β_t, margin of error (±) for 95% confidence level	0.402	0.403	0.452	0.598	0.808
Q_s fitting parameter	1.792	2.343	2.702	3.070	2.432
Q_s, margin of error (±) for 95% confidence level	0.098	0.278	0.443	0.833	0.662
f	0.149	0.195	0.225	0.256	0.203
f, margin of error (±) for 95% confidence level	0.011	0.026	0.040	0.072	0.058
Adjusted R-Square Goodness of Fit	0.996	0.993	0.990	0.982	0.965

Table A.22: Data obtained from the fitted curves to the mean tangential contact displacement and tangential load data for the loading steps from the SU3 test.

Unloading Step	1	2	3	4	5
K_{t0}/A_n (kN/mm^3)	338.330	341.977	333.225	322.505	311.430
K_{t0}/A_n (kN/mm^3), margin of error of fit	62.558	141.815	190.186	341.396	332.832
α_t fitting parameter	1.444	1.576	2.939	3.971	3.108
α_t, margin of error (±) for 95% confidence level	0.330	0.789	1.779	4.273	3.683
β_t fitting parameter	2.291	2.194	1.386	1.052	1.141
β_t, margin of error (±) for 95% confidence level	0.311	0.666	0.568	0.796	0.874
Q_s fitting parameter	-2.954	-3.118	-4.809	-6.133	-5.458
Q_s, margin of error (±) for 95% confidence level	0.371	0.880	1.910	4.539	4.068
f	0.246	0.260	0.401	0.511	0.455
f, margin of error (±) for 95% confidence level	0.034	0.076	0.164	0.384	0.344
Adjusted R-Square Goodness of Fit	0.996	0.983	0.987	0.974	0.967

Table A.23: Data obtained from the fitted curves to the mean tangential contact displacement and tangential load data for the unloading steps from the SU3 test.

Loading Step	1	2	3	4	5	Units
Mean K_{t0}/A_n	410.930	353.144	329.180	302.864	309.579	kN/mm^3
Margin of error (±) for mean row stiffness value for 95% confidence level	46.187	28.231	32.323	36.383	36.171	kN/mm^3
Largest K_{t0}/A_n value	493.413	408.111	393.249	376.411	382.524	kN/mm^3
Lowest K_{t0}/A_n value	320.035	295.366	268.388	242.028	251.485	kN/mm^3

Table A.24: Data obtained from the fitted curves to the mean tangential contact displacement and tangential load data for the unloading steps from the SU3 test.

Unloading Step	1	2	3	4	5	Units
Mean K_{t0}/A_n	314.903	312.919	298.486	285.786	271.492	kN/mm^3
Margin of error (±) for mean row stiffness value for 95% confidence level	41.039	38.949	39.859	43.334	52.837	kN/mm^3
Largest K_{t0}/A_n value	387.786	377.640	367.502	364.806	380.701	kN/mm^3
Lowest K_{t0}/A_n value	243.832	244.373	232.966	222.414	203.850	kN/mm^3

Table A.25: Data obtained from the fitted curves to the mean tangential contact displacement and tangential load data for the unloading steps from the SU3 test.

A.4 Roughness Parameters for Structured Surfaces

	R_a (nm)	R_q (nm)	R_z (μm)	Profile length (mm)	Profile width(nm)	λ_c (μm)
Test S3, 2μm wavelength specimen						
Normal to pattern	585	719	3.540	5	671	800
Parallel to pattern	393	731	9.402	5	670	800
Pad A	878	1208	11.002	4	671	800
Pad B	806	1129	8.698	4	671	800
Test S2, 5μm wavelength specimen						
Normal to pattern	346	497	3.621	5	671	800
Parallel to pattern	314	407	2.343	5	671	800
Pad A	711	1122	10.882	4	671	800
Pad B	756	941	5.562	4	671	800
Test S1, 10μm wavelength specimen						
Normal to pattern	656	824	5.873	4.98	671	800
Parallel to pattern	318	421	2.628	5	671	800
Pad A	651	838	5.353	4	671	800
Pad B	690	874	5.175	4	671	800

Table A.26: Profile roughness parameters calculated as the average of 5 measurements for the specimen and pad surfaces used in the tests with structured surfaces. Vertical resolution 50 nm, lateral resolution of 2.01 μm, with 20X magnification objective were used for the measurement with the Alicona optical profilometer.

	S_a (nm)	S_q (nm)	S_p (μm)	S_{tr}	Fractal Dimension	Sample Area (mm^2)	λ_c
Test S3, 2μm wavelength specimen							
Specimen	499	752	28.690	0.595	2.002	2	800
Pad A	858	1146	35.363	0.872	2.007	2	800
Pad B	797	1057	23.818	0.858	2.006	2	800
Test S2, 5μm wavelength specimen							
Specimen	335	432	4.345	0.614	2.001	2	800
Pad A	661	868	23.628	0.869	2.010	2	800
Pad B	765	1003	23.322	0.869	2.013	2	800
Test S1, 10μm wavelength specimen							
Specimen	608	761	3.555	0.002	2.001	2	800
Pad A	711	978	22.715	0.857	2.005	2	800
Pad B	744	1016	26.668	0.857	2.005	2	800

Table A.27: Areal roughness parameters calculated as the average of 5 measurements for the specimen and pad surfaces used in the tests with structured surfaces. Vertical resolution 50 nm, lateral resolution of 2.01 μm, with 20X magnification objective ere used for the measurement with the Alicona optical profilometer.

A.5 Tangential Stiffness Test Results for Structured Surfaces

Loading Step	1	2	3	4	5
K_{t0}/A_n (kN/mm^3)	133.721	62.194	63.045	63.073	64.077
K_{t0}/A_n (kN/mm^3), margin of error of fit	34.253	65.636	163.648	68.044	112.099
α_t fitting parameter	-1.007	-3.683	-7.180	-4.105	-7.043
α_t, margin of error ($\pm$) for 95% confidence level	0.083	3.002	13.781	3.378	9.124
β_t fitting parameter	-2.478	-0.308	-0.168	-0.284	-0.173
β_t, margin of error ($\pm$) for 95% confidence level	0.590	0.232	0.309	0.219	0.215
Q_s fitting parameter	1.079	4.035	7.514	4.442	7.393
Q_s, margin of error ($\pm$) for 95% confidence level	0.102	2.981	13.753	3.359	9.104
f	0.135	0.504	0.939	0.555	0.924
f, margin of error ($\pm$) for 95% confidence level	0.015	0.378	1.729	0.426	1.148
Adjusted R-Square Goodness of Fit	0.987	0.973	0.955	0.976	0.976

Table A.28: Data obtained from the fitted curves to the mean tangential contact displacement and tangential load data for the loading steps from the S1 test.

Unloading Step	1	2	3	4	5
K_{t0}/A_n (kN/mm^3)	67.633	70.171	72.008	72.548	72.060
K_{t0}/A_n (kN/mm^3), margin of error of fit	30.428	29.612	24.985	34.387	24.633
α_t fitting parameter	1.259	1.531	1.577	1.689	1.615
α_t, margin of error ($\pm$) for 95% confidence level	0.502	0.507	0.418	0.594	0.410
β_t fitting parameter	0.849	0.830	0.843	0.818	0.849
β_t, margin of error ($\pm$) for 95% confidence level	0.285	0.261	0.219	0.288	0.218
Q_s fitting parameter	-1.593	-1.690	-1.708	-1.773	-1.697
Q_s, margin of error ($\pm$) for 95% confidence level	0.478	0.476	0.393	0.563	0.384
f	0.199	0.211	0.213	0.222	0.212
f, margin of error ($\pm$) for 95% confidence level	0.062	0.062	0.052	0.073	0.051
Adjusted R-Square Goodness of Fit	0.959	0.970	0.976	0.963	0.978

Table A.29: Data obtained from the fitted curves to the mean tangential contact displacement and tangential load data for the unloading steps from the S1 test.

Loading Step	1	2	3	4	5	Units
Mean K_{t0}/A_n	130.519	61.580	60.920	61.953	63.061	kN/mm^3
Margin of error ($\pm$) for mean row stiffness value for 95% confidence level	20.319	1.524	1.695	1.717	1.954	kN/mm^3
Largest K_{t0}/A_n value	240.869	69.553	69.459	70.297	72.889	kN/mm^3
Lowest K_{t0}/A_n value	77.829	54.941	55.119	54.210	54.309	kN/mm^3

Table A.30: Stiffness data obtained by fitting tangential load and tangential contact displacement data for each row in the displacement field for test S1 for the loading steps.

Unloading Step	1	2	3	4	5	Units
Mean K_{t0}/A_n	65.344	69.951	71.093	70.172	70.731	kN/mm^3
Margin of error (±) for mean row stiffness value for 95% confidence level	3.683	3.708	3.753	2.949	3.599	kN/mm^3
Largest K_{t0}/A_n value	83.716	87.956	90.798	84.931	90.649	kN/mm^3
Lowest K_{t0}/A_n value	54.578	56.530	57.482	57.810	58.341	kN/mm^3

Table A.31: Stiffness data obtained by fitting tangential load and tangential contact displacement data for each row in the displacement field for test S1 for the unloading steps.

Loading Step	1	2	3	4	5
K_{t0}/A_n (kN/mm^3)	63.780	46.214	44.108	43.678	43.342
K_{t0}/A_n (kN/mm^3), margin of error of fit	13.846	21.387	25.254	27.223	31.060
α_t fitting parameter	-2.007	-1.832	-2.162	-2.325	-2.553
α_t, margin of error (±) for 95% confidence level	0.245	0.704	0.998	1.155	1.441
β_t fitting parameter	-0.619	-0.426	-0.355	-0.331	-0.303
β_t, margin of error (±) for 95% confidence level	0.110	0.144	0.148	0.150	0.157
Q_s fitting parameter	2.061	2.171	2.483	2.640	2.861
Q_s, margin of error (±) for 95% confidence level	0.256	0.684	0.976	1.133	1.416
f	0.258	0.271	0.310	0.330	0.358
f, margin of error (±) for 95% confidence level	0.036	0.089	0.126	0.145	0.181
Adjusted R-Square Goodness of Fit	0.999	0.988	0.987	0.987	0.986

Table A.32: Data obtained from the fitted curves to the mean tangential contact displacement and tangential load data for the loading steps from the S2 test.

Unloading Step	1	2	3	4	5
K_{t0}/A_n (kN/mm^3)	50.115	46.280	45.186	44.953	44.969
K_{t0}/A_n (kN/mm^3), margin of error of fit	5.984	13.788	15.749	15.587	16.560
α_t fitting parameter	1.270	1.727	1.921	1.857	1.995
α_t, margin of error (±) for 95% confidence level	0.131	0.390	0.496	0.478	0.539
β_t fitting parameter	0.648	0.504	0.453	0.465	0.438
β_t, margin of error (±) for 95% confidence level	0.058	0.110	0.115	0.118	0.118
Q_s fitting parameter	-1.548	-1.835	-1.996	-1.932	-2.054
Q_s, margin of error (±) for 95% confidence level	0.123	0.371	0.475	0.456	0.517
f	0.193	0.229	0.249	0.241	0.257
f, margin of error (±) for 95% confidence level	0.019	0.049	0.063	0.060	0.068
Adjusted R-Square Goodness of Fit	0.998	0.993	0.992	0.992	0.992

Table A.33: Data obtained from the fitted curves to the mean tangential contact displacement and tangential load data for the unloading steps from the S2 test.

Loading Step	1	2	3	4	5	Units
Mean K_{t0}/A_n	63.209	46.612	44.547	44.170	43.843	kN/mm^3
Margin of error (±) for mean row stiffness value for 95% confidence level	3.482	0.987	0.949	0.972	0.998	kN/mm^3
Largest K_{t0}/A_n value	84.630	50.708	48.355	47.643	47.225	kN/mm^3
Lowest K_{t0}/A_n value	51.193	42.707	40.689	40.085	39.927	kN/mm^3

Table A.34: Stiffness data obtained by fitting tangential load and tangential contact displacement data for each row in the displacement field for test S2 for the loading steps.

Unloading Step	1	2	3	4	5	Units
Mean K_{t0}/A_n	50.773	46.873	45.721	45.514	45.557	kN/mm^3
Margin of error (±) for mean row stiffness value for 95% confidence level	1.831	1.578	1.538	1.503	1.541	kN/mm^3
Largest K_{t0}/A_n value	58.452	53.026	52.304	51.590	51.992	kN/mm^3
Lowest K_{t0}/A_n value	44.401	41.441	40.482	40.308	40.375	kN/mm^3

Table A.35: Stiffness data obtained by fitting tangential load and tangential contact displacement data for each row in the displacement field for test S2 for the unloading steps.

Loading Step	1	2	3	4	5
K_{t0}/A_n (kN/mm^3)	13.383	12.300	12.123	12.093	12.078
K_{t0}/A_n (kN/mm^3), margin of error of fit	2.466	1.333	1.698	1.866	1.983
α_t fitting parameter	-2.771	-2.101	-2.177	-2.186	-2.231
α_t, margin of error (±) for 95% confidence level	0.320	0.178	0.237	0.262	0.283
β_t fitting parameter	-0.094	-0.105	-0.101	-0.100	-0.098
β_t, margin of error (±) for 95% confidence level	0.014	0.008	0.010	0.011	0.012
Q_s fitting parameter	2.834	2.332	2.406	2.412	2.455
Q_s, margin of error (±) for 95% confidence level	0.325	0.172	0.230	0.254	0.276
f	0.354	0.291	0.301	0.302	0.307
f, margin of error (±) for 95% confidence level	0.046	0.027	0.034	0.037	0.039
Adjusted R-Square Goodness of Fit	1.000	0.999	0.999	0.999	0.999

Table A.36: Data obtained from the fitted curves to the mean tangential contact displacement and tangential load data for the loading steps from the S3 test.

Unloading Step	1	2	3	4	5
K_{t0}/A_n (kN/mm^3)	11.502	11.460	11.442	11.464	11.503
K_{t0}/A_n (kN/mm^3), margin of error of fit	2.269	2.659	3.643	3.908	4.345
α_t fitting parameter	5.400	6.834	8.115	8.722	8.570
α_t, margin of error (±) for 95% confidence level	0.772	1.131	1.836	2.111	2.298
β_t fitting parameter	0.042	0.033	0.028	0.026	0.027
β_t, margin of error (±) for 95% confidence level	0.006	0.005	0.006	0.006	0.007
Q_s fitting parameter	-5.525	-6.888	-8.151	-8.751	-8.597
Q_s, margin of error (±) for 95% confidence level	0.768	1.127	1.832	2.106	2.292
f	0.691	0.861	1.019	1.094	1.075
f, margin of error (±) for 95% confidence level	0.106	0.153	0.242	0.277	0.300
Adjusted R-Square Goodness of Fit	1.000	1.000	1.000	1.000	0.999

Table A.37: Data obtained from the fitted curves to the mean tangential contact displacement and tangential load data for the unloading steps from the S3 test.

Loading Step	1	2	3	4	5	Units
Mean K_{t0}/A_n	13.334	12.357	12.172	12.134	12.119	kN/mm^3
Margin of error (±) for mean row stiffness value for 95% confidence level	0.337	0.169	0.155	0.163	0.174	kN/mm^3
Largest K_{t0}/A_n value	14.676	12.950	12.688	12.702	12.722	kN/mm^3
Lowest K_{t0}/A_n value	11.603	11.811	11.611	11.607	11.570	kN/mm^3

Table A.38: Stiffness data obtained by fitting tangential load and tangential contact displacement data for each row in the displacement field for test S3 for the unloading steps.

Unloading Step	1	2	3	4	5	Units
Mean K_{t0}/A_n	11.556	11.509	11.489	11.506	11.552	kN/mm^3
Margin of error (±) for mean row stiffness value for 95% confidence level	0.111	0.117	0.119	0.126	0.116	kN/mm^3
Largest K_{t0}/A_n value	12.029	11.952	11.927	11.972	12.009	kN/mm^3
Lowest K_{t0}/A_n value	11.079	11.063	11.057	11.077	11.118	kN/mm^3

Table A.39: Stiffness data obtained by fitting tangential load and tangential contact displacement data for each row in the displacement field for test S3 for the unloading steps.

Appendix B

Appendix for Receding Contact Analysis

B.1 Green's Functions for a Dislocation in the Half-Plane

$$H_{yxy}\left(\hat{x},\hat{\xi}\right) = 8\left[\frac{3}{\left[4+(\hat{x}-\hat{\xi})^2\right]^2} - \frac{16}{\left[4+(\hat{x}-\hat{\xi})^2\right]^3}\right],$$

$$H_{yyy}\left(\hat{x},\hat{\xi}\right) = \frac{1}{\hat{x}-\hat{\xi}} + \left[\begin{array}{c} -\dfrac{\hat{x}-\hat{\xi}}{4+(\hat{x}-\hat{\xi})^2} - \dfrac{4(\hat{x}-\hat{\xi})}{\left[4+(\hat{x}-\hat{\xi})^2\right]^2} \\ -\dfrac{64(\hat{x}-\hat{\xi})}{\left[4+(\hat{x}-\hat{\xi})^2\right]^3} \end{array}\right],$$

$$H_{xxy}\left(\hat{x},\hat{\xi}\right) = \frac{1}{\hat{x}-\hat{\xi}} + \left[\begin{array}{c} -\dfrac{\hat{x}-\hat{\xi}}{4+(\hat{x}-\hat{\xi})^2} + \dfrac{12(\hat{x}-\hat{\xi})}{\left[4+(\hat{x}-\hat{\xi})^2\right]^2} \\ -\dfrac{64(\hat{x}-\hat{\xi})}{\left[4+(\hat{x}-\hat{\xi})^2\right]^3} \end{array}\right],$$

$$H_{xyy}\left(\hat{x},\hat{\xi}\right) = 8\left[-\frac{3}{\left[4+(\hat{x}-\hat{\xi})^2\right]^2} + \frac{16}{\left[4+(\hat{x}-\hat{\xi})^2\right]^3}\right].$$

($\hat{x} \equiv x/c$ and $\hat{\xi} \equiv \xi/c$).

B.2 Surface Displacements and Gradients at Remote Points Due to Distributed Loads

B.2.1 General Case

In §6.3 it was assumed, intuitively, that the remote surface displacements, and subsequently the remote surface displacement gradients, of the half-plane loaded by normal traction and shear traction approach that for the half-plane loaded by statically equivalent line loads. In this section, it will be shown mathematically that the remote surface gradients will approach that for a half-plane loaded by equivalent line loads, and the total surface displacements approach the surface displacements due to the line loads with additive constants.

Consider a half-plane, $y \leq 0$, loaded by a tangential line load F at (ξ,0). By Flamant's theorem [66, p. 175], for $x > \xi$

$$u_x(x) = -\frac{F(\kappa+1)}{4\pi\mu}\ln(x-\xi), \tag{B.1}$$

where $u_x(x)$ is the tangential displacement of a point $(x, 0)$ with respect to the tangential displacement of a point at (ξ,0). The tangential displacement gradient is therefore, for $x > \xi$

$$\frac{du_x(x)}{dx} = -\frac{F(\kappa+1)}{4\pi\mu}\frac{1}{(x-\xi)}. \tag{B.2}$$

The series expansion at $x \to \infty$ of this expression is

$$\frac{du_x(x)}{dx} = -\frac{F(\kappa+1)}{4\pi\mu}\left(\frac{1}{x} + \frac{\xi}{x^2} + \frac{\xi^2}{x^3}... + \frac{\xi^{n-1}}{x^n}\right). \tag{B.3}$$

The tangential displacement gradient due to a distributed tangential load $S(\xi)$ applied over an interval $\xi \in [\alpha \quad \beta]$ on the half-plane surface by principle of superposition is therefore given by, for $x > \beta$,

$$\begin{aligned}\frac{du_x(x)}{dx} &= -\frac{(\kappa+1)}{4\pi\mu}\left(\frac{\int_\alpha^\beta S(\xi)d\xi}{x} + \frac{\int_\alpha^\beta \xi S(\xi)d\xi}{x^2} + ... + \frac{\int_\alpha^\beta \xi^{n-1}S(\xi)d\xi}{x^n}\right)\\ &= -\frac{(\kappa+1)}{4\pi\mu}\left(\frac{F_{eq}}{x} + \frac{F_{eq}\xi_{eq}}{x^2} + O[\frac{1}{x^3}]\right)\\ &= -F_{eq}\frac{(\kappa+1)}{4\pi\mu}\left(\frac{1}{x} + \frac{\xi_{eq}}{x^2} + O[\frac{1}{x^3}]\right)\end{aligned} \tag{B.4}$$

where $F_{eq} = \int_\alpha^\beta S(\xi)d\xi$ and ξ_{eq} is defined such that $F_{eq}\xi_{eq} = \int_\alpha^\beta \xi S(\xi)d\xi$.

F_{eq} is the statically equivalent load for $S(x)$ pressure distribution. If a half-plane is loaded by tangential load F_{eq} at $(\xi_{eq}, 0)$, it will lead to a tangential surface displacement gradient, from equation (B.3),

$$\frac{du_x(x)}{dx} = -F_{eq}\frac{(\kappa+1)}{4\pi\mu}\left(\frac{1}{x} + \frac{\xi_{eq}}{x^2} + O[\frac{1}{x^3}]\right) \tag{B.5}$$

From equations (B.4) and (B.5), it is therefore clear that for increasing x the tangential surface displacement gradient due to a distributed tangential load approaches that for an equivalent line load.

The tangential displacement gradient due to a distributed load $S(\xi)$ can be therefore deduced from equation (B.2) to be given by

$$\frac{du_x(x)}{dx} = -\frac{F_{eq}(\kappa+1)}{4\pi\mu}\frac{1}{(x-\xi_{eq})} + O[\frac{1}{x^3}]$$

If the total relative tangential displacement $u_x(x_1)$ is C_{x1}, where x_1 is a remote point, then for remote points $x > x_1$

$$\begin{aligned} u_x(x) &= C_{x1} + \int_{x_1}^{x}\left(-\frac{F_{eq}(\kappa+1)}{4\pi\mu}\frac{1}{(x-\xi_{eq})} + O[\frac{1}{x^3}]\right)dx \\ &= C_{x1} + \int_{x_1}^{x}\left(-\frac{F_{eq}(\kappa+1)}{4\pi\mu}\frac{1}{(x-\xi_{eq})}\right)dx + \int_{x_1}^{x}\left(O[\frac{1}{x^3}]\right)dx \\ &= C_{x1} + C_{x2} - \frac{F_{eq}(\kappa+1)}{4\pi\mu}\ln(x-\xi_{eq}) + O[\frac{1}{x^2}] \\ &= -\frac{F_{eq}(\kappa+1)}{4\pi\mu}\ln(x-\xi_{eq}) + C_x + O[\frac{1}{x^2}] \end{aligned} \tag{B.6}$$

where C_{x2} and C_x are constants. Therefore the relative remote tangential surface displacements approach the relationship for an equivalent tangential load, given in equation (B.1), with an additive constant.

The relative normal displacement of the half-plane surface due to a tangential line load, F, is a step function given by, for $x > 0$, [66, p. 175]

$$u_y = -\frac{F(\kappa-1)}{8\mu}.$$

It is trivial to show that the relative normal displacement at remote points due to a tangential distributed load is exactly given by this relationship for an equivalent tangential line load, and that the normal surface displacement gradient will be 0 at remote points.

The relative normal displacement gradient at remote points due to a normal load distribution

$N(\xi)$ applied over a finite region $\xi \in [\alpha \quad \beta]$ on the surface of half-plane can be shown in an identical analysis to approach that given by an equivalent normal line load applied on the half-plane surface. The total relative normal displacement will also be given by the expression for an equivalent line load with an additive constant.

The tangential surface displacement due to normal pressure at remote points can also be shown to be given exactly by the relationship for an equivalent normal line load, and the tangential surface displacement gradient will be 0 at remote points.

B.2.2 Special Case of an Anti-symmetric Shear Traction

If $S(x)$, the shear traction applied onto the half-plane surface, at $x \in [\alpha \quad \beta]$ is anti-symmetric, it may be tempting to assume its effect on remote displacement gradients can be modelled by a single statically equivalent line load F_{eq}, where $F_{eq} = \int_\alpha^\beta S(\xi)d\xi = 0$, as in the above analysis. However this would not be valid since $\int_\alpha^\beta \xi S(\xi)d\xi$ is finite, and no finite value of ξ_{eq} can be found such that $F_{eq}\xi_{eq} = \int_\alpha^\beta \xi S(\xi)d\xi$.

In this case, a suitable work around would be to the model $S(x)$ traction as a pair of equivalent shear line loads, $-F_{eq}$ and F_{eq} applied at ξ_1 and ξ_2, such that

$$-F_{eq}\xi_1 + F_{eq}\xi_2 = \int_\alpha^\beta \xi S(\xi)d\xi. \tag{B.7}$$

From equation (B.3), by superposition the tangential displacement gradient due to the two shear line loads is given by

$$\begin{aligned}\frac{du_x(x)}{dx} &= \left[\begin{array}{c} -\dfrac{-F_{eq}(\kappa+1)}{4\pi\mu}\left(\dfrac{1}{x} + \dfrac{\xi_1}{x^2} + \dfrac{\xi_1^2}{x^3}... + \dfrac{\xi_1^{n-1}}{x^n}\right) \\ -\dfrac{F_{eq}(\kappa+1)}{4\pi\mu}\left(\dfrac{1}{x} + \dfrac{\xi_2}{x^2} + \dfrac{\xi_2^2}{x^3}... + \dfrac{\xi_2^{n-1}}{x^n}\right) \end{array}\right] \\ &= -\frac{(\kappa+1)}{4\pi\mu}\left(\frac{-F_{eq}\xi_1 + F_{eq}\xi_2}{x^2} + O[\frac{1}{x^3}]\right)\end{aligned} \tag{B.8}$$

And from equation (B.4) the tangential displacement gradient due to the anti-symmetric shear distribution $S(x)$ applied on the surface at $x \in [\alpha \quad \beta]$ is given by

$$\begin{aligned}\frac{du_x(x)}{dx} &= -\frac{(\kappa+1)}{4\pi\mu}\left(\frac{\int_\alpha^\beta S(\xi)d\xi}{x} + \frac{\int_\alpha^\beta \xi S(\xi)d\xi}{x^2} + ... + \frac{\int_\alpha^\beta \xi^{n-1}S(\xi)d\xi}{x^n}\right) \\ &= -\frac{(\kappa+1)}{4\pi\mu}\left(\frac{-F_{eq}\xi_1 + F_{eq}\xi_2}{x^2} + O[\frac{1}{x^3}]\right),\end{aligned} \tag{B.9}$$

since $\int_\alpha^\beta S(\xi)d\xi = 0$ and from equation (B.7) $-F_{eq}\xi_1 + F_{eq}\xi_2 = \int_\alpha^\beta \xi S(\xi)d\xi$. It is clear from equations (B.8) and (B.9) that the expression for surface tangential displacement gradient due to a pair of line loads approaches that for an anti-symmetric shear traction, for large x.

B.3 Integration to Find Stress Components due to Preformed Distribution of Dislocations

The most challenging and tedious aspect of the solution of these problems is obtaining expressions for the stress components at $y = 0$ of the augmented half-plane $y \leq c$ due to the presence of the preformed climb dislocation density, i.e. solving equations (7.24) and (7.25). In this section, some discussion is provided on the process of solving these integrals, particularly as used to solve the integrals for the square root singular problem of Chapter 7 (the process is similar for the other problems, with more terms solved analytically than numerically). While closed form solution were obtained for some of the problems for all useful intervals, the easiest solution procedure, particularly for problems with more complicated integral terms, is to use a mixture of closed form solutions and numerical integration, as was done for the square root singular problem. The closed form solutions found for the various component integral terms can be re-used in other problems.

The integrals that need to be computed are

$$\int_{-\infty}^{\infty} a_y(\xi) H_{yyy}(\hat{x}, \hat{\xi}) d\hat{\xi},$$
$$\int_{-\infty}^{\infty} a_y(\xi) H_{yxy}(\hat{x}, \hat{\xi}) d\hat{\xi}.$$

These are expanded to their component parts

$$\begin{aligned}\int_{-\infty}^{\infty} a_y(\xi) H_{yyy}(\hat{x}, \hat{\xi}) d\hat{\xi} = &\int_{-\infty}^{-\hat{e}} b_{yl}(\xi) H_{yyy}(\hat{x}, \hat{\xi}) d\hat{\xi} + \int_{-\hat{e}}^{-\hat{b}} r_y(\xi) H_{yyy}(\hat{x}, \hat{\xi}) d\hat{\xi} \\ &+ \int_{\hat{b}}^{\hat{e}} r_y(\xi) H_{yyy}(\hat{x}, \hat{\xi}) d\hat{\xi} + \int_{\hat{e}}^{\infty} b_{yl}(\xi) H_{yyy}(\hat{x}, \hat{\xi}) d\hat{\xi}\end{aligned} \tag{B.10}$$

$$\begin{aligned}\int_{-\infty}^{\infty} a_y(\xi) H_{yxy}(\hat{x}, \hat{\xi}) d\hat{\xi} = &\int_{-\infty}^{-\hat{e}} b_{yl}(\xi) H_{yxy}(\hat{x}, \hat{\xi}) d\hat{\xi} + \int_{-\hat{e}}^{-\hat{b}} r_y(\xi) H_{yxy}(\hat{x}, \hat{\xi}) d\hat{\xi} \\ &+ \int_{\hat{b}}^{\hat{e}} r_y(\xi) H_{yxy}(\hat{x}, \hat{\xi}) d\hat{\xi} + \int_{\hat{e}}^{\infty} b_{yl}(\xi) H_{yxy}(\hat{x}, \hat{\xi}) d\hat{\xi}\end{aligned} \tag{B.11}$$

Here $b_{yl}(x)$ is defined so that $B_{yl}(x) = \frac{2\mu}{\pi(1+\kappa)A_N} b_{yl}(x)$. The integral terms are further expanded in terms of each individual component of the $b_{yl}(x)$ function. For instance, for the square root

singular problem

$$\int_{\hat{e}}^{\infty} b_{yl}(\xi) H_{yyy}(\hat{x},\hat{\xi}) d\hat{\xi} = \int_{\hat{e}}^{\infty} \frac{1}{\sqrt{\hat{\xi}^2 - \hat{w}^2}} H_{yyy}(\hat{x},\hat{\xi}) d\hat{\xi} - \int_{\hat{e}}^{\infty} K_3 H_{yyy}(\hat{x},\hat{\xi}) d\hat{\xi} \tag{B.12}$$

$$\int_{\hat{e}}^{\infty} b_{yl}(\xi) H_{yxy}(\hat{x},\hat{\xi}) d\hat{\xi} = \int_{\hat{e}}^{\infty} \frac{1}{\sqrt{\hat{\xi}^2 - \hat{w}^2}} H_{yxy}(\hat{x},\hat{\xi}) d\hat{\xi} - \int_{\hat{e}}^{\infty} K_3 H_{yxy}(\hat{x},\hat{\xi}) d\hat{\xi}. \tag{B.13}$$

and similar expressions are written for integral terms with $b_{yl}(x)$ function with the negative intervals.

Each integral term in equation (B.10) corresponds to the normal stress component (with a multiplier) due to a component of preformed climb dislocation density distribution, and the same is true for each integral term in equation (B.10) for the shear stress components.

The solution can be simplified on the basis of a few observations, given the anti-symmetry of the preformed distributions (or the symmetry of the separation of surfaces they correspond to).

1. If $\sigma^R_{yyD}(x)$ is the normal stress component at $(x, 0)$ due to a climb dislocation distribution applied on the right side of the origin, then $\sigma^R_{yyD}(-x)$ is the normal stress component at $(x, 0)$ due to an equivalent but anti-symmetric climb dislocation density applied on the left side of the origin.

2. Similarly if $\sigma^R_{xyD}(x)$ is the shear stress component at $(x, 0)$ due to a climb dislocation distribution applied on the right side of the origin, then the stress component at $(x, 0)$ due to an equivalent anti-symmetric climb dislocation density applied at the left side of the origin is given by $-\sigma^R_{xyD}(-x)$.

The implication of these two observations is that when closed form solutions are obtained for integral terms with the positive intervals for all x, the solution can be used to find the result of the corresponding integral terms with negative intervals. For instance, in the square root singular problem closed form solutions were known for the following integral terms (they were computed

earlier for the other problems)

$$
\begin{aligned}
CF1(x) &= \int_{\hat{b}}^{\hat{e}} r_y(\xi) H_{yyy}(\hat{x},\hat{\xi}) d\hat{\xi}, \\
CF2(x) &= \int_{\hat{b}}^{\hat{e}} r_y(\xi) H_{yxy}(\hat{x},\hat{\xi}) d\hat{\xi}, \\
CF3(x) &= \int_{\hat{e}}^{\infty} K_3 H_{yyy}(\hat{x},\hat{\xi}) d\hat{\xi}, \\
CF4(x) &= \int_{\hat{e}}^{\infty} K_3 H_{yxy}(\hat{x},\hat{\xi}) d\hat{\xi}.
\end{aligned}
$$

and therefore closed form solutions for these integral terms are given by

$$\int_{-\hat{e}}^{-\hat{b}} r_y(\xi) H_{yyy}(\hat{x},\hat{\xi}) d\hat{\xi} = CF1(-x), \tag{B.14}$$

$$\int_{-\hat{e}}^{-\hat{b}} r_y(\xi) H_{yxy}(\hat{x},\hat{\xi}) d\hat{\xi} = -CF2(-x), \tag{B.15}$$

$$\int_{-\infty}^{-\hat{e}} K_3 H_{yyy}(\hat{x},\hat{\xi}) d\hat{\xi} = CF3(-x), \tag{B.16}$$

$$\int_{-\infty}^{-\hat{e}} K_3 H_{yxy}(\hat{x},\hat{\xi}) d\hat{\xi} = -CF4(-x). \tag{B.17}$$

Many of these integrals are singular, particularly the ones with the $H_{yyy}(\cdot)$ kernel, and therefore Cauchy principal value had been used in finding closed form expressions for them.

A third observation is made. If $E_y(x)$ function is anti-symmetric then

$$\begin{bmatrix} \int_{\hat{e}}^{\infty} E_y(\xi) H_{yyy}(x,\xi) d\xi \\ + \int_{-\infty}^{-\hat{e}} E_y(\xi) H_{yyy}(x,\xi) d\xi \end{bmatrix} = \int_{\hat{e}}^{\infty} \left[H_{yyy}(x,\xi) - H_{yyy}(x,-\xi) \right] E_y(\xi) d\hat{\xi}, \tag{B.18}$$

$$\begin{bmatrix} \int_{\hat{e}}^{\infty} E_y(\xi) H_{yxy}(x,\xi) d\xi \\ + \int_{-\infty}^{-\hat{e}} E_y(\xi) H_{yxy}(x,\xi) d\xi \end{bmatrix} = \int_{\hat{e}}^{\infty} \left[H_{yxy}(x,\xi) - H_{yyy}(x,-\xi) \right] E_y(\xi) d\hat{\xi}. \tag{B.19}$$

This is found by substituting the variable $-\xi$ for ξ in the integral term with negative intervals, and using the anti-symmetric properties of the distribution: $E_y(-\xi) = -E_y(\xi)$. In the case of the square root singular pressure problem, the integral terms for which closed form solutions were not known for all x were summed this way, i.e.

$$\left[\begin{array}{l} \displaystyle\int_{\hat{e}}^{\infty} \frac{1}{\sqrt{\hat{\xi}^2-\hat{z}^2}} H_{yyy}(x,\xi)d\xi \\ \displaystyle+\int_{-\infty}^{-\hat{e}} \frac{1}{\sqrt{\hat{\xi}^2-\hat{w}^2}} H_{yyy}(x,\xi)d\xi \end{array}\right] = \int_{\hat{e}}^{\infty} \left[H_{yyy}(x,\xi) - H_{yyy}(x,-\xi)\right] \frac{1}{\sqrt{\hat{\xi}^2-\hat{w}^2}} d\hat{\xi} \qquad \text{(B.20)}$$

$$\left[\begin{array}{l} \displaystyle\int_{\hat{e}}^{\infty} \frac{1}{\sqrt{\hat{\xi}^2-\hat{z}^2}} H_{yxy}(x,\xi)d\xi \\ \displaystyle+\int_{-\infty}^{-\hat{e}} \frac{1}{\sqrt{\hat{\xi}^2-\hat{w}^2}} H_{yxy}(x,\xi)d\xi \end{array}\right] = \int_{\hat{e}}^{\infty} \left[H_{yxy}(x,\xi) - H_{yxy}(x,-\xi)\right] \frac{1}{\sqrt{\hat{\xi}^2-\hat{w}^2}} d\hat{\xi} \qquad \text{(B.21)}$$

$\hat{e}$ is defined $> \hat{w}$. It should be noted that the integral on the right hand side of equation (B.20) is singular for $x > \hat{e}$ and $x < -\hat{e}$. The right hand side of equation (B.21) however is regular for all intervals of x

Numerical integration is suitable when the integration is regular and was used for solving the integral on the right hand side of of equation (B.20) for $-\hat{e} < x < \hat{e}$, and for all x for the integral in the right hand side of equation (B.21). A closed form expression was found for the integral on the right hand side of (B.20) for $x > \hat{e}$ using Cauchy principal value. (Due to the symmetry of separation of surfaces associated with these climb dislocation functions, the normal stress component due to it is symmetric and therefore the solution for $x < -\hat{e}$ can be found from the closed form expression for $x > \hat{e}$ interval, by substituting $-x$ in the place of x.)

B.4 Relationship between the Total Slip, the Slope of the Layer and the Shear Traction

As in Chapter 6, the relationship between the total slip of the layer at remote points, the slope of the layer at remote points, and the shear traction is derived, by inserting the remote form of glide dislocation density and climb dislocation density at the location of the contact interface and pair of corrective glide and climb dislocations near the origin. In the case of the constant pressure patch problem, in the augmented half-plane ($y \leq c$) at the location of the interface ($y = 0$) the following were inserted

1. A climb dislocation distribution of the form $-sign(\hat{x})k_l$ at $x \in [-\infty \quad -w] \cup [w \quad \infty]$. This is a component of the expected form of the remote climb dislocation density, B_{yl1} given in equation (7.12). (k_l is the slope of the layer at remote points).

2. A climb dislocation distribution of the form $sign(\hat{x})\frac{A_1(\kappa+1)}{4\pi\mu}\left[\ln(|\hat{x}|+\hat{w})-\ln(|\hat{x}|-\hat{w})\right]$ at $x \in [-\infty \quad -1-w]\cup[1+w \quad \infty]$. This is the remaining component of the expected form of the remote climb dislocation density, B_{yl1} given in equation (7.12).

3. Glide dislocation density $B_{xl}(x)$ given in equation (7.11) is inserted at all points in $x \in [-\infty \quad \infty]$.

4. Two corrective glide dislocations, each of magnitude b_x applied on either side of the origin.

5. Two corrective climb dislocations, $-b_y$, and b_y, applied at either side of the origin.

The sum of the slowest decaying terms for the stress components due to these eigenstrains and the external loading at remote points, $x >> c$, along the location of the interface is given by

$$\frac{N(\hat{x})}{A_1} = \frac{-4\hat{w}}{\pi\hat{x}^4}-\frac{48M_1\hat{b_x}}{\hat{x}^4}+\frac{12\pi M_1F^*}{\hat{x}^4}-\frac{24M_1k_l}{\hat{x}^4}-\frac{16\hat{w}M_1k_c\pi}{\hat{x}^4}=0, \tag{B.22}$$

$$\frac{S(\hat{x})}{A_1} = \frac{2\hat{w}}{\pi\hat{x}^3}+\frac{32M_1\hat{b_x}}{\hat{x}^3}-\frac{8\pi M_1F^*}{\hat{x}^3}+\frac{16M_1k_l}{\hat{x}^3}+\frac{8\hat{w}M_1\pi k_c}{\hat{x}^3}=0 \tag{B.23}$$

$$M_1=\frac{2\mu}{\pi(\kappa+1)A_i}, \quad k_c=\frac{A_1(1+\kappa)}{4\pi\mu}.$$

($F^* \equiv \frac{F\hat{d}(1+\kappa)}{2\mu\pi c}$, $\hat{x} \equiv x/c$ and $\hat{b_x} \equiv b_x/c$). The stress components due to the pair of discrete climb dislocations involve only higher order terms and can be neglected. Solving the above leads to the relationship

$$\hat{b_x}=\frac{-A_1\hat{w}(1+\kappa)}{8\mu}-\frac{k_l}{2}+\frac{F\hat{d}(1+\kappa)}{8\mu c}. \tag{B.24}$$

It can be shown (as was in Chapter 6) that

$$\hat{b_x}=\int_0^\infty B_x(\hat{\xi})d\hat{\xi},$$

and so

$$M_1\int_0^\infty B_x(\hat{\xi})d\hat{\xi}=\frac{-\hat{w}}{4\pi}-\frac{M_1k_l}{2}+\frac{1}{4\pi}\int_0^{\hat{b}}\hat{\xi}\frac{S(\hat{\xi})}{A_1}d\hat{\xi}. \tag{B.25}$$

$M_1 \equiv \frac{2\mu}{\pi(\kappa+1)A_1}$

A similar analysis can be done for the square root bounded pressure problem and the square root singular pressure problem to derive similar expressions for these problems. The expressions

for all three problems can be generalised to be given by

$$\frac{M\int_0^\infty B_x(\xi)d\hat{\xi}}{T} = \frac{-1}{8\pi} + \frac{Mk_l}{2T} + \frac{1}{4\pi}\int_0^{\hat{b}} \hat{\xi}\frac{S(\xi)}{T}d\hat{\xi}. \tag{B.26}$$

where

$$M = \frac{2\mu}{\pi(1+\kappa)}, \quad T = \left(\int_w^{-w} p(x)dx\right)/c.$$

This is the exact relationship derived in Chapter 6 for the layer loaded by a line load of magnitude Tc. It is not difficult to see that the bilateral solution of any finite normal pressure distribution will approach that of a normal line load at remote points, and the slowest decaying stress term will be the same. It can also be shown that for any finite symmetric pressure loading, the remote glide and climb dislocation densities, and the stress components at remote points due to them, will approach the same form for the line load problem (See Appendix of Chapter 6), i.e. the slowest decaying component of the remote form of the glide and climb dislocation densities will be the same as for a line loading problem. The constant terms (F^* and k_l) may vary. Therefore, for any symmetric finite pressure loading, the magnitude of the corrective discrete glide dislocations required to satisfy the contact conditions at remote points will have the same relationship with k_l and the shear traction, as that for the line load problem, since the slowest decaying stress components due to the other inserted eigenstrains and the external loading will have the same form.

B.5 Finite Approximations of Semi-Infinite Pressure Distributions

If w is increased sufficiently, the solution to finite pressure distribution problems can be used to estimate the solutions to semi-infinite problems. Coordinate x_e is defined with respect to the right edge of the pressure distributions, i.e $x_e = x - w$. The three corresponding semi-infinite problems are defined when pressure is applied to the layer free surface, $y = c$, from $x_e \in [-\infty \quad 0]$ such that

1.

$$p(x_e) = -B_1$$

or

$$\frac{p(x_e)}{B_1} = -1$$

2.

$$p(x_e) = -B_2\sqrt{-x_e}$$

or

$$\frac{p(x_e)}{B_2\sqrt{c}} = -\sqrt{-\hat{x_e}}$$

3.

$$p(x_e) = -\frac{B_3}{\sqrt{-x_e}}$$

or

$$\frac{p(x_e)}{(B_3/\sqrt{c})} = -\sqrt{-\hat{x_e}}$$

In the case of the constant pressure patch problem, it is clear $B_1 \approx A_1$ when $\hat{w} \to \infty$. The expressions of B_2 and B_3 in terms of A_2, A_3 and $\hat{w}$ are required to interpolate the solutions for the semi-infinite problems from solutions of the finite problems with large $\hat{w}$.

For the square root singular loading problem

$$p(x) = -A_2\sqrt{w^2 - x^2}.$$

Changing the coordinate system gives

$$\begin{aligned} p(x_e) &= -A_2\sqrt{w^2 - (x_e + w)^2} \\ &= -A_2\sqrt{-x_e^2 - 2x_e w} \\ &= -(A_2\sqrt{w})\sqrt{-\frac{x_e^2}{w} - 2x_e} \end{aligned}$$

taking $\lim w \to \infty$

$$p(x_e) \approx -(A_2\sqrt{2w})\sqrt{-x_e}$$

This implies for large w

$$B_2 \approx (A_2\sqrt{2w})$$

or

$$B_2\sqrt{c} \approx (A_2 c\sqrt{2\hat{w}}) \tag{B.27}$$

For the square root singular problem

$$p(x_e) = -\frac{A_3}{\sqrt{w^2 - x^2}}.$$

which on changing coordinate system gives

$$p(x_e) = -\frac{(A_3/\sqrt{w})}{\sqrt{-\frac{x_e^2}{w} - 2x_e}}.$$

taking $\lim w \to \infty$

$$p(x_e) \approx -\frac{(A_3/\sqrt{2w})}{\sqrt{-x_e}}.$$

implying

$$B_3 \approx (A_3/\sqrt{2w})$$

or

$$B_3/\sqrt{c} \approx \left(\frac{A_3}{c\sqrt{2\hat{w}}}\right) \tag{B.28}$$

Bibliography

[1] M. Urbakh, J. Klafter, D. Gourdon, and J. Israelachvili. The nonlinear nature of friction. *Nature*, 430(6999):525, 2004.

[2] E. Petrov and D. Ewins. Effects of damping and varying contact area at blade-disk joints in forced response analysis of bladed disk assemblies. *Journal of Turbomachinery*, 128(2):403–410, 2006.

[3] A. Sackfield, D. Hills, and D. Nowell. *Mechanics of elastic contacts*. Elsevier, 1993.

[4] S. Medina, D. Nowell, and D. Dini. Analytical and numerical models for tangential stiffness of rough elastic contacts. *Tribology Letters*, 49(1):103–115, 2013.

[5] D. Wang, A. Ueckermann, A. Schacht, M. Oeser, B. Steinauer, and B. N. J. Persson. Tire–road contact stiffness. *Tribology Letters*, 56(2):397–402, 2014.

[6] E. Rabinowicz. The nature of the static and kinetic coefficients of friction. *Journal of Applied Physics*, 22(11):1373–1379, 1951.

[7] Z. Yang, H. P. Zhang, and M. Marder. Dynamics of static friction between steel and silicon. *Proceedings of the National Academy of Sciences of the United States of America*, 105(36):13264–8, Sep 2008.

[8] M. H. Müser. How static is static friction? *Proceedings of the National Academy of Sciences*, 105(36):13187–13188, 2008.

[9] P. Berthoud and T. Baumberger. Shear stiffness of a solid–solid multicontact interface. *Proceedings of the Royal Society of London. Series A: Mathematical, Physical and Engineering Sciences*, 454(1974):1615–1634, 1998.

[10] D. Mulvihill, H. Brunskill, M. Kartal, R. Dwyer-Joyce, and D. Nowell. A comparison of contact stiffness measurements obtained by the digital image correlation and ultrasound techniques. *Experimental Mechanics*, 53(7):1245–1263, 2013.

[11] X. Shi and A. A. Polycarpou. Measurement and modeling of normal contact stiffness and contact damping at the meso scale. *Journal of Vibration and Acoustics*, 127(1):52–60, 2005.

[12] J. Greenwood and J. Williamson. Contact of nominally flat surfaces. *Proceedings of the Royal Society of London. Series A. Mathematical and Physical Sciences*, 295(1442):300–319, 1966.

[13] D. Bogy. An elastic-plastic model for the contact of rough surfaces. *Journal of Tribology*, 109:257, 1987.

[14] B. N. J. Persson. Contact mechanics for randomly rough surfaces. *Surface Science Reports*, 61(4):201–227, 2006.

[15] A. Bush, R. Gibson, and T. Thomas. The elastic contact of a rough surface. *Wear*, 35(1):87–111, 1975.

[16] B. N. J. Persson. Relation between interfacial separation and load: a general theory of contact mechanics. *Physical Review Letters*, 99(12):125502, 2007.

[17] M. Ciavarella, J. Greenwood, and M. Paggi. Inclusion of "interaction" in the Greenwood and Williamson contact theory. *Wear*, 265(5):729–734, 2008.

[18] A. A. Polycarpou and I. Etsion. Analytical approximations in modeling contacting rough surfaces. *Journal of Tribology*, 121(2):234–239, 1999.

[19] C. Campana, B. N. J. Persson, and M. H. Müser. Transverse and normal interfacial stiffness of solids with randomly rough surfaces. *Journal of Physics: Condensed Matter*, 23(8):085001, 2011.

[20] B. N. J. Persson. Elastoplastic contact between randomly rough surfaces. *Physical Review Letters*, 87(11):116101, 2001.

[21] B. N. J. Persson, F. Bucher, and B. Chiaia. Elastic contact between randomly rough surfaces: comparison of theory with numerical results. *Physical Review B*, 65(18):184106, 2002.

[22] L. Pei, S. Hyun, J.-F. Molinari, and M. O. Robbins. Finite element modeling of elasto-plastic contact between rough surfaces. *Journal of the Mechanics and Physics of Solids*, 53(11):2385–2409, 2005.
[23] S. Hyun, L. Pei, J.-F. Molinari, and M. O. Robbins. Finite-element analysis of contact between elastic self-affine surfaces. *Physical Review E*, 70(2):026117, 2004.
[24] S. Akarapu, T. Sharp, and M. O. Robbins. Stiffness of contacts between rough surfaces. *Physical Review Letters*, 106(20):204301, 2011.
[25] R. Pohrt and V. L. Popov. Normal contact stiffness of elastic solids with fractal rough surfaces. *Physical Review Letters*, 108(10):104301, 2012.
[26] B. N. J. Persson. Contact mechanics for randomly rough surfaces: On the validity of the method of reduction of dimensionality. *Tribology Letters*, 58(1):1–4, 2015.
[27] L. Pastewka, N. Prodanov, B. Lorenz, M. H. Müser, M. O. Robbins, and B. N. J. Persson. Finite-size scaling in the interfacial stiffness of rough elastic contacts. *Physical Review E*, 87(6):062809, 2013.
[28] M. Paggi, R. Pohrt, and V. L. Popov. Partial-slip frictional response of rough surfaces. *Scientific Reports*, 4, 2014.
[29] R. Dwyer-Joyce, B. Drinkwater, and A. Quinn. The use of ultrasound in the investigation of rough surface interfaces. *Journal of Tribology*, 123(1):8–16, 2001.
[30] M. Kartal, D. Mulvihill, D. Nowell, and D. Hills. Determination of the frictional properties of titanium and nickel alloys using the digital image correlation method. *Experimental Mechanics*, 51(3):359–371, 2011.
[31] M. Eriten, C.-H. Lee, and A. A. Polycarpou. Measurements of tangential stiffness and damping of mechanical joints: Direct versus indirect contact resonance methods. *Tribology International*, 50:35–44, 2012.
[32] D. Nowell, D. Mulvihill, H. Brunskill, M. Kartal, and R. Dwyer-Joyce. Measurement and modelling of interface stiffness in frictional contacts. *World Tribology Congress 2013*, 2013.
[33] M. Schoenberg. Elastic wave behavior across linear slip interfaces. *The Journal of the Acoustical Society of America*, 68(5):1516–1521, 1980.
[34] J. Greenwood and J. Tripp. The contact of two nominally flat rough surfaces. *Proceedings of the Institution of Mechanical Engineers*, 185(1):625–633, 1970.
[35] P. Nayak. Random process model of rough surfaces in plastic contact. *Wear*, 26(3):305–333, 1973.
[36] C. Ruiz and D. Nowell. Designing against fretting fatigue in aeroengines. *European Structural Integrity Society*, 26:73–95, 2000.
[37] L. Witek. Failure analysis of turbine disc of an aero engine. *Engineering Failure Analysis*, 13(1):9–17, 2006.
[38] J. R. Barber, A. Klarbring, and M. Ciavarella. Shakedown in frictional contact problems for the continuum. *Comptes Rendus Mécanique*, 336(1-2):34–41, 2008.
[39] *Druck DPI 104 user manual-K0394.*
[40] ENERPAC. *Sepcification sheet for RC-50 model in RC-Series, Single-Acting Cylinders.*
[41] *IFM manual, Alicona Infinite Focus, IFM 2.15 EN 30.07.2008.*
[42] *BS EN ISO 4287:1998, Geometrical product specifications (GPS)–Surface texture: Profile method–Terms, definitions and surface texture parameters.*
[43] *BS EN ISO 4288:1998, Surface Texture: Profile Method–Rules and Procedures for the Assessment of Surface Texture.*
[44] *BS EN ISO 25178:2012, Geometrical products specifications (GPS)–Surface texture: Areal.*
[45] R. Leach. *Measurement good practice guide no. 37: The measurement of surface texture using stylus instruments.* National Physical Laboratory, 2014.
[46] J. Taylor. *Introduction to error analysis, the study of uncertainties in physical measurements.* University Science Books, 2nd edition, 1997.
[47] K. B. Datta. *Mathematical methods in science and engineering.* Cengage Learning, 2012.
[48] *Material Data Sheet for Titanium Alloy (Ti-Al-4V; ASTM Grade 5) Rod, MatWeb, www.matweb.com.*
[49] K. Johnson. *Contact mechanics.* Cambridge University Press, 1987.
[50] J. Dundurs and M. Stippes. Role of elastic constants in certain contact problems. *Journal of Applied Mechanics*, 37(4):965–970, 1970.

[51] Y. J. Ahn and J. R. Barber. Response of frictional receding contact problems to cyclic loading. *International Journal of Mechanical Sciences*, 50(10):1519–1525, 2008.
[52] L. Keer, J. Dundurs, and K. Tsai. Problems involving a receding contact between a layer and a half space. *Journal of Applied Mechanics*, 39(4):1115–1120, 1972.
[53] K. Tsai, J. Dundurs, and L. Keer. Contact between an elastic layer with a slightly curved bottom and a substrate. *Journal of Applied Mechanics*, 39(3):821–823, 1972.
[54] S. El-Borgi, R. Abdelmoula, and L. Keer. A receding contact plane problem between a functionally graded layer and a homogeneous substrate. *International Journal of Solids and Structures*, 43(3):658–674, 2006.
[55] M. Rhimi, S. El-Borgi, W. Ben Saïd, and F. Ben Jemaa. A receding contact axisymmetric problem between a functionally graded layer and a homogeneous substrate. *International Journal of Solids and Structures*, 46(20):3633–3642, 2009.
[56] J. Yan and X. Li. Double receding contact plane problem between a functionally graded layer and an elastic layer. *European Journal of Mechanics-A/Solids*, 53:143–150, 2015.
[57] V. Kahya, T. S. Ozsahin, A. Birinci, and R. Erdol. A receding contact problem for an anisotropic elastic medium consisting of a layer and a half plane. *International Journal of Solids and Structures*, 44(17):5695–5710, 2007.
[58] M. Yaylacı, E. Öner, and A. Birinci. Comparison between analytical and ansys calculations for a receding contact problem. *Journal of Engineering Mechanics*, 140(9):04014070, 2014.
[59] İ. Çömez. Frictional contact problem for a rigid cylindrical stamp and an elastic layer resting on a half plane. *International Journal of Solids and Structures*, 47(7):1090–1097, 2010.
[60] S. El-Borgi, S. Usman, and M. A. Güler. A frictional receding contact plane problem between a functionally graded layer and a homogeneous substrate. *International Journal of Solids and Structures*, 51(25):4462–4476, 2014.
[61] T. Chaise, R. Paynter, and D. Hills. Contact analysis of a semi-infinite strip pressed onto a half plane by a line force. *International Journal of Mechanical Sciences*, 81:60–64, 2014.
[62] D. Hills, P. Kelly, D. Dai, and A. Korsunsky. *Solution of crack problems: the distributed dislocation technique*. Kluwer Academic Publishers, 1996.
[63] F. Erdogan, G. D. Gupta, and T. Cook. *Numerical solution of singular integral equations*. Springer, 1973.
[64] J. Dundurs. Elastic interaction of dislocations with inhomogeneities. *Mathematical Theory of Dislocations*, pages 70–115, 1969.
[65] K. Parel and D. Hills. Frictional receding contact analysis of a layer on a half-plane subjected to semi-infinite surface pressure. *International Journal of Mechanical Sciences*, 2016.
[66] J. R. Barber. *Elasticity*, volume 172. Springer, 2009.
[67] D. Hills, R. Ramesh, R. Fleury, and K. Parel. A unified approach for representing fretting and damage at the edges of incomplete and receding contacts. *Tribology International*, 108:16–22, 2017.